UNIVERSITY OF CALIFORNIA, SAN DIEGO

Long-term geomagnetic variations: Linking paleomagnetic observations, statistical analyses, and numerical geodynamo simulations

A dissertation submitted in partial satisfaction of the
requirements for the degree
Doctor of Philosophy

in

Earth Sciences

by

Margaret S. Avery

Committee in charge:

Professor Catherine G. Constable, Chair
Professor Steven Cande
Professor Patrick Diamond
Professor Jeffrey S. Gee
Professor David Gubbins
Professor Lisa Tauxe

2017

The dissertation of Margaret S. Avery is approved, and it is acceptable in quality and form for publication on microfilm and electronically:

_____

_____

_____

_____

_____

_____

Chair

University of California, San Diego

2017

DEDICATION

For my mother and nieces.

EPIGRAPH

I am among those who think that science has great beauty. A scientist in his laboratory is not only a technician, he is also a child placed before natural phenomenon, which impress him like a fairy tale.

– Marie Curie

Your assumptions are your windows on the world. Scrub them off every once in a while, or the light won't come in.

–Isaac Asimov

TABLE OF CONTENTS

LIST OF FIGURES

LIST OF TABLES

ACKNOWLEDGEMENTS

I would like to begin by acknowledging my advisor Cathy Constable. I have learned a tremendous amount about being a good scientist due to her thoughtful mentorship. Without her guidance this dissertation would not have been possible. I am also grateful for the opportunities I have had to present my research at conferences and workshops. Thank you, Cathy, for your support, generosity, and friendship.

Next, I would like to thank the members of my doctoral committee for their helpful discussions and advice. I am grateful to Jeff Gee for his patience, and for the example he sets of being a careful and thorough scientist. I appreciate the opportunity to assist Jeff with field work in the Bishop Tuff, and all his help furthering my understanding of marine magnetism. Thanks to Dave Gubbins for all the trips he made to UCSD, for advice on geodynamos and helping supply me with computer time, and great a walk on the Ilkley Moor! I would like to thank Lisa Tauxe for lots of helpful advice about both research and life, and for her paleomagnetism class which provided me with an opportunity for field work in Georgia. Thank you to Lisa also for Thanksgiving dinners and visits from the taco cart! Thanks to Steve Cande for helpful discussions about marine magnetic anomalies and his enthusiastic support of our new work with old deep-tow data. Thank you to Patrick Diamond for his timely responses to all my emails and for making time for our meetings. Thanks to Dave Stegman for his service on my committee and for having my as a TA for his undergraduate class; congratulations on the birth of Nevada!

I would like to thank my other coauthors, Julie Bowles, Mike Jackson, and Chris

Davies. Julie and Mike contributed to the research presented in Chapter 2, and greatly to my knowledge of rock magnetism. Thanks to Chris Davies for all of the useful discussions about geodynamics and beginning a career in academia.

I want to acknowledge all past and current members of the Geomagnetism and Paleomagnetism Group at SIO. Thanks to Jason Steindorf for laboratory help during my paleointensity experiments. I appreciate the kind support and advice from other magnetism students and postdocs with whom I overlapped: Ron Shaar, Saiko Sugisaki, Shuhui Cai, Chris Davies, Leah Ziegler, Lindsay Smith-Boughner, Geoff Cromwell, Rachel Marcuson, Shelby Jones-Cervantes, Sarah Maher, Hanna Asefaw, and Christeanne Santos. Thanks for all the group meetings, paper discussions, and other "team-building" shenanigans.

Thanks to the other students that have made studying at Scripps such a pleasure. Especially my geoscience and geophysics friends: Erica Aaron, Jasmeet Dhaliwai, Wenyaun Fan, Soli Garcia, James Holmes, Shannon Klotsko, Nick Mancinelli, Brad Peters, Robert Peterson, Anand Ray, Shi Sim, Kang Wang, Wei Wang, Kyle Withers, and Qian Yao.

Thank you to all of the staff in the SIO Graduate Program and Earth Section Business Offices whose administrative help has been indispensable.

Last, but certainly not least, I am grateful to my family for their encouragement and support. Thanks to my parents and grandparents for encouraging my academic success. Thanks to my brothers for all the dad jokes. I am especially grateful to Lucas for his loving support, and to Higgins for his affectionate companionship. You guys are the best co-conspirators.

Chapter 2, in part, is currently being prepared for submission for publication of the material. Avery, Margaret S., Gee, Jeffrey S., Bowles, Julie A., and Jackson, Michael J. The dissertation author was the primary investigator and author of this material. This material is based on work supported by National Science Foundation grant number EAR0943999.

Chapter 3, in full, is a reprint of the material as it appears in *Earth and Planetary Science Letters*, vol.467, doi:10.1016/j.epsl.2017.03.020, 2017. Avery, Margaret S., Constable, Catherine G., and Gee, Jeffrey S. The dissertation author was the primary investigator and author of this paper. This work was funded by the National Science Foundation CSEDI program grant number EAR1065597.

Chapter 4, in part, has been submitted for publication of the material as it may appear in *Physics of Earth and Planetary Interiors*. Avery, Margaret S., Constable, Catherine G., Davies, Christopher, and Gubbins, David. The dissertation author was the primary investigator and author of this paper. This work was funded by the NSF grant numbers EAR1065597 and EAR1623786. This work used the Extreme Science and Engineering Discovery Environment (XSEDE), which is supported by National Science Foundation grant number ACI1053575.

Chapter 5, in part, is currently being prepared for submission for publication of the material. Avery, Margaret S., Constable, Catherine G., Davies, Christopher, and Gubbins, David. The dissertation author was the primary investigator and author of this material. This work was funded by the NSF grant numbers EAR1065597 and EAR1623786. This work used the Extreme Science and Engineering Discovery Environment (XSEDE), which is supported by National Science Foundation grant number ACI1053575.

VITA

2017	Ph. D. in Earth Sciences, University of California, San Diego
2014	M. S. in Earth Sciences, University of California, San Diego
2009	B. A. in Physics, State University of New York at Geneseo

PUBLICATIONS

Avery, M.S., J.S. Gee, J.A., Bowles, M.J. Jackson. Paleointensity estimates from ignimbrites: The Bishop Tuff revisited. *Geochem. Geophys. Geosyst.*, (in-prep).

Avery, M.S., C.G. Constable, D. Gubbins, and C. Davies. Asymmetric growth and decay of the geomagnetic dipole field examined with numerical dynamo simulations. *Physics of the Earth and Planetary Interiors*, (in-prep).

Avery, M.S., C.G. Constable, C. Davies, and D. Gubbins. Spectral methods for analyzing energy balances in geodynamo simulations. *Physics of the Earth and Planetary Interiors*, (submitted).

Avery, M.S., C.G. Constable, and J.S. Gee, 2017. Asymmetry in Growth and Decay of the Geomagnetic Dipole Revealed in Seafloor Magnetization. *Earth and Planetary Science Letters*, 467 (1), 79-88.

Chourasia, A., **M. Avery**, A. Willis, S. Greenwood, C. Davies, C. Constable, and D. Gubbins, 2016. Visualization of Geodynamo Simulations. In Proceedings of the XSEDE16 Conference on Diversity, Big Data, and Science at Scale (XSEDE16). 58:1-58:3.

Matsui, H., et al., 2016. Performance benchmarks for a next generation numerical dynamo model. *Geochem. Geophys. Geosyst.*, 17(5), 1586-1607.

Bowles, J.A., J.S. Gee, M.J. Jackson, and **M.S. Avery**, 2015. Geomagnetic paleointensity in historical pyroclastic density currents: Testing the effects of emplacement temperature and postemplacement alteration. *Geochem. Geophys. Geosyst.*, 16(10), 3607-3625.

ABSTRACT OF THE DISSERTATION

Long-term geomagnetic variations: Linking paleomagnetic observations, statistical analyses, and numerical geodynamo simulations

by

Margaret S. Avery

Doctor of Philosophy in Earth Sciences

University of California, San Diego, 2017

Professor Catherine G. Constable, Chair

An interdisciplinary approach that combines the gathering of paleomagnetic observations with the use of sophisticated analysis and numerical geodynamo simulations can help progress our knowledge of long-term variations in paleomagnetic intensity. Paleointensity is difficult to determine accurately, and made more difficult by the limited geologic materials suitable for paleointensity experiments. In this dissertation we add a new paleointensity estimate from the Bishop tuff ignimbrite, which erupted in central California ∼767 thousand years ago. We study the impact of post-emplacement alteration on the recording of a

thermal remanent magnetization (TRM). Ignimbrites are potentially valuable for estimating paleointensity, but we find care must be taken to avoid regions of alteration. The seafloor also records a TRM and therefore paleointensity, and because seafloor is continuously spreading from mid-ocean ridges it has the advantage of preserving a time series of geomagnetic field behavior. We analyze near-bottom marine magnetic anomaly data. We find confirmation of an asymmetry between rates of dipole growth and decay previously observed in sedimentary data, by low-pass filtering stacked magnetization solutions and assessing the distribution of its derivatives. We also observe this field behavior during another time period, 9.3-11.2 Ma in addition to 0-2 Ma. The combined effects of magnetic induction and diffusion control changes in magnetic energy, but with different characteristic time and length scales. We use geodynamo simulations to help evaluate if different processes control dipole growth and decay. We introduce power spectral tools for assessing the energy balance as a function of frequency. Within our collection of geodynamo simulations we find several examples of Earth-like asymmetry in dipole rates of change. In these simulations changes in magnetic energy are more coherent with ohmic dissipation than with induction within the frequency range where the dynamos display an Earth-like distribution of dipole derivatives. We find this asymmetry between growth and decay is associated with a transition in the dominant length scale of the flow. Geomagnetic dipole variability provides an important constraint on the temporal dynamics of the geodynamo; these studies of the paleomagnetic record and computational dynamo simulations complement each other.

Chapter 1

Introduction

1.1 Preface

Earth generates its own magnetic field, which is shaped by the solar wind into the magnetosphere. This geomagnetic field varies in morphology and strength with time due to Earth's own internal dynamics and its interactions with the external solar wind. The geomagnetic field is an important part of Earth's environment; it shields life on Earth's surface from harmful solar radiation. Organisms that can sense the magnetic field use it as a reference frame for navigation (e.g. sea turtles, pigeons, magnetotactic bacteria). Humans are unable to sense magnetic fields, and must use instruments to make observations. Direct observations of the geomagnetic field have been carried out for only the past few centuries, but with indirect methods of measuring the magnetic field recorded by geologic and archeological materials we can piece together an understanding of field behavior extending billions of years back in time. Experiments to determine the paleointensity are difficult, and as a

result there are fewer paleointensity than directional data and we know less about the past intensity variations. This dissertation expands our knowledge of the long-term behavior of geomagnetic intensity by contributing 1) new paleointensity data from the Bishop tuff, 2) confirmation in seafloor magnetization of an asymmetry between growth and decay rates of the field strength previously observed in sedimentary records, and 3) a conceptual model for the asymmetric growth and decay based on the behavior of numerical geodynamo simulations and spectral tools for analyzing simulations.

1.1.1 Geomagnetic impact on society

The magnetosphere, the region of space surrounding Earth where charged particles are influenced by the geomagnetic field, acts as a shield deflecting solar radiation and cosmic rays. The strength of the geomagnetic field determines the ability of the magnetosphere to protect the surface from these charged particles. A weak geomagnetic field will deflect less space weather, which is damaging to human electronic systems (Lanzerotti, 2001). Without a magnetosphere solar wind would strip away the upper atmosphere including the ozone layer which absorbs ultaviolet radiation that is harmful to life (Diffey, 1991). To predict and adapt to future changes in the geomagnetic field, we must have knowledge of past field variations. As our society grows increasingly dependent on electronic systems for our critical infrastructure (e.g. communication, transportation, food and water supply, public health, etc.) it is important that we address geomagnetic questions, such as: How strong/weak can the field get? How quickly can it change?

1.1.2 Earth's deep interior, a cooling Earth and dynamic core

Observations of the geomagnetic field made at the surface can be used to gain insights into Earth's deep interior. Convective motion of the molten iron outer core generates the geomagnetic field and sustains it against ohmic dissipation in a process called the geodynamo. The liquid iron in the outer core has viscosity comparable to water at Earth's surface (Poirier, 1988), and high thermal and electrical conductivities (Pozzo et al., 2012). We believe the current driving energy for the geodynamo comes from the secular cooling of Earth causing freezing of the inner-core, which releases latent heat and excludes light elements generating thermal and compositional buoyancy (Nimmo, 2015; Davies et al., 2015). A detailed record of long-term paleomagnetic field variations is needed to reconstruct the evolution of the geodynamo and can provide important information on Earth's thermal history.

1.2 Ways to study the geomagnetic field

The paleomagnetic studies presented in Chapters 2 and 3 are based on theoretical underpinnings and historical context outlined here.

1.2.1 Highlights in the history of geomagnetic knowledge

The past few millennia have seen a progressive evolution in our knowledge of the geomagnetic field. Here we present some key advances in our understanding. A more complete history can be found in the Treatise on Geophysics (Kono, 2015). Ancient Greek and Chinese scholars made discoveries of natural magnets and Earth's magnetic field. Aristotle attributed

the earliest known observations of natural magnets to the Greek philosopher Thales of Miletus (624 - 546 BC). In 1088 AD Shen Kua recorded how to magnetize a compass needle, and made the first mention of magnetic declination (the horizontal angle between magnetic and true north). Accelerated progress began when these discoveries migrated to Europe, especially during the Scientific Revolution. Petrus Peregrinus in his 1269 AD letter, *Epistola*, explained various properties of magnets including: magnets have two poles, opposite poles attract and similar poles repel, and there are no magnetic monopoles. Georg Hartmann first documented magnetic inclination (the vertical angle between the magnetic field and horizontal plane) at the start of the Scientific Revolution in 1544. The seminal work of William Gilbert, *De Magnete*, was published in 1600. In it he described the similar dipolar magnetic fields produced by a spherical magnet and the earth, and that magnetic inclination is a function of latitude for both. Once the geomagnetic field could be used as a reference frame for navigation magnetic observations flourished. The temporal variability (secular variation) of the geomagnetic field was discovered through a series of declination measurements made in London by William Borough, Edmund Gunter, and Henry Gellibrand between 1580 and 1635. Edmond Halley conducted an expedition dedicated to mapping magnetic declination in the Atlantic, and published the first magnetic chart in 1701. Carl Friedrich Gauss devised a method of measuring the absolute field intensity published in 1832, and with Wilhelm Weber, organized the first network of geomagnetic observatories. Gauss also invented spherical harmonics to separate the internal and external field sources finding the internal source was the larger contribution to the field at Earth's surface.

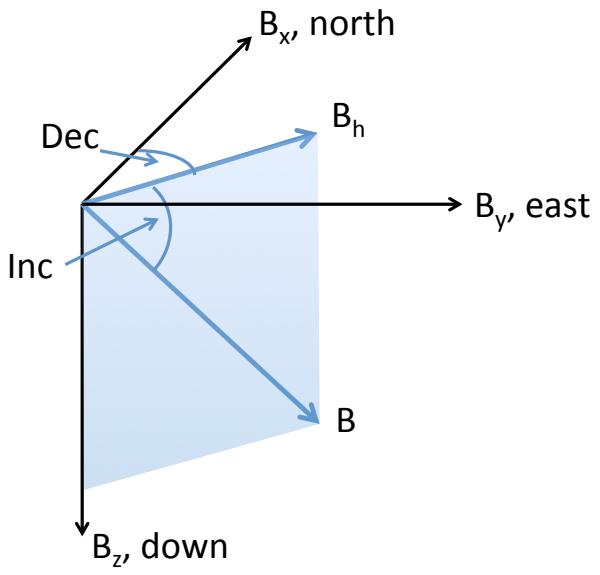

Figure 1.1: Geomagnetic elements in a local coordinate system.

1.2.2 Descriptions of Earth's Magnetic Field

From these historical works we know that magnetic fields are vector fields with both direction and magnitude at any point. Magnetic measurements made at Earth's surface are often made in a local coordinate system. The components B_x, B_y, B_z of the magnetic field vector $\mathbf{B}$ have axes pointing toward geographic north, geographic east, and vertically down respectively (Figure 1.1). Declination is the angle between geographic north and the horizontal projection of the field, $Dec = \tan^{-1}(B_y/B_x)$. Inclination is the angle between the horizontal place and the field vector, $Inc = \tan^{-1}(B_z/\sqrt{(B_x^2 + B_y^2)}$. The total field intensity is $B = |\mathbf{B}| = \sqrt{(B_x^2 + B_y^2 + B_z^2)}$. Alternatively, geomagnetic observations can be described in a geocentric coordinate system as spherical components B_r, B_θ, B_ϕ, where $\mathbf{r}$ is radius, θ and ϕ are the angular coordinates colatitude and longitude.

The magnetic field vector, $\mathbf{B}$, at the mean radius of Earth's surface, a, can be repre-

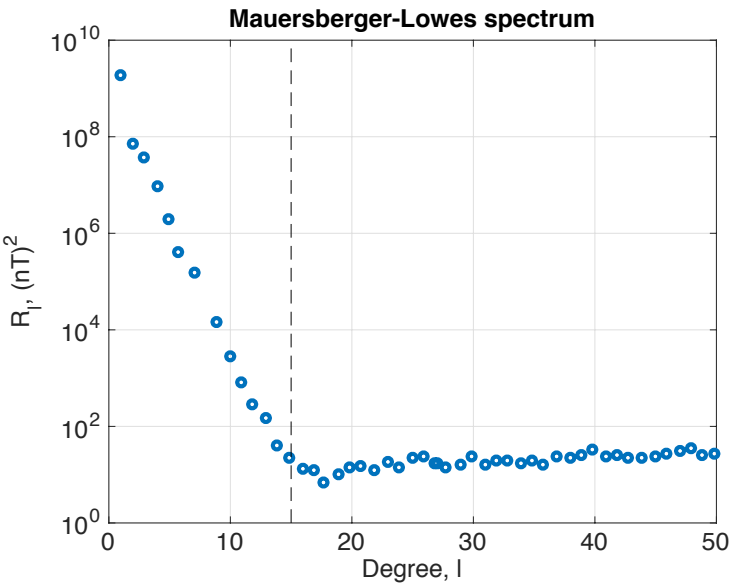

Figure 1.2: Spatial power spectrum of the geomagnetic field at Earth's surface.

sented as the superposition of internal and external sources

$$\mathbf{B}(a,\theta,\phi,t) = \mathbf{B}_i(a,\theta,\phi,t) + \mathbf{B}_e(a,\theta,\phi,t) \tag{1.1}$$

At Earth's surface the external field is small compared to the internal field and typically varies on short time scales (seconds to months), so for this study we neglect the external field. The internal field can be expressed as the gradient of an internal field potential $\mathbf{\Psi}_i$, $\mathbf{B}_i(a,\theta,\phi,t) = -\nabla\mathbf{\Psi}_i(a,\theta,\phi,t)$. The potential $\mathbf{\Psi}_i$ satisfies Laplace's equation $[\nabla^2\mathbf{\Psi}_i = 0]$ everywhere outside the source region, so the solution can be expressed in a spherical harmonic basis

$$\mathbf{\Psi}_i(a,\theta,\phi,t) = a\sum_{l=1}^{\infty}\frac{a}{\mathbf{r}}^{l+1}\sum_{m=0}^{l}\left[g_l^m(t)\mathrm{cos}m\phi + h_l^m(t)\mathrm{sin}m\phi\right]P_l^m(\mathrm{cos}\theta) \tag{1.2}$$

where l and m are the degree and order of the spherical harmonic expansion, $g_l^m(t)$ and $h_l^m(t)$ are the time-dependent Gauss coefficients, the P_l^m are Schmidt-normalized associated Legendre functions. The Gauss coefficients g_l^m and h_l^m are retrieved given a set of geomagnetic

observations and they have the same units as the observed magnetic field vector. An example of a field model for the present day field will be discussed in section 1.3.1. The contribution of different length scales of the internal field at any radius **r** in the area free of magnetic sources (i.e. down to the core mantle boundary (CMB), based on the approximation that the mantle is an insulator) can be visualized by the spatial power spectrum, also called the Mauersberger-Lowes spectrum (Figure 1.2),

$$R_l(\mathbf{r}) = (l+1)\left(\frac{a}{r}\right)^{(2l+4)} \sum_{m=0}^{l} \left[(g_l^m)^2 + (h_l^m)^2\right]. \tag{1.3}$$

At Earth's surface the magnetic field is dominantly dipolar. Power decreases exponentially with decreasing length scale until approximately degree 14, where it flattens due to the contribution of the crustal magnetization. The internal magnetic field is therefore masked beyond degree 14.

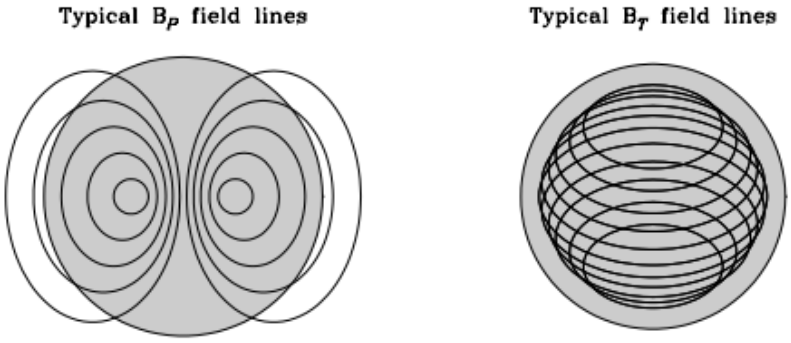

Figure 1.3: Poloidal and toroidal magnetic field parts.

Another useful representation of the magnetic field is as the superposition of poloidal and toroidal parts:

$$\mathbf{B} = \nabla \times (\mathcal{T}\mathbf{r}) + \nabla \times \nabla \times (\mathcal{P}\mathbf{r}) = \mathbf{B}_{\mathcal{T}} + \mathbf{B}_{\mathcal{P}} \tag{1.4}$$

where $\mathcal{T}$ and $\mathcal{P}$ are scalar functions of $\mathbf{r}$. The toroidal part can be written as $\mathbf{B}_{\mathcal{T}} = (\nabla \times \mathbf{r})\mathcal{T} = -\mathbf{r} \times \nabla\mathcal{T}$ because $\nabla \times \mathbf{r} = 0$, so $\mathbf{r} \cdot \mathbf{B}_{\mathcal{T}} = 0$. The toroidal magnetic field has no radial component. Its force lines are confined to the interior of the conducting sphere, and are not visible outside of the conducting region (Figure 1.3b). Only the poloidal part of $\mathbf{B}$ is observable at Earth's surface (Figure 1.3a). The core's currents can also be represented in terms of poloidal and toroidal parts. Toroidal magnetic fields are generated by poloidal currents, and poloidal fields by toroidal currents.

1.2.3 Thermal Remanent Magnetization, Néel theory

The crustal magnetization which flattens the spatial power spectrum of the geomagnetic field above $l = 14$ holds a record of past geomagnetic field behavior, and using laboratory experiments we can interpret this magnetization. To do this it is important to understand how some geologic materials become and remain magnetized. Further detail can be found in Tauxe et al. (2016) and Dunlop and Özdemir (2015). An external magnetic field will align the electron spins of the atoms within a material inducing a net magnetization. For relatively weak external fields, the induced magnetization is proportional to the intensity of the external field. Ferromagnetic materials possess magnetic remanence i.e. they generate a magnetic field even in the absence of an applied field. Spontaneous remanence is caused by the strong exchange interactions between neighboring unpaired electron spins. This behavior is temperature dependent. Above the Curie temperature (T_C) cooperative spin behavior disappears entirely and the material becomes paramagnetic (Figure 1.4a). Different magnetic minerals have different T_C. Ferromagnetic particles will seek a configuration that minimizes

their total energy balance, which controls the magnetization. Single-domain sized grains are uniformly magnetized meaning their magnetic energy is minimized when the magnetic moments of each atom are all parallel.

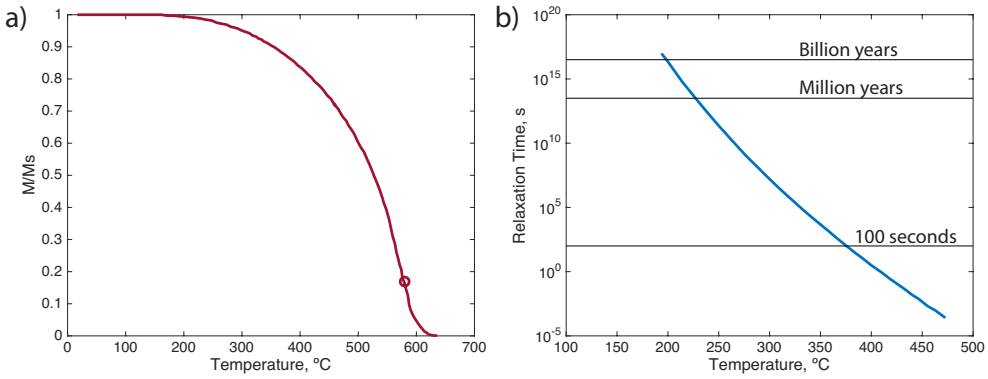

Figure 1.4: Thermal remanent magnetization properties, Curie temperature and relaxation time. a) Variation in magnetization as a function of temperature for a ferromagnetic grain. The Curie temperature is marked with a circle. Below the Curie temperature the grain is ferromagnetic and above the Curie temperature it is paramagnetic. b) Variation of relaxation time as a function of temperature of magnetite grains with a width of 30 nm and a length to width ratio of 1.3:1. Modified from Tauxe et al. (2016).

Naturally ferromagnetic materials such as magnetite and hematite can preserve a record of remanent magnetization for long periods of time. This remanence is called the natural remanent magnetization (NRM), and can be acquired by several mechanisms: the alignment of magnetic sediments with an external field during deposition produces a depositional remanent magnetization (DRM), the chemical alteration or growth of magnetic minerals in the presence of an external magnetic field produces a chemical remanent magnetization (CRM), and cooling a magnetic mineral in the presence of an external field produces a thermal remanent magnetization (TRM).

For our studies of paleointensity recorded by the Bishop tuff and seafloor magnetization it is important to understand TRM acquisition. Louis Néel established the theoretical

basis for how magnetic materials preserve magnetic fields. Thermal remanent magnetization is controlled by the relaxation time, τ, of the magnetic grain, i.e. the time it would take for the spontaneous magnetization of the grain to decay to $1/e$ in the absence of an external magnetic field (the e-folding time). The relaxation time is controlled by competition between magnetic anisotropy energy and thermal energy,

$$\tau = C^{-1} e^{\frac{Kv}{kT}} \tag{1.5}$$

where C is a frequency factor, K the magnetocrystalline anisotropy parameter, v grain volume, and k the Boltzmann constant. The relationship between relaxation time and temperature is exponential. The temperature above which the grain is superparamagnetic and below which the magnetization is locked is called the blocking temperature, T_b (Figure 1.4b). Below T_b relaxation time increases sharply and the magnetization is set, the material acquires a thermal remanent magnetization (TRM). A grain held at a temperature above its T_b in an external field will equilibrate with the applied field, when the grain cools below T_b it will lock in the conditions of the magnetic field, recording it for long time scales determined by the grain size, shape, and composition.

A natural sample (e.g. volcanic rock) will have an assemblage of magnetic minerals with a distribution of grain shapes, sizes, and compositions, and a corresponding range of blocking temperatures over which they acquire a TRM. The remanence acquired over a range of temperatures is a partial TRM (pTRM). According to Néel theory for single-domain grains pTRMs are additive and reciprocal: 1) each pTRM is a vector and the total TRM is the vector sum of pTRMs, and 2) the blocking temperature on cooling for each pTRM

is the same as its unblocking temperature on heating. By heating a rock in the absence of an external magnetic field to some temperature T, grains with T_b less than T will become randomized, a process used to thermally demagnetize samples to assess their TRM vector. For paleomagnetic samples collected in situ and for which geographic orientation is also recorded, the direction of the ancient magnetic field recorded by the NRM can be recovered by progressive thermal demagnetization.

1.2.4 Absolute paleointensity

The magnetization of single-domain grains is proportional to the strength of weak external fields such as the geomagnetic field at Earth's surface, so:

$$M_{NRM} \propto \alpha_{anc} B_{anc} \quad \text{and} \quad M_{lab} \propto \alpha_{lab} B_{lab} \tag{1.6}$$

where α_{anc} and α_{lab} are dimensionless constants of proportionality. If the mechanism of remanence acquisition can be approximated in the laboratory and $\alpha_{anc} = \alpha_{lab}$, the ancient field strength, B_{anc}, can be found with the relationship: $B_{anc} = \frac{M_{NRM}}{M_{lab}} B_{lab}$, by measuring the sample's ancient magnetization, M_{NRM}, and then using a laboratory field of known intensity, B_{lab}, to produce a laboratory magnetization, M_{lab}. See Tauxe and Yamazaki (2015) for a review.

In practice however, measuring a sample's paleointensity is not this simple. The remanence acquired in the lab may not have the same proportionality constant as the ancient remanence ($\alpha_{anc} \neq \alpha_{lab}$), if for example the specimen's capacity to acquire remanence has altered. The assumption of linearity between the remanence and the applied field may not

hold. The NRM may have multiple components acquired at different times, with different proportionality constants or by different mechanisms. The preferred laboratory protocol for determining paleointensity, which includes checks for alteration and non-single-domain behavior, requires many (30 - 40) heating cycles; it is difficult to find materials that do not alter during the experiment.

Because it is experimentally difficult to determine, the history of intensity fluctuations is challenging to establish. The paleointensity database is sparsely populated for times older than 5 Ma, and there are even fewer studies the farther back in time one looks. Fundamental properties of the paleomagnetic field such as its strength and variation over time are debated (Tauxe et al., 2013). This scarcity of absolute intensity information is partially the result of the difficulty in finding geological materials that contain dominantly single-domain particles that are also thermally stable enough to withstand the many laboratory heating cycles required in paleointensity experiments. Chapter 2 is an example of a paleointensity experiment addressing this issue. It tests if the Bishop tuff ignimbrite (volcanic ash flow) can reliably record paleointensity. Ignimbrites are potentially valuable for paleointensity experiments; some ignimbrites have been shown to contain single domain sized magnetite grains preserved in silicic glass (Geissman et al., 1983; Schlinger et al., 1991; Worm and Jackson, 1999), and ignimbrites are usually well suited for radiometric dating (e.g. McIntosh et al., 1990; Van den Bogaard and Schirnick, 1995; Sarna-Wojcicki et al., 2000; Crowley et al., 2007). Paleointensity studies from a single time are important, but we can learn about past geomagnetic field behavior more efficiently by studying time series of magnetic remanence such as is recorded by the seafloor perpendicular to tectonic spreading ridges.

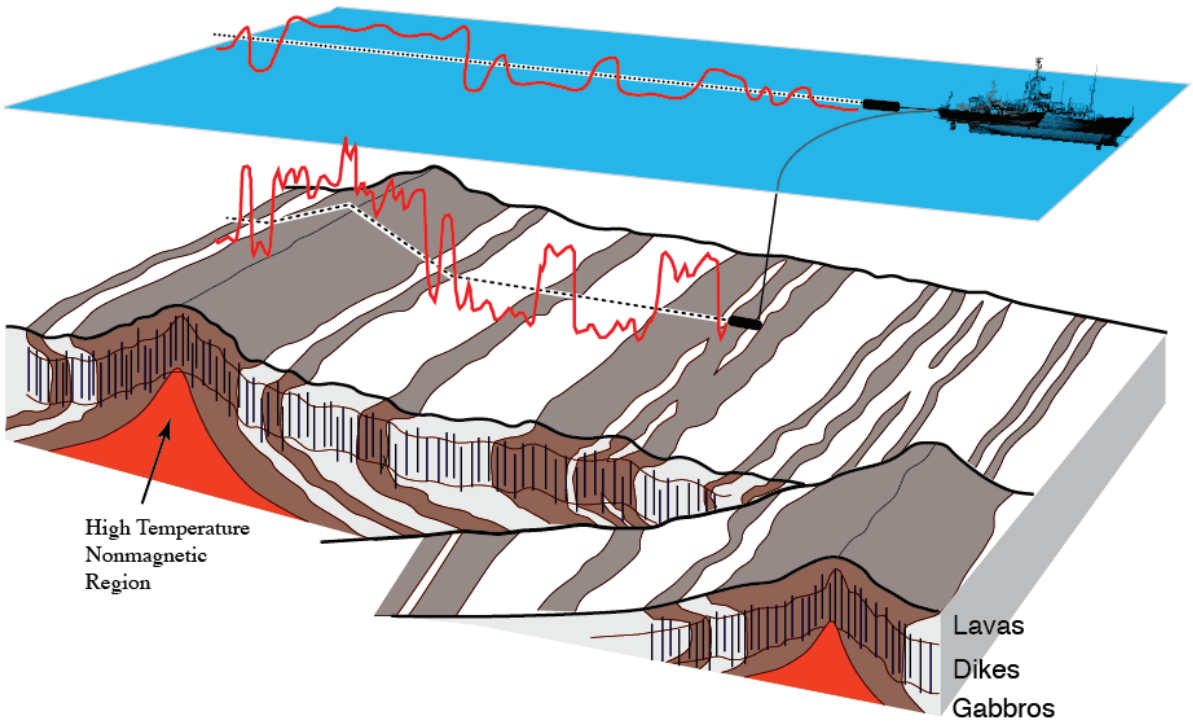

Figure 1.5: A cartoon of marine magnetic anomaly source layers and measurement. Geomagnetic polarity time scale is represented with grey normal polarity crust and white reverse. Red lines are the measured magnetic anomaly. The near-bottom data constrains more high frequency signal than the sea-surface data. Modified from Gee and Kent (2007).

1.2.5 Crustal magnetization and marine magnetic anomalies

The rocks that make up Earth's crust contain magnetic minerals that record an NRM if they are at a temperature below their blocking temperature. The type of rock, concentration of ferromagnetic minerals, alteration history, and geomagnetic field state at the time of NRM acquisition all control spatial variations in crustal magnetization. This crustal magnetization is visible in the global spatial geomagnetic spectrum as a flattening in the spatial power spectrum around and above degree 14 (Figure 1.2). When geomagnetic surveys are conducted, the spatial patterns of magnetization remaining after the background

core field contribution is subtracted are referred to as magnetic anomalies. Continental crustal magnetization can be very complex, but oceanic crust generally has a simpler signal.

As new seafloor is created at an oceanic ridge, it cools and acquires a TRM that captures the state of the geomagnetic field at that time. As the seafloor spreads it produces a log of past geomagnetic field variations. The dominant geomagnetic signal recorded in the oceanic crust is the pattern of field reversals. The rapid transition between normal and reverse polarity creates a large crustal magnetization contrast that produces variations in the magnetic field that can be measured at the sea surface. Magnetic anomalies are lineated parallel to their mid-ocean ridge, which has been essential for documenting the global pattern of geomagnetic reversals since ∼160 Ma. The reversal pattern, calibrated with ages from seafloor samples, provides the basis for the geomagnetic polarity time scale (GPTS). Gee and Kent (2007) provide a review of seafloor magnetization.

The seafloor also records magnetic anomalies at length scales both longer and shorter than those dominated by reversals. These anomalies are the combined product of a geomagnetic signal (e.g., paleointensity variations, directional excursions, and polarity reversals), modulated by crustal accretionary processes (e.g., variations in geochemistry or the pattern of lava accumulation), and geometry of the source region. Despite the challenge in decoupling the crustal accretionary signal, significant progress has been made in documenting short-wavelength anomaly fluctuations that may be due to geomagnetic field behavior. Marine magnetic surveys are usually conducted with a magnetometer at the sea surface, but collecting anomaly data near the seafloor magnetic source layer preserves higher-frequency variations ('tiny wiggles' or cryptochrons) that are attenuated in sea-surface anomaly data

that is a vital component of these studies (Figure 1.5). Some tiny wiggles are coherent between near-bottom profiles and also similar to independent records of field intensity from sediments; this suggests a significant geomagnetic intensity signal may be preserved in the oceanic crustal magnetization (Gee et al., 2000; Bowers et al., 2001; Bowles et al., 2003).

1.3 Overview of geomagnetic field behavior

1.3.1 Present day field

The present day geomagnetic field at the surface is mostly dipolar in structure, but also has some important deviations from a geocentric axial dipole field (GAD, a dipolar field aligned along the spin axis and centered in the earth). A widely used geomagnetic field model is the International Geomagnetic Reference Field (IGRF), and elements of the 2015 version of are plotted in Figure 1.6. Contours of the radial component of the geomagnetic field at Earth's surface are shown in Figure 1.6a. The magnetic equator corresponds to the zero contour $B_r = 0$ and differs from the geographic equator. At the magnetic poles the field is vertical (inclination is $\pm 90°$). The northern magnetic pole lies in the Arctic, at about 86° N, 160° W. Since ∼1850 the magnetic north pole has been moving northward, currently the rate is about 40 km per year. The field strength, shown in Figure 1.6b, is lowest in the South Atlantic region, a feature called the South Atlantic Anomaly. At high latitudes pairs of approximately symmetric flux patches dominate the geomagnetic field. The Pacific region shows relatively weak temporal variations compared to the rest of the globe (Figure 1.6c). These are just snapshots of the ever changing geomagnetic field.

1.3.2 Temporal geomagnetic variations

Earth's magnetic field varies in strength and direction on a broad range of time scales (Constable and Johnson, 2005). The power spectrum of a time series is the Fourier transform ($\mathfrak{F}$) of the autocovariance

$$P(f) = \mathfrak{F}\left[A(t)\right] = \int_{-\infty}^{\infty} A(t)e^{-2\pi i f t}dt, \tag{1.7}$$

it describes how much the time series varies as a function of frequency. The autocovariance of a stationary process, X, is defined as the covariance between X at time t and X at time $t + \triangle t$

$$A(t) = \mathscr{C}[X(t), X(t + \triangle t)] = \mathscr{E}[(X(t) - \bar{x})(X(t + \triangle t) - \bar{x})] \tag{1.8}$$

where $\triangle t$ is the lag and $\mathscr{E}$ the expectation operator. The power spectrum of the axial dipole component of the geomagnetic field shows the highest amplitude variations occur at low frequency (Figure 1.7).

The high latitude flux patches observed in the current field (Figure 1.6) have been present through the Holocene, and they have varied in strength and location (Korte et al., 2011) (Figure 1.8). The field has had stronger secular variation in the Atlantic hemisphere than the Pacific for at least the past 10 ka (Constable et al., 2016). This secular variation is the product of advection as well as magnetic diffusion (e.g. Amit and Christensen, 2008; Chulliat and Olsen, 2010; Chulliat et al., 2010).

Using relative paleointensity variations recorded by sediments calibrated by absolute paleointensity data, the past 2 Myr of axial dipole moment (ADM) variation was reconstructed and is shown in Figure 1.9a (Ziegler et al., 2011). On time scales longer than 15

thousand years, the dipole field has a skewed distribution of rates of change; the average growth rate is larger than the average decay (Ziegler and Constable, 2011). On million-year time scales, variations in dipole field strength can be described as a stochastic model with a balance between slow adjustments toward an average value and short-period random fluctuations (Buffett et al., 2013). The terms of this stochastic model are interpreted as the effects of magnetic diffusion and advection (Buffett et al., 2014). The frozen-flux approximation (Roberts and Scott, 1965) of neglecting diffusion is not applicable for millennial and longer time scales of field variation.

Polarity reversals occur randomly on average every few hundred thousand years, excursions (incomplete reversals) are more frequent, and both are accompanied by low field strength (Ziegler et al., 2011). The rate of polarity reversals is well established from marine magnetic anomaly studies and varies on time scales of tens of millions of years (Ogg, 2012) (Figure 1.9b). Despite progress towards a more complete understanding of paleointensity from studies such as the one described in Chapter 2, the sparseness of the paleointensity dataset makes is hard to establish fundamental properties of the paleomagnetic field such as its strength and variation over time (Tauxe et al., 2013) (Figure 1.9b), but we can say that the geomagnetic field has been present in some form for $\sim$4 Gyr.

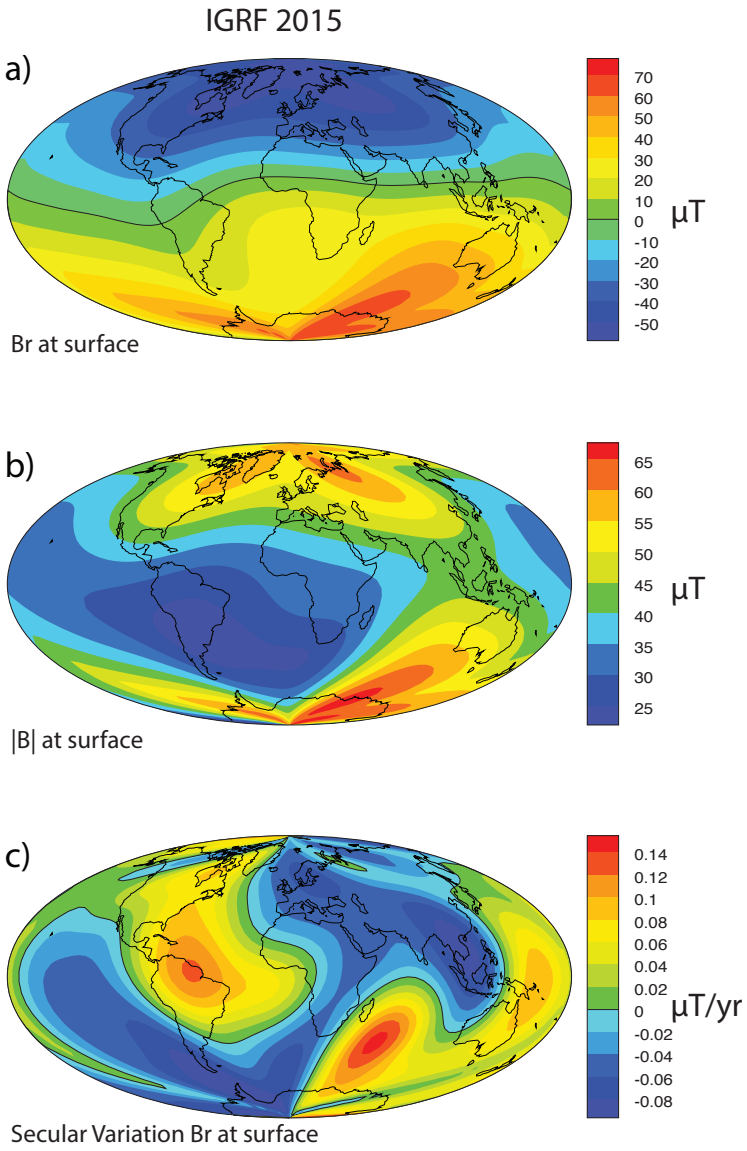

Figure 1.6: IGRF 2015 a) Radial magnetic field B_r at Earth's surface ($r = a$) in μT. b) Total field intensity $|\mathbf{B}|$ at Earth's surface in μT. c) The rate of change of B_r at Earth's surface for the year 2015 in μT/yr.

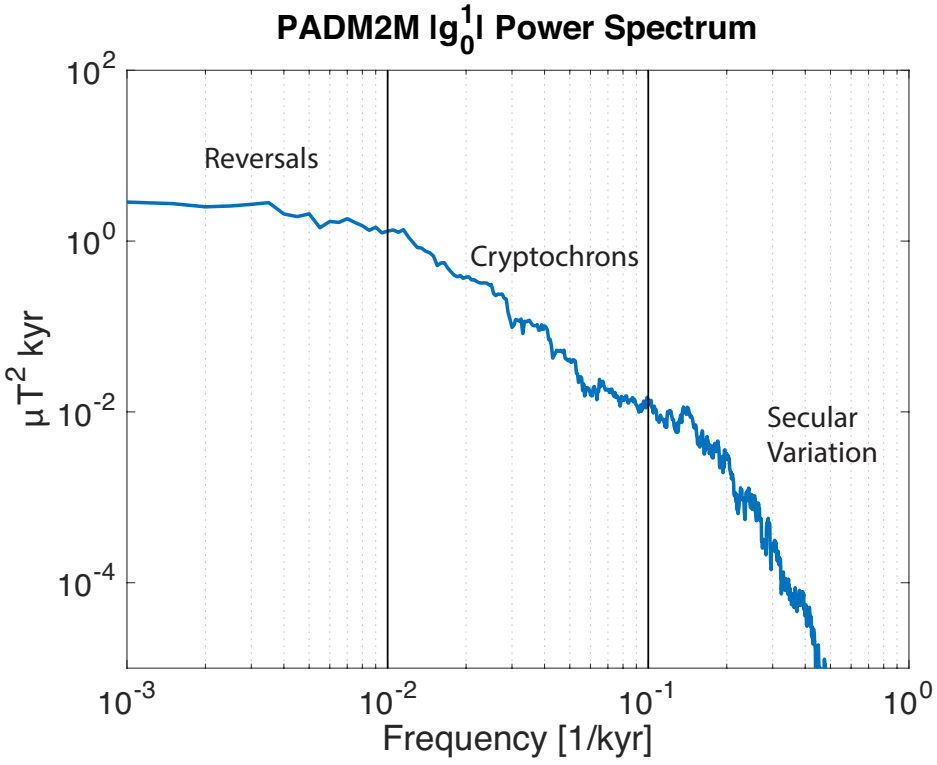

Figure 1.7: Power spectral density of g_0^1 variations as a function of frequency from the axial dipole model PADM2M (Ziegler et al., 2011).

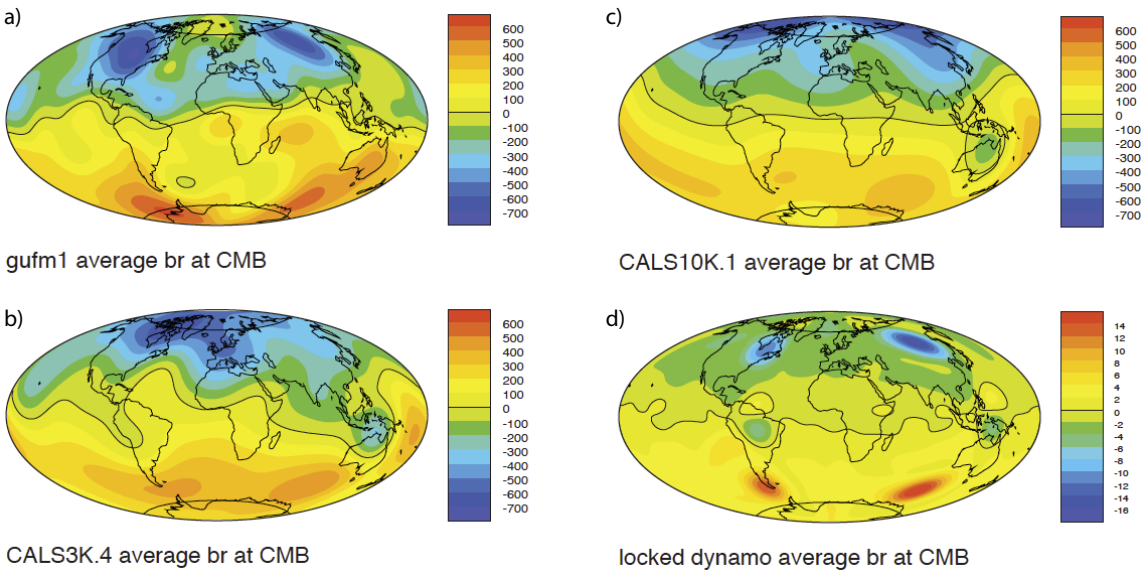

Figure 1.8: Comparison of radial magnetic field B_r at the CMB averaged over the last a) 400 years, b) 3 ka, c)10 ka, and d) the 'locked' dynamo in Gubbins et al. (2007).

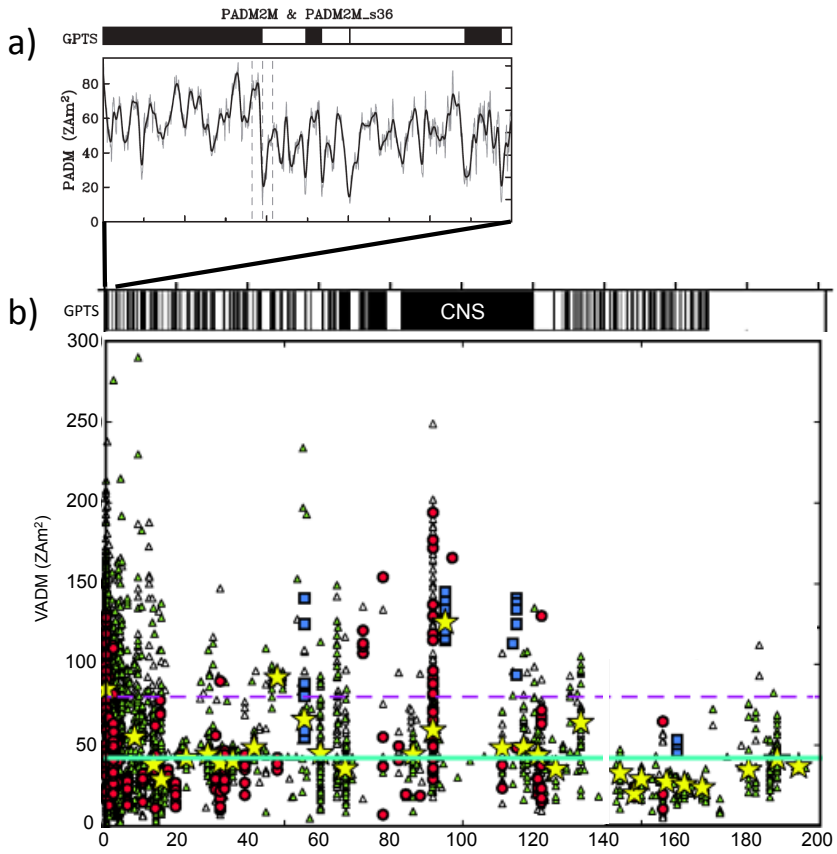

Figure 1.9: Temporal variations in paleointensity and polarity. Geomagnetic polarity time scale is plotted with normal polarity black and reverse white.a) PADM2M reconstruction of paleointensity for the past 2 Ma. b) Summary of published absolute paleointensity data downloaded from the MagIC database for the last 200 Myr reported as virtual axial dipole moment (VADM) (ZAm^2). The magenta dashed line is the present day field and the solid cyan line is a long-term average value for the last 140 Myr. Median values calculated for 5 Myr bins are shown as yellow stars. Red dots are submarine basaltic glass data. Blue squares are single crystal results. Triangles are all other data and the light green triangles meet the consistency criteria ($< 15\%$ of mean or < 5 μT). From a) Ziegler and Constable (2011) and b) Tauxe and Yamazaki (2015).

1.4 Geodynamo simulations, MHD theory and limitations

Numerical simulations of the geodynamo can help address open paleomagnetic questions such as: How has the dynamo continued to sustain itself for 4 Gyr? Why do geomagnetic reversals occur? What drives secular variation and long-term variations in paleointensity? We use geodynamo simulations to address the latter. The internal geomagnetic field is generated by convection currents in the liquid outer core of the earth, which is composed of iron, nickel, and some lighter components, likely sulfur, silicon, and oxygen. The energy for this convection is thought to come partially from the cooling of the core and partially from the thermal and compositional buoyancies of the core fluid caused by the freezing of the pure iron inner core (Nimmo, 2015; Davies et al., 2015). The buoyancy of the liquid, the spin of Earth, and the interaction of the fluid with the magnetic field control motions of this conducting fluid. The motion of the highly conductive fluid and magnetic field induces electrical currents, generating secondary magnetic field that in turn interacts with the flow. The rotating flow under convection generates helical flows, closely aligned with Earth's rotation axis. The helical flow configuration produces a nearly dipolar geomagnetic field at Earth's surface. The electromagnetic induction depends on two main phenomena, advection and diffusion of the magnetic field:

$$\frac{\partial \mathbf{B}}{\partial t} = \eta \nabla^2 \mathbf{B} + \nabla \times (\mathbf{u} \times \mathbf{B}) \tag{1.9}$$

where t is time, $\mathbf{B}$ is magnetic field, η is magnetic diffusivity, and $\mathbf{u}$ is core fluid velocity. If advection is ignored, the magnetic field will decay by diffusion. The e-folding time for dipole field decay is ∼50 kyr. Paleomagnetic observations have shown the geomagnetic field has persisted for billions of years, demonstrating the important role of advection. If magnetic diffusion is instead ignored – if the fluid were a perfect conductor – the magnetic field would be locked to the fluid motion. This condition is referred to as the 'frozen flux' approximation (Roberts and Scott, 1965) and has been widely used in the estimation of flow velocities at the core surface. Using this approximation the mean flow velocity at the CMB has been estimated at ∼0.5 mm/s (Holme, 2015).

How the geodynamo generates many features of the geomagnetic field is still not fully understood. In order to investigate the diverse physical processes of the dynamo system the equations of magnetohydodynamics (MHD) representing conservation of mass, momentum, energy, and magnetic flux (Equation 1.10), the magnetic induction equation (Equation 1.11), and an equation of state (Equation 1.12) are solved numerically.

$$\frac{1}{Pr}(\partial_t + \mathbf{u}\cdot\nabla)\mathbf{u} - \nabla^2\mathbf{u} = -\nabla\widehat{p} + \frac{1}{qE}(\nabla\times\mathbf{B})\times\mathbf{B} + Ra\Theta\mathbf{r} - \frac{1}{E}\widehat{z}\times\mathbf{u} \tag{1.10}$$

$$(\partial_t + \frac{1}{q}\nabla^2)\mathbf{B} = \nabla\times(\mathbf{u}\times\mathbf{B}) \tag{1.11}$$

$$(\partial_t + \frac{1}{q}\nabla^2)\Theta = S - \mathbf{u}\cdot\nabla\Theta \tag{1.12}$$

where Θ is the temperature profile due to the heat source S, and

$$Ra = \frac{g\alpha\beta d^5}{\kappa\nu}, \qquad E = \frac{\nu}{2\Omega d^2}, \qquad Pr = \frac{\nu}{\kappa}, \qquad Pr = \frac{\nu}{\eta}, \qquad q = \frac{Pm}{Pr} = \frac{\kappa}{\eta}$$

are the dimensionless scaling parameters: the Rayleigh, Ekman, Prandtl, magnetic Prandtl, and Roberts numbers. g is the acceleration due to gravity, α the coefficient of thermal

expansion, β is the temperature gradient at the outer boundary, d the thickness of the shell, κ thermal diffusivity, ν viscosity, and Ω is the rate of rotation. The Ekman number describes the ratio between viscous and Coriolis forces. The Rayleigh number indicates the presence and vigor of convection. The Prandtl number is the ratio of viscous to thermal diffusion rates, and the magnetic Prandtl number the viscous to magnetic diffusion rates. These dimensionless parameters and the boundary conditions are the controls for numerical geodynamo simulations. A computer solves this system of equations, one numerical time-step at a time typically for millions of time-steps, to provide the temporal evolution of the fluid velocity, the magnetic field, and the temperature in a three-dimensional, rotating, spherical shell of electrically conducting fluid.

Because of computational limitations, geodynamo simulations cannot run with Earth-like parameters. The Ekman number of Earth is estimated to be $\sim 10^{-15}$, current simulations use Ekman numbers of $10^{-3} - 10^{-7}$, so their rotation rate is in effect too slow. The outer core has very low viscosity and thermal diffusivity, relative to the magnetic diffusivity. The Prandtl number for liquid metal is typically ~ 0.1 whereas the magnetic Prandtl number is $\sim 10^{-6}$. Most simulations assume that turbulence equalizes the diffusivities and adopt Prandtl and magnetic Prandtl numbers of the order of unity, though this approximation is not well tested. Despite these limitations geodynamo simulations have produced magnetic fields with some features similar to Earth's.

In Chapters 4 and 5 we analyze million-year magnetic field behaviors of geodynamo simulations computed with the Boussinesq Leeds Spherical Dynamo Code. This dynamo code uses a conventional pseudospectral method in which the velocity and magnetic fields

are represented as toroidal and poloidal scalars expanded in θ and ϕ directions as spherical harmonics. Radial variations are represented by variable order, variable spacing, finite differences. Time-stepping is done with a predictor-corrector method (Willis et al., 2007; Davies and Gubbins, 2011). The Boussinesq Leeds Spherical Dynamo Code performs well in comparison with other dynamo codes which use various different computational methods; it is fast and scales well (Matsui et al., 2016).

Geodynamo simulations have been successful in reproducing magnetic fields with features that are similar to the geomagnetic field in some regards. External magnetic fields that are dominantly dipolar in structure have been produced. Persistent high latitude flux patches similar to the recent field have been produced using thermal boundary conditions at the CMB set by scaling the spatial distribution of lower mantle seismic structures (Willis et al., 2007; Gubbins et al., 2007) (Figure 1.8d). Davies and Constable (2014) used the frequency dependence of the power spectral density of a geomagnetic model of the dipole moment for the past 2 Myr (PADM2M Ziegler et al., 2011) to compare the temporal variation of simulations to Earth and found Earth-like dipole moment spectra (e.g. Case 1 simulations from Davies and Gubbins, 2011). Polarity reversals have been produced (e.g. Glatzmaier and Roberts, 1995; Olson et al., 2009). Buffett et al. (2014) used geodynamo simulation dipole moment variations to physically interpret the terms of the stochastic model of Buffett et al. (2013); they placed bounds on the electrical conductivity and magnetic diffusivity from paleomagnetic observations. Geodynamo simulations with variable reversal frequencies have been produced by varying the morphology and amplitude of heat flux variations (e.g. Glatzmaier et al., 1999; Driscoll and Olson, 2009; Olson et al., 2010; Olson and Amit, 2014).

The underlying assumption is that when a computer simulation generates a magnetic field that looks qualitatively similar to the geomagnetic field, it is possible that the flow and field inside the model core could be qualitatively similar to those in Earth's core.

1.5 Objectives and outline

1.5.1 Motivation for this study

An interdisciplinary approach linking paleomagnetic observations and numerical geodynamo simulations is useful because neither is perfect. The paleomagnetic record is fragmentary and noisy. Numerical dynamo simulations allow detailed knowledge of the interior magnetic field, temperature, and dynamics within the simulated fluid shell, but due to computational limitations they cannot yet run with Earth-like diffusivities or rotation rates. Simulations and paleomagnetic observations complement one another. Our goal is to identify significant phenomena seen in geomagnetic behaviors, develop a hypothesis for the underlying physical processes, and design dynamo runs to test this hypothesis. Linking dynamo theory with paleomagnetism can help the interpretation of paleomagnetic measurements and guide the direction of theoretical dynamo research. My goal as a researcher is to build further links between paleomagnetism and core geodynamics through a broad range of research topics.

1.5.2 Outline

Exploiting an interdisciplinary approach, the research contributions of this dissertation are organized as follows. In Chapter 2 we investigate if ignimbrites from the Bishop tuff are reliable recorders of paleointensity with the goal of adding to the catalog of geologic materials available for absolute paleointensity studies. Chapter 3 presents evidence that an asymmetry between ADM growth and decay rates is found in marine magnetic anomaly data, confirming a behavior previously observed in sedimentary records. In Chapters 4 and 5 geodynamo simulations are used to study what drives this asymmetry in long-term variations in paleointensity. Chapter 4 introduces spectral analytical methods for identifying the origins of asymmetry between ADM growth and decay rates in geodynamo simulations and analyzing the time scales of magnetic diffusion and induction. In Chapter 5, I apply the methods presented in Chapter 4 to a suite of geodynamo simulations spanning a section of q and Ra parameter space, and provide visualizations of the magnetic and velocity fields of dynamos with asymmetric ADM growth and decay to link ADM variations with internal dynamics. Chapter 6 summarizes the conclusions of these studies, their relevance to the community, and prospects for future investigations.

References

Amit, H. and Christensen, U. R. (2008). Accounting for magnetic diffusion in core flow inversions from geomagnetic secular variation. *Geophysical Journal International*, 175(3):913–924.

Bowers, N. E., Cande, S. C., Gee, J. S., Hildebrand, J. A., and Parker, R. L. (2001). Fluctuations of the paleomagnetic field during chron C5 as recorded in near-bottom marine magnetic anomaly data. *Journal of Geophysical Research: Solid Earth*, 106(B11):26379–26396.

Bowles, J., Tauxe, L., Gee, J., McMillan, D., and Cande, S. (2003). Source of tiny wiggles in Chron C5: A comparison of sedimentary relative intensity and marine magnetic anomalies. *Geochemistry, Geophysics, Geosystems*, 4(6):1049.

Buffett, B. A., King, E. M., and Matsui, H. (2014). A physical interpretation of stochastic models for fluctuations in the Earth's dipole field. *Geophysical Journal International*, 198(1):597–608.

Buffett, B. A., Ziegler, L., and Constable, C. G. (2013). A stochastic model for palaeomagnetic field variations. *Geophysical Journal International*, 195(1):86–97.

Chulliat, A., Hulot, G., Newitt, L. R., and Orgeval, J.-J. (2010). What caused recent acceleration of the north magnetic pole drift? *Eos, Transactions American Geophysical Union*, 91(51):501–502.

Chulliat, A. and Olsen, N. (2010). Observation of magnetic diffusion in the earth's outer core from magsat, ørsted, and champ data. *Journal of Geophysical Research: Solid Earth*, 115(B5).

Constable, C. and Johnson, C. (2005). A paleomagnetic power spectrum. *Physics of the Earth and Planetary Interiors*, 153(1):61–73.

Constable, C., Korte, M., and Panovska, S. (2016). Persistent high paleosecular variation activity in Southern hemisphere for at least 10,000 years. *Earth and Planetary Science Letters*, 453(7043):78–86.

Crowley, J., Schoene, B., and Bowring, S. (2007). U-Pb dating of zircon in the Bishop Tuff at the millennial scale. *Geology*, 35(12):1123–1126.

Davies, C. and Gubbins, D. (2011). A buoyancy profile for the Earth's core. *Geophysical Journal International*, 187(2):549–563.

Davies, C., Pozzo, M., Gubbins, D., and Alfè, D. (2015). Constraints from material properties on the dynamics and evolution of Earth's core. *Nature Geoscience*, 8(9):678.

Davies, C. J. and Constable, C. G. (2014). Insights from geodynamo simulations into long-term geomagnetic field behaviour. *Earth and Planetary Science Letters*, 404:238–249.

Diffey, B. (1991). Solar ultraviolet radiation effects on biological systems. *Physics in medicine and biology*, 36(3):299.

Driscoll, P. and Olson, P. (2009). Polarity reversals in geodynamo models with core evolution. *Earth and Planetary Science Letters*, 282(1):24–33.

Dunlop, D. and Özdemir, O. (2015). Magnetizations in rocks and minerals. In Schubert, G., editor, *Treatise on Geophysics*, volume 5, chapter 8, pages 277 – 336. Elsevier, Amsterdam, 2 edition.

Gee, J. S., Cande, S. C., Hildebrand, J. A., Donnelly, K., and Parker, R. L. (2000). Geomagnetic intensity variations over the past 780 kyr obtained from near-seafloor magnetic anomalies. *Nature*, 408(6814):827–832.

Gee, J. S. and Kent, D. V. (2007). Source of oceanic magnetic anomalies and the geomagnetic polarity time scale. In Schubert, G., editor, *Treatise on Geophysics*, volume 5, chapter 12, pages 461–509. Elsevier, Amsterdam, 1 edition.

Geissman, J. W., Newberry, N. G., and Peacor, D. R. (1983). Discrete single-domain and pseudo-single-domain titanomagnetite particles in silicic glass of an ash-flow tuff. *Canadian Journal of Earth Sciences*, 20(2):334–338.

Glatzmaier, G. A., Coe, R. S., Hongre, L., and Roberts, P. H. (1999). The role of the earth's mantle in controlling the frequency of geomagnetic reversals. *Nature*, 401(6756):885.

Glatzmaier, G. A. and Roberts, P. H. (1995). A three-dimensional convective dynamo solution with rotating and finitely conducting inner core and mantle. *Physics of the Earth and Planetary Interiors*, 91(1-3):63–75.

Gubbins, D., Willis, A. P., and Sreenivasan, B. (2007). Correlation of Earth's magnetic field with lower mantle thermal and seismic structure. *Physics of the Earth and Planetary Interiors*, 162(3):256–260.

Holme, R. (2015). Large-scale flow in the core. In Schubert, G., editor, *Treatise on Geophysics*, volume 8, chapter 4, pages 91–113. Elsevier, Amsterdam, 2 edition.

Kono, M. (2015). Geomagnetism: An Introduction and Overview. In Schubert, G., editor, *Treatise on Geophysics*, volume 5, chapter 1, pages 1–31. Elsevier, Amsterdam, 2 edition.

Korte, M., Constable, C., Donadini, F., and Holme, R. (2011). Reconstructing the holocene geomagnetic field. *Earth and Planetary Science Letters*, 312(3):497–505.

Lanzerotti, L. J. (2001). Space weather effects on technologies. *Space weather*, pages 11–22.

Matsui, H., Heien, E., Aubert, J., Aurnou, J. M., Avery, M., Brown, B., Buffett, B. A., Busse, F., Christensen, U. R., Davies, C. J., et al. (2016). Performance benchmarks for a next generation numerical dynamo model. *Geochemistry, Geophysics, Geosystems*, 17(5):1586–1607.

McIntosh, W. C., Sutter, J. F., Chapin, C. E., and Kedzie, L. L. (1990). High-precision ^{40}ar/^{39}ar sanidine geochronology of ignimbrites in the Mogollon-Datil volcanic field, southwestern New Mexico. *Bulletin of Volcanology*, 52(8):584–601.

Nimmo, F. (2015). Energetics of the Core. In Schubert, G., editor, *Treatise on Geophysics*, volume 8, chapter 2, pages 27–55. Elsevier, Amsterdam, 2 edition.

Ogg, J. (2012). Geomagnetic polarity time scale. In Gradstein, F. M., Ogg, J., Schmitz, M., and Ogg, G., editors, *The Geologic Time Scale*, pages 85–114. Elsevier, Oxford, U. K.

Olson, P. and Amit, H. (2014). Magnetic reversal frequency scaling in dynamos with thermochemical convection. *Physics of the Earth and Planetary Interiors*, 229:122–133.

Olson, P., Driscoll, P., and Amit, H. (2009). Dipole collapse and reversal precursors in a numerical dynamo. *Physics of the Earth and Planetary Interiors*, 173(1):121–140.

Olson, P. L., Coe, R. S., Driscoll, P. E., Glatzmaier, G. A., and Roberts, P. H. (2010). Geodynamo reversal frequency and heterogeneous core–mantle boundary heat flow. *Physics of the Earth and Planetary Interiors*, 180(1):66–79.

Poirier, J. (1988). Transport properties of liquid metals and viscosity of the Earth's core. *Geophysical Journal International*, 92(1):99–105.

Pozzo, M., Davies, C., Gubbins, D., and Alfè, D. (2012). Thermal and electrical conductivity of iron at Earth's core conditions. *Nature*, 485(7398):355–358.

Roberts, P. and Scott, S. (1965). On analysis of the secular variation. *Journal of geomagnetism and geoelectricity*, 17(2):137–151.

Sarna-Wojcicki, A. M., Pringle, M. S., and Wijbrans, J. (2000). New ^{40}ar/^{39}ar age of the Bishop Tuff from multiple sites and sediment rate calibration for the Matuyama-Brunhes boundary. *Journal of Geophysical Research: Solid Earth*, 105(B9):21431–21443.

Schlinger, C. M., Veblen, D. R., and Rosenbaum, J. G. (1991). Magnetism and magnetic mineralogy of ash flow tuffs from Yucca Mountain, Nevada. *Journal of Geophysical Research: Solid Earth*, 96(B4):6035–6052.

Tauxe, L., Banerjee, S., Butler, R., and van der Voo, R. (2016). Essentials of Paleomagnetism. 4th Web Edition, earthref.org/MagIC/books/Tauxe/Essentials/.

Tauxe, L., Gee, J., Steiner, M., and Staudigel, H. (2013). Paleointensity results from the Jurassic: New constraints from submarine basaltic glasses of ODP Site 801C. *Geochemistry, Geophysics, Geosystems*, 14(10):4718–4733.

Tauxe, L. and Yamazaki, T. (2015). Paleointensities. In Schubert, G., editor, *Treatise on Geophysics*, volume 5, chapter 13, pages 461–509. Elsevier, Amsterdam, 2 edition.

Van den Bogaard, P. and Schirnick, C. (1995). ^{40}ar/^{39}ar laser probe ages of Bishop Tuff quartz phenocrysts substantiate long-lived silicic magma chamber at Long Valley, United States. *Geology*, 23(8):759–762.

Willis, A. P., Sreenivasan, B., and Gubbins, D. (2007). Thermal core-mantle interaction: Exploring regimes for 'locked' dynamo action. *Physics of the Earth and Planetary Interiors*, 165(1):83–92.

Worm, H.-U. and Jackson, M. (1999). The superparamagnetism of Yucca Mountain tuff. *Journal of Geophysical Research: Solid Earth*, 104(B11):25415–25425.

Ziegler, L. and Constable, C. (2011). Asymmetry in growth and decay of the geomagnetic dipole. *Earth and Planetary Science Letters*, 312(3):300–304.

Ziegler, L., Constable, C., Johnson, C., and Tauxe, L. (2011). PADM2M: a penalized maximum likelihood model of the 0–2 Ma palaeomagnetic axial dipole moment. *Geophysical Journal International*, 184(3):1069–1089.

Chapter 2

Paleointensity estimates from ignimbrites: The Bishop Tuff revisited

Abstract

Volcanic ash flow tuffs (ignimbrite) may contain single domain sized (titano)magnetite that should be good for recording geomagnetic field intensity, but due to their complex thermal histories also contain other magnetic grains which are less ideal for recording paleointensity such as multi-domain phenocrysts of titanomagnetite and products of alteration. An initial study of the suitability of the Bishop Tuff for measuring paleointensity found that the ∼0.77 Ma ignimbrite provided an internally consistent estimate of 43.0 ± 3.2 μT. This initial study also showed a spatial heterogeneity in reliable paleointensity estimates that is possibility associated with fumarolic activity which motivated resampling of the Bishop Tuff to examine spatial magnetic changes. Three new stratigraphic sections of the Bishop

Tuff within the Owens River gorge were sampled, and the paleointensity results from the initial study in the Owens river gorge were reinterpreted. The mean of all sites is 41.9 ± 11.8 μT; this agrees with the initial study's finding but with substantially greater scatter. Two sections show evidence of hydrothermal alteration where the presence of titanohematite carrying a thermochemical remanence produces non-ideal behavior on the natural remanent magnetization – partial thermal magnetization (Arai) plots. This thermochemical remanence in the upper portion of the section does produce some paleointensity estimates of technically high quality that are significantly higher intensity than the rest of the tuff. We add an additional filter of ignimbrite density to select estimates from high density i.e. low porosity ignimbrite. Our best estimate for paleointensity is 39.6 ± 9.9 μT and comes from the densely welded ignimbrite that was emplaced above the Curie temperature of magnetite, and its low permeability may have shielded it from hydrothermal alteration. Care must be taken to avoid the misinterpretation of non-thermal remanence.

2.1 Introduction

The geomagnetic field varies both temporally and spatially. Learning about its past variations can help us to better understand its current behavior. Additionally, a detailed record of long-term paleomagnetic field variations is needed to reconstruct the evolution of the geodynamo and can provide important information on Earth's thermal history (i.e. Davies and Constable, 2014; Driscoll, 2016; Smirnov et al., 2016). Although the pattern of past reversals of the geomagnetic field is relatively well known, the history of the magnetic

field's intensity is not as well constrained, in part because of the difficulty in identifying geological materials that are suitable for paleointensity studies. Volcanic ash flows (ignimbrites) could potentially be useful as they occur throughout the global geologic record and are usually well suited for radiometric dating (e.g. McIntosh et al., 1990; Van den Bogaard and Schirnick, 1995; Sarna-Wojcicki et al., 2000; Crowley et al., 2007), both important factors in our goal of fleshing out the spatial and temporal variations of the paleofield.

Portions of some ignimbrites have been shown to contain fine-grained (superparamagnetic, SP, to single domain, SD) cubic iron oxides preserved in silicic glass (Geissman et al., 1983; Schlinger et al., 1991; Worm and Jackson, 1999). The fine-grained magnetic minerals are thought to crystallize within the flow after emplacement and above the glass transition temperature (typically 550-600°C for silicic glasses, Giordano et al., 2005), and therefore possibly record a thermoremanent magnetization (TRM). Moreover, this glassy matrix if fresh should reduce alteration that often occurs due to exposure to air during the multiple laboratory heatings required to estimate the paleointensity.

Although the fine-grained magnetic particles in silicic glass of tuffs should be suitable for producing accurate absolute paleointensity estimates, there are several factors that will complicate paleointensity studies. Along with the fine-grained iron oxides within the glassy matrix, tuffs also commonly contain coarser-grained titanomagnetite phenocrysts which would be multidomain and poor remanence recorders (Geissman et al., 1983). In the Bishop Tuff titanomagnetite phenocrysts have ulvöspinel contents of 25-28 mol % (Hildreth, 1979). Cooling history can also affect the observed Curie temperature (T_c) in some titanomagnetites due to cation reordering (Bowles et al., 2013), which can complicate pale-

ointensity studies (Bowles et al., 2015). Moreover, post-emplacement alteration may result in magnetizations that are not pure TRM, but instead are thermochemical remanence (TCRM) (Perrin et al., 2013). Finally, the magnetic mineralogy, and consequently the reliability of paleointensity estimates, from tuffs might vary considerably with stratigraphic level, depending on variations in emplacement temperature, cooling history, and post-emplacement vapor phase alteration (Schlinger et al., 1991).

An important test of the reliability of absolute paleointensity is to compare paleointensity estimates from historical flows with the known field intensity at the time of eruption. Bowles et al. (2015) analyzed the paleointensity recorded by two historical pyroclastic flows and found two sources of non-ideal behavior: unstable remanence of multidomain titanomagnetites due to cation reordering, and nonlinear Arai plots linked to post-emplacement alteration leading to underestimates of the paleointensity within alteration zones. Samples displaying these behaviors were rejected and the historical paleointensity value was successfully recovered.

There is mounting evidence that ignimbrites may not all be suitable for paleointensity studies without thoroughly examining the nature of the remanence (whether thermal, chemical or a mixture). Recent studies have sampled ignimbrite of varying density (Gee et al., 2010), sampled whole rock and glass from welded tuffs (Mochizuki et al., 2013), and sampled both basalt and ignimbrite (Perrin et al., 2013) to test the consistency of their paleointensity estimates. Both Mochizuki et al. (2013) and Perrin et al. (2013) observed Arai plots from ignimbrites that passed their selection criteria but which produced both inexplicably high or low paleofield estimates. These studies present troubling examples where potentially a

chemical remanent magnetization (CRM) or TRCM may produce high quality paleointensity data that gives a biased paleointensity estimate if misinterpreted as a TRM.

The pilot study of Gee et al. (2010) determined paleointensity as a function of stratigraphic level in the Bishop Tuff and produced an internally consistent paleofield estimate; however, not all stratigraphic profiles through the tuff produced paleointensity estimates that met the selection criteria (e.g., one of the three sections produced no reliable results). Here we extend the sampling of Gee et al. (2010) to better evaluate the spatial variability of paleofield estimates in the Bishop Tuff. This heterogeneity is likely controlled by the thermal history of the tuff; either by the emplacement temperature or vapor-phase alteration associated with fumarolic activity. Interestingly, the paleointensity estimate from the Bishop Tuff of Fu et al. (2017), which used single zircon crystal samples, agrees with Gee et al. (2010) when they rejected samples with high temperature remanence possibly carried by maghemite inclusions that gave systematically higher paleointensities. By returning to the large and complex Bishop Tuff, we can test more thoroughly the spatial variations in magnetic mineralogy and magnetization with respect to areas with fossil fumaroles (i.e. vents for volcanic gases), emplacement temperature, and cooling rate, and their affect on the success rate of the modified Thellier-Thellier paleointensity experiment.

The Bishop Tuff is a suitable location to study the reliability of paleointensity estimates because its eruptive and cooling history (Wilson and Hildreth, 2003), post-emplacement alteration (Sheridan, 1970; Holt and Taylor, 1998), and magnetic remanence (Palmer et al., 1996; Gee et al., 2010) have all been previously studied. The Bishop Tuff, located in eastern California (Figure 1a), erupted at 767.1 $\pm$ 0.9 ka (Crowley et al., 2007) following the collapse

of the Long Valley caldera. A large volume ($\sim$200 km^3) of high-silica rhyolite erupted over a period of days to a few years (Wilson and Hildreth, 1997; Sheridan and Wang, 2005). Within the Owens River Gorge, northwest of Bishop, CA, the Bishop Tuff is well exposed with a local thickness up to 170 m.

We find the Bishop Tuff produces high quality paleointensity estimates with a bimodal distribution. A portion of the tuff produces paleointensity estimates that are significantly higher intensity than the rest of the tuff, probably due to a chemical remanence acquired during hydrothermal alteration. The most likely place in the Bishop Tuff to find a TRM is in the densely welded ignimbrite. Future studies of paleointensity determined from ignimbrites should to be very specific in their documentation of the geologic material (density and alteration) and where it came from within the ash flow. Sampling should be done with caution, aiming for a TRM.

2.2 Sampling and Methods

2.2.1 Owens gorge outcrop field investigations

Samples of the Bishop Tuff were collected in the Owens River Gorge where several eruptive packages are well exposed. We sampled three vertical profiles called EE, FF, and GG (Table 2.1), on the eastern wall of the gorge in similar locations as sections E, F, and G of Wilson and Hildreth (2003) to place our paleomagnetic study in the context of their extensive petrologic work on the eruption, composition, and thermal history of the Bishop Tuff. The three vertical sections we sampled offered a range of welding as well as degrees

Table 2.1: Bishop tuff sampling section descriptions. Welding information is from Wilson and Hildreth (2003), and fumarole information is from Sheridan and Wang (2005). Location coordinates (WGS84) of the base and top of each sampled section. We intended to revisit sections E, F, and G from Wilson and Hildreth (2003). The top 45 m of section G was accessed from the western wall of the gorge.

Section	EE	FF	GG
Eruptive Unit(s)	Ig1Eb	Ig1Eb and Ig2Eb	Ig1Eb and Ig2Eb
Welding (with increasing height)	non-welded to welded	Ig1Eb - densely welded to sintered Ig2Eb - sintered to poorly welded	Ig1Eb - densely to poorly welded Ig2Eb - sintered to densely welded to sintered
Alteration zone	Vapor phase zone	Fumarolic mound zone	Fumarolic mound zone
Number of sampling sites	22	25	23
Base Northing	4156654	4151853	4149603 (east) 4149674 (west)
Base Easting	359700	361493	362454 (east) 362016 (west)
Top Northing	4156670	4151833	4149669 (east) 4149718 (west)
Top Easting	359874	361616	362540 (east) 361966 (west)

of post-emplacement alteration within eruptive packages Ig1Eb and Ig2Eb of Wilson and Hildreth (1997) (Table 2.1 and Figure 2.1).

Each profile consisted of more than 20 sites, with 3-4 cores drilled with a portable gasoline powered drill and/or unoriented hand samples collected at each site. The core samples were oriented in situ with a clinometer and magnetic compass, and when possible a sun compass. GPS location was recorded at the bottom and top of each vertical profile (Table 2.1), and a Jacob's staff was used to measure the height above the river of each sampling site (above basement rock for profile EE).

At each profile, susceptibility variations were measured (at $\sim$2 m interval) using a portable SM-20 susceptibility meter. These readings were calibrated using susceptibilities from core samples measured on a Kappabridge KLY-4S.

2.2.2 Laboratory measurements

We used the IZZI variant of the Thellier-Thellier method (e.g., Tauxe and Staudigel, 2004; Yu et al., 2004) to determine the paleointensity of 55 standard 2.5 cm diameter cores and 381 small chips mounted in glass tubes. Specimens were heated to a maximum temperature of 600°C, or 680°C when a significant fraction of the remanence remained after 600°C. A laboratory field of 40 μT was used for the in-field steps. The paleointensity was estimated using the PmagPy Thellier GUI of Shaar and Tauxe (2013) using the auto-interpreter tool. For comparison we also reinterpreted the data from the GB and GF sections of Gee et al. (2010) using the Thellier GUI. To filter out poor quality data we used the selection criteria: the maximum deviation of the partial thermal remanent magnetization (pTRM) check nor-

malized by the length of the best fit line (DRAT ≤ 5.0 Selkin and Tauxe, 2000), an estimate of the scatter about the fit line normalized by the slope ($\beta = \sigma/|b| \leq 0.05$ Coe et al., 1978), and the fraction of the total remanence used to calculate paleointensity ($f_{vds} \geq 0.85$ Tauxe and Staudigel, 2004). An evaluation of these limits can be found in the discussion section. We used the STDEV-OPT algorithm within the Thellier GUI. It selects estimates of paleointensity (B_{anc}), which minimize the site standard deviation, from the all estimates of B_{anc} that pass the criteria.

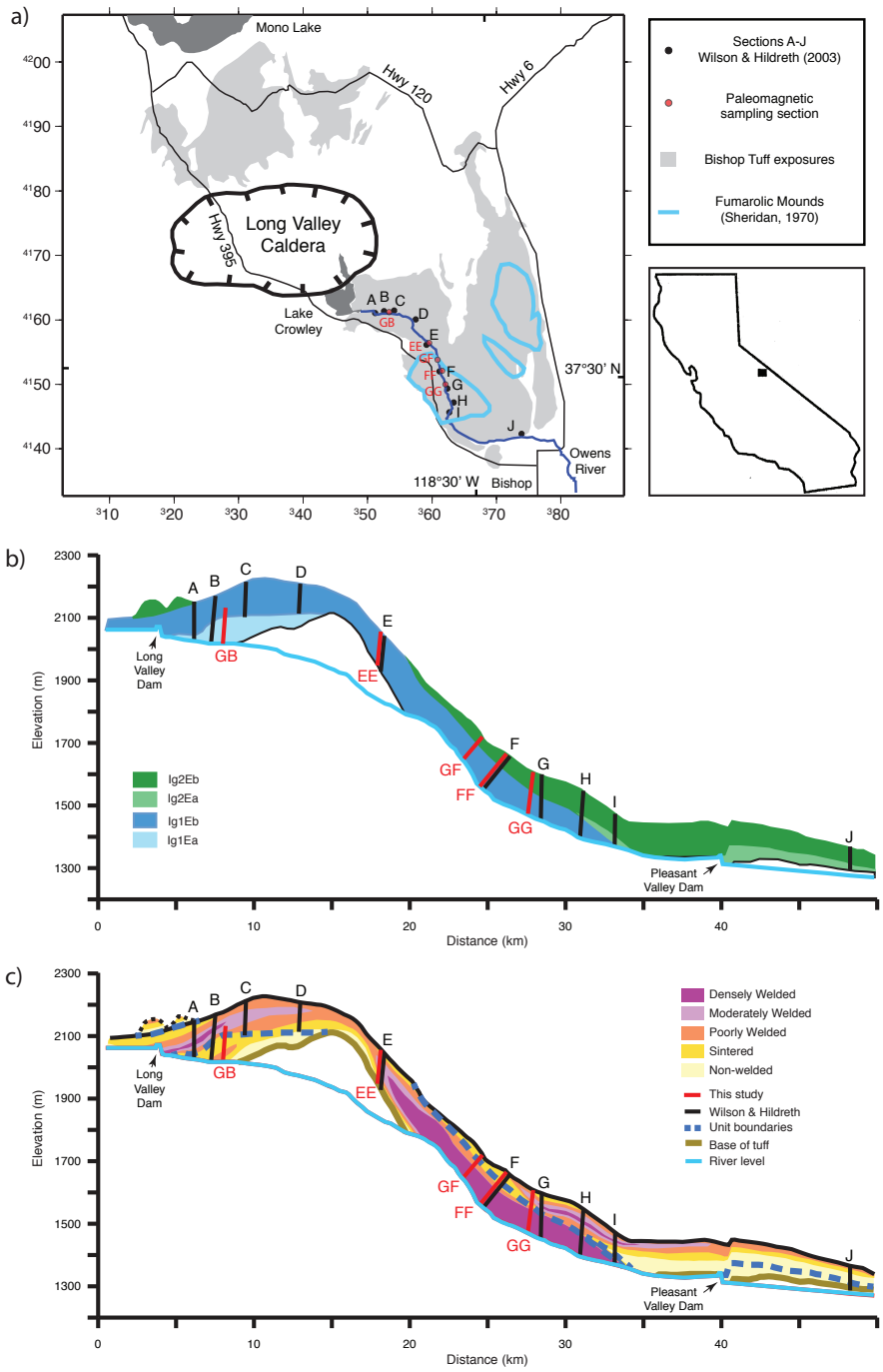

Figure 2.1: a) Map of paleomagnetic sampling sections in the Bishop Tuff. Sections EE, FF, and GG were collected as part of this study. GB and GF were sampled previously (Gee et al., 2010). The location of sections from Wilson and Hildreth (2003), Bishop Tuff outcrop pattern after Wilson and Hildreth (1997), and approximate outcrop of fumarole zones (Sheridan, 1970) are shown for reference. b) Profile of flow units of the Bishop Tuff along the Owens River gorge. Modified from Wilson and Hildreth (2003). c) Profile of degree of welding of the Bishop Tuff along the Owens River gorge. Modified from Wilson and Hildreth (2003).

A number of additional laboratory experiments were used to determine the magnetic mineralogy and estimate the thermal history of the tuff. These facilitate our assessment of the ability of a large and complex ash-flow tuff to record the paleointensity of the geomagnetic field. One or more standard 2.5 cm specimens were cut from each oriented core, and the hand samples were cut into 2.5 cm cubes. The volume and mass of all the specimens were measured in order to calculate their dry-weight densities, as a means to estimate the degree of welding, and in turn, the emplacement temperature (Sheridan and Wang, 2005)]. The anisotropy of magnetic susceptibility (AMS) tensor was measured with a Kappabridge KLY-4S and analyzed with AMSSpin software of Gee et al. (2008). AMS fabrics can be useful in identifying emplacement or post-emplacement textual changes. The natural remanent magnetization (NRM) of all the specimens was measured with the 2G three axis cryogenic magnetometer at Scripps Institution of Oceanography, UCSD. Representative pilot specimens from each site were thermally demagnetized to inform selection of temperature steps for the paleointensity experiments. Characteristic remanent magnetization (ChRM) directions and AMS results are reported and discussed in the supplementary materials Section 2.

Describing the magnetic mineralogy and rock magnetic properties of the tuff supports the evaluation of thermal and chemical contributions to the NRM. To determine the magnetic mineralogy, a suite of rock-magnetic properties were measured at the Institute for Rock Magnetism, University of Minnesota. Hysteresis loops and backfield curves were measured on a Princeton Vibrating Sample Magnetometers (VSM) at room temperature, and frequency dependent susceptibility was measured on the MAGNON Variable Frequency

Susceptibility Meter; these give information about the domain state of the magnetic minerals. Temperature-dependent susceptibility was measured on the Kappabridge KLY-2, and the minima in the derivative of the $k(T)$ heating curve were used to determine the Curie temperature of the magnetic minerals. Low temperature, frequency- and field-dependent susceptibility was measured on the Magnetic Property Measurement System (MPMS) in order to identify magnetic minerals by low-temperature crystallographic transitions and to characterize particle size distributions.

As an additional check for a possible mixture of magnetic minerals with different coercivities, the mineralogy of the remanence-carrying fraction of the magnetic minerals was determined with the thermal demagnetization of a 3-component isothermal remanent magnetization (IRM) (Lowrie, 1990). IRM acquisition curves were measured for representative specimens from approximately half of the sites in 18 field steps from 50 mT to 2.5 T, magnetizing all magnetic minerals into the $+z$ direction. Then the $+y$ and $+x$ directions were magnetized with a pulse magnetizer at 0.4 T and 0.1 T fields respectively. The specimens were then thermally demagnetized. The temperature at which each component has been demagnetized by 90% of their initial value was evaluated. The relative contribution of each IRM component's demagnetization curve is represented by the parameter F_n: the fraction of demagnetization curve area. The area, A_n, under the demagnetization curve of each component, n, is normalized by the sum of the areas $(A_x + A_y + A_z)$, $F_n = A_n/(A_x + A_y + A_z)$, where $n = x, y, z$.

2.3 Results

2.3.1 Density

For samples in the Bishop Tuff we determine densities to estimate the degree of welding and hence emplacement temperature that is critical for constraining the temperature of remanence acquisition. The density of the specimens varies with stratigraphic height (Figures 2.2 a, d, and g) and correlates well with densities measured by Wilson and Hildreth (2003). For example, the thermal modeling results of Riehle et al. (1995) indicate that for a simple cooling unit, densities $\geq$2.0 Mg/m^3 are achieved only for thick flows (initial thickness $\geq$80 m) emplaced at temperatures of $\geq$660°C. In section EE the density increases from about 1.2 Mg/m^3 at the contact with the basement rock to almost 2 Mg/m^3 at a height of 50 m (zone c, Wilson and Hildreth, 2003) and then decreases to 1.45 Mg/m^3 at the top of the section. The density of section FF varies between 2.2 and 2.35 Mg/m^3 (zone c, Wilson and Hildreth, 2003) until a height of $\sim$50 m where it begins to decrease. The lowest density of the FF section, 1.16 Mg/m^3, occurs at 125.7 m (10 m above the boundary between units Ig1Eb and Ig2Eb). Above this level the density increases to 1.5 Mg/m^3 at the top of the section (zone d, Wilson and Hildreth, 2003). Section GG's pattern of density variation starts at $\sim$2.2 Mg/m^3 at the base of the section up until 67.5 m (zone c, Wilson and Hildreth, 2003) where the density deceases rapidly through the flow unit boundary to a local minima of 1.47 Mg/m^3 at $\sim$80 m (just above the flow boundary at 75 m). The density then increases through the Ig2Eb unit reaching a local maxima of 1.93 Mg/m^3 at 98 m (zone d, Wilson and Hildreth, 2003), then deceases back to $\sim$1.4 Mg/m^3 at the top

of the section. Maximum welding occurs where the deposited tuff was hottest, and welding minimums reflect where cooler material was emplaced (Wilson and Hildreth, 2003). Thus the lower portions of sections FF and GG were likely emplaced at temperatures of $\geq$660°C.

2.3.2 Rock magnetism and magnetic mineralogy

There is a potential for complex magnetic remanence in ignimbrites due to their cooling and alteration histories, so it is important to characterize the remanence carriers and to evaluate thermal and chemical remanence contributions to the NRM. The first indication of complex rock magnetic properties came from the magnetic susceptibility measurements made in the field (green triangles in Figures 2.2 b, j, and r). Susceptibility parallels density in some broad scale features where poorly welded tuff has low susceptibility, but is decoupled elsewhere. The most obvious signal is in section FF. The susceptibility increases from $\sim 4\times10^{-3}$ SI at the base of the section up to a peak of $\sim 6\times10^{-3}$ SI at 70 m above the canyon base, then between 70 m and 80 m susceptibility decreases rapidly by an order of magnitude, and this low susceptibility continues to the top of the section. A similar drop in susceptibility was observed in section GF in Gee et al. (2010) at 100 m. The order of magnitude drop in susceptibility cannot be explained by compaction alone, and likely related to hydrothermal alteration. Section EE's susceptibility variation with height has two local highs. It increases from $\sim 2\times10^{-3}$ SI at the base of the section to 4.5×10^{-3} SI at 47 m, decreases to $\sim 3\times10^{-3}$ SI at 70 m, increases to $\sim 4.6\times10^{-3}$ SI units at 94 m, and finally decreases back to $\sim 2\times10^{-3}$ SI at the top of the EE section. The susceptibility in the GG section is generally more scattered than in the other two sections. It is steadily between 2 and 5×10^{-3} SI, with a

distinct minimum of $\sim 0.9 \times 10^{-3}$ SI at $\sim$80 m concurrent with the minimum of the density of that section. In all three sections the field susceptibility variation is corroborated by the block susceptibility measurements made on the Kappabridge (yellow circles in Figures 2.2 b, j, and r). The presence of frequency dependence in the magnetic susceptibility indicates superparamagnetic (SP) populations (i.e. Worm and Jackson, 1999; Eick and Schlinger, 1990; Mullins and Tite, 1973). There are high values of frequency dependence in the magnetic susceptibility only in a few places, the lower part of EE and upper part of FF, that could be due to SP grains (Figures 2.2 h and p). Frequency dependence in the magnetic susceptibility in these sections occur in poorly welded tuff.

Figure 2.2: Density and magnetic properties as functions of stratigraphic height. The dashed lines in sections FF and GG plots are the flow unit boundaries. a), i), and q) show the density throughout the EE, FF, and GG sections respectively. The red triangles are from this study see text for measurement details. The filled red triangles are site means with the standard deviation. The open red triangle is a site with only one sample available. The blue squares are the density measurements from Wilson and Hildreth (2003) for reference. b), j), and r) show the magnetic susceptibility for sections EE, FF, and GG. The green triangles were measured in the field and the yellow circles were measured on the kappabridge- see text for measurement details. Dark blue circles in c), k), and s) are the NRM. Cyan circles in d), l), and t) are M_r/M_s. Yellow squares in e), m) and u) are B_{cr}. The red arrow in m) indicates a sample with an outlying B_{cr} value of 190.39 mT, an outlier. Blue triangles in f), n), and v) are σ_{hys} vakues are according to method of Fabian (2003). g), o), and x) are the Curie temperatures as determined by the minimum of dk/dT heating curves. Black triangles are the minimum and red triangles are local minima. Green stars in h) and p) are frequency dependent susceptibility over a frequency range of 109–9901 Hz.

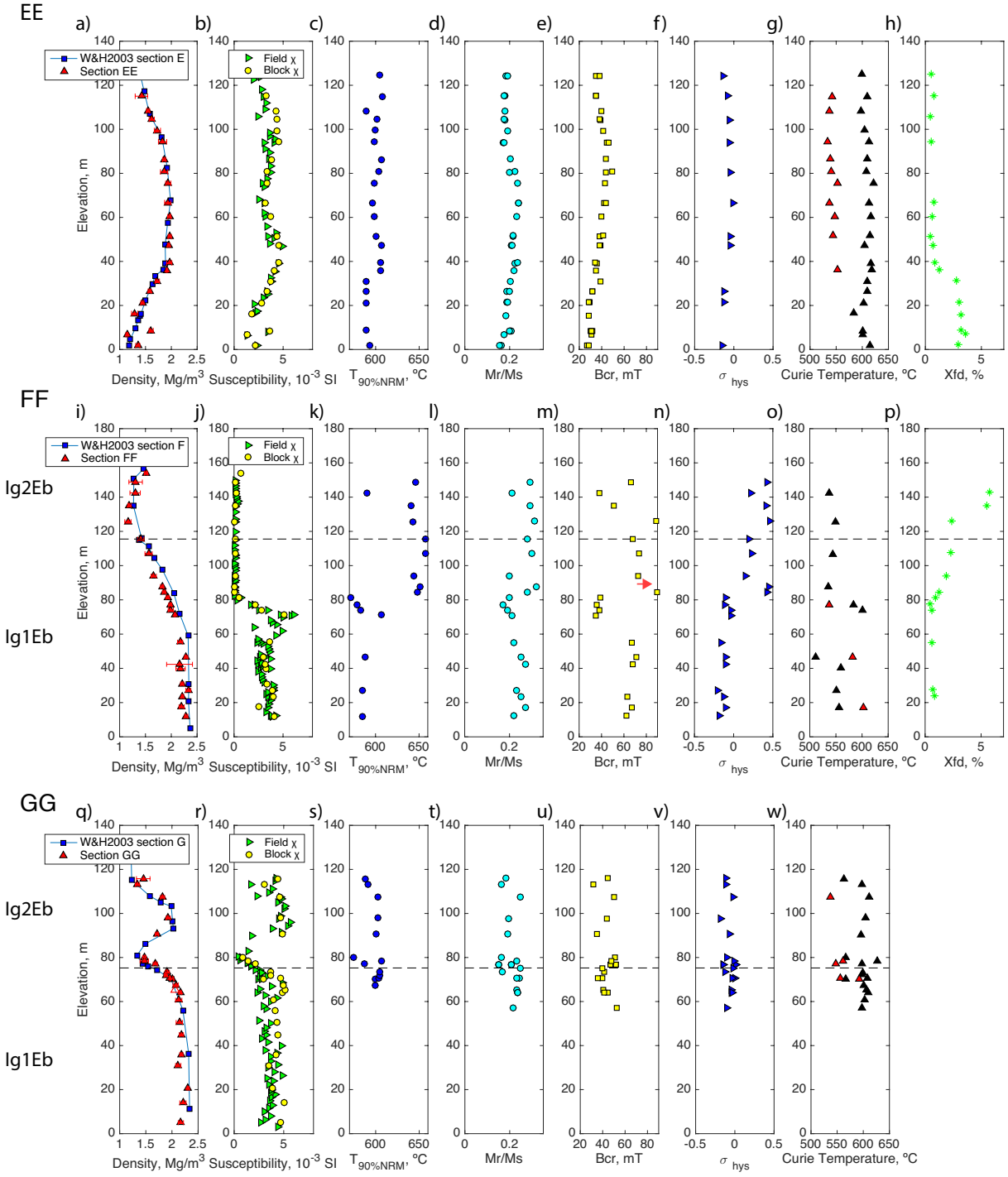
EE
a)
b)
c)
d)
e)
f)
g)
h)
W&H2003 section E
Section EE
Field χ
Block χ
Elevation, m
Density, Mg/m3
Susceptibility, 10-3 SI
T90%NRM, °C
Mr/Ms
Bcr, mT
σ hys
Curie Temperature, °C
Xfd, %
FF
i)
j)
k)
l)
m)
n)
o)
p)
W&H2003 section F
Section FF
lg2Eb
lg1Eb
GG
q)
r)
s)
t)
u)
v)
w)
W&H2003 section G
Section GG

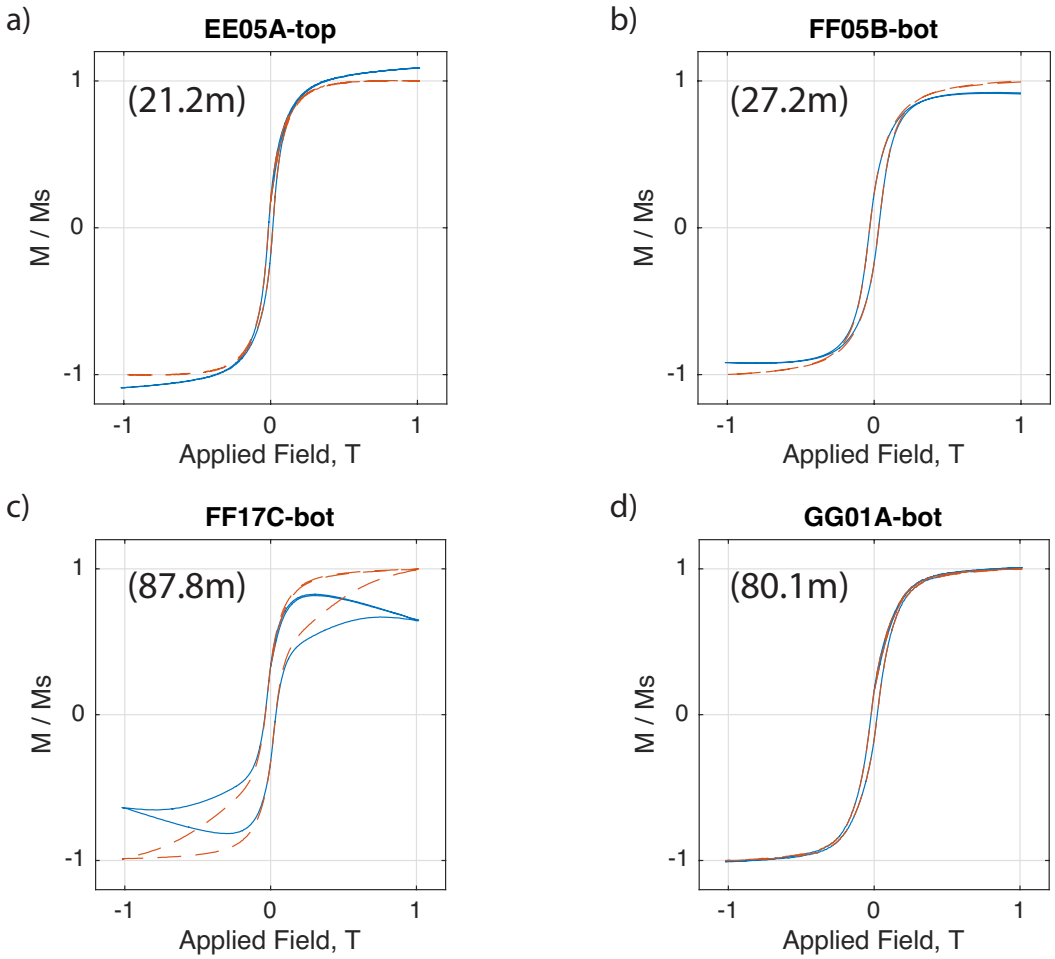

Figure 2.3: Representative hysteresis loops illustrating pot-bellied (a,d), normal (b), and wasp-waisted (c) behaviors. a) Section EE - site EE05, b) section FF - site FF05 and c) site FF17, and d) section GG - site GG01. The solid blue line is the original curve, and the dashed red line is the high-field slope corrected curve. Results from samples from these same sites are plotted in Figures 5, 6, and 8. Much of the Bishop tuff samples span the pseudo-single domain range (a, b, d). The upper portion of section FF has wasp-waisted hysteresis loops indicating a mixture of high and low coercivity phases (c).

Hysteresis data show a range of behaviors from the majority of specimens which have pseudo-single domain loops typical of natural samples to wasp-waisting (Tauxe et al., 1996); e.g. the goose-necked behavior is a good indicator of a mixture of magnetite and hematite. Four representative hysteresis loops are plotted in Figure 2.3. Values of saturation magnetization (M_s), saturation remanence (M_r), the remanence coercivity (B_{cr}), and the

loop shape parameter ($\sigma_{hys} = \log(E_{hys}/(M_s B_c))$, where E_{hys} is the area of the hysteresis loop and B_c is the coercive force) from Fabian (2003) were computed. The hysteresis properties of the Bishop tuff, M_r/M_s, B_{cr}, and σ_{hys}, vary with stratigraphic height, which we interpret as a signal of alteration products with low coercivity (Figure 2.2). As with the magnetic susceptibility, the strongest signal is seen above 84 m in section FF where the hysteresis loops display wasp-waisted behavior indicative of a mixture of high and low coercivity groups. This is best characterized by the change in σ_{hys} (Figures 2.2 f,n, and v): in section EE, GG, and the bottom of FF σ_{hys} is close to zero or slightly negative (pot-bellied), above 84 m in section FF σ_{hys} is larger and positive (wasp-waisted). M_r/M_s also increases above 84 m in section FF, and B_{cr} spikes (red arrow in Figure 2.2m). Specimen FF17D-top, from the upper section of FF, was unusually wasp-waisted, so a series of high temperature hysteresis loops were measured (Figure 2.4). The soft-coercivity phase has a T_c of $\sim$525°C as most clearly seen in the variation of B_{cr} and σ_{hys} with temperature (Figures 2.4b and c). We interpret the soft-coercivity phase as low-Ti titanomagnetite, and the hard-coercivity phase as hematite, so the wasp-waisted behavior is a good indicator of a mixture of magnetite and hematite.

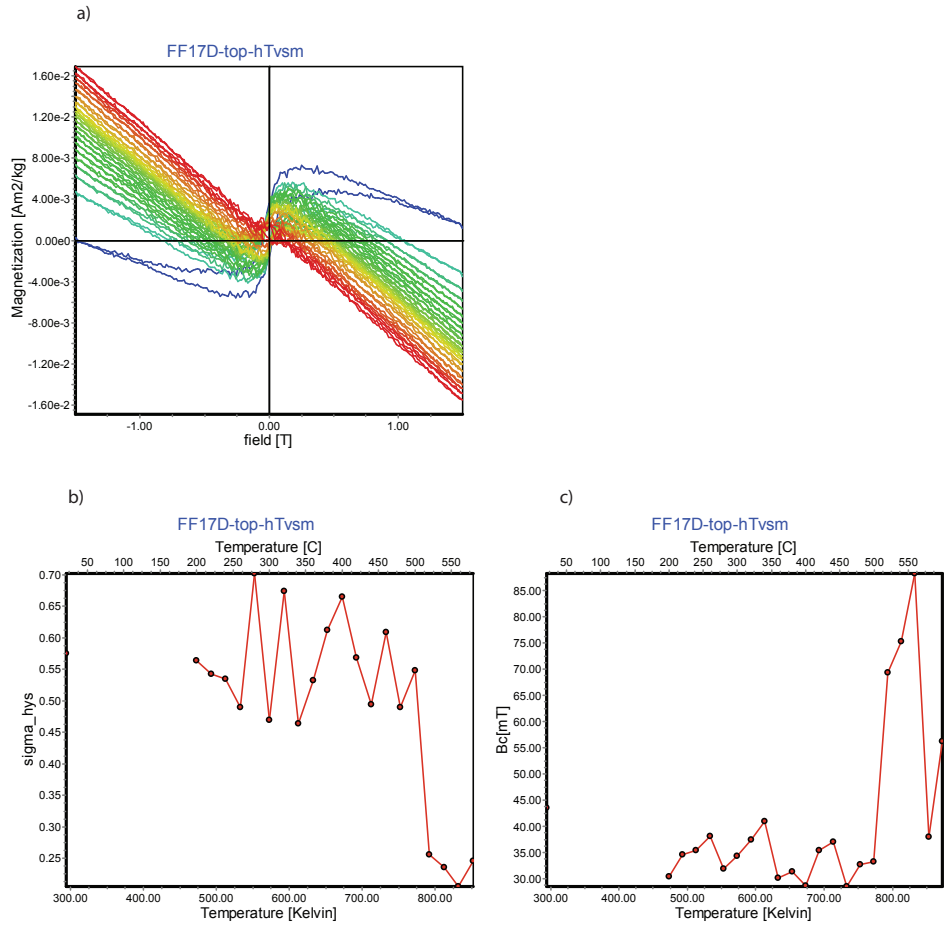

Figure 2.4: Hysteresis as a function of temperature for wasp-waisted sample FF17D. a) Temperature dependent hysteresis loops. Hysteresis properties b) σ_{hys} and c) B_c as functions of temperature. They indicate the lower coercivity phase has T_c ~525°C.

The Curie temperatures and thermal demagnetization of samples both give the thermal dependence of the remanence, which provides important evidence for identifying the magnetic mineralogy. We find two principal Curie temperature groups of 520-580°C and 600-620°C, with some stratigraphic variability. Figures 2.2g, o, and w show the resulting T_c variation with height, the black triangles are the minimum dk/dT (Figure 5 insets), and the red triangles are secondary local minima. In most of section EE (Figure 2.2g) there are two T_c present at ~550°C and ~610°C, and the primary T_c on heating is always the higher

temperature ∼610°C. This is corroborated by the results of the thermal demagnetization experiment, 90% of the NRM is demagnetized at a temperature of ∼600°C (Figure 2.2c). Below 84 m in section FF there are also two T_c, though the T_c are more scattered and in two of three cases the secondary T_c (red triangle) is higher than the primary T_c (black triangle). Above 84 m in section FF there is a single T_c at ∼550°C (Figure 2.2o). The $k(T)$ and dk/dT curves from this section of tuff are noisier so other Curie temperatures may be masked (Figure 2.5c). The thermal demagnetization experiment shows that 90% of the NRM is not demagnetized until a temperature of ∼640°C (Figure 2.2k). In section GG there are a few T_c ∼550°C, but most are >590°C (Figure 2.2w). Like sections EE and the bottom of FF the thermal demagnetization experiment shows 90% of the NRM is demagnetized at a temperature of ∼600°C (Figure 2.2s). The thermal demagnetization experiment also shows specimens from all three sections generally display a single component remanence which decays to the origin after the 250°C or 300°C heating step as can be seen in the Zijderveld plots (Figure 2.6).

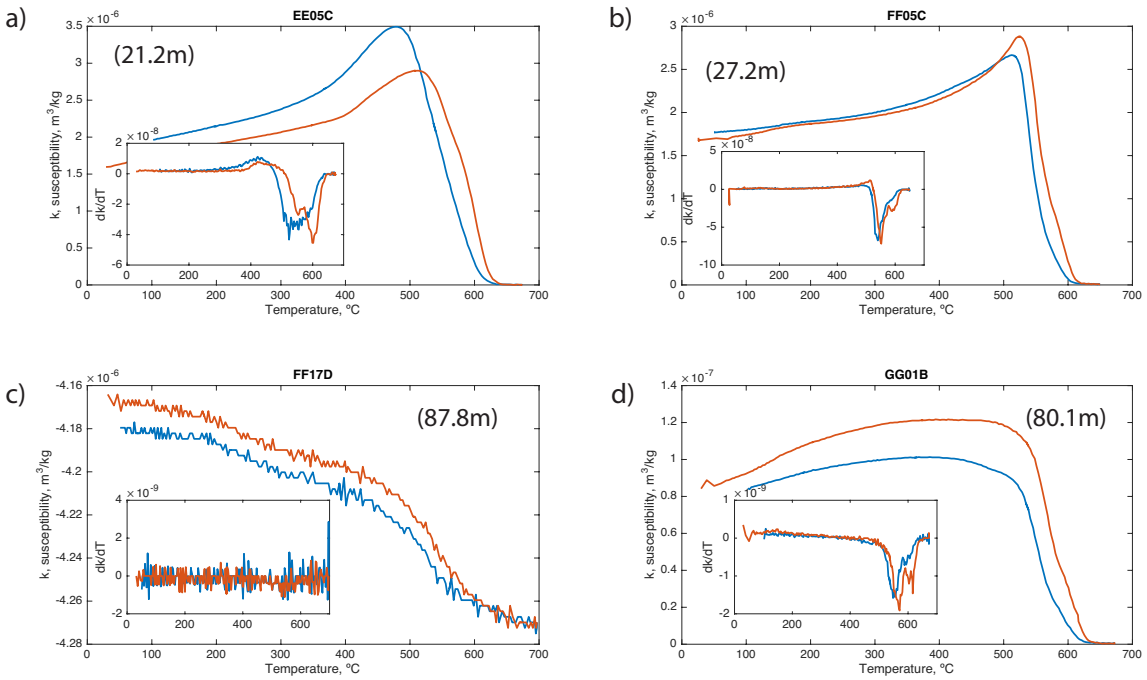

Figure 2.5: Representative thermomagnetic curves, $k(T)$, and their derivative (insets), dk/dT. a) Section EE - site EE05, b) section FF - site FF05 and c) site FF17, and d) section GG - site GG01. Results from samples from these same sites are plotted in Figures 3, 6 and 8.

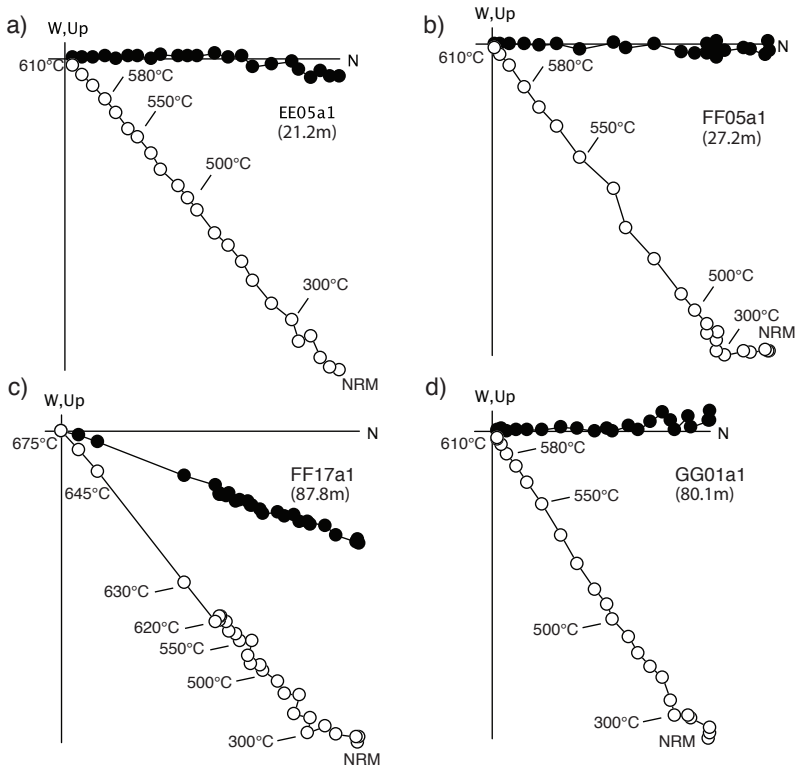

Figure 2.6: Vector endpoint diagrams illustrating thermal demagnetization results for four representative samples. Filled (open) circles are horizontal (vertical) projections. a) Section EE - site EE05, b) section FF - site FF05 and c) site FF17, and d) section GG - site GG01. These samples were chosen because they are representative of the behavior of that section of tuff; results from samples from these same sites are plotted in Figures 3, 5, and 8.

Figure 2.7: Summary of IRM acquisition and unblocking of a 3-component IRM from stratigraphic profiles in Bishop Tuff. Panels a), d), and g) show IRM acquisition curves as a function of height. The color indicates the IRM/sIRM with red = 90-100%, and the dot dashed lines are at 100 mT and 400mT, the fields used to impart IRMs along the x and y directions. Panels b), e), and h) show the 90% unblocking temperatures for the 3 components of the IRM as a function of height. A zero value indicates that directional component did not carry any of the remanence. Panels c), f), and i) are the percentage of the area under the demagnetization curve of each component as a function of height.

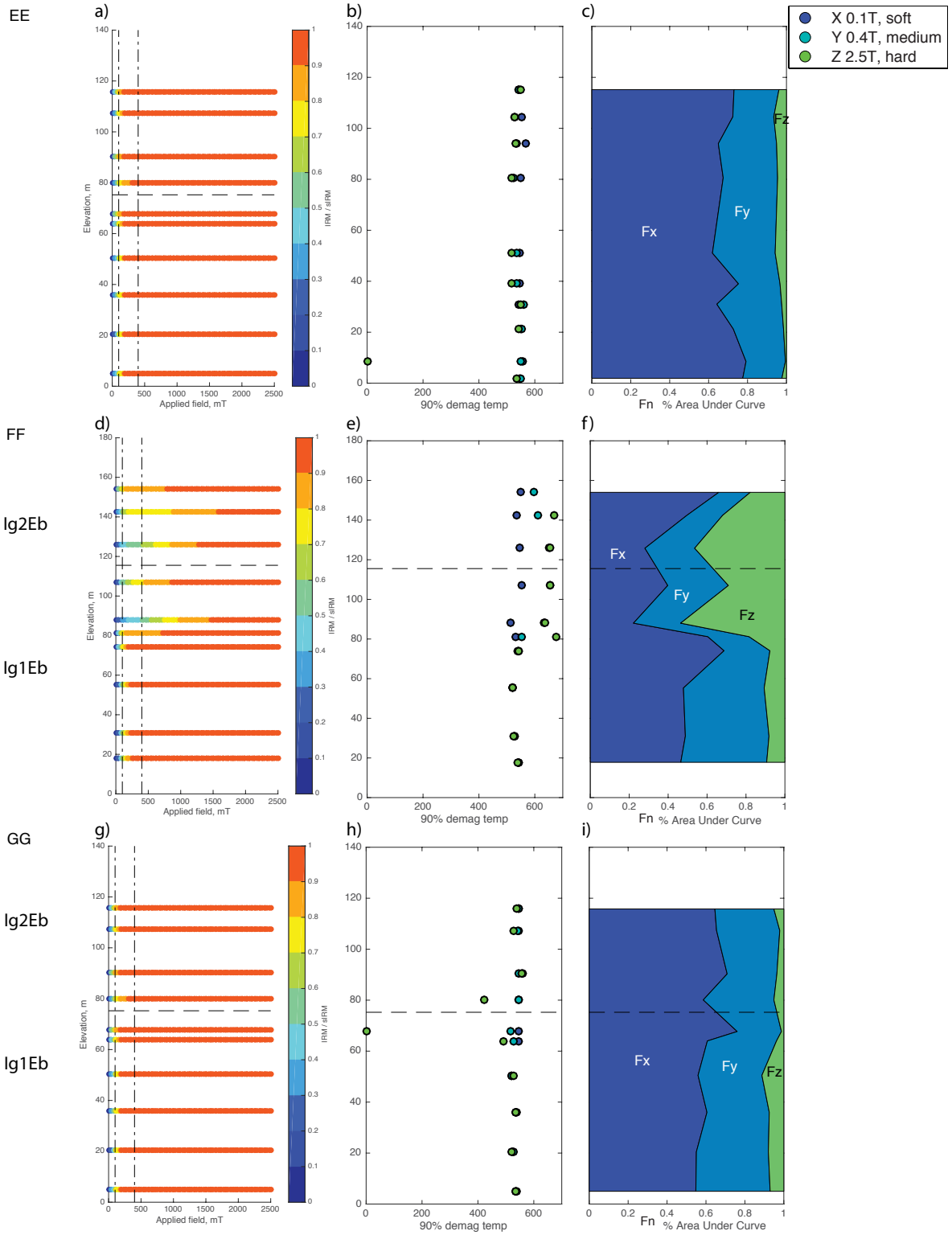
EE
a)
b)
c)
X 0.1T, soft
Y 0.4T, medium
Z 2.5T, hard
Elevation, m
Applied field, mT
IRM / sIRM
90% demag temp
Fn
% Area Under Curve
Fx
Fy
Fz
FF
d)
e)
f)
lg2Eb
lg1Eb
GG
g)
h)
i)

The thermal demagnetization of a 3-component IRM also corroborates these two principal temperature groups of 520-580°C and 600-620°C(Lowrie, 1990). We find the top of section FF has a larger contribution of a magnetic mineral with high coercivity and a 90% unblocking temperature of ∼640°C. The results are summarized in Figure 2.7. Panels a, d, and g show the IRM acquisition curves. Most specimens reach saturation IRM (sIRM) by 400 mT, except for specimens from section FF above 84 m that may not be saturated even in a 1.0 T field (Figure 2.7d). The hard fraction (z direction) with coercivities >400 mT (max applied field was 2.5 T) generally carries little of the magnetization, except above 84 m in the FF section where it carries 20-50% of the remanence (Figure 2.7f). The hard fraction is 90% demagnetized at a temperature of ∼650°C (Figure 2.7e). There are two occurrences of a 0°C 90% unblocking temperature of the hard fraction, this indicates the hard fraction carries a negligible portion of the remanence in that specimen. The intermediate fraction (y direction), which contains minerals with coercivities between 100 mT and 400 mT, carries a significant fraction of the remanence. This component is 90% demagnetized at temperatures between 520°C and 550°C, although above 84 m in FF several sites have remanence in the y direction remaining above 600°C. The soft fraction, with coercivities <100 mT, carries the majority of the magnetization except above a height of 84 m in FF. It is 90% demagnetized consistently at temperatures between 515°C and 565°C.

The MPMS low-temperature susceptibility experiments also provides important evidence for identifying the magnetic mineralogy, and generally show evidence of maghemitized magnetite. A smeared and suppressed Verwey transition is a hallmark of maghemitization (Özdemir and Dunlop, 2010). There is no evidence of a Morin transition (263 K) indicating

a lack of pure hematite.

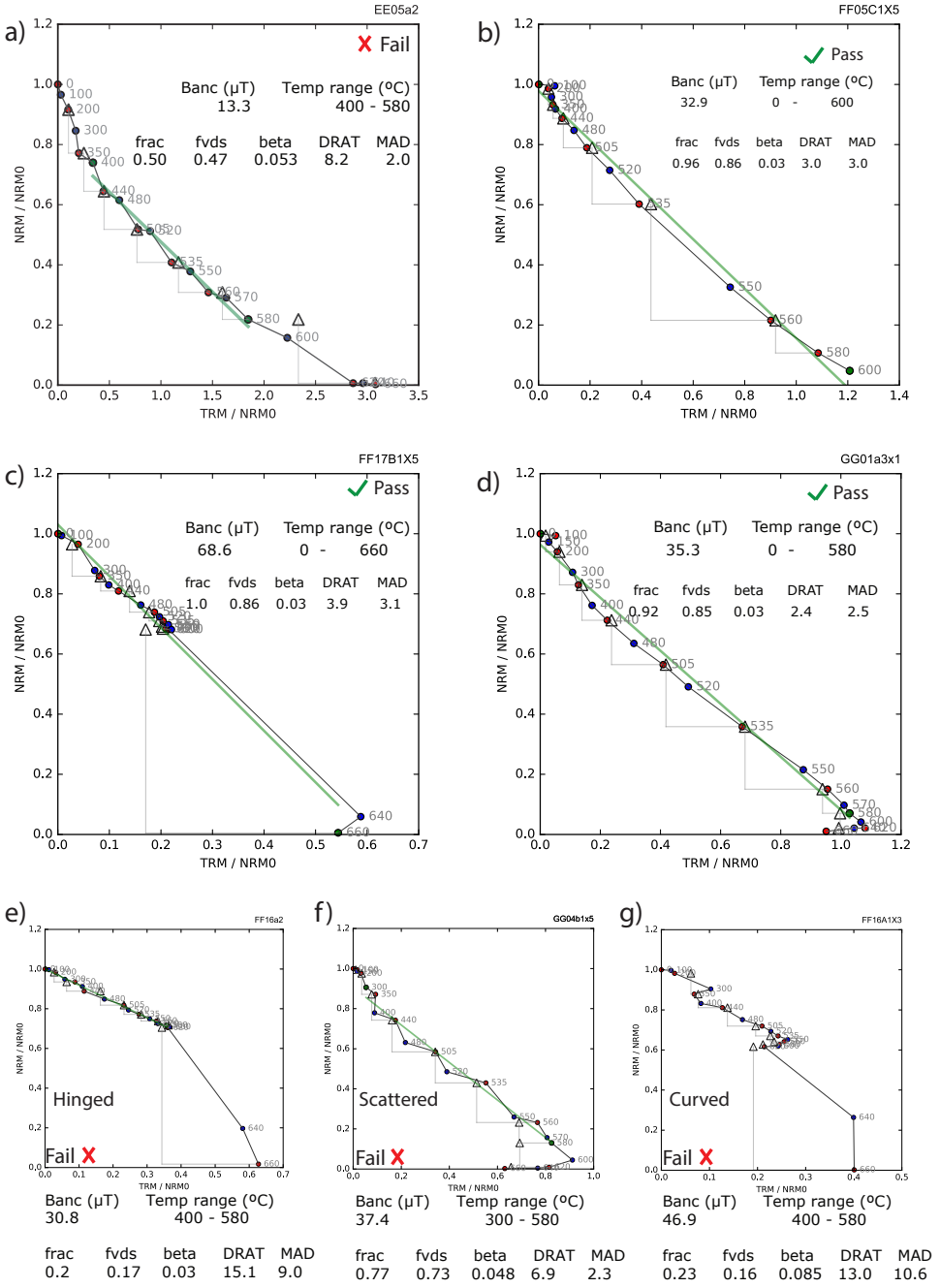

Figure 2.8: Representative Arai plots. Zero-field followed by in-field cooling (ZI) steps are shown in blue, and in-field followed by zero-field (IZ) steps are shown in red. The pTRM checks are shown with triangles. Temperature values between the green circles were used to calculate the slope and B_{anc}, and were chosen by the Thellier GUI to minimize the site level standard deviation. a-d) These samples were chosen because they are representative of the behavior of that section of tuff; results from samples from these same sites are plotted in Figures 3, 5, and 6. e-f) These samples represent some typical non-ideal behaviors that fail our experiment.

2.3.3 Paleointensity

Our Thellier-Thellier experiment produces a range of results: 34% of the specimens have nearly straight Arai plots (Figures 2.8 b, c, and d), 46% are concave (Figure 2.8a), 4% are scattered (Figure 2.8f), 4% are hinged with two distinct slopes at low temperature and high temperature (Figure 2.8e), and 11% are curved (Figure 2.8g).

If the STDEV-OPT algorithm within the Thellier GUI Shaar and Tauxe (2013) is used to apply selection criteria too loose to reject any specimen and the temperature ranges that minimize the site level standard deviation is used to estimate B_{anc}, the data produce B_{anc} estimates ranging from 7.8 ?T to 139.8 ?T. The Arai plots (NRM remaining versus pTRM gained) for some specimens display non-ideal behavior (e.g. nonlinear or scattered Arai plots, and failed pTRM checks).

We chose reliability criteria to pick specimens that do not alter during the experiment (DRAT ≤ 5.0), do not have scattered Arai plots ($\beta \leq 0.05$), and paleointensity estimates that are based on a large fraction of the remanence ($f_{vds} \geq 0.85$). Of the 436 specimens measured, 142 specimens from 33 sites produced one or more temperature ranges that passed these strict selection criteria. Of the 62 specimens from sections GB and GF that were reinterpreted with these selection criteria, 28 specimens from 9 sites within section GF passed. There were no passing estimates from sections GB or EE. The Arai plots from the GB and EE sections, and some specimens from the other sections, are concave (Figure 2.8a), and had a failing β if their f_{vds} was acceptable - or visa versa. The trade-off between $\beta \leq 0.05$ and $f_{vds} \geq 0.85$ also excludes some specimens from the top of section FF with hinged Arai plots,

Table 2.2: Average paleointesity estimates for various groupings of the 43 passing site estimates based of sampling location, flow unit, or density. The mean of site means is a simple mean, we did not weight by the scatter within the sites.

Group	Number of sites	Mean of site means (μT)	Standard deviation of site means (μT)	Standard error of site means (μT)	Minimum passing estimate (μT)	Maximum passing estimate (μT)
All	**42**	**41.9**	**11.8**	**1.8**	**16.3**	**81.5**
GF	9	44.6	2.4	0.8	40.0	49.9
FF	18	46.6	14.2	0.6	25.9	81.5
GG	15	34.7	8.2	2.1	16.3	52.4
FF <75 m	9	33.7	3.9	1.3	25.9	49.5
FF >75 m	9	59.5	6.4	2.1	40.1	81.5
Density>2.0 Mg/m^3	21	39.6	9.9	2.2	16.9	75.0

where the slope above the 580°C heating steps is much steeper (Figure 2.8e). Specimen and site level data can be found in supplemental Tables. Site means divided by section and density can be found in Table 2.2. Many specimens had multiple temperature ranges that passed the selection criteria. These different passing paleointensity estimates from the same specimen should be similar; the mean of this within-specimen variation is 1.6 μT. The site standard deviation ranges from 0.05 μT to 10.1 μT. Sites in GF have much smaller scatter than sections FF and GG (Figure 2.9). The site with the largest scatter is FF14 (78 m) in the FF section. Above this height in FF the estimates of B_{anc} are higher and more scattered. The mean of all 42 sites means is 41.9 $\pm$ 11.8 μT. This agrees with the 43.0 $\pm$ 3.2 μT value of Gee et al. (2010), but with larger scatter.

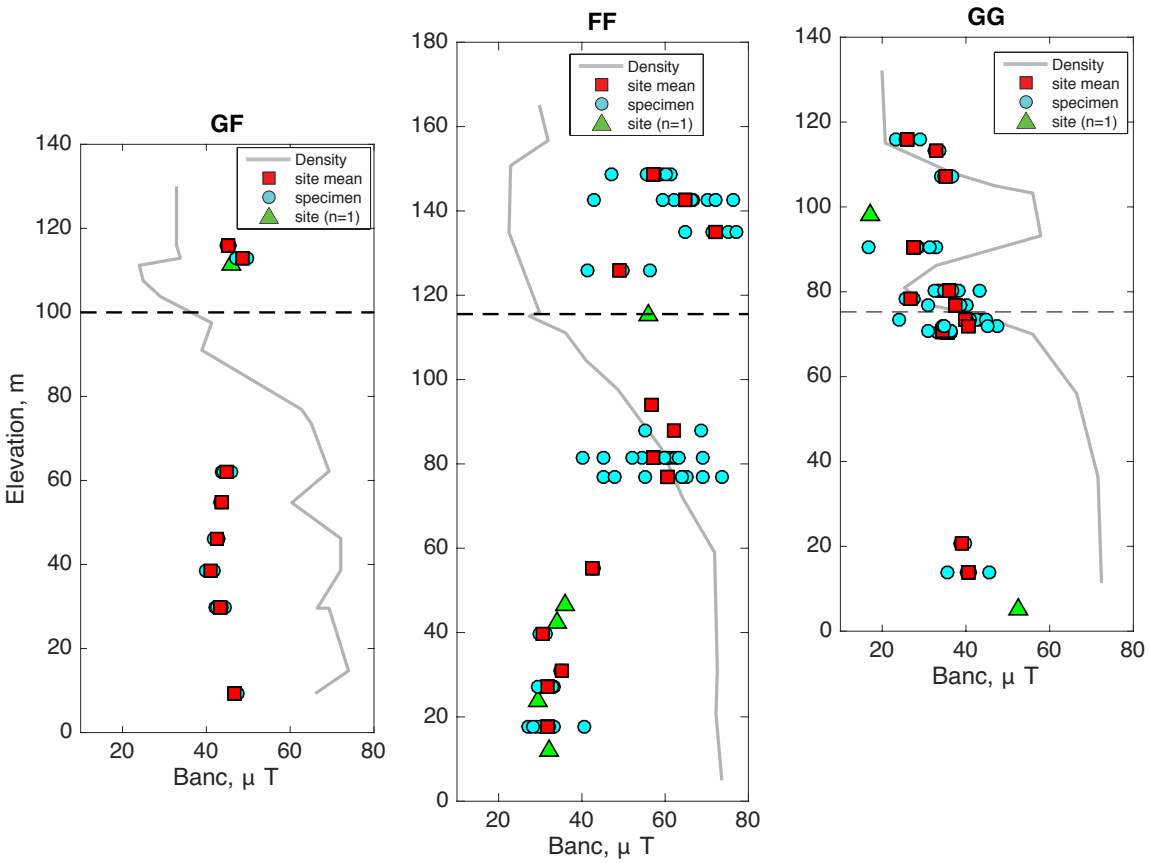

Figure 2.9: B_{anc} estimates found using our strictest criteria: $\beta \leq 0.05$, DRAT ≤ 5, and $f_{vds} \geq 0.85$ as a function of height. Red squares are site means, blue circles are specimen estimates, and green triangles are specimen estimates for sites with only one passing specimen. Grey line is bulk rock density for reference. The dashed line indicates the boundary between eruptive units Ig1Eb and Ig2Eb of Wilson and Hildreth (1997).

2.4 Discussion

As the body of work assessing ignimbrites as a recording material for paleointensity grows there is mounting evidence that their post-emplacement histories have a significant effect on their ability to record paleointensity. The timing and nature of remanence acquisition in ignimbrites needs to be assessed for confident interpretation of paleointensity data. Disturbingly, we see evidence that a non-TRM remanence may produce a passing paleointensity estimate if it is misinterpreted as a TRM even with increasingly strict selection criteria. In the Bishop Tuff we find a stratigraphic variation in magnetic mineralogy and paleointensity estimates both of which are linked to the tuff's thermal history and alteration.

2.4.1 Thermal history and magnetic mineralogy

The results of the rock magnetic studies presented in section 3.2 display evidence the magnetic remanence is carried by three main magnetic minerals: titanomagnetite, maghemite, and titanohematite. Following Gee et al. (2010) we divide our samples into groups based on magnetic mineralogy, which are broadly correlated with stratigraphy. Group A is found at the top of sections GF (within unit Ig2Eb) and FF (above ∼80 m). Group A is interpreted as having a remanence carried by (titano)hematite and (titano)magnetite. The evidence for this interpretation is:

- The hysteresis loops in group A are wasp-waisted.
- Samples from group A do not reach a saturation IRM by 1T.
- A large fraction of the remanence in group A is carried by a mineral with high coercivity.

- Group A has a single Curie temperature of ∼540°C consistent with the presence of low-Ti titanomagnetite, but the $k(T)$ curves from group A are noisy possibly masking other Curie temperatures.
- The temperature of 90% NRM unblocking in group A is >640°C.
- Low-temperature susceptibility (MPMS) results show no Morin transition, so the titanohematite is not pure hematite.
- Group A has significantly lower NRM strength and bulk susceptibility.

Magnetic mineralogy group B is found in sections EE and GG and the lower portions of sections GF and FF. Group B is interpreted as having a remanence carried by fine-grained, low-Ti (titano)magnetite and (titano)maghemite. The evidence for this interpretation is:

- A smeared Verwey transition in the MPMS low temperature susceptibility experiment indicates partial maghemitization where only the surface of the titanomagnetite crystal lattice is oxidized (Dunlop and Özdemir, 2015).
- Group B has two Curie temperature groups at 520°C-580°C and at 600°C-620°C, which we interpret as low-Ti (titano)magnetite and (titano)maghemite respectively.
- Group B has much less, if any, of the hard coercivity phase. The hysteresis loops are not wasp-waisted, and the Lowrie 3D IRM experiment shows little remanence carried by the z-direction.

For conducting a Thellier-Thellier type paleointensity experiments we need to consider the origin of these minerals and the nature of their remanence, whether TRM, pTRM,

CRM, or TCRM. Sheridan and Wang (2005) modeled density profiles from north and east of the Long Valley caldera and calculated the emplacement temperature to be typically ∼650°C, and significant welding and density ≥2.0 Mg/m^3 indicate the tuff was emplaced at temperatures above 660°C. After emplacement the ash flow can viscously deform, compact and flatten while above the glass transition temperature, T_g (Sheridan and Wang, 2005). The welding is controlled by the time-temperature-pressure path followed by the flow, with densely welded sections typically having spent more time at higher temperatures. Thicker sections are more likely to develop dense welding because of the greater pressures and slower cooling rates. So the densely welded material found in sections GF, FF, and GG spent more time at higher temperatures.

The Bishop Tuff contains two types of titanomagnetite: phenocrysts and microcrystals that we interpret grew within the glass after emplacement. We find the fine-grained, glass-hosted titanomagnetite to be the primary remanence carrier of mineralogy group B. Titanomagnetite phenocrysts are common in the Bishop Tuff but are unlikely to contribute significantly to the remanence of samples that yielded successful paleointensity estimates. Titanomagnetite constitutes only 0.05%-0.5% of the total phenocryst assemblage (total phenocrysts range from <1% to 24%) and therefore less than 0.1% by volume of tuff samples (Hildreth and Wilson, 2007). The titanomagnetite phenocryst composition is relatively uniform, with ulvöspinel contents of 25-28 mol % (Hildreth, 1979). These grains should have Curie temperatures <450°C (e.g. Dunlop and Özdemir, 2001). Specimens with substantial (>30%) unblocking of NRM below 450°C are found mostly in section EE and are associated with concave Arai plots (Figure 2.8b), which is consistent with the presence of multidomain-

sized crystals. The largest unblocking of NRM below 450°C is 40% of the original NRM and most samples unblock <20% below 450°C; the titanomagnetite phenocrysts do not contribute much to the total remanence.

The fine-grained titanomagnetites may have precipitated after emplacement (Schlinger et al., 1988b,a; Geissman et al., 1983), if this occurred above their T_c they would record a TRM. The presence of welding or partial welding also strongly suggests the flow was emplaced above T_g, the glass transition temperature, which depending on the water content of the flow occurs at ∼550-600°C (Giordano et al., 2005). Minimum estimates of temperature required for welding vary from 575°C to over 600°C (Riehle et al., 1995; Grunder et al., 2005), which are higher than the T_c of the low-Ti titanomagnetite (∼540°C) we find as the main remanence carrier for group B. Titanomagnetite microcrystals may precipitate at temperatures above T_g, and below T_c of titanomagnetite ($T_g < T < T_c$); these microcrystals would carry a TCRM. Below T_g, remanence acquired during cooling would be pTRM. Models show that compaction of ignimbrites occurs over weeks to 2-3 years, and near emplacement temperatures can last for decades depending on the flow thickness and amount of rainfall (Riehle, 1973; Riehle et al., 1995). Magnetic remanence would be acquired on a similar time scale. Fortunately, the titanomagnetite is low in Ti and we see no evidence of the unstable remanence due to cation reordering observed in the Novarupta and Mt. St. Helens ignimbrites (Bowles et al., 2013; Jackson and Bowles, 2014; Bowles et al., 2015).

The titanohematite in mineralogy group A is likely a product of post-emplacement alteration. The products of vapor phase and hydrothermal alteration are altered phenocrysts, precipitates in cavities and coatings of magnetite as well as hematite and goethite (Keith and

Muffler, 1978; Keith, 1991). Hematite and goethite are also found to replace both phenocryst and vapor phase magnetite (Keith and Muffler, 1978). Holt and Taylor (1998) - their site CG is roughly coincident with our GF section - showed δ^{18}O varies considerably with depth within the fumarole zone, where values are dramatically depleted due to meteoric-hydrothermal alteration. Holt and Taylor (1998, 2001) found groundmass with depleted oxygen isotope coincident along with feldspar phenocrysts that preserve their magmatic $^{18}O/^{16}O$ ratio. This shows vapor phase alteration occurs during initial short-lived high-temperature (>500°C) exchange with meteoric water, followed by longer exchange at lower temperature (<150°C). The welded units in Bishop Tuff restrict this δ^{18}O depletion, so the more densely welded material lower in the same sections may not have experienced this alteration because of their lower permeability (Holt and Taylor, 1998).

The titanomaghemite found in group B was formed by oxidation of titanomagnetite. The timing of this oxidation is not clear. The presence of maghemitization in the densely welded lower portions of sections FF, GF, and GG indicate that it was not associated with an exchange with hydrothermal fluids, as these portions of the Bishop Tuff experienced little exchange with meteoric hydrothermal fluids (Holt and Taylor, 1998). Thin sections of our samples show oxidation of titanomagnetite phenocrysts increases with stratigraphic height in EE, FF, and GG. The oxidation may have occurred below the Tc of titanomaghemite (∼645°C) in which case the NRM would be in part a TCRM acquired under the combined effects of chemical change and temperature decrease.

Due to the Bishop Tuff's complex thermal history the NRM of some specimens is a mixture of thermal and chemical remanences; our primary concern in this study is to de-

termine if a CRM or TCRM are able to produce paleointensity estimates of high technical quality that are different from the true paleointensity, which for ancient flows is unknown. Draeger et al. (2006) showed experimentally that CRM and TCRM can produce semi-linear Arai plots, and that a CRM will underestimate paleointensity if treated as TRM. Their samples with a CRM had concave Arai plots at low temperatures with more NRM lost than pTRM gained. Fabian (2009) shows theoretically a CRM due to isothermal SD grain growth underestimates paleointensity, a TCRM due to dissolution of the remanence carrying minerals after TRM acquisition overestimate paleointensity, and a TCRM due to low-temperature oxidation after TRM acquisition also overestimate paleointensity. Theoretically TCRM in both cases have straight Arai plots.

2.4.2 Paleointensity Interpretation

Here we test a range of selection criteria to filter out the non-ideal Arai plot behaviors. We used the selection criteria β, DRAT, and f_{vds}. To assess the effect of these criteria we plot the cumulative distribution functions (CDFs) for these reliability criteria (Figure 2.10a-d), and plot the B_{anc} estimate versus the reliability criteria value for each passing specimen (Figure 2.10e-h). The blue lines in Figure 2.10a-d, and blue circles in Figure 2.10e-h show the B_{anc} estimated by applying selection criteria too loose to reject any specimen (called 'no limits'). We initially apply loose criteria $\beta \leq 0.1$, DRAT ≤ 10, and $f_{vds} \geq 0.5$) to filter the most non-ideal data (red lines Figure 10a-d, and red triangles Figure 2.10e-h). For reference, the PICRIT03 (Modified) and SELCRIT2 (Modified) sets of selection criteria apply $\beta \leq 0.1$, DRAT ≤ 10, and $f \geq 0.35$ along with other criteria (Paterson et al., 2014). For our

498 specimens analyzed β, DRAT, and f_{vds} filter out the most extreme B_{anc} estimates, but there is still a large range of paleointensities and a non-Gaussian paleointensity CDF with two steep sections at $\sim$40 μT and $\sim$60 μT (Figure 2.10a).

We then applied stricter criteria $\beta \leq 0.05$, DRAT ≤ 5, and $f_{vds} \geq 0.65$), and we increased our f_{vds} threshold in increments of 0.05 to reject the hinged behavior which produced high paleointensities (grey lines Figure 2.10a-d, and grey squares Figure 2.10e-h). Even $f_{vds} \geq 0.85$ does not filter out all the paleointensity estimates >52 μT (yellow lines Figure 2.10a-d, and yellow squares Figure 2.10e-h). These high B_{anc} estimates are of good technical quality. We interpret the remanence in the top of the FF section as TCRM, but our paleointensity experimental protocol alone does not reveal this. For discussion we define paleointensity groups: type 1 B_{anc} <35 μT, type 2 B_{anc} =35-52 μT, type 3 B_{anc} >52 μT.

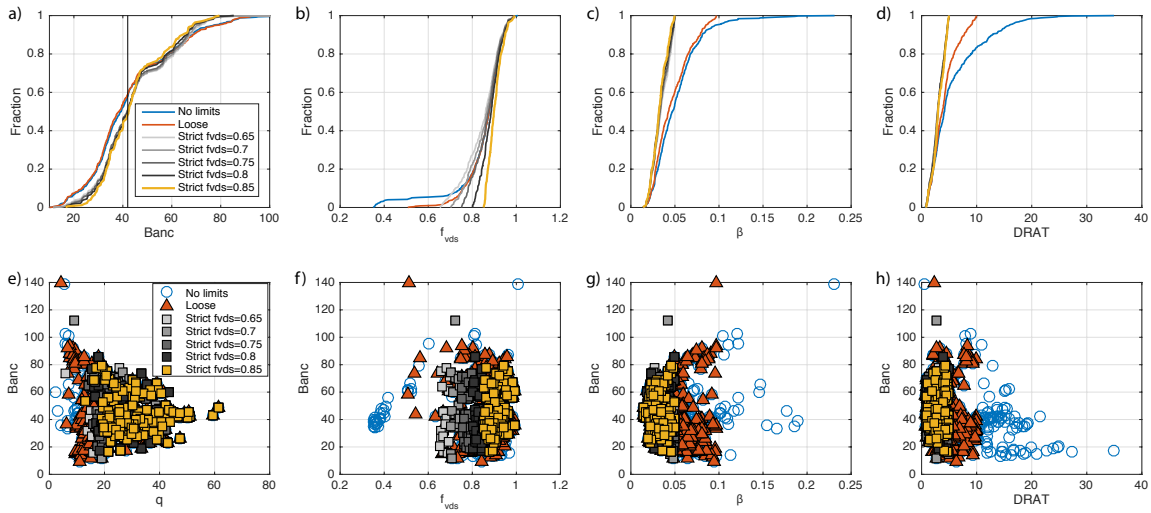

Figure 2.10: The effect of the selection criteria on the B_{anc} dataset. a-d) Cumulative distribution functions (CDFs) of B_{anc} estimates, f_{vds}, β, and DRAT. Blue lines are B_{anc} estimates found using all temperature steps for each specimen. Red line are B_{anc} estimates that pass loose selection criteria: $\beta \leq 0.1$, DRAT ≤ 10, and $f_{vds} \geq 0.5$. Gray and yellow lines are estimates that pass strict selection criteria: $\beta \leq 0.05$, DRAT ≤ 5, and $f_{vds} \geq 0.65$-0.85. e-h) B_{anc} as a function of q (Coe et al., 1978, quality factor), f_{vds}, β, and DRAT.

Both the magnetic mineralogy subgroups and paleointensity subgroups are broadly correlated with stratigraphic and cooling units. All specimens from sections GB and EE have concave Arai plots with positive pTRM checks suggesting they contain abundant coarse-grained Fe oxides. Additionally, if any magnetite precipitated after emplacement at a temperature $T < T_c$ then they would record a CRM. Paleointensity estimates from specimens in sections GB and EE produce low estimates of the field strength of type 1 (Figure 2.8a, Figures 2.11 g and h). Bowles et al. (2015) observed similar non-ideal Arai plots with a large loss of NRM at low temperatures with little pTRM gain in samples from the 1912 Novarupta flow sampled that they interpret as features of vapor phase alteration, this non-ideal behavior underestimated the known paleointensity value. There are no obvious rock magnetic properties that distinguish sections GB and EE from the rest of mineralogy group

B. These sections have lower densities and degrees of welding (Figure 2.11f). They were emplaced at a similar temperature as the other sections, but their initial thickness was less and they cooled faster giving less time for the growth of glass-hosted microcrystals of low-Ti titanomagnetite. The other sections of the tuff with group B magnetic mineralogy (section GG, and the lower portions of GF and FF) produce paleointensity estimates mostly of types 1 and 2.

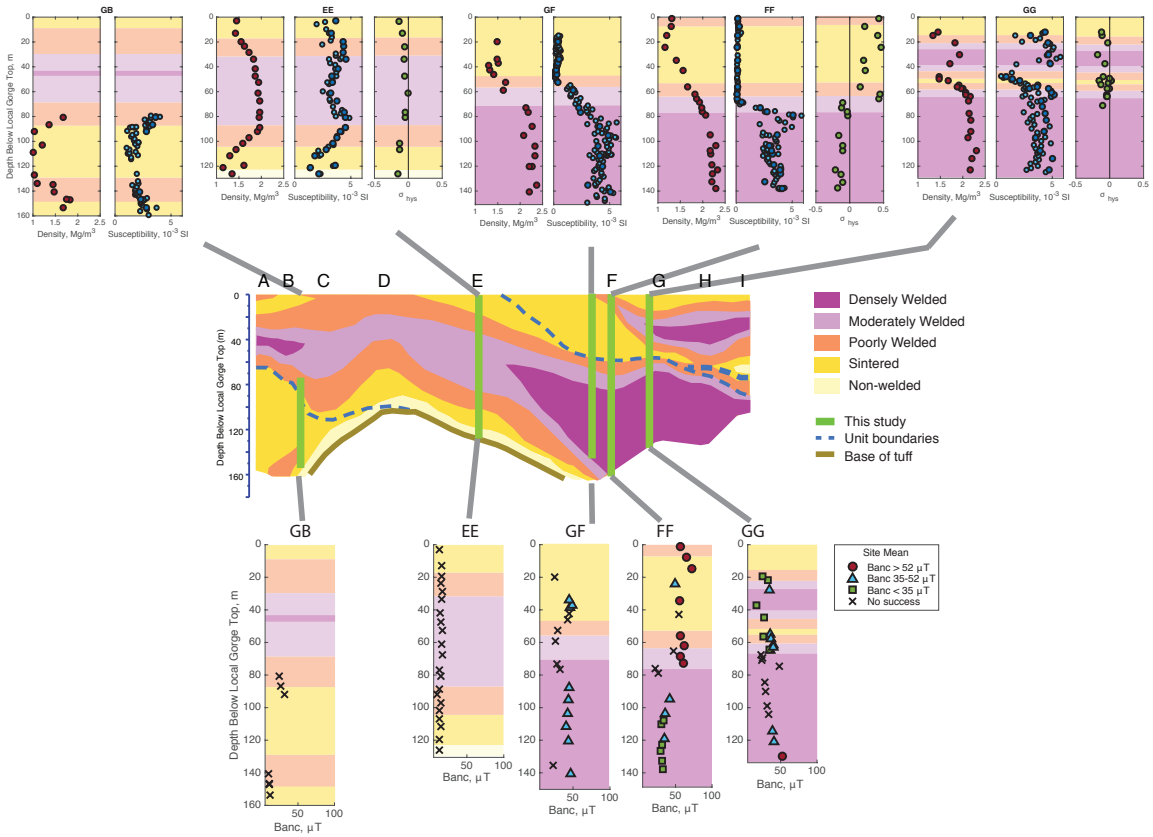

Figure 2.11: Summary of welding, density, magnetic properties, and B_{anc} estimates as functions of stratigraphic depth. Panels a-e) show density, magnetic susceptibility, and σ_{hys} for each section. f) Profile of degree of welding of the Bishop Tuff along the Owens River gorge. Modified fromWilson and Hildreth (2003). g-k) Paleointensity results divided into subgroups: Type 1 $B_{anc} < 35$ μT (red circle), Type 2 B_{anc} =35-52 μT (blue triangle), and Type 3 $B_{anc} > 50\mu$T (green square). Black x's indicate sites with no passing paleointensity data, plotted at the site mean of paleointensity estimated using the all temperature steps.

Mineralogy group A which is found in the upper part of the GF and FF sections displays decreased NRM, decreased susceptibility, increased high-coercivity phase titanohematite due to hydrothermal alteration, increased paleointensity, and increased paleointensity scatter. Many Arai plots from this mineralogy group are hinged, the higher temperature hematite component has a steeper slope than the lower temperature magnetite component, and these fail our criteria (Figure 2.8e). However the upper portion of section FF does produce some type 3 paleointensity estimates that pass our selection criteria, which are significantly higher than the bottom of section FF, GF and GG sections (Figure 2.8c and Figure 2.11j). The average estimate from the upper portion of section FF is 1.6 times larger and specimen estimates from each site have much larger scatter than the estimates from the lower portion. This difference cannot be explained by cooling rate; the lower part of FF has a higher degree of welding indicating it cooled more slowly than the upper portion. If the difference in B_{anc} estimates were due to cooling rate, the bottom of FF would have a higher B_{anc}.

We need independent information about the nature of the remanence to decide where a reliable estimate of B_{anc} can be found. Our best estimate for B_{anc} comes from the densely welded bottom portions of unit Ig1Eb that was emplaced above the Curie temperature of magnetite and possibly above the Curie temperature of maghemite, and its low permeability shielded it from vapor phase alteration. This section of the Bishop Tuff produces an estimate of B_{anc} =39.6 $\pm$ 9.9 μT.

2.5 Conclusions

Our study produces a few implications for future studies. Very careful reporting of location and context of alteration and thermal history is needed to show independent evidence of a TRM. Strict paleointensity selection criteria will not necessarily reject all non-thermal remanences, as suggested experimentally (Fabian, 2009; Draeger et al., 2006). Susceptibility measurements while sampling in the field are useful for documenting spatial variations in magnetic properties and alteration. We recommend sampling densely welded, proximal deposits where the remanence is more likely to be a TRM. Our best estimate for B_{anc} comes from the densely welded base of unit Ig1Eb, $B_{anc} = 39.6 \pm 9.9$ μT.

Acknowledgements

Chapter 2, in part, is currently being prepared for submission for publication of the material. Avery, Margaret S., Gee, Jeffrey S., Bowles, Julie A., and Jackson, Michael J. The dissertation author was the primary investigator and author of this material. This work was supported by National Science Foundation grant number EAR0943999.

Appendices

2.A Paleointensity Results

Table 2.S1: Site level paleointensity results. Height is stratigraphic height above the canyon base. n is the number of specimens at that site. SD is the standard deviation and SE is standard error estimated by $SD/\sqrt{n}$.

Site	Height	n	Site mean B_{anc}, μT	SD site mean, μT	SD site mean, %	SE site mean, μT
FF01	12.09	1	32.2	-	-	-
FF02	17.54	7	31.63	4.42	13.98	1.67
FF04	23.68	1	29.6	-	-	-
FF05	27.18	6	31.82	1.43	4.5	0.58
FF06	31	2	35.03	0.05	0.14	0.04
FF07	39.8	2	30.59	1.26	4.11	0.89
FF08	42.35	1	33.9	-	-	-
FF09	46.51	1	36.1	-	-	-
FF10	55.3	4	42.52	0.18	0.41	0.09
FF14	77.07	8	60.57	10.06	16.61	3.56
FF15	81.46	11	57.14	8.48	14.84	2.56
FF17	87.79	2	61.96	9.33	15.06	6.60
FF18	93.86	3	56.83	0.1	0.18	0.06
FF20	115.4	1	56.1	-	-	-
FF21	125.7	3	49.19	7.48	15.21	4.32
FF22	135.16	4	72.02	5.43	7.54	2.72
FF23	142.46	11	64.76	8.57	13.23	2.58
FF24	148.81	7	56.95	4.74	8.32	1.79
GF01	9.3	5	46.83	0.28	0.59	0.13
GF03	29.6	4	43.27	1.08	2.5	0.54
GF04	38.6	2	40.89	1.23	3.01	0.87
GF05	46.2	2	42.35	0.82	1.94	0.58
GF06	54.7	3	43.62	0.16	0.36	0.09
GF07	62.2	4	44.64	1.05	2.35	0.53
GF14	111.2	1	46.1	-	-	-
GF15	112.9	3	48.54	1.4	2.88	0.81
GF16	116	4	45.24	0.29	0.64	0.15
GG01	80.07	11	35.89	3.02	8.42	0.91
GG02	77.01	10	37.35	2.37	6.36	0.75
GG03	73.33	8	39.94	6.63	16.59	2.34

Table 2.S1 Site level paleointensity results (continued).

Site	Height	n	Site mean B_{anc}, μT	SD site mean, μT	SD site mean, %	SE site mean, μT
GG04	70.32	5	35.39	1.43	4.03	0.64
GG50	5	1	52.4	-	-	-
GG51	14	4	40.58	4.03	9.92	2.02
GG52	20.5	2	39.2	0.7	1.79	0.49
GG92	70.71	4	34.6	2.52	7.29	1.26
GG93	72	4	40.4	6.83	16.9	3.42
GG94	78.45	2	26.54	1.32	4.97	0.93
GG95	90.51	6	27.53	5.66	20.57	2.31
GG96	97.93	1	17.2	-	-	-
GG97	107.33	3	35.21	1.36	3.86	0.79
GG98	113.12	2	33.02	0.82	2.49	0.58
GG99	115.79	4	25.85	2.35	9.09	1.18

Table 2.S2: Specimen level paleointensity results. B_{anc} is paleointensity estimate in μT. T_{min} and T_{max} are the minimum and maximum temperature steps used to compute this specimen's paleointensity estimate. n_{ptrm} is the number of pTRM checks, and n_{int} is the number of measurements used to estimate paleointensity. $\beta = \sigma/|b| \leq 0.05$ is a measure of the data scatter around the best-fit line and is the ratio of the standard error of the slope to the absolute value of the slope (Coe et al., 1978). $f_{vds} \geq 0.85$ NRM fraction used for the best-fit line calculated as a vector difference sum (Tauxe and Staudigel, 2004). $DRAT \leq 5$ is the maximum absolute difference produced by a pTRM check normalized by the length of the best-fit line (Selkin and Tauxe, 2000). g_{max} is the maximum gap between two points determined by vector arithmetic (Shaar and Tauxe, 2013). MAD is the Maximum Angular Deviation of the directional fits to the paleomagnetic vector on a vector component diagram (Kirschvink, 1980). DANG is the Deviation ANGle: the angle between the free-floating best-fit direction and the direction between data center of mass and the origin of the vector component diagram (Tauxe and Staudigel, 2004). q is a measure of the overall quality of the paleointensity estimate and combines the relative scatter of the best-fit line, the NRM fraction and the gap factor (Coe et al., 1978).

Site	Specimen	B_{anc} , μT	T_{min}	T_{max}	n_{ptrm}	n_{int}	β	f_{vds}	DRAT	g_{max}	MAD	DANG	q
FF01	FF01b1	32.2	0	600	6	16	0.03	0.91	2.66	0.26	2.13	1.26	34.7
FF02	FF02B1X2	31	0	580	6	14	0.03	0.85	3.12	0.21	2.99	2.29	25.7
FF02	FF02B1X4	33.2	0	600	6	15	0.05	0.86	2.36	0.19	3.57	1.42	19.4
FF02	FF02a1	27	0	600	6	16	0.03	0.91	3.28	0.18	2.89	1.77	27.0
FF02	FF02d1x1	40.4	400	620	7	12	0.01	0.86	3.65	0.23	1.12	0.64	65.7
FF02	FF02d1x2	32	100	620	7	16	0.04	0.90	2.06	0.17	1.67	0.52	21.0
FF02	FF02d1x4	29.6	0	580	6	15	0.03	0.87	4.57	0.24	2.19	0.86	24.4
FF02	FF02d1x5	28.1	0	580	6	15	0.04	0.86	2.96	0.21	3.75	2.21	23.5
FF04	FF04a1	29.6	0	640	7	18	0.02	0.91	3.56	0.20	2.00	0.70	39.8
FF05	FF05C1X1	31.7	0	600	6	15	0.04	0.91	3.20	0.26	2.56	1.33	24.0
FF05	FF05C1X2	31.9	0	580	6	14	0.04	0.86	3.55	0.28	2.76	1.36	19.8
FF05	FF05C1X3	31.7	300	600	6	12	0.04	0.85	3.24	0.29	1.93	0.87	18.4
FF05	FF05C1X4	33.4	200	600	6	13	0.05	0.87	2.52	0.28	1.96	0.66	17.9
FF05	FF05C1X5	32.9	0	600	6	15	0.03	0.86	3.00	0.26	2.97	0.93	27.8
FF05	FF05b1	29.3	0	600	6	16	0.03	0.93	2.69	0.23	1.99	1.13	32.4
FF06	FF06x1x4	35.1	100	600	7	15	0.04	0.94	3.84	0.17	1.58	0.84	25.3
FF06	FF06x1x5	35	0	620	7	17	0.05	0.88	1.17	0.16	2.82	1.91	19.9
FF07	FF07B1X2	31.5	200	600	6	13	0.05	0.86	4.72	0.19	3.22	2.00	18.7

Table 2.S2 Specimen level paleointensity results (continued).

Site	Specimen	B_{anc} , μT	T_{min}	T_{max}	n_{ptrm}	n_{int}	β	f_{vds}	DRAT	g_{max}	MAD	DANG	q
FF07	FF07c1	29.7	0	600	6	16	0.04	0.96	4.53	0.17	1.23	0.92	24.8
FF08	FF08A1X1	33.9	0	600	5	14	0.04	0.92	4.52	0.19	2.28	1.13	21.8
FF09	FF09A1X1	36.1	0	600	6	15	0.05	0.99	4.15	0.21	1.83	1.72	19.3
FF10	FF10d1x1	42.5	100	600	7	15	0.04	0.89	3.93	0.18	1.99	2.14	20.9
FF10	FF10d1x2	42.8	300	620	7	14	0.04	0.86	3.38	0.23	1.83	1.52	20.5
FF10	FF10d1x3	42.5	0	600	7	16	0.05	0.85	1.17	0.20	3.09	1.69	19.8
FF10	FF10d1x5	42.3	300	620	7	14	0.03	0.85	2.89	0.24	1.97	1.04	30.1
FF14	FF14A3X2	55.3	0	580	6	14	0.04	0.90	1.45	0.17	3.20	1.79	19.9
FF14	FF14A3X3	64.1	200	600	6	13	0.05	0.87	2.63	0.18	2.28	1.36	17.6
FF14	FF14A3X4	65.3	200	600	6	13	0.03	0.87	1.26	0.15	2.15	2.35	31.0
FF14	FF14A3X5	73.7	100	600	6	14	0.05	0.86	2.23	0.17	3.44	1.53	17.2
FF14	FF14B1X1	63.9	200	600	6	13	0.03	0.86	4.89	0.15	2.99	2.00	26.5
FF14	FF14B1X2	45.3	0	580	6	14	0.04	0.86	1.09	0.13	5.09	3.80	23.1
FF14	FF14B1X4	68.9	100	600	6	14	0.05	0.95	3.15	0.18	1.96	1.85	19.8
FF14	FF14a2	48	0	570	5	14	0.04	0.86	1.99	0.15	1.52	0.90	22.1
FF15	FF15B1X1	61.3	0	600	6	15	0.03	0.90	2.77	0.12	3.69	1.76	29.1
FF15	FF15B1X2	60.2	0	580	6	14	0.04	0.88	2.94	0.13	3.36	1.74	23.0
FF15	FF15B1X3	60.5	0	580	6	14	0.03	0.87	3.82	0.11	2.42	1.24	23.7
FF15	FF15B1X4	54.5	100	600	6	14	0.04	0.87	4.87	0.14	3.24	2.34	19.4
FF15	FF15B1X5	62.7	0	600	6	15	0.03	0.89	3.14	0.12	3.65	1.11	25.3
FF15	FF15B2X1	63.3	0	600	6	15	0.03	0.85	2.78	0.11	3.56	1.40	29.0
FF15	FF15B2X2	40.2	0	600	6	15	0.03	0.87	3.78	0.13	3.04	1.82	33.2
FF15	FF15B2X3	52	100	600	6	14	0.04	0.86	4.08	0.12	3.83	3.01	20.1
FF15	FF15B2X4	69	0	600	6	15	0.04	0.86	4.22	0.13	3.15	1.59	20.3
FF15	FF15B2X5	59.7	0	560	5	13	0.03	0.85	2.43	0.14	2.58	2.27	28.2
FF15	FF15a2	45.1	100	600	6	15	0.02	0.88	2.97	0.12	2.66	1.23	42.5
FF17	FF17B1X5	68.6	0	660	8	18	0.03	0.86	3.95	0.55	3.13	0.85	16.3
FF17	FF17a2	55.4	200	660	8	17	0.05	0.88	2.47	0.58	2.32	0.34	11.9
FF18	FF18A3X1	56.9	0	660	8	18	0.03	0.86	2.91	0.49	4.17	1.29	24.4

Table 2.S2 Specimen level paleointensity results (continued).

Site	Specimen	B_{anc} , μT	T_{min}	T_{max}	n_{ptrm}	n_{int}	β	f_{vds}	DRAT	g_{max}	MAD	DANG	q
FF18	FF18B1X2	56.7	100	660	8	17	0.02	0.86	0.90	0.50	3.06	0.75	30.6
FF18	FF18B1X4	56.9	0	660	8	18	0.02	0.89	4.19	0.47	3.15	1.03	30.3
FF20	FF20b1	56.1	0	660	8	19	0.03	0.86	3.40	0.41	3.66	1.15	21.1
FF21	FF21A1X1	41.4	0	660	8	18	0.03	0.87	2.61	0.39	10.04	7.04	24.0
FF21	FF21A1X4	56.3	0	660	8	18	0.04	0.86	4.05	0.27	6.36	3.19	21.4
FF21	FF21c1	49.9	0	660	8	19	0.02	0.93	1.75	0.29	3.05	0.33	42.3
FF22	FF22a1	64.7	300	660	8	16	0.04	0.95	1.96	0.15	2.14	3.13	22.1
FF22	FF22c1x2	75.2	0	660	9	20	0.04	0.96	2.80	0.16	2.52	0.85	20.8
FF22	FF22c1x3	71.2	200	660	9	17	0.04	0.89	2.69	0.15	2.64	0.50	22.0
FF22	FF22c1x4	77	0	660	9	20	0.04	0.94	4.29	0.16	3.50	1.16	19.5
FF23	FF23b2	43	100	660	8	18	0.02	0.87	3.09	0.09	4.35	1.92	54.3
FF23	FF23c1x1	65.2	0	640	8	19	0.04	0.85	4.91	0.13	2.02	3.30	21.3
FF23	FF23c1x2	65	100	680	9	20	0.04	0.88	4.86	0.13	2.22	2.21	20.9
FF23	FF23c1x3	62.1	100	660	9	19	0.02	0.90	4.54	0.13	1.66	1.89	34.8
FF23	FF23c1x4	65.8	0	640	8	19	0.03	0.91	4.24	0.13	1.63	2.70	28.7
FF23	FF23c1x5	66.7	0	680	9	21	0.04	0.90	3.83	0.10	2.93	3.03	23.5
FF23	FF23c2x1	70.3	0	640	8	19	0.04	0.85	4.82	0.13	1.94	1.86	18.8
FF23	FF23c2x2	66.5	0	680	9	21	0.03	0.89	4.36	0.11	2.39	0.99	31.4
FF23	FF23c2x3	76.2	0	660	9	20	0.05	0.85	4.07	0.14	2.91	1.87	17.2
FF23	FF23c2x4	72.1	0	600	7	17	0.03	0.87	3.43	0.12	2.61	0.50	29.1
FF23	FF23c2x5	59.5	200	680	9	18	0.04	0.88	3.89	0.12	0.99	1.69	21.3
FF24	FF24a1x2	58	200	680	9	18	0.03	0.88	4.35	0.11	2.36	0.88	32.1
FF24	FF24a1x3	47	200	680	9	18	0.04	0.92	4.65	0.11	1.31	2.67	22.1
FF24	FF24a2x1	61.2	0	680	9	21	0.03	0.95	4.77	0.11	2.35	0.92	36.5
FF24	FF24a2x2	58.9	100	680	9	20	0.03	0.89	4.98	0.10	4.01	3.21	30.7
FF24	FF24a2x3	55.6	0	680	9	21	0.03	0.98	4.25	0.11	2.11	0.60	31.1
FF24	FF24a2x4	60.3	150	680	9	19	0.04	0.94	4.57	0.12	2.02	1.61	24.6
FF24	FF24a2x5	57.6	0	680	9	21	0.03	0.96	4.51	0.09	1.79	0.43	36.9
GF01	GF01A1	46.8	0	600	5	14	0.04	0.87	2.67	0.31	3.45	1.05	23.1

Table 2.S2 Specimen level paleointensity results (continued).

Site	Specimen	B_{anc} , μT	T_{min}	T_{max}	n_{ptrm}	n_{int}	β	f_{vds}	DRAT	g_{max}	MAD	DANG	q
GF01	GF01B2	46.7	0	600	5	14	0.03	0.92	2.61	0.32	2.12	0.58	25.8
GF01	GF01C2	46.6	100	590	6	14	0.03	0.85	1.12	0.32	3.03	0.32	26.4
GF01	GF01D1	46.7	0	600	5	14	0.03	0.89	2.50	0.31	2.49	0.67	26.4
GF01	GF01D2	47.3	400	600	5	11	0.03	0.86	2.40	0.38	1.78	0.52	26.5
GF03	GF03A1	42.2	0	580	5	13	0.02	0.89	1.70	0.32	2.72	0.91	38.3
GF03	GF03C2	42.6	0	600	5	14	0.02	0.92	1.19	0.25	3.04	1.19	41.8
GF03	GF03C3	44.6	250	600	6	13	0.02	0.87	2.95	0.29	2.16	0.33	32.4
GF03	GF03E1	43.7	0	600	5	14	0.02	0.90	2.72	0.25	3.44	1.66	36.4
GF04	GF04C1	40	0	600	5	14	0.03	0.89	2.40	0.16	4.87	2.58	32.3
GF04	GF04G1	41.8	250	600	6	13	0.03	0.89	1.89	0.22	1.89	0.45	32.0
GF05	GF05D1	41.8	0	600	5	14	0.02	0.89	2.68	0.17	2.82	2.22	50.2
GF05	GF05E1	42.9	300	600	5	13	0.02	0.88	1.07	0.20	2.76	1.90	37.7
GF06	GF06C1	43.8	0	600	5	14	0.04	0.96	3.57	0.28	2.60	1.21	21.0
GF06	GF06D1	43.7	0	600	5	14	0.04	0.96	4.59	0.28	2.96	1.47	23.9
GF06	GF06E1	43.4	0	600	5	14	0.03	0.93	4.98	0.28	3.04	1.41	25.4
GF07	GF07A1	43.8	0	600	5	14	0.04	0.93	2.02	0.19	0.90	0.07	24.6
GF07	GF07B1	46	250	600	6	13	0.05	0.87	0.89	0.21	1.04	0.28	16.6
GF07	GF07C2	44.8	0	600	5	14	0.04	0.95	2.99	0.29	0.89	0.45	25.0
GF07	GF07E1	43.9	0	570	4	12	0.04	0.88	1.94	0.24	0.80	1.29	24.3
GF14	GF14B1	46.1	0	600	5	14	0.02	0.86	1.02	0.18	3.50	1.16	44.3
GF15	GF15B3	47.1	0	600	5	14	0.02	0.89	4.19	0.16	3.65	0.42	43.4
GF15	GF15C2	49.9	0	600	5	14	0.03	0.88	2.29	0.15	4.14	0.82	30.3
GF15	GF15H2	48.6	0	600	5	14	0.01	0.88	1.20	0.16	3.43	0.72	61.5
GF16	GF16C2	44.8	0	600	6	16	0.02	0.87	1.44	0.27	3.10	0.95	38.4
GF16	GF16F2	45.5	0	600	5	14	0.02	0.91	1.46	0.21	2.73	0.48	44.8
GF16	GF16G1	45.4	0	600	5	14	0.02	0.88	1.95	0.18	4.91	1.66	50.7
GF16	GF16H1	45.3	0	600	5	14	0.02	0.89	1.18	0.19	3.36	0.44	39.6
GG01	GG01a2	35	0	640	7	18	0.02	0.91	2.30	0.14	1.98	0.52	39.5
GG01	GG01a3x1	35.3	0	580	7	16	0.03	0.85	2.40	0.15	2.45	1.82	27.6

Table 2.S2 Specimen level paleointensity results (continued).

Site	Specimen	B_{anc} , μT	T_{min}	T_{max}	n_{ptrm}	n_{int}	β	f_{vds}	DRAT	g_{max}	MAD	DANG	q
GG01	GG01a3x2	43.3	150	600	7	15	0.02	0.86	2.02	0.20	2.47	1.82	36.5
GG01	GG01a3x3	33.1	0	640	8	19	0.03	0.87	2.56	0.15	2.47	2.07	30.8
GG01	GG01a3x4	35	0	570	6	15	0.05	0.86	1.17	0.14	2.38	2.82	18.9
GG01	GG01a3x5	37.4	200	620	8	15	0.04	0.87	3.16	0.18	1.49	1.10	23.2
GG01	GG01b1x1	33.8	0	600	7	17	0.03	0.87	1.37	0.16	3.14	2.89	27.2
GG01	GG01b1x2	38.2	100	620	8	17	0.02	0.85	2.13	0.17	3.10	2.35	39.2
GG01	GG01b1x3	32.4	0	640	8	19	0.03	0.86	2.67	0.14	2.99	2.63	30.0
GG01	GG01b1x4	34.7	0	640	8	19	0.03	0.87	3.32	0.15	3.43	2.51	35.3
GG01	GG01b1x5	36.6	0	640	8	19	0.02	0.87	1.61	0.13	2.94	1.60	38.1
GG02	GG02b1	31	0	640	7	18	0.02	0.89	2.29	0.14	2.65	0.86	37.7
GG02	GG02b2x2	40.1	0	600	7	17	0.03	0.86	2.36	0.17	2.92	2.85	34.9
GG02	GG02b2x3	38.6	0	600	7	17	0.03	0.86	2.71	0.16	2.47	1.67	28.1
GG02	GG02b2x4	37.3	150	600	7	15	0.03	0.88	2.79	0.20	1.98	2.48	27.8
GG02	GG02b2x5	37.5	150	600	7	15	0.02	0.87	2.30	0.20	2.21	2.50	38.9
GG02	GG02b3x1	38	150	600	7	15	0.02	0.86	1.92	0.17	2.40	2.72	34.9
GG02	GG02b3x2	37.6	200	600	7	14	0.04	0.87	1.88	0.22	1.55	1.74	24.4
GG02	GG02b3x3	37.5	0	600	7	17	0.02	0.85	1.51	0.17	2.89	2.70	36.9
GG02	GG02b3x4	37.3	0	640	8	19	0.03	0.90	3.59	0.19	2.45	2.24	34.3
GG02	GG02b3x5	38.5	100	600	7	16	0.04	0.85	3.74	0.17	2.50	2.30	21.0
GG03	GG03a2	24.1	0	620	7	17	0.04	0.91	1.34	0.17	3.02	1.32	22.3
GG03	GG03b1x1	44.3	0	600	7	17	0.03	0.86	3.04	0.16	2.34	2.02	25.4
GG03	GG03b1x3	40.1	0	640	8	19	0.03	0.87	4.64	0.11	2.62	1.60	25.2
GG03	GG03b1x5	43.1	100	600	7	16	0.03	0.85	3.41	0.16	2.22	2.17	25.8
GG03	GG03b2x2	42.4	0	600	7	17	0.03	0.85	2.40	0.14	2.43	3.02	25.3
GG03	GG03b2x3	44.7	200	620	8	15	0.03	0.87	2.49	0.13	2.69	2.62	30.8
GG03	GG03b2x4	40.9	100	640	8	18	0.03	0.89	4.45	0.13	2.77	2.10	30.5
GG03	GG03b2x5	40.1	0	640	8	19	0.03	0.91	4.19	0.14	2.03	1.61	31.2
GG04	GG04b1x3	36.4	0	600	7	17	0.04	0.86	4.03	0.15	2.90	3.37	24.2
GG04	GG04b1x4	34.6	0	600	7	17	0.04	0.89	4.95	0.16	2.58	2.93	21.8

Table 2.S2 Specimen level paleointensity results (continued).

Site	Specimen	B_{anc} , μT	T_{min}	T_{max}	n_{ptrm}	n_{int}	β	f_{vds}	DRAT	g_{max}	MAD	DANG	q
GG04	GG04b2x1	36.5	100	600	7	16	0.03	0.85	3.63	0.12	2.64	3.02	29.0
GG04	GG04b2x3	36.2	100	600	7	16	0.03	0.85	0.91	0.18	3.41	2.43	26.1
GG04	GG04b2x4	33.2	0	600	7	17	0.03	0.87	4.24	0.10	2.34	2.79	25.7
GG50	GG50x1x4	52.4	0	620	7	17	0.05	0.90	3.97	0.16	2.42	1.66	19.3
GG51	GG51x2x1	35.6	0	600	7	15	0.05	0.89	1.15	0.17	2.70	2.10	19.1
GG51	GG51x2x2	45.5	100	620	7	16	0.05	0.85	3.08	0.14	2.74	1.86	20.2
GG51	GG51x2x4	40.3	0	620	7	17	0.05	0.91	3.23	0.15	2.21	2.34	19.1
GG51	GG51x2x5	41	200	620	7	15	0.04	0.86	0.88	0.14	2.66	1.99	22.6
GG52	GG52a1x2	38.7	0	620	7	17	0.05	0.88	1.94	0.14	2.80	2.16	21.0
GG52	GG52a1x3	39.7	200	620	7	15	0.04	0.86	2.80	0.16	2.44	2.30	20.9
GG92	GG92b1x4	34.8	350	620	8	13	0.04	0.85	4.08	0.13	0.77	0.61	22.5
GG92	GG92d1x1	36.4	100	600	7	16	0.05	0.88	2.96	0.13	1.73	1.07	18.4
GG92	GG92d1x3	31	0	620	7	17	0.05	0.91	4.70	0.14	2.96	2.68	20.0
GG92	GG92d1x5	36.2	0	600	7	17	0.03	0.87	1.66	0.12	2.21	1.79	28.7
GG93	GG93a3x1	47.3	100	620	8	17	0.04	0.85	3.01	0.15	2.29	1.34	23.1
GG93	GG93a3x4	45.2	0	620	8	18	0.03	0.86	4.38	0.14	3.28	1.54	25.4
GG93	GG93b1x4	34.3	0	620	8	18	0.03	0.88	2.23	0.13	3.34	2.29	29.8
GG93	GG93b1x5	34.8	0	620	8	18	0.02	0.94	1.17	0.16	1.28	0.59	40.8
GG94	GG94c1x2	27.5	0	620	8	18	0.04	0.87	2.86	0.09	5.55	4.46	23.8
GG94	GG94c1x3	25.6	0	620	8	18	0.03	0.87	1.82	0.09	4.26	3.57	28.2
GG95	GG95a1x1	28.5	0	620	8	18	0.03	0.88	3.52	0.10	3.85	3.01	34.3
GG95	GG95a1x2	27.6	0	620	8	18	0.03	0.90	4.05	0.10	3.62	2.92	31.6
GG95	GG95a1x4	28.5	150	600	7	15	0.04	0.85	2.62	0.11	3.60	4.62	24.5
GG95	GG95a2x4	32.8	0	620	8	18	0.04	0.86	4.85	0.13	4.20	3.67	24.0
GG95	GG95a2x5	31.2	0	620	8	18	0.05	0.86	2.57	0.11	4.08	2.93	21.0
GG95	GG95b2	16.7	0	640	7	18	0.05	0.88	4.64	0.11	3.98	2.70	21.4
GG96	GG96a2	17.2	0	640	7	18	0.04	0.89	4.08	0.17	2.92	1.41	25.8
GG97	GG97b2x4	34.2	0	620	7	17	0.05	0.89	4.55	0.10	4.18	4.15	19.9
GG97	GG97b2x5	34.7	0	600	7	16	0.05	0.88	3.19	0.15	1.97	1.73	18.4

Table 2.S2 Specimen level paleointensity results (continued).

Site	Specimen	B_{anc} , μT	T_{min}	T_{max}	n_{ptrm}	n_{int}	β	f_{vds}	DRAT	g_{max}	MAD	DANG	q
GG97	GG97c1x5	36.8	100	620	7	16	0.04	0.86	2.39	0.20	3.34	2.38	24.1
GG98	GG98b1x3	33.6	0	620	7	17	0.03	0.85	4.83	0.11	6.76	3.86	30.6
GG98	GG98b1x5	32.4	100	620	7	16	0.04	0.86	4.50	0.18	4.00	2.42	21.6
GG99	GG99a3x2	23.2	0	620	7	17	0.02	0.90	2.97	0.13	4.33	2.45	42.9
GG99	GG99a3x4	25.4	0	620	7	17	0.02	0.90	1.55	0.13	3.38	2.09	39.1
GG99	GG99b1x2	28.9	0	620	7	17	0.04	0.86	3.14	0.13	6.57	5.02	25.6
GG99	GG99b1x5	25.9	0	620	7	17	0.02	0.88	2.68	0.12	4.19	3.49	47.4

2.B Magnetic remanence directions and AMS

Specimens generally display a single component remanence which decays to the origin after the 250°C or 300°C heating step (main document Figure 3). Most specimens from sections EE, GG, and the bottom of section FF are fully demagnetized by 610°C. However, some specimens from the top portion (above 84 m) of FF required further heating steps up to 675°C to fully demagnetize their NRM. ChRMs were determined for 18 specimens from section EE, 16 from section FF, and 14 from section GG (Figure 2.S1a,b, and c). The average of all 48 specimens is Dec = 5.7° and Inc = 40.9°, with a Kent 95% confidence ellipse with major and minor axes of $\eta 95 = 7.0°$ and $\zeta 95 = 3.9°$. This is shallower and eastward of what Palmer et al. (1996) found: Dec = ∼348°, Inc = ∼53°. Mean ChRM directions broken down by section and flow unit are in Table 2.S3.

To test if there are variations in paleomagnetic direction with stratigraphic location we grouped the data by height for sections EE and FF and by side of the gorge for GG as shown by difference marker colors in Figure 2.S1a,b, and c. We find in sections EE and FF the upper portions of the tuff have ChRM directions that are shallower and eastward of the Palmer et al. (1996) result (blue and green circles in 2.S1a and b) while the lower portions of those sections agree with Palmer et al. (1996) (red circles). The specimens that were sampled from the western wall of the canyon in profile GG have ChRM directions that are shallower and westward of of the Palmer et al. (1996) result (green circles in 2.S1c).

As Palmer et al. (1996) showed, AMS is a useful tool for analyzing the fabric of the Bishop Tuff. The AMS ellipses are mostly oblate. Figure 2.S1 b, d, and f summarize the

Table 2.S3: Summary of characteristic remanence magnetization directions averages of different subsets of the data from the thermal demagnetization experiment. n is the number of specimens, Dec is declination, Inc is inclination, η_{95} and ζ_{95} are the major and minor axes of the Kent 95% confidence ellipse. Characteristic remanence direction from Palmer et al. (1996): Dec = 348°, Inc = 53°.

	n	**Dec**	**Inc**	η_{95}	ζ_{95}
EE	18	10.8°	24.6°	11.8°	7.3°
FF	16	13.4°	47.0°	8.3°	2.9°
GG	14	346.8°	51.7°	2.6°	5.1°
Ig1Eb	34	9.7°	35.9°	8.8°	5.0°
Ig2Eb	14	353.6°	51.6°	2.6°	6.6°
All	**48**	**5.7°**	**40.9°**	**7.0°**	**3.9°**

directions of the site mean minimum eigenvector of the susceptibility ellipsoids (K_3). The average of the K_3 directions is Dec = 64.2°, Inc = 74.4°. Sections EE and FF each have several specimens with K_3 directions much shallower than the average and mostly in the NE quadrant, although section EE has much greater scatter (Figure 2.S1 b and d).

In the upper portions of the tuff ChRM and AMS K_3 directions are deflected from the average of Palmer et al. (1996) to shallower and eastward (westward for west side of GG) here we discuss the source of this directional offset. The presence of lithics that were not remagnetized would add more scatter to the data, but this would not systematically tilt the ChRM directions. The columnar jointing in our sampling sections is subvertical and columns are in situ, so it is unlikely that the tilting is due to block rotation. If the tilting were due solely to fabric, we would expect the bottom of the sections, which are more compacted, to be affected. The tilting may be caused by interaction of the tuff with the paleo-topography (there was a preexisting gorge). This would explain GG east and west deflected in opposite directions. Another possible explanation is interaction of the magnetic fabric with the stress field associated with the column formation Wright et al. (2011). While this tilting was an

interesting finding, it is not relevant to the Bishop Tuff's ability to record paleointensity.

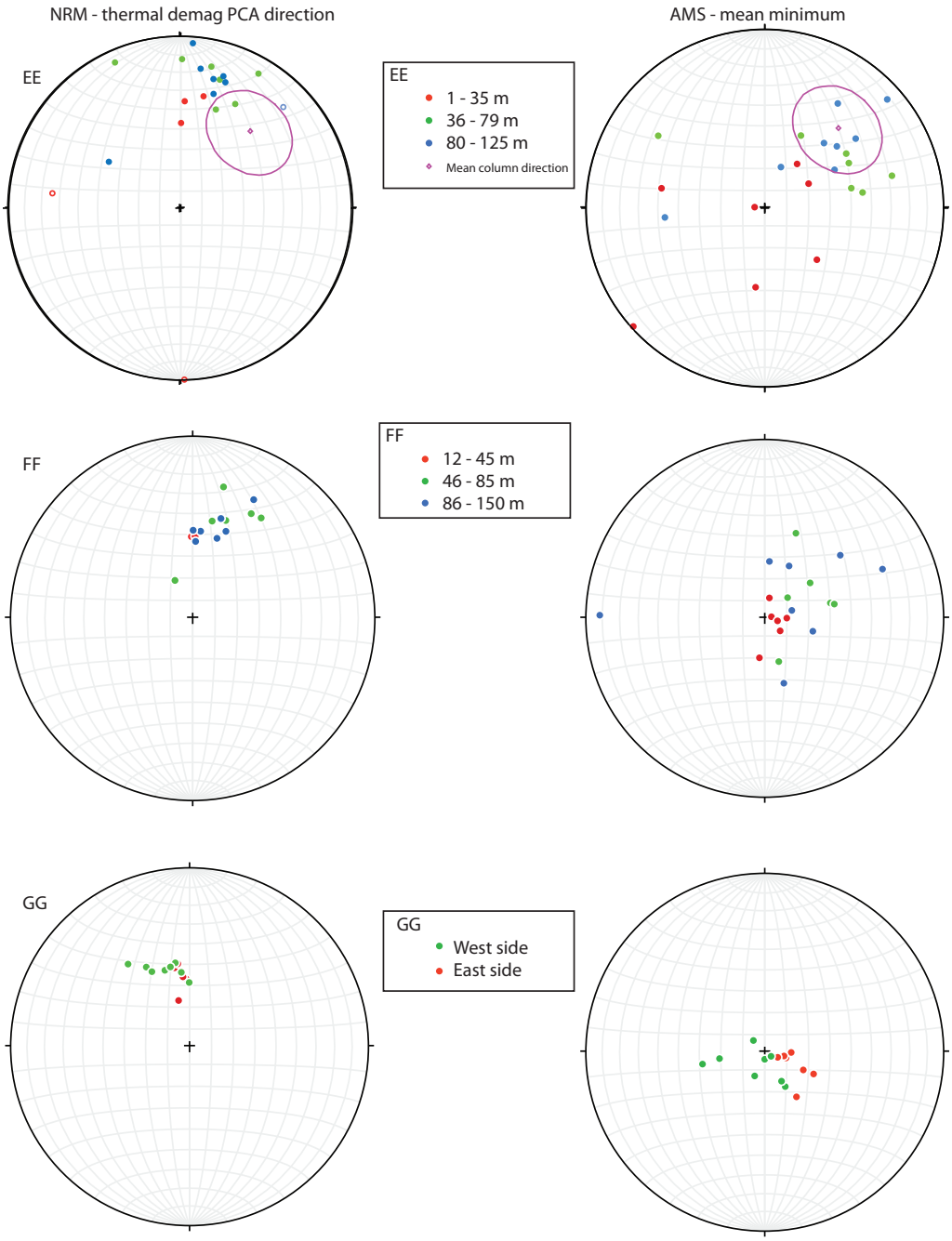

Figure 2.S1: Thermal demagnetization PCA direction and AMS mean minimum.

References

Bowles, J. A., Gee, J. S., Jackson, M. J., and Avery, M. S. (2015). Geomagnetic paleointensity in historical pyroclastic density currents: Testing the effects of emplacement temperature and postemplacement alteration. *Geochemistry, Geophysics, Geosystems*, 16(10):3607–3625.

Bowles, J. A., Jackson, M. J., Berquó, T. S., Sølheid, P. A., and Gee, J. S. (2013). Inferred time-and temperature-dependent cation ordering in natural titanomagnetites. *Nature communications*, 4:1916.

Coe, R. S., Grommé, S., and Mankinen, E. A. (1978). Geomagnetic paleointensities from radiocarbon-dated lava flows on hawaii and the question of the Pacific nondipole low. *Journal of Geophysical Research: Solid Earth*, 83(B4):1740–1756.

Crowley, J., Schoene, B., and Bowring, S. (2007). U-Pb dating of zircon in the Bishop Tuff at the millennial scale. *Geology*, 35(12):1123–1126.

Davies, C. J. and Constable, C. G. (2014). Insights from geodynamo simulations into long-term geomagnetic field behaviour. *Earth and Planetary Science Letters*, 404:238–249.

Draeger, U., Prévot, M., Poidras, T., and Riisager, J. (2006). Single-domain chemical, thermochemical and thermal remanences in a basaltic rock. *Geophysical Journal International*, 166(1):12–32.

Driscoll, P. E. (2016). Simulating 2 Ga of geodynamo history. *Geophysical Research Letters*, 43(11):5680–5687.

Dunlop, D. and Özdemir, O. (2015). Magnetizations in rocks and minerals. In Schubert, G., editor, *Treatise on Geophysics*, volume 5, chapter 8, pages 277 – 336. Elsevier, Amsterdam, 2 edition.

Dunlop, D. J. and Özdemir, Ö. (2001). *Rock magnetism: fundamentals and frontiers*, volume 3. Cambridge university press.

Eick, P. M. and Schlinger, C. M. (1990). The use of magnetic susceptibility and its frequency dependence for delineation of a magnetic stratigraphy in ash-flow tuffs. *Geophysical Research Letters*, 17(6):783–786.

Fabian, K. (2003). Some additional parameters to estimate domain state from isothermal magnetization measurements. *Earth and Planetary Science Letters*, 213(3):337–345.

Fabian, K. (2009). Thermochemical remanence acquisition in single-domain particle ensembles: A case for possible overestimation of the geomagnetic paleointensity. *Geochemistry, Geophysics, Geosystems*, 10(6).

Fu, R. R., Weiss, B. P., Lima, E. A., Kehayias, P., Araujo, J. F., Glenn, D. R., Gelb, J., Einsle, J. F., Bauer, A. M., Harrison, R. J., Ali, G., and Walsworth, R. L. (2017). Evaluating the paleomagnetic potential of single zircon crystals using the Bishop Tuff. *Earth and Planetary Science Letters*, 458:1–13.

Gee, J. S., Tauxe, L., and Constable, C. (2008). AMSSpin: A LabVIEW program for measuring the anisotropy of magnetic susceptibility with the Kappabridge KLY-4S. *Geochemistry, Geophysics, Geosystems*, 9(8).

Gee, J. S., Yu, Y., and Bowles, J. (2010). Paleointensity estimates from ignimbrites: An evaluation of the Bishop Tuff. *Geochemistry, Geophysics, Geosystems*, 11(3).

Geissman, J. W., Newberry, N. G., and Peacor, D. R. (1983). Discrete single-domain and pseudo-single-domain titanomagnetite particles in silicic glass of an ash-flow tuff. *Canadian Journal of Earth Sciences*, 20(2):334–338.

Giordano, D., Nichols, A. R., and Dingwell, D. B. (2005). Glass transition temperatures of natural hydrous melts: a relationship with shear viscosity and implications for the welding process. *Journal of Volcanology and Geothermal Research*, 142(1):105–118.

Grunder, A. L., Laporte, D., and Druitt, T. H. (2005). Experimental and textural investigation of welding: effects of compaction, sintering, and vapor-phase crystallization in the rhyolitic Rattlesnake Tuff. *Journal of volcanology and geothermal research*, 142(1):89–104.

Hildreth, W. (1979). The Bishop Tuff: evidence for the origin of compositional zonation in silicic magma chambers. *Geological Society of America Special Papers*, 180:43–76.

Hildreth, W. and Wilson, C. J. (2007). Compositional zoning of the Bishop Tuff. *Journal of Petrology*, 48(5):951–999.

Holt, E. W. and Taylor, H. P. (1998). $^{18}O/^{16}O$ mapping and hydrogeology of a short-lived ($\approx$10 years) fumarolic (>500°C) meteoric-hydrothermal event in the upper part of the 0.76 Ma Bishop Tuff outflow sheet, California. *Journal of volcanology and geothermal research*, 83(1):115–139.

Holt, E. W. and Taylor, H. P. (2001). $^{18}O/^{16}O$ studies of fossil fissure fumaroles from the Valley of Ten Thousand Smokes, Alaska. *Bulletin of volcanology*, 63(2):151–163.

Jackson, M. and Bowles, J. A. (2014). Curie temperatures of titanomagnetite in ignimbrites: Effects of emplacement temperatures, cooling rates, exsolution, and cation ordering. *Geochemistry, Geophysics, Geosystems*, 15(11):4343–4368.

Keith, T. E. (1991). Fossil and active fumaroles in the 1912 eruptive deposits, Valley of Ten Thousand Smokes, Alaska. *Journal of Volcanology and Geothermal Research*, 45(3-4):227–254.

Keith, T. E. and Muffler, L. (1978). Minerals produced during cooling and hydrothermal alteration of ash flow tuff from yellowstone drill hole y-5. *Journal of Volcanology and Geothermal Research*, 3(3-4):373–402.

Kirschvink, J. (1980). The least-squares line and plane and the analysis of palaeomagnetic data. *Geophysical Journal International*, 62(3):699–718.

Lowrie, W. (1990). Identification of ferromagnetic minerals in a rock by coercivity and unblocking temperature properties. *Geophysical research letters*, 17(2):159–162.

McIntosh, W. C., Sutter, J. F., Chapin, C. E., and Kedzie, L. L. (1990). High-precision $^{40}Ar/^{39}Ar$ sanidine geochronology of ignimbrites in the Mogollon-Datil volcanic field, southwestern New Mexico. *Bulletin of Volcanology*, 52(8):584–601.

Mochizuki, N., Maruuchi, T., Yamamoto, Y., and Shibuya, H. (2013). Multi-level consistency tests in paleointensity determinations from the welded tuffs of the Aso pyroclastic-flow deposits. *Physics of the Earth and Planetary Interiors*, 223:40–54.

Mullins, C. and Tite, M. (1973). Magnetic viscosity, quadrature susceptibility, and frequency dependence of susceptibility in single-domain assemblies of magnetite and maghemite. *Journal of Geophysical Research*, 78(5):804–809.

Özdemir, Ö. and Dunlop, D. J. (2010). Hallmarks of maghemitization in low-temperature remanence cycling of partially oxidized magnetite nanoparticles. *Journal of Geophysical Research: Solid Earth*, 115(B2).

Palmer, H., MacDonald, W., Gromme, C., and Ellwood, B. (1996). Magnetic properties and emplacement of the Bishop tuff, California. *Bulletin of volcanology*, 58(2):101–116.

Paterson, G. A., Tauxe, L., Biggin, A. J., Shaar, R., and Jonestrask, L. C. (2014). On improving the selection of Thellier-type paleointensity data. *Geochemistry, Geophysics, Geosystems*, 15(4):1180–1192.

Perrin, M., Alva-Valdivia, L., Lopez-Martinez, M., Rosas-Elguera, J., Benammi, M., Gonzalez-Rangel, J., and Camps, P. (2013). Palaeomagnetism of the upper volcanic supergroup, southern part of the Sierra Madre Occidental, Mexico. *Geophysical Journal International*, 193(3):1250–1264.

Riehle, J., Miller, T., and Bailey, R. (1995). Cooling, degassing and compaction of rhyolitic ash flow tuffs: a computational model. *Bulletin of Volcanology*, 57(5):319–336.

Riehle, J. R. (1973). Calculated compaction profiles of rhyolitic ash-flow tuffs. *Geological Society of America Bulletin*, 84(7):2193–2216.

Sarna-Wojcicki, A. M., Pringle, M. S., and Wijbrans, J. (2000). New $^{40}Ar/^{39}Ar$ age of the Bishop Tuff from multiple sites and sediment rate calibration for the Matuyama-Brunhes boundary. *Journal of Geophysical Research: Solid Earth*, 105(B9):21431–21443.

Schlinger, C. M., Griscom, D., Papaefthymiou, G. C., and Veblen, D. R. (1988a). The nature of magnetic single domains in volcanic glasses of the kbs tuff. *Journal of Geophysical Research: Solid Earth*, 93(B8):9137–9156.

Schlinger, C. M., Rosenbaum, J., and Veblen, D. R. (1988b). Fe-oxide microcrystals in welded tuff from southern Nevada: origin of remanence carriers by precipitation in volcanic glass. *Geology*, 16(6):556–559.

Schlinger, C. M., Veblen, D. R., and Rosenbaum, J. G. (1991). Magnetism and magnetic mineralogy of ash flow tuffs from Yucca Mountain, Nevada. *Journal of Geophysical Research: Solid Earth*, 96(B4):6035–6052.

Selkin, P. A. and Tauxe, L. (2000). Long-term variations in palaeointensity. *Philosophical Transactions of the Royal Society of London A: Mathematical, Physical and Engineering Sciences*, 358(1768):1065–1088.

Shaar, R. and Tauxe, L. (2013). Thellier GUI: An integrated tool for analyzing paleointensity data from Thellier-type experiments. *Geochemistry, Geophysics, Geosystems*, 14(3):677–692.

Sheridan, M. F. (1970). Fuarmolic mounds and ridges of the Bishop Tuff, California. *Geological Society of America Bulletin*, 81(3):851–868.

Sheridan, M. F. and Wang, Y. (2005). Cooling and welding history of the Bishop Tuff in Adobe Valley and Chidago Canyon, California. *Journal of Volcanology and Geothermal Research*, 142(1):119–144.

Smirnov, A. V., Tarduno, J. A., Kulakov, E. V., McEnroe, S. A., and Bono, R. K. (2016). Palaeointensity, core thermal conductivity and the unknown age of the inner core. *Geophysical Journal International*, 205(2):1190–1195.

Tauxe, L., Mullender, T., and Pick, T. (1996). Potbellies, wasp-waists, and superparamagnetism in magnetic hysteresis. *Journal of Geophysical Research: Solid Earth*, 101(B1):571–583.

Tauxe, L. and Staudigel, H. (2004). Strength of the geomagnetic field in the Cretaceous Normal Superchron: New data from submarine basaltic glass of the Troodos Ophiolite. *Geochemistry, Geophysics, Geosystems*, 5(2).

Van den Bogaard, P. and Schirnick, C. (1995). $^{40}Ar/^{39}Ar$ laser probe ages of Bishop Tuff quartz phenocrysts substantiate long-lived silicic magma chamber at Long Valley, United States. *Geology*, 23(8):759–762.

Wilson, C. J. and Hildreth, W. (1997). The Bishop Tuff: new insights from eruptive stratigraphy. *The Journal of Geology*, 105(4):407–440.

Wilson, C. J. and Hildreth, W. (2003). Assembling an ignimbrite: Mechanical and thermal building blocks in the Bishop Tuff, California. *The Journal of geology*, 111(6):653–670.

Worm, H.-U. and Jackson, M. (1999). The superparamagnetism of Yucca Mountain tuff. *Journal of Geophysical Research: Solid Earth*, 104(B11):25415–25425.

Wright, H. M., Lesti, C., Cas, R. A., Porreca, M., Viramonte, J. G., Folkes, C. B., and Giordano, G. (2011). Columnar jointing in vapor-phase-altered, non-welded Cerro Galán Ignimbrite, Paycuqui, Argentina. *Bulletin of volcanology*, 73(10):1567–1582.

Yu, Y., Tauxe, L., and Genevey, A. (2004). Toward an optimal geomagnetic field intensity determination technique. *Geochemistry, Geophysics, Geosystems*, 5(2).

Chapter 3

Asymmetry in Growth and Decay of the Geomagnetic Dipole Revealed in Seafloor Magnetization

Abstract

Geomagnetic intensity fluctuations provide important constraints on time-scales associated with dynamical processes in the outer core. PADM2M is a reconstructed time series of the 0–2 Ma axial dipole moment (ADM). After smoothing to reject high frequency variations PADM2M's average growth rate is larger than its decay rate. The observed asymmetry in rates of change is compatible with longer term diffusive decay of the ADM balanced by advective growth on shorter time scales, and provides a potentially useful diagnostic for evaluating numerical geodynamo simulations. We re-analyze the PADM2M record using

improved low-pass filtering to identify asymmetry and quantify its uncertainty via bootstrap methods before applying the new methodology to other kinds of records. Asymmetry in distribution of axial dipole moment derivatives is quantified using the geomagnetic skewness coefficient, s_g. A positive value indicates the distribution has a longer positive tail and the average growth rate is greater than the average decay rate. The original asymmetry noted by Ziegler and Constable (2011) is significant and does not depend on the specifics of the analysis.

A long-term record of geomagnetic intensity should also be preserved in the thermoremanent magnetization of oceanic crust recovered by inversion of stacked profiles of marine magnetic anomalies. These provide an independent means of verifying the asymmetry seen in PADM2M. We examine three near-bottom surveys: a 0 to 780 ka record from the East Pacific Rise at 19°S, a 0 to 5.2 Ma record from the Pacific Antarctic Ridge at 51°S, and a chron C4Ar–C5r (9.3–11.2 Ma) record from the NE Pacific. All three records show an asymmetry similar in sense to PADM2M with geomagnetic skewness coefficients, $s_g > 0$. Results from PADM2M and C4Ar–C5r are most robust, reflecting the higher quality of these geomagnetic records. Our results confirm that marine magnetic anomalies can carry a record of the asymmetric geomagnetic field behavior first found for 0–2 Ma in PADM2M, and show that it was also present during the earlier time interval from 9.3–11.2 Ma.

3.1 Introduction

Motion of liquid-iron in Earth's outer core generates the geomagnetic field, which exhibits directional and intensity changes on a broad array of timescales. These variations are recorded in newly forming igneous rocks and sediments on land and beneath the seafloor where numerous paleomagnetic and marine magnetic anomaly studies have been conducted. The resulting data can be used to constrain global time-varying models of past field behavior.

Much of our understanding of geomagnetic field variations over the past few million years comes from paleofield direction and relative paleointensity (RPI) variations recorded by marine sediments (Roberts et al., 2013; Tauxe and Yamazaki, 2015; Valet and Fournier, 2016). Absolute paleointensity data derived from igneous rocks are necessary to calibrate the RPI. Polarity reversals occur aperiodically every few hundred thousand years and are accompanied by lows in intensity. Directional excursions are incomplete reversals, also featuring low field strength, which occur more frequently than reversals but are not always global in extent. Within polarity chrons there are also globally coherent higher frequency variations in paleointensity. These higher frequency variations are evident in sedimentary RPI records and are sometimes observed as globally coherent tiny-wiggles in marine magnetic anomaly records (Cande and LaBrecque, 1974; Cande and Kent, 1992b). Marine magnetic anomaly records provide a robust record of polarity reversals (Cande and Kent, 1995) and high quality anomaly data are also a viable alternative for studying geomagnetic intensity variations (Gee et al., 2000).

The temporal resolution of individual time series of RPI and magnetic anomaly data

are determined locally by sedimentation or spreading rate, respectively, and by other geological and environmental factors that may influence the quality of the geomagnetic record. When multiple records are combined to study regional or global variations the limiting factor is the ability to match the chronology across records.

In one example of a 0–4 Ma record from sediments from the equatorial Pacific sampled during Leg 138 of the Ocean Drilling Program, Valet and Meynadier (1993) observed a saw-toothed intensity variation. The intensity decreased gradually over the course of a polarity interval (with a characteristic relaxation time of ∼0.5 Myr) then rapidly rebounded over a few thousand years after the field reversed direction, restarting the cycle. The saw-tooth intensity pattern is not observed in all sedimentary records, nor is it universally accepted as caused by field behavior. For example, the 0.5 Myr relaxation timescale observed by Valet and Meynadier (1993) may be due to a viscous remanent magnetization (Kok and Tauxe, 1996a,b); see Tauxe and Yamazaki (2015) for a review and discussion. However, differing rates of growth and decay before and after a reversal have been observed in other sedimentary records and stacks, including Sint-2000 (Valet et al., 2005) where a decrease in dipole strength is observed over 60-80 kyr, followed by a recovery period of only a few thousand years.

A global view of geomagnetic field strength over 0–2 Ma is provided by PADM2M (Ziegler et al., 2011), a reconstruction of ADM variations using 76 time series of sedimentary RPI and more than 5000 absolute paleointensity data from igneous and archaeological materials. The restriction to ADM variations is a consequence of chronological constraints which determine the temporal resolution, combined with limited geographical coverage and

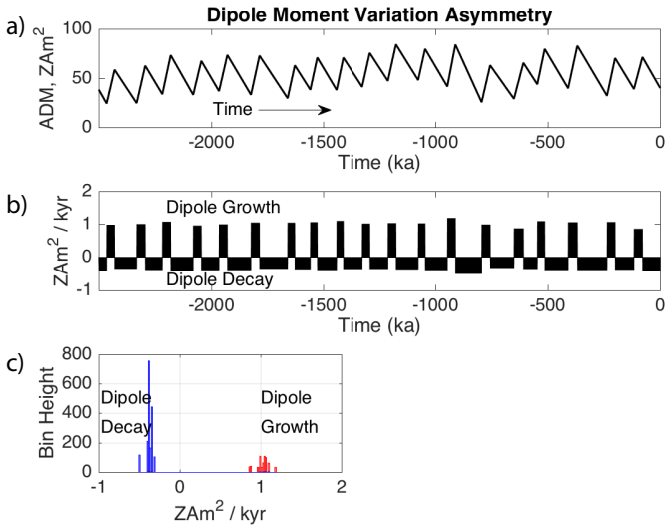

Figure 3.1: a) A cartoon of ADM time variations displaying asymmetry between growth and decay rates. b) The first derivative of the ADM model in a) evaluated every 1 kyr. c) Histogram showing the distribution of the derivatives from b).

an absence of complementary directional information in the data compilation. PADM2M provides a robust measure of ADM variations at about 10 kyr temporal resolution, and yields an average ADM for the past 2 Ma of 5.3×10^{22} Am^2 with a standard deviation of 1.5×10^{22} Am^2. The average for the Brunhes chron (0–780 ka, 6.23×10^{22} Am^2) is higher than during the Matuyama chron (780 ka – 1.77 Ma, 4.8×10^{22} Am^2).

PADM2M offers the possibility of identifying characteristic time scales associated with specific aspects of core dynamics. Ziegler and Constable (2011) examined long-term (25–150 kyr) variations of PADM2M and its derivative, and found an asymmetry in the distribution of growth and decay rates. When variations shorter than 36 kyr are smoothed out in the PADM2M model, they found an average growth rate that is 20% larger than the average decay rate: the field spends 54% of its time decaying compared with 46% growing. This behavior is not limited to intervals immediately surrounding field reversals. Ziegler

and Constable (2011) attributed this asymmetry to physical processes occurring on different timescales, a long decay timescale associated with diffusive losses in ADM, and the more rapid growth related to a temporally filtered view of advective processes.

A simplified cartoon of an ADM model with this kind of behavior is plotted in Figure 3.1. Age is specified as negative time and time progresses from left to right, so negative slopes are periods of decay and positive slopes are periods of field growth. This convention allows straightforward comparison with advancing time steps in geodynamo simulation results. The field spends more time decaying than growing, but the rates of growth are greater in magnitude.

The rate of change of the geomagnetic field is controlled by contributions from diffusion and advection in the outer core, as described by the first and second terms, respectively, on the right hand side of the magnetic induction equation:

$$\frac{\partial \mathbf{B}}{\partial t} = \eta \nabla^2 \mathbf{B} + \nabla \times (\mathbf{u} \times \mathbf{B}), \tag{3.1}$$

where t is time, $\mathbf{B}$ is magnetic field, η is magnetic diffusivity, and $\mathbf{u}$ is core fluid velocity. The longer, slower decay of the dipole suggests periods where the field is dominated by diffusion, and the shorter, faster periods of growth suggest advection is (on average) acting to increase the dipole strength. The timescale of diffusion for the ADM is characterized by $t_d = \frac{r_o^2}{\pi^2 \eta}$ ~54 kyr, the e-folding time for dipole magnetic field decay if fluid motion in the outer core ceased (Backus et al., 1996). Here r_o is the outer core radius (3.5×10^6 m) and η is the magnetic diffusivity (0.72 m^2/s, Pozzo et al., 2012). The advection timescale is described by the time it takes fluid to move from the inner core boundary to the core mantle

boundary: $t_a = d/U$ ∼200 yr, where $d = r_o - r_i$ the outer core thickness (2.2×10^6 m) and U is the characteristic outer core fluid velocity (∼5 $\times 10^{-4}$ m/s, Holme, 2015).

In what follows we first evaluate the robustness of the initial asymmetry result from PADM2M presented by Ziegler and Constable (2011) through development of improved analysis methods that sharpen the earlier results and provide uncertainty estimates (Section 2).We explore the possibility of identifying the asymmetry in rate of change of the thermoremanent magnetization (TRM) of the oceanic crust and the associated marine magnetic anomalies. Seafloor magnetization recovered from inversion of stacks of near-bottom marine magnetic anomalies are considered as a proxy for RPI and used as an independent means of assessing the asymmetry seen in PADM2M (Section 3). Seafloor magnetization records that span a similar time period (0–780 ka and 0–5.2 Ma) to that covered by PADM2M are analyzed using the same techniques. To test the persistence through time of the asymmetric behavior, we also examine high quality near-bottom marine magnetic anomaly records from chrons C4Ar–C5r that record field behavior from 9.3–11.2 Ma. The asymmetry between growth and decay rates observed in PADM2M is robust, and the peak asymmetry is most evident when fluctuations faster than ∼50 kyr are filtered out. All three records show an asymmetry between growth and decay similar in sense to PADM2M: the distribution of ADM derivatives has a longer positive tail. We discuss the robustness of these results in the context of the greater reliability of the records provided by PADM2M and C4Ar–C5r, compared with the younger marine magnetic anomaly records.

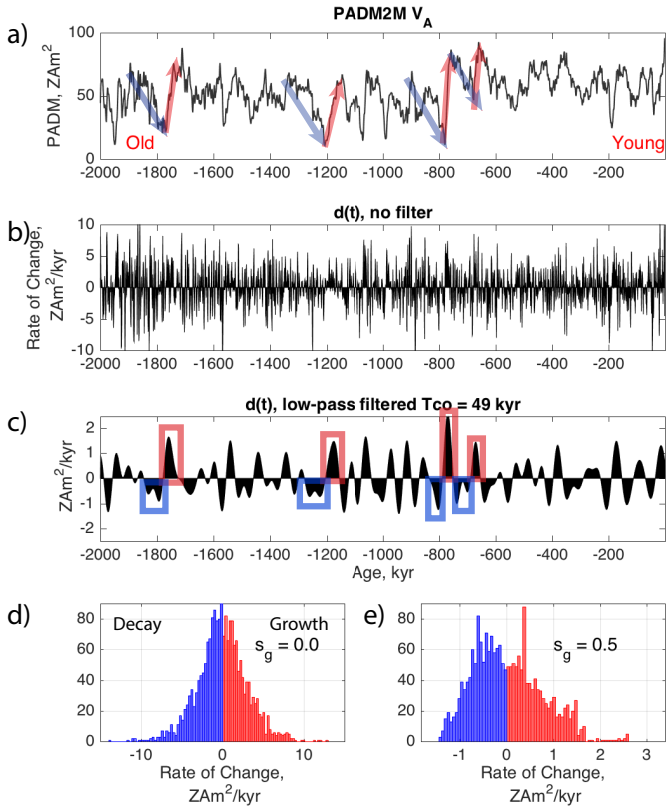

Figure 3.2: An example of asymmetry between growth and decay rate observed after low-pass filtering. a) unfiltered PADM2M time series (1 $\mathrm{ZAm}^2 = 10^{21}\mathrm{Am}^2$) and b) its first derivative evaluated at 1 kyr intervals, c) is an example of a low-pass filtered version of the derivatives of PADM2M, using the methods described in the text, d) shows the histogram of values for the unfiltered time series in b), with geomagnetic skewness coefficient $s_g = 0.0$, and e) same as d) but for the filtered rates of change given in c) with $s_g = 0.5$.

3.2 Identifying asymmetry in time series of paleointensity

We outline the methods used to identify asymmetry in growth and decay rate, using PADM2M as an illustration (Figure 3.2). The blue and red arrows in Figure 3.2a highlight some readily identifiable intervals where the dipole moment is on average decaying slowly and is followed by a period of more rapid growth. To study these in more detail we evaluate

the rate of change with time before (Figure 3.2b) and after (Figure 3.2c) low-pass filtering of the time derivative of PADM2M to remove variations at frequencies higher than a cutoff frequency of $f_{co} = 1/T_{co}$ (that is for periods shorter than T_{co}). The associated distributions of rates of decay are provided in Figure 3.2d and Figure 3.2e. In the unfiltered series the time spent growing and decaying is well balanced, but applying a low-pass filter uncovers an imbalance in the rates of change: positive values, which correspond to a growing dipole, are larger on average and occur less frequently than negative rates of decay. As we show below, the maximum asymmetry is found at a cutoff period of $T_{co} = 49$ kyr.

The ADM (V_A) is expressed as a spline variation in time. We calculate the analytical derivative

$$d(t) = \frac{\mathrm{d}V_A}{\mathrm{d}t}, \tag{3.2}$$

and evaluate it at uniformly spaced intervals of 1 kyr over 0–2 Ma as the starting point for our analysis. We used a Parks-McClellan equiripple low-pass filter as implemented in MatLab routine firpm (Parks and McClellan, 1972), which produces a sharp exclusion of variations below the specified cutoff period T_{co}. As discussed in the supplementary material (Section 1.1) it is more effective than the method previously used by Ziegler and Constable (2011). By varying T_{co}, from 10 to 150 kyr we can study how the asymmetry varies as a function of successively longer timescales. A diagnostic for the level of asymmetry in growth and decay, is provided by the skewness in the distribution of decay rates, which we call the geomagnetic skewness.

In a skewed or asymmetric distribution (Figure 3.2e) the average rate of decay is different from the average rate of growth, and the field spends more time in one state

than the other. A robust estimate of asymmetry is provided by the geomagnetic skewness coefficient, s_g, for the distribution of dipole field derivatives, d_i. The geomagnetic skewness of a distribution is the third moment about the mean. The geomagnetic skewness coefficient, s_g, is rendered dimensionless through normalization by the standard deviation cubed, and is convenient for making comparisons across the various distributions considered later.

$$s_g = \frac{\frac{1}{m}\sum_{i=1}^{m}\left(d_i - \overline{d}\right)^3}{\left(\sqrt{\frac{1}{m}\sum_{i=1}^{m}\left(d_i - \overline{d}\right)^2}\right)^3} \tag{3.3}$$

The asymmetry manifests as a distribution of derivatives with a longer positive tail, $s_g > 0$. Figures 3.2d and e show two example distributions of rates of change: in Figure 3.2d, the unfiltered PADM2M record exhibits no asymmetry ($s_g = 0.0$), while in Figure 3.2e there is asymmetry between growth and decay rates and $s_g = 0.5 \pm 0.1$, corresponding to more time spent in decay mode and shorter intervals of more rapid growth. The uncertainty value is estimated with a delete-one jackknife resampling of the original 76 records making up PADM2M, and using the variability in geomagnetic skewness coefficient across the various pseudo-sampled models to calculate the standard error, $\widehat{se}_{jack}$, (see the supplement Section 1.2). The updated results for PADM2M are shown in Figure 4.1 and reported in Table 3.1. This is the same result found by Ziegler and Constable (2011) although they parameterize the asymmetry with the percentages of time spent growing and decaying, which are unequal. It is important to note that, because of the direction of the time axis in our study, field decay corresponds to negative derivatives while in Ziegler and Constable (2011) field decay corresponded to positive derivatives. The geomagnetic skewness coefficient has the advantage of containing information about the mean rate of change making it a more robust estimator

than the percentage growth criterion used previously.

Details about the different filtering methods can be found in the supplementary materials Section 1.1. Here we simply note that the method used here simplifies specification of T_{co}. The Parks-McClellan equiripple low-pass filter we used has a sharper frequency response than the spline method previously used by Ziegler and Constable (2011) (see Figure S1). The improved low-pass filtering does not affect the basic conclusion that there is asymmetry in the distribution of growth and decay. For PADM2M the peak magnitude of the geomagnetic skewness coefficient ($s_g = 0.5$) occurs at $T_{co} = 49$ kyr (see Table 3.1).

Table 3.1: Summary of asymmetry geomagnetic skewness results. n = number of sedimentary records (PADM2M) or anomaly profiles, R_+ = period range of significantly positive s_g. Chron C5 refers to the Northeastern Pacific Chron C5 record. Less robust results from the Brunhes 19°S East Pacific Rise (EPR) record and 0-5.2 Ma 51°S Pacific Antarctic Ridge (PAR) record are shown in italics.

Study	**n**	**peak** s_g	T_{co} **of peak** s_g	R_+ **in** T_{co}
PADM2M	76	0.5	49 kyr	15-107 kyr
Chron C5 43°N	12	0.5	39 kyr	15-107 kyr
EPR 19°S	*8*	*1.1*	*15 kyr*	< 25 *kyr and* > 39 *kyr*
PAR 51°S	*3*	*0.7*	*10 kyr*	> 78 *kyr*

We need to know how long a record is needed for unambiguous identification of non-zero geomagnetic skewness coefficient. This was evaluated using sequentially longer distinct test subsets from PADM2M after filtering at $T_{co} = 49$ kyr (see the supplement Section 1.3). We find that a record of at least ∼800 kyr, and preferably longer, is needed to confidently observe this asymmetry.

Having established the basic methods for identifying asymmetry in rates of change we turn now to the question of whether the signal found in PADM2M is detected in the

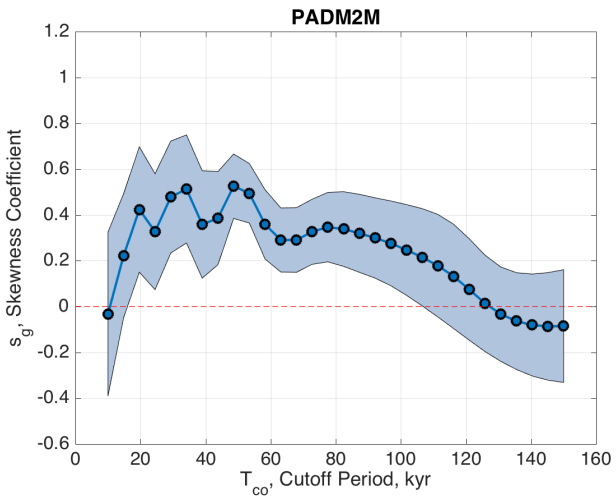

Figure 3.3: Geomagnetic skewness coefficient s_g as a function of cutoff period T_{co} for PADM2M. Error bars are $\pm$ 1 $\widehat{se}_{jack}$ (standard error estimated using a jackknife method).

marine magnetic anomaly record, either in the time period spanned by PADM2M or during other time intervals.

3.3 Geomagnetic records from marine magnetic anomalies

The main geomagnetic signal recorded in the oceanic crust is the pattern of reversals that are combined with absolute ages to provide the geomagnetic polarity timescale (GPTS) (Cande and Kent, 1992a, 1995). The seafloor's ability to record the geomagnetic field is affected by the crustal accretion process, and there are a number of potentially confounding variables, including source layer thickness, pattern of lava accumulation, alteration, and the geochemistry of lavas. Generally, we do not expect these processes to be coherent for profiles that are sufficiently separated, so we should be able to see a geomagnetic core-field signal

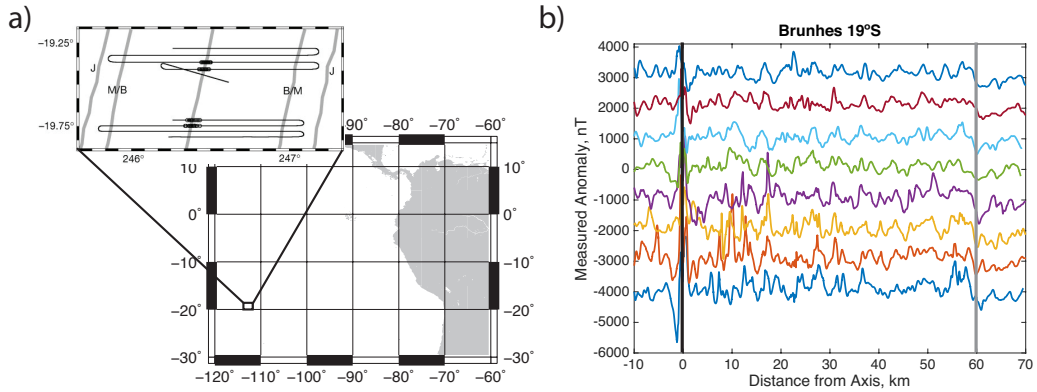

Figure 3.4: Brunhes near-bottom marine magnetic anomalies from southern East Pacific Rise (EPR) (Gee et al., 2000) at 19°S. a) Location map modified from Gee et al. (2000). b) Measured near-bottom anomaly profiles from the eastern ridge flank, offset by 1000 nT for clarity. The ridge axis is marked with a black vertical line, and the Brunhes-Matuyama boundary is marked by a grey vertical line.

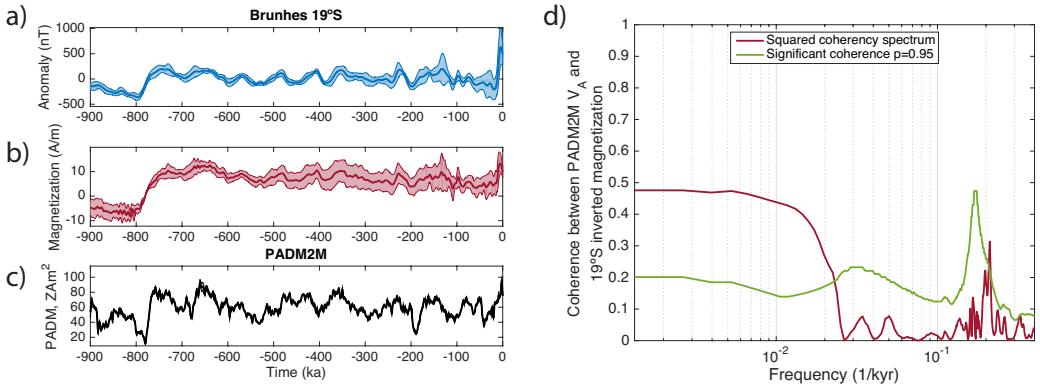

Figure 3.5: 19°S EPR Brunhes marine magnetic anomaly. a) Upward continued (to 2.57 km or about 400 m above seafloor) and stacked anomaly, b) inverted magnetization solution, c) PADM2M for comparison. Error bars in panels a, b, and c are ± 1 standard error estimated using a jackknife method. Note: the x-axes in panels a,b, and c are age instead of distance, and therefore the anomaly is reflected compared to Figure 3.4b. d) Coherence between 0–780 ka 19°S marine magnetic anomaly record and 0–780 ka of PADM2M in red. Green line indicates the level below which no significant coherence can be infered at the 95% confidence level. See supplementary Section 2 for details of the anomaly processing and inversion.

through these. By averaging a significant number of profiles we can be more confident that the coherent signal we observe is of geomagnetic origin.

On smaller spatial and temporal scales than the reversals in the GPTS there are globally coherent anomalies (tiny-wiggles) attributed to either short polarity reversals or intensity fluctuations (Cande and LaBrecque, 1974; Klitgord et al., 1975; Cande and Kent, 1992b). The depth to the magnetization source layer controls the wavelength of the observed anomaly and hence the temporal resolution of the decipherable geomagnetic variations. Sea surface magnetic anomaly profiles are thought to provide a complete record of polarity intervals longer than about 30 kyr (e.g., Cande and Kent, 1992b). Field behavior occurring on timescales shorter than ∼30 kyr requires higher-resolution data collected nearer to the source layer. Several studies have found tiny-wiggles that are likely produced by geomagnetic field variations (e.g., Bowers et al., 2001).

It is important to distinguish between the geomagnetic skewness coefficient, s_g, as defined in equation 3 and the terms skewness and anomalous skewness as applied to marine magnetic anomalies. We use geomagnetic skewness to refer to the observed skewed distribution of geomagnetic dipole moment derivatives. The skewness of magnetic anomalies arises from the geometry of the two dimensional source and the direction of the ambient field and remanence. Nonvertical magnetization contrasts, tilting of the magnetization source or systematic changes in geomagnetic intensity may further modify the anomaly shape and this additional contribution is termed anomalous skewness. Although both the source geometry and anomalous skewness may affect our estimate of geomagnetic skewness, we find that the uncertainty associated with these effects is small (Supplemental Section 2.2).

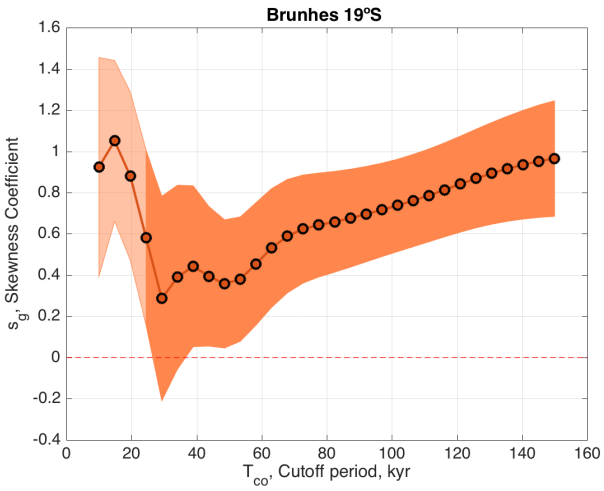

Figure 3.6: Geomagnetic skewness coefficient as a function of cutoff period $s_g(T_{co})$ for Brunhes-age anomalies from the EPR near 19°S. Error bars are $\pm$ 1 $\widehat{se}_{jack}$. The lighter orange shading over cutoff periods $<$ 25 kyr indicates the timescale associated with the transition zone width of 1.8 km (Sempere et al., 1987).

The presence of a saw-toothed pattern (slow decay and more rapid rebound of paleointensity about a reversal) was tested in marine magnetization models (Westphal and Munschy, 1999), and tested as a cause of anomalous marine magnetic anomaly skewness (Dyment and Arkani-Hamed, 2005). These studies did not find the saw-toothed intensity pattern fit their seafloor magnetization models. The three marine magnetic anomaly surveys we examine here are from fast-spreading ridges where anomalous skewness is less pronounced.

3.3.1 East Pacific Rise at 19°–20°S

We reanalyze the 0–780 ka near-bottom magnetic anomalies from 19°–20°S of the East Pacific Rise (EPR) discussed by Gee et al. (2000) (Figure 3.4). We will refer to this record as "EPR 19°S". These near-bottom anomalies show some similarities with stacked sedimentary relative-paleointensity sequences, and also with the past 50 kyr of absolute-paleointensities

from archeomagnetic and volcanic material (Gee et al., 2000). Absolute paleointensities determined from submarine basaltic glass collected at the same study area of the EPR also parallel the near-ridge magnetization values, providing additional support for the importance of geomagnetic intensity fluctuations in modulating crustal magnetization (Gee et al., 2000). Eight anomaly profiles recorded over the faster-spreading eastern flank (76 mm/yr east flank, 142 mm/yr full spreading rate) of the EPR at 19°-20°S were upward continued to a level surface at 2.57 km depth, stacked, and then inverted for magnetization. To upward continue the anomalies, which were measured on an uneven track of the magnetometer above the seafloor, we used the method described in Parker and Klitgord (1972) with 20 line segments to represent the variable-elevation magnetometer track. We stacked the anomalies using the ridge and the Brunhes-Matuyama boundary as the only tie points (Figure 3.5a). We inverted the stack of anomalies for the magnetization of a 500 m thick source layer with constant magnetization direction (with inclination determined from the present day latitude) using the two-dimensional Fourier inversion method of Parker and Huestis (1974) (Figure 3.5b). Cosine-taper high and low-pass filters reduce the effect of noise at high and low wavenumbers that is amplified during the inversion. To pick the filter parameters (Table S2) we explored a range of magnetization solutions, balancing RMS misfit between the measured and forward modeled anomalies and the $\ell 1$ norm of the magnetization solution (see supplementary Section 2.2 for details).

Similarities between EPR 19°S near-bottom anomalies and PADM2M are evident in Figures 3.5b and c and indicate that geomagnetic intensity fluctuations are recorded in the seafloor magnetization. However, the maximum coherence, computed with a multitaper

method, between these two records (Figure 3.5d) is about 0.5 at long periods (red line) and falls at periods shorter than ∼50 kyr (red line coherence falls below the green line 95% confidence level). This modest coherence is to be expected from the relatively low magnetic field strength and shallow inclination associated with anomalies recorded at this low latitude and is evident also in the low between-line coherence in Figure 3.4b. The extrusive layer, thought to represent the dominant source of the anomalies, accumulates over a spatial scale of 2–3 km (e.g., Carbotte et al., 1997) and crustal accretion processes may obscure any coherent signal at shorter periods (< 25–40 kyr). Indeed, variations in the pattern of crustal accretion may substantially reduce between-line coherence of nearby anomaly profiles (see supplementary Section 3 material).

We repeat the low-pass filter analysis described in Section 2 to determine $s_g(T_{co})$, the geomagnetic skewness coefficient as a function of the filter cutoff period for this stacked magnetization solution. Departures of s_g from zero are statistically significant at periods below 25 kyr and above 39 kyr, $s_g = 1.1 \pm 0.4$ at $T_{co} = 15$ kyr and $s_g = 0.4 \pm 0.3$ at $T_{co} = 49$ kyr, as shown in Figure 3.6 and reported in Table 3.1. We examine this outcome in greater detail in the Discussion section.

3.3.2 Pacific Antarctic Ridge 51°S

A limited number of near-bottom anomaly records from the Pacific Antarctic Ridge (PAR) provide a much longer geomagnetic field record that may also be used to assess asymmetry. The PAR has been spreading at a relatively uniform half-rate of 42.6 mm/yr for the past 10 Ma (Klitgord et al., 1975). Three near-bottom profiles were collected over the

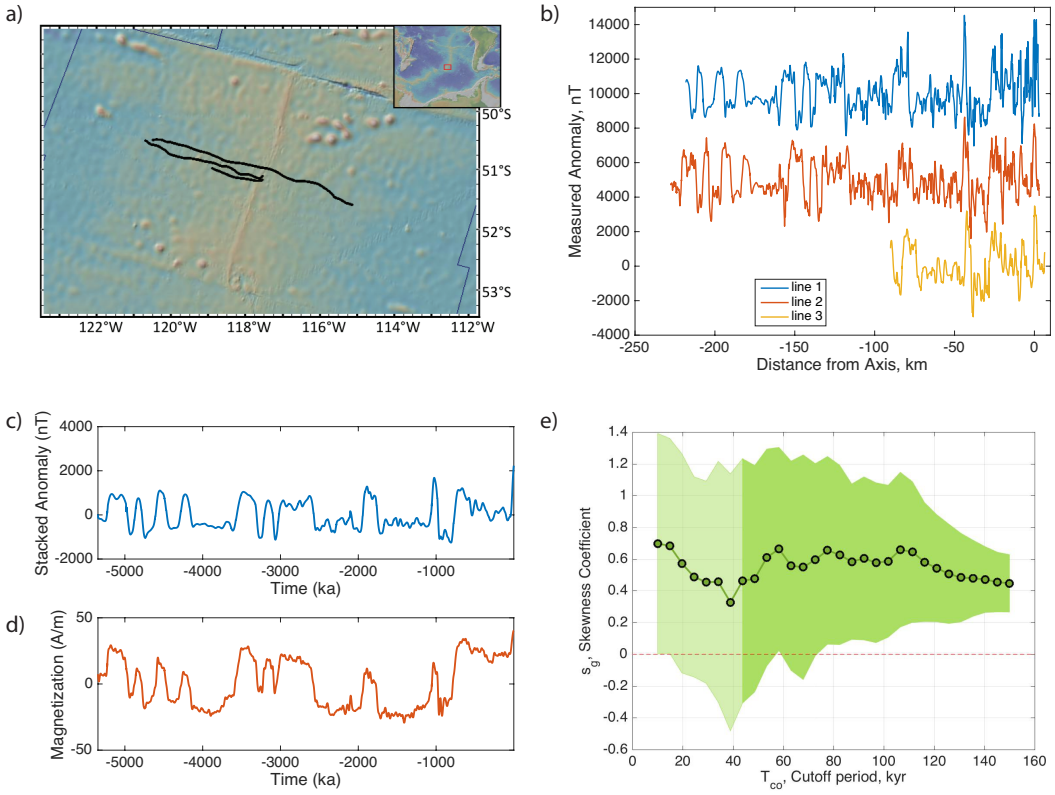

Figure 3.7: Pacific Antarctic Ridge near-bottom anomaly data (Klitgord et al., 1975). a) Survey map with isochrons for anomaly 5 (10.9 Ma) and shaded topography. b) Measured anomalies from the eastern side of the ridge offset by 5000 nT for clarity. c) Stacked anomaly after polarity reversal locations were picked. d) Magnetization solution. e) Geomagnetic skewness coefficient s_g as a function of cutoff period T_{co}. Error bars are $\pm$ 1 $\widehat{se}_{jack}$. The lighter green shading over cutoff periods $<$ 44 kyr indicates the timescale associated with the transition zone width of 2.0 km (Klitgord et al., 1975).

PAR at 51°S during the Southtow Expedition Leg 2 in 1972 (Figures 3.7a,b). We will refer to this record as "PAR 51°S". The longest of these lines (traversing both flanks out to anomaly C3n.4n, ∼5.2 Myr) was used by Klitgord et al. (1975) in a study of transition zone widths and the central anomaly high at the mid-ocean ridge in the Pacific. The other two near-bottom profiles were recovered from archival tapes providing the total of three lines analyzed here. Although the overall velocity of the eastern flank of the PAR profile is the same as the western flank it exhibits erratic spreading that Klitgord et al. (1975) attribute to ridge jumps. We only used the three profiles from the western flank of the PAR because there were more abundant and consistent data there. We upward continued the three lines to a level track (at 2.1 km depth), stacked them using polarity reversals as tie points (Figure 3.7c), and then inverted for magnetization (Figure 3.7d). At the polarity boundaries we flip the sign of the magnetization during reversed intervals so that positive slopes correspond with times of field growth and negative slopes decay. We repeat the low-pass filtering and jackknife error analyses described above to estimate $s_g(T_{co})$. Because of the slow survey speeds needed for near-bottom surveys, the 0-5.2 Ma 51°S PAR record $s_g(T_{co})$ is represented by only two long lines (and a third shorter line), resulting in large uncertainty estimates. Nonetheless, the overall pattern of geomagnetic skewness coefficient is positive and significantly greater than zero for cutoff periods above 78 kyr, and the sense of geomagnetic skewness coefficient is also similar to that of PADM2M at shorter periods although not significantly different from zero (Figure 3.7e and Table 3.1). Similar to the result from 19°S (Figure 3.6) at long periods ($>$ 100 kyr) s_g is significantly greater than zero, unlike PADM2M (Figure 4.1).

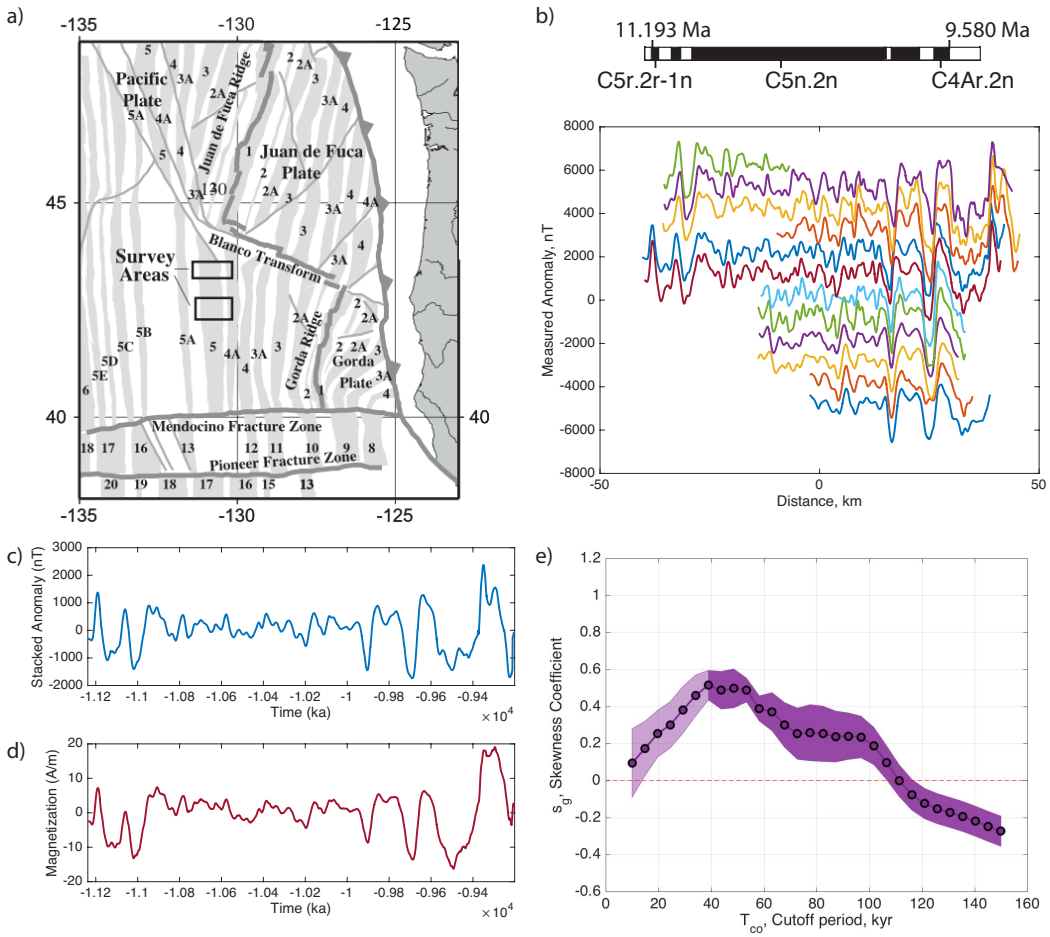

Figure 3.8: Northern Pacific chron C5 near-bottom anomaly data (Bowers et al., 2001). a) Survey map modified from Bowles et al. (2003). b) Measured anomalies offset by 1000 nT for clarity with polarity timescale. c) Stacked anomaly after polarity reversal location were picked see text for details. d) Magnetization solution. e) Geomagnetic skewness coefficient s_g as a function of cutoff period T_{co}. Error bars are $\pm$ 1 $\widehat{se}_{jack}$. The lighter purple shading over cutoff periods < 39 kyr indicates the timescale associated with the transition zone width of 1.7 km (Bowers et al., 2001).

3.3.3 Northeast Pacific Chron C5

Perhaps the most robust and best documented near-bottom record of geomagnetic field variations is from the northeast Pacific. Near-bottom magnetic anomaly data from chrons C4Ar–C5r (9.3–11.2 Ma) in the northeast Pacific provide the opportunity to examine whether the asymmetry in the field growth/decay noted over the past few million years is a more general feature of the field. Normal polarity chron C5n.2n is one of the longest periods (∼1 Myr) of mostly single polarity with a set of globally coherent tiny-wiggles observed in sea-surface anomaly data (Cande and LaBrecque, 1974). Roberts and Lewin-Harris (2000) presented a Miocene magnetostratigraphic record from ODP Site 884 in the NW Pacific and reported three reversed polarity intervals within C5n.2n. They calculated the durations of these reversed intervals as 6, 26, and 28 kyr. While the shortest (6 kyr) would be poorly represented in sea-surface anomalies (and might be unrecognized), reversed polarity intervals of 26-28 kyr should be readily recognized in near-bottom anomaly profiles and in many sea surface profiles. In another sedimentary record, South Atlantic ODP Site 1092, with a higher sedimentation rate of ∼3 cm/kyr (vs ∼1cm/kyr at ODP Site 887) there is evidence that three of the cryptochrons within chron C5n.2n may be excursions (Evans et al., 2007). Bowers et al. (2001) used the complex character of the near-bottom anomalies to argue that the tiny-wiggles in chron C5n.2n were formed by intensity fluctuations rather than short reversals. Bowles et al. (2003) showed that in the North Pacific the tiny-wiggles are highly correlated with an independent record of chron C5 intensity, sedimentary RPI (ODP Site 887) and they found no evidence of reversed polarity intervals within chron C5n.2n.

Twelve near-bottom anomaly lines measured at two survey areas separated by up to ∼120 km (eight at the southern area centered at 42°30'N, and four at the northern area centered at 43°30'N) show high between-line coherence as expected at this higher latitude (Figure 3.8), and are also well correlated with a single long line covering anomaly 5 from the west flank of the EPR at 19°S (Bowers et al., 2001). We will refer to this record as "chron C5 43°N". Crust in the area is generated at a half spreading rate of 42 mm/yr. Here we start with the raw magnetic anomaly measurements (there was no need to upward continue because data were acquired on a horizontal plane) (Figure 3.8b), stack the anomalies (Figure 3.8c), and invert for magnetization (Figure 3.8d). We use the location of reversals as tie points to stack the lines. One or more brief excursions or reversed polarity intervals may be present within C5n.2n. However, there was no discernible impact on our magnetization interpretation. Accordingly, we have treated it as a long normal polarity period. The reversals are located by iteratively adjusting the polarity boundaries and sigma value (reversal width reflecting spillover of lavas) to minimize the misfit between the measured and forward modeled anomalies (see supplement Section 2). We perform the same analysis as above for $s(T_{co})$. There is significant asymmetry in the ranges of T_{co} = 15–107 kyr with a maximum of $s_g = 0.5 \pm 0.1$ at $T_{co} = 39$ kyr (Figure 3.8e and Table 3.1).

3.4 Discussion

All three of the near-bottom marine magnetization records we analyze here display asymmetry between growth and decay rates in the same sense as PADM2M over at least part

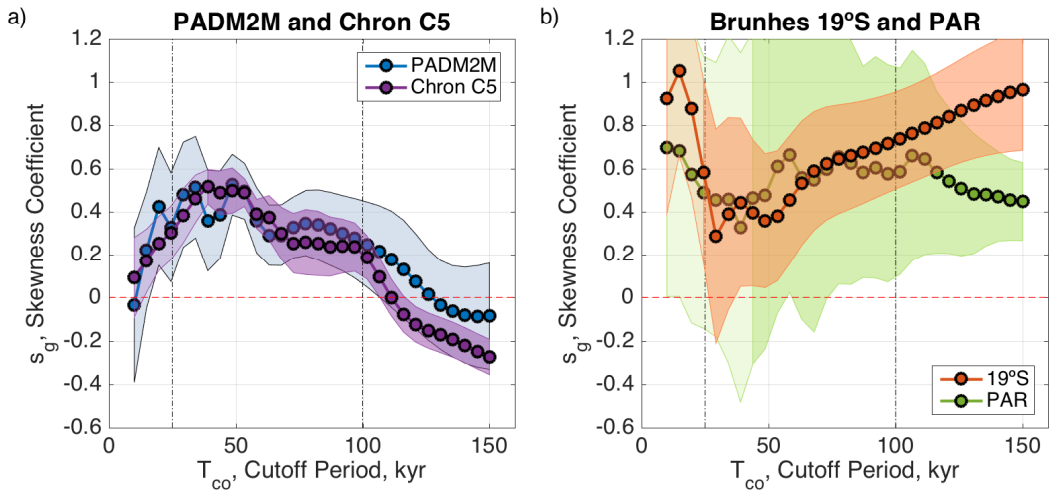

Figure 3.9: Comparison of geomagnetic skewness coefficient s_g as a function of cutoff period T_{co} between PADM2M and the three near-bottom marine magnetization studies discussed above. Black dot-dashed vertical lines delineate the three period ranges we compare: short ($T_{co} < 25$ kyr), intermediate ($T_{co} = 25 - 100$ kyr), and long periods ($T_{co} > 100$ kyr). a) The $s_g(T_{co})$ patterns of PADM2M and chron C5 43°N record agree at all periods. b) The EPR 19°S and PAR 51°S records have positive s_g, but their $s_g(T_{co})$ patterns are different from PADM2M and the chron C5 anomaly record.

of the frequency range studied. We compare the results of the three seafloor magnetization records with PADM2M over three period ranges: short period ($T_{co} < 25$ kyr), intermediate period ($T_{co} = 25 - 100$ kyr), and long period ($T_{co} > 100$ kyr) (as indicated by the black dot-dashed vertical lines in Figure 3.9). Based on the number of profiles and between-line coherence we consider the chron C5 43°N record to be the most reliable of the three near-bottom marine magnetic anomaly records we examined.

The chron C5 43°N record has remarkably high between-line coherence and the $s_g(T_{co})$ (Figure 3.9a) results agree remarkably well with PADM2M at all three periods. An important feature of the chron C5 43°N magnetization stack is the data were collected from two survey areas separated by ∼120 km. While this stack would still be considered a regional record it is encouraging that it displays a similar $s_g(T_{co})$ signal to PADM2M, which is a global

record. This same general asymmetry is present when the two survey areas are analyzed separately, though the two patterns differ at $T_{co} < \sim$40 kyr (see supplementary Section 4 for details).

The EPR 19°S and PAR 51°S records have positive geomagnetic skewness coefficient in the intermediate period (significantly different from zero above 39 kyr for the EPR 19°S and above 78 kyr for the PAR 51°S) that parallels that of PADM2M and the chron C5 43°N, but their patterns of $s_g(T_{co})$ differ at both long and shorter periods (Figure 3.9b). At low cutoff periods (10–25 kyr) they have positive s_g coefficients while PADM2M and the chron C5 43°N stack are much less skewed. However, the positive s_g at short period seen in the PAR record is not significantly different from zero. Stochastic models of mid-ocean ridge flow accretion indicate that little coherence between anomaly profiles is expected at periods $<$ 30 kyr (see supplementary Section 3 for details). This may explain the significant positive s_g seen in the EPR 19°S record at low cutoff periods.

At long periods ($T_{co} >$ 100 kyr) all three marine magnetization records show significant geomagnetic skewness coefficient but not all in the same sense. Both the EPR 19°S and PAR 51°S records are positive and the chron C5 43°N record is negative. The chron C5 43°N record signal at long periods agrees with the PADM2M result within their uncertainties. The EPR 19°S record may be too short to constrain the long periods; as we show in the supplement (Section 1.3) at least ∼800 kyr is needed. The standard error on the PAR 51°S $s_g(T_{co})$ pattern is generally larger than the other dataset because the stack is comprised of only two long and one shorter profiles. The EPR 19°S and PAR 51°S records include the ridge and we expect alteration to produce a long period signal in the magnetization, though

we find in our stochastic lava accretion models an exponential decay term makes s_g at long T_{co} more negative – the opposite of the EPR 19°S and PAR 51°S long period signal (see supplementary Section 3 for details, Figure S5a).

The similarity of asymmetry in PADM2M and the marine magnetic anomaly records (particularly the chron C5 43°N, but also at intermediate periods for the PAR 51°S and EPR 19°S) suggests that both recording media preserve a record of geomagnetic field asymmetry. Changes in axial dipole strength at the CMB are due to the combined effects of advection and diffusion (Olson and Amit, 2006). Diffusion results in changes that are slow and always decrease the field strength, while changes due to advection are more rapid and can act to increase or decrease the field strength. On long timescales (> 100 kyr) we might expect advection and diffusion to be in balance. If changes in the longterm average magnetic field are relatively small, the diffusion and advection terms of the induction equation will balance. This is consistent with absence of significant geomagnetic skewness coefficient signal above 107 kyr in PADM2M.

Our results here confirm that asymmetry between growth and decay rates observed in PADM2M by Ziegler and Constable (2011) is significant and that it is recorded by seafloor magnetization as well as sediments. When fluctuations faster than 15 kyr are filtered out, both PADM2M and our best quality marine magnetization record (the chron C5 43°N dataset) show geomagnetic skewness of the distribution of their rates of change with a peak at ∼40–50 kyr. We interpret this as the signature of diffusion in the axial dipole. To better understand the physical processes driving this asymmetric growth and decay of the dipole we need information about the geomagnetic field morphology at higher spatial resolution

than the ADM. The asymmetry between growth and decay rates may provide a valuable criterion for evaluating whether geodynamo simulations are Earth-like. The dynamics of simulations in which the dipole field spends more time decaying than growing and the mean growth is stronger than the mean decay rate can then be examined. For example, on advective timescales reverse flux patches moving from the equatorial region to the poles will weaken the ADM. Similarly, intense normal patches moving from the equator to the poles would increase the ADM. Diffusion will result in overall decreases in field strength (Olson and Amit, 2006).

3.5 Conclusions

From this study we draw three main conclusions:

1. We parameterize the asymmetry between growth and decay rates in PADM2M in terms of geomagnetic skewness coefficient s_g. The asymmetry is a robust feature and peaks when fluctuations faster than 49 kyr are filtered out.

2. This asymmetry is a feature of geomagnetic field behavior. The fact that it is found in seafloor magnetization as well as the predominantly sedimentary records of PADM2M, indicates it is not a product of the recording processes.

3. This asymmetry is present during two distinct time intervals (0–2 Ma and 9.3–11.2 Ma), and that suggests it is a fundamental feature of secular variation.

The timescale of the most skewed distribution of derivatives in PADM2M and the chron C5

43°N dataset (∼40–50 kyr) is similar to the characteristic diffusion dipole decay timescale of the outer core. This does not provide a direct link to the physical mechanism for this behavior, however, it does provide a new observational criterion for comparing Earth's magnetic field to those produced by geodynamo simulations. It is also useful to know that at least ∼800 kyr of ADM data is needed to make this analysis, which corresponds to ∼4 non-dimensional diffusion times for geodynamo simulations. By studying geodynamo simulations we can assess the outer core flow structures and behaviors that produce this magnetic field behavior. Our study also demonstrates the utility of examining near-bottom marine magnetic anomaly data for geomagnetic field behavior beyond just reversal records.

Data Availability

PADM2M is available through the EarthRef.org Digital Archive (ERDA) [http:// earthref.org/ERDA/1138/]. MGD77 files (and other data) for the near bottom surveys may be found on the SIO Geological Data Center database [http:// gdc.ucsd.edu/index.php] (cruise IDs: WEST15MV, SOTW02WT, PANR06MV). Magnetization solutions used in this study and the raw near-bottom magnetics measurements for the PAR are available through ERDA [http://earthref.org/ERDA /2208/].

Acknowledgements

The authors thank Stephen Miller for providing a tape of the Southtow Leg 2 dataset, Steve Cande for helpful discussions, and Leah Ziegler for providing the jackknife resampled

PADM2M models. This work was funded by the NSF CSEDI program grant number EAR 1065597. Location maps were drafted using GMT (Wessel et al., 2013) and GeoMapApp (http://www.geomapapp.org/). The authors thank two anonymous reviewers, whose thorough and helpful reviews improved the quality of this manuscript.

Chapter 3, in full, is a reprint of the material as it appears in *Earth and Planetary Science Letters*, vol.467, doi:10.1016/j.epsl.2017.03.020, 2017. Avery, Margaret S., Constable, Catherine G., and Gee, Jeffrey S. The dissertation author was the primary investigator and author of this paper.

Appendices

This supplement provides details of the methodology used to obtain results described in the main body of the paper.

3.A Evaluating Asymmetry in the ADM Time Series

3.A.1 Low-pass Filtering

Ziegler and Constable (2011) constructed a series of smoothed ADM models using penalized smoothing splines as a low-pass filter to determine the timescales on which asymmetry in rate of change is present. The choice of splines as an effective low-pass filter has the advantage of providing a simple analytical description for the time derivatives; however, as we will show, splines do not have a sharp enough frequency response for our purpose of separating the effects occurring over different timescales. Ziegler and Constable (2011) formulated T_{co} as the period at which the smoothed model's power spectrum is damped to half of PADM2M's (green circles in Figures 3.S1a,b,c). Examples of this ratio are plotted in Figure 3.S1b, the power spectra used to calculate them are plotted in Figure 3.S1a, and the distribution of $s_g(f_{co})$ from this method is shown in Figure 3.S1c. There is a maximum in $s_g(T_{co})$ of $s_g = 0.6$ at $T_{co} = 54$ kyr. The frequency response of the spline falls off gradually. If you define T_{co} as the period at which power is dampened by a factor of 100 instead of 2 the maximum in $s_g(T_{co})$ is shifted to $T_{co} = 26$ kyr (blue squares in Figures 3.S1a,b,c). Because the frequency response of the spline is not sharp, the frequency where the peak asymmetry

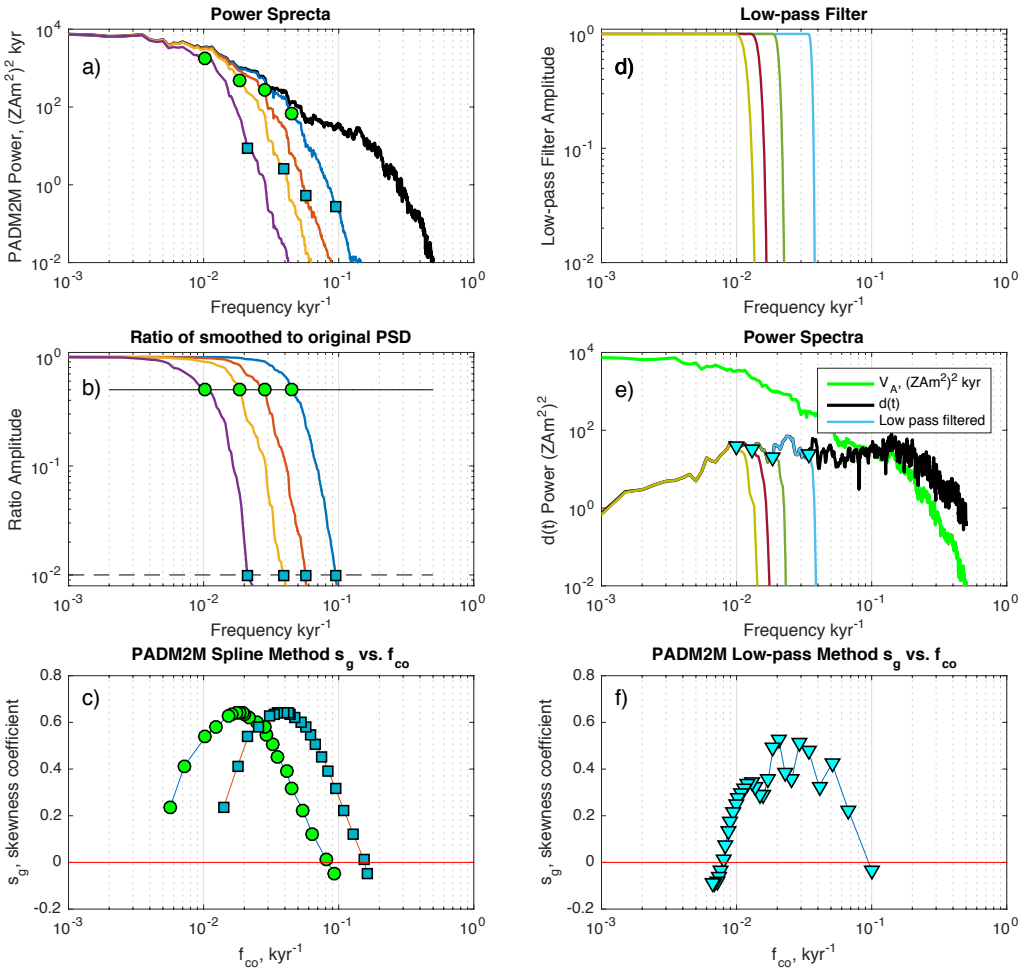

Figure 3.S1: A demonstration that Parks-McClellan equiripple low-pass filter have a sharper frequency response than splines, allowing unambiguous quantification of T_{co}(the cut-off period below which fluctuations have been removed). a) The power spectra of PADM2M, unfiltered is shown by the thick black line and after spline smoothing by the thin, colored lines. b) Ratio between smoothed and original PADM2M power spectra. The frequency at which this ratio is 0.5 defines f_{co} in the spline smoothing method (green circles). Using a different ratio to define f_{co} for example 0.01 (blue squares) gives a different f_{co}. c) The geomagnetic skewness coefficient $s_g(f_{co})$ distribution for the spline smoothing method. By changing the definition of f_{co} in panel b the peak asymmetry is shifted from $f_{co} = 0.019$ kyr^{-1} to $f_{co} = 0.039$ kyr^{-1}. d) Examples of our Parks-McClellan equiripple low-pass filter design. e) The effect of the Parks-McClellan equiripple low-pass filters on the power spectra of the PADM2M rates of change. f) The $s_g(f_{co})$ distribution for the low-pass filtering method.

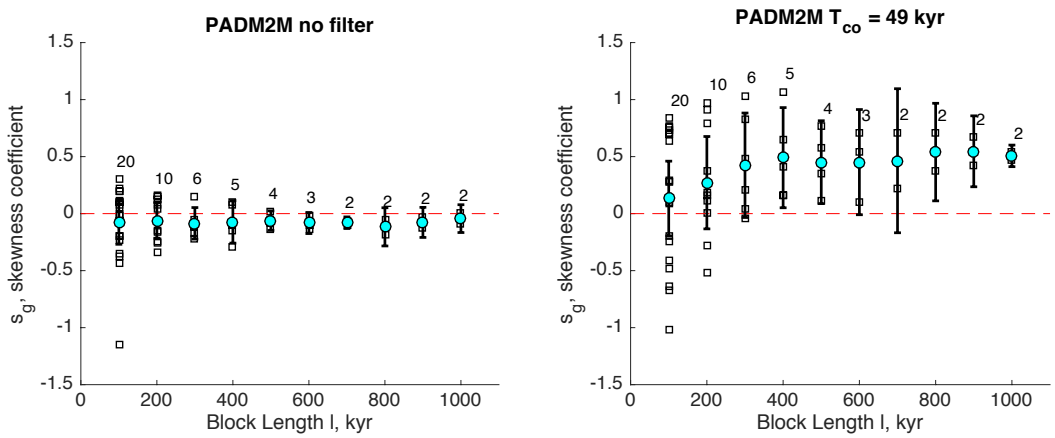

Figure 3.S2: Geomagnetic skewness analysis for non-overlapping subsets of PADM2M time series. Numbers indicate the number of subsets, k. a) The unfiltered PADM2M time series was split into k blocks of length l kyr and s_g was computed for each block. The distributions of these s_g estimates are shown with open boxes. The blue circles with error bars indicate the mean s_g for that block length $\pm$ 99% confidence interval. As expected in the unfiltered PADM2M, zero is always within the distribution of s_g. b) This process was repeated with the model of PADM2M with fluctuations shorter than 49 kyr filtered out. With block lengths greater than 800 kyr zero is no longer within the distribution of s_g. Note, this is the same model plotted in main text Figures 2c and e.

occurs is influenced by changing the definition of T_{co}.

Our preferred method for estimating T_{co} is to fit the time series with a low misfit spline in order to calculate a time series of first derivatives, and then filter the derivatives with a Parks-McClellan equiripple low-pass filter which results in a sharp, monotonic decrease with frequency. The frequency responses of a few low-pass filters are plotted in Figure 3.S1d. It is much sharper than the spline response, which allows T_{co} to be defined without ambiguity as the corner of the low-pass filter. The power spectra of the resulting low-pass filtered time series of first derivatives are plotted in Figure 3.S1e. The resulting s(f_{co}) has a maximum of $s_g = 0.5$ at $T_{co} = 49$ kyr (cyan triangles in Figures 3.S1e,f).

3.A.2 Uncertainty Estimates

To test if s_g is significantly different from zero we estimate its standard error using a jackknife resampling method. The jackknife standard error, $\widehat{se}_{jack}$, was estimated using equation 11.5 from Efron and Tibshirani (1994)(pg. 141). The 76 records that make up PADM2M compose the sample $\mathbf{x} = (\mathbf{x}_1, \mathbf{x}_2, \ldots, \mathbf{x}_n)$ (n=76), and the geomagnetic skewness coefficient is our estimator $s_g(\mathbf{x})$. A jackknife resample leaves out one observation at a time: $\mathbf{x}_j = (\mathbf{x}_1, \mathbf{x}_2, \ldots, \mathbf{x}_{j-1}, \mathbf{x}_{j+1}, \ldots, \mathbf{x}_n)$, the jth jackknife sample is the data set with the jth record removed. $s_g(\mathbf{x}_j)$ is the jth replication of $s_g(\mathbf{x})$. The jackknife estimate of standard error is defined as:

$$\widehat{se}_{jack} = \left[\frac{n-1}{n} \sum \left(s(\mathbf{x}_j) - s(\mathbf{x}_\bullet) \right)^2 \right]^{1/2} \tag{3.4}$$

where $s_g(\mathbf{x}_\bullet) = \sum_{j=1}^{n} s(\mathbf{x}_j)/n$ the average of all the jackknife replications. The factor of $\frac{(n-1)}{n}$ in the definition of $\widehat{se}_{jack}$, which Efron and Tibshirani (1994) call an "inflation factor," seems large (instead of $\frac{1}{(n-1)}$ or $\frac{1}{n}$) but is required for an unbiased estimate of the variance. This results in the shaded error bars shown in main text Figures 3, 6, 7e, and 8e. For PADM2M 1 $\widehat{se}_{jack} \sim 0.2$ at all T_{co}.

3.A.3 How long a record is required?

Next, we will address how much of the PADM2M (or a similar model of ADM) is needed to confidently observe the asymmetry between growth and decay rates. To approach this question we determine the distribution of s_g estimates as a function of length of record. The PADM2M model was split into k nonoverlapping blocks of length l kyr. The geomagnetic

skewness coefficient s_g was calculated for each block and we examine the distribution of s_g as a function of l (Figure 3.S2a). We assume that s_g estimates from different blocks of time are normally distributed, though this does not require that the ADM derivatives are normally distributed. Therefore the standard error and 99% confidence interval of s_g indicates whether an individual s_g measurement is from a distribution that does not include zero. Small block lengths produce a distribution with large variance, but there are more of them. Estimates of s_g from large blocks are not as variable, but there are fewer estimates in the distribution. The result of this is shown in Figure 3.S2, where s_g distributions as a function of block length l are plotted for unsmoothed PADM2M (Figure 3.S2a) and a smoothed model of PADM2M with a cutoff period of 49 kyr (Figure 3.S2b), which is the most asymmetric model. In the absence of smoothing, as expected, zero is always within the distribution of s_g. For the smoothed model of PADM2M at l of 800 kyr and longer zero is outside of the s_g distribution. Generally the longer the record the more reliable the results, but this study tells us the minimum record length we should analyze is ∼800 kyr.

3.B Stacking and Inversion of Marine Magnetic Anomalies

3.B.1 Stacking

For near-bottom profiles spanning several reversals, we locate the reversals boundaries with an algorithm that iteratively adjusts the polarity boundaries and sigma value (of a

gaussian filter that approximates the width of the transition zone imparted by the finite width of lava accretion) to minimize the misfit between the measured and forward modeled anomalies. For the EPR 19°S and PAR 51°S records we used the mean spreading rate and known timescale to compute the width in km of each polarity chron. For the chron C5 43°N record we computed the mean width of each polarity chron, and use the mean spreading rate to update the polarity reversal timescale. The differences are slight and the revised ages are shown in Table 3.S1. We then stretch or shrink each profile using the reversal boundaries as tie points for alignment. Then we average the aligned anomaly profiles. The stacked anomaly profiles and bathymetry are used as data in the inversion for seafloor magnetization for a 500 m thick source layer.

Table 3.S1: Revised geomagnetic polarity timescale for Anomaly 5. *C5r.2r is marked with an asterisk because it continues on after subchron C5r.2r-1n.

Polarity Chron	**Age Range (Ma)**
C4Ar.1n	9.230 - 9.353
C4A4.2r	9.353 - 9.555
C4Ar.2n	9.555 - 9.645
C4Ar.3r	9.645 - 9.709
C5n.1n	9.709 - 9.872
C5n.1r	9.872 - 9.902
C5n.2n	9.902 - 10.958
C5r.1r	10.958 - 11.034
C5r.1n	11.034 - 11.060
C5r.2r*	11.060 - 11.161
C5r.2r-1n	11.161 - 11.193

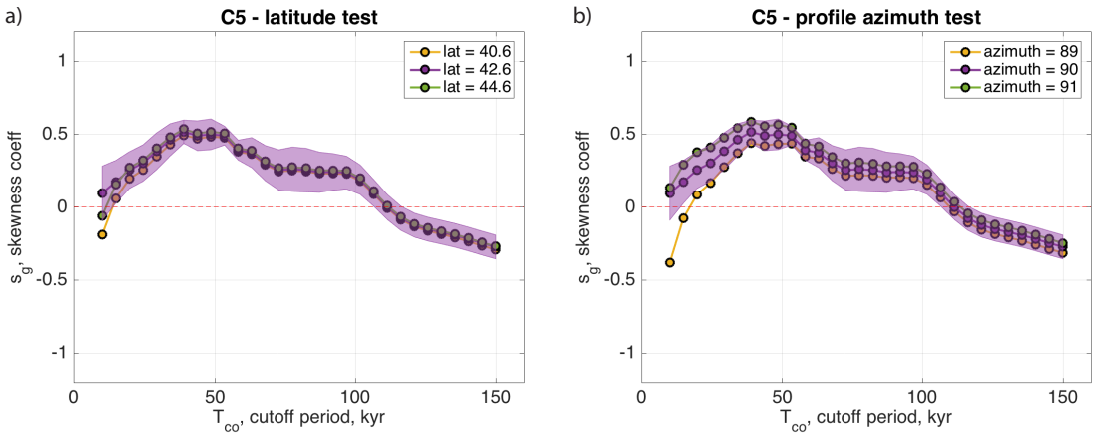

Figure 3.S3: Northern Pacific chron C5 near-bottom geomagnetic skewness coefficient s_g as a function of cutoff period T_{co}. A test of the impact of uncertainties in the paleolatitude of the ridge and azimuth of the profile. Error bars are $\pm$ 1 $\widehat{se}_{jack}$.

Table 3.S2: Filter parameters for the inversion of near-bottom magnetic anomalies. The limits of the cosine taper used in the inversion are λ_{high} and λ_{low}. Wavelengths between $\lambda_{low,1.0}$ and $\lambda_{high,1.0}$ are not filtered, and wavelength below $\lambda_{low,0.0}$ and above $\lambda_{high,0.0}$ are completely suppressed.

		EPR 19°S		**PAR 51°S**		**Chron C5 43°N**	
dx, data spacing (km)		0.025		0.1045		0.05	
λ_{max}, max wavelength (km)		204.8		426.8		204.8	
$\lambda_{low,0.0}$ (km)	$\lambda_{low,1.0}$ (km)	0.4	0.5	0.9	1.7	0.4	0.5
$\lambda_{high,1.0}$ (km)	$\lambda_{high,0.0}$ (km)	68.3	204.8	171.2	285.4	51.2	102.4

3.B.2 Inversion

The inversion of marine magnetic data amplifies noise at high and low wavenumbers. The iterative two-dimensional Fourier inversion scheme of Parker and Huestis (1974) uses high and low-pass cosine-taper filters to reduce this amplification. Possible sources of this noise at wavelengths comparable to the length of the survey include diurnal field variations, inaccuracies in the regional field, and contributions arising from the three dimensionality of the source (Klitgord et al., 1975; Shure and Parker, 1981). We assumed a source layer

of uniform 500 m thickness with constant magnetization direction along the profile (with inclination determined from the present day latitude), and no variations of magnetization with depth. We tested the impact of our assumption about the magnetization direction by repeating the inversion of the chron C5 43°N stacked anomalies with ±2° latitude and ±1° profile azimuth, which we consider reasonable estimates of the uncertainties on the paleolatitude and paleo-azimuth (Figure 3.S3). These changes do affect the s_g estimates, but it is within the ± 1 $\widehat{se}_{jack}$ error bars.

We tested a range of limits for the cosine tapers: wavelengths below $\lambda_{low,0.0}$ are filtered out, the low-pass cosine filter is applied to wavelengths between $\lambda_{low,0.0}$ and $\lambda_{low,1.0}$, wavelengths between $\lambda_{low,1.0}$ and $\lambda_{high,1.0}$ are not filtered, the high-pass cosine filter is applied to wavelengths between $\lambda_{high,1.0}$ and $\lambda_{high,0.0}$, and wavelengths longer than $\lambda_{high,0.0}$ are completely suppressed. Magnetization solutions with $\lambda_{high,0.0} = \infty$ have the lowest possible RMS misfit between the measured and forward modeled anomalies, but suffer from unrealistic long-period oscillations in magnetization. We approach this by comparing not just the RMS misfit (measured by an $\ell 2$ norm) but also the total length of the solution (parameterized by the $\ell 1$ or "taxicab" norm $\|x\|_1 = \sum_{i=1}^{m} |x_i|$ where x is magnetization and m is the number of data). We select a solution with both low misfit and low $\ell 1$ norm. This process is illustrated for the chron C5 43°N dataset in Figure 3.S4. Figures 3.S4e and f show the RMS misfit and $\ell 1$ norm for the suite of inversion solutions we considered. Figures 3.S4a, b, c, and d show the measured and forward modeled anomalies (a and c) and resulting inversion (b and d) for two sets of inversion filter parameters that were rejected. The solution in Figure 3.S4b which has the lowest RMS misfit was rejected because of the long wavelength

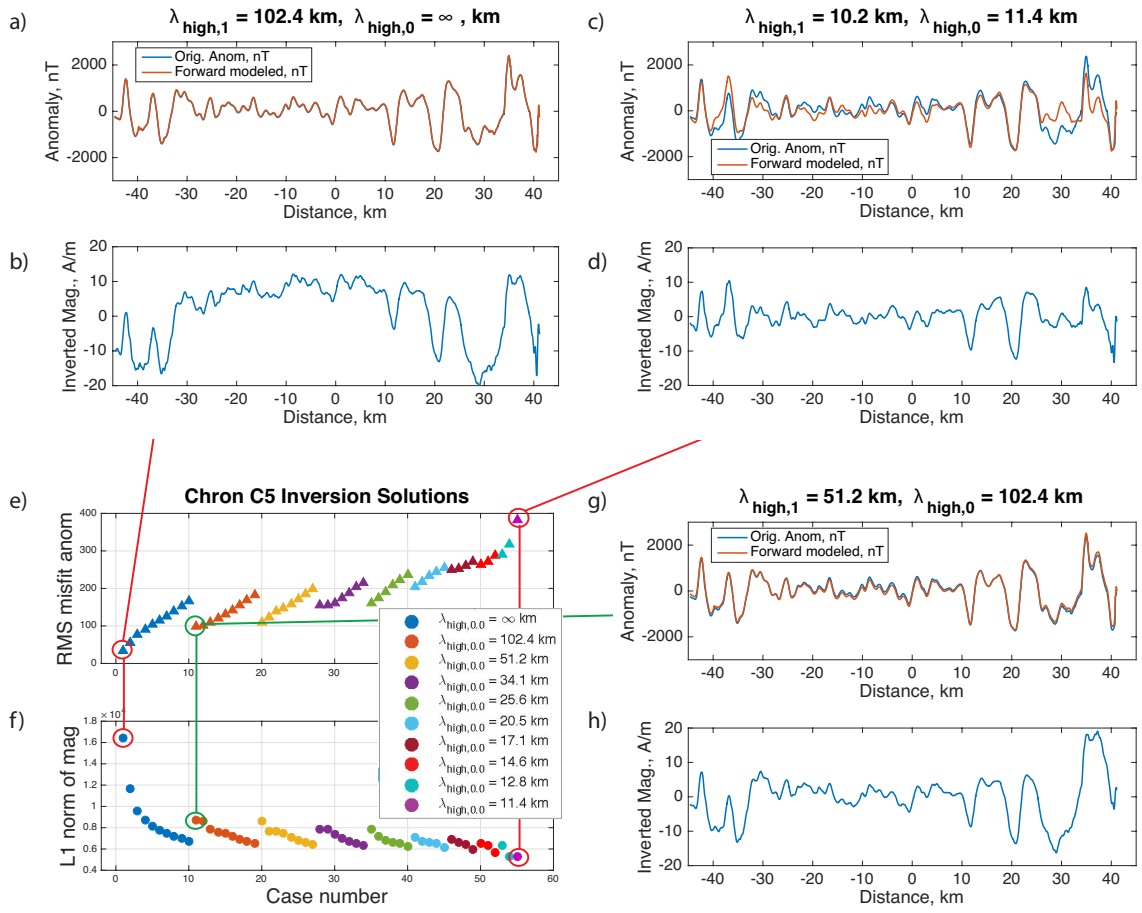

Figure 3.S4: Demonstration of the inversion filter parameters selection process. Panels a, b, c, and d show the measured and forward modeled anomalies and resulting inversion for two sets of inversion filter parameters that were rejected. Panels e and f show the RMS misfit (triangles) and $\ell 1$ norm (circles) for the suite of inversion solutions we considered. Marker color corresponds to $\lambda_{high,0.0}$ wavelength, and for each $\lambda_{high,0.0}$ wavelength we tested multiple $\lambda_{high,1.0}$ wavelengths which decrease with case number. Panels g and h show the measured and forward modeled anomalies and resulting inversion for the inversion solution we selected based on its low RMS misfit and low $\ell 1$ norm.

variation in the magnetization solution. The solution in Figure 3.S4d was rejected because of its high RMS misfit (Figure 3.S4c). Figures 3.S4g and h show the measured and forward modeled anomalies and resulting inversion for the inversion solution we selected based on its low RMS misfit and low $\ell 1$ norm. The cosine taper parameters for each selected inversion solution are recorded in Table 3.S2.

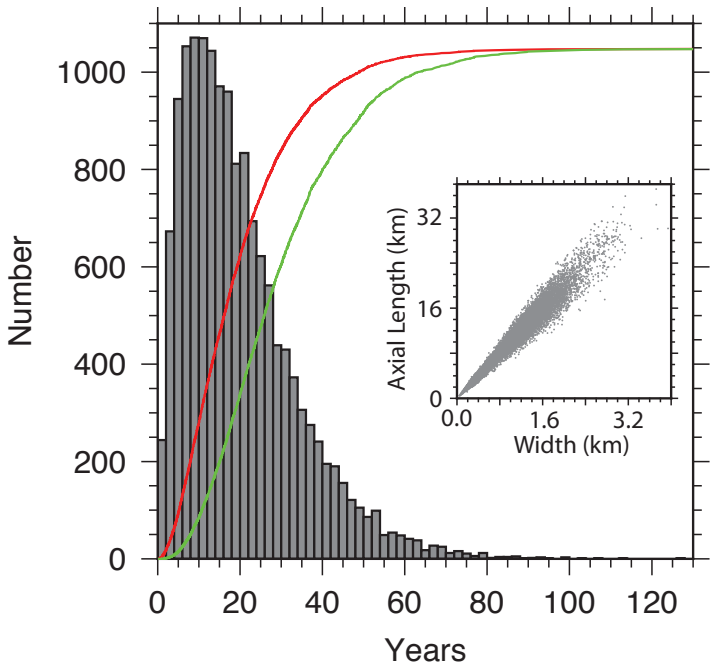

Figure 3.S5: Example distribution of lava flow volumes from stochastic model as a function of waiting time since last eruption. The red line is the cumulative curve for the number of flows and the green line is the cumulative volume of flows. The inset shows the flow width vs axial length (the average aspect ratio used was 10:1).

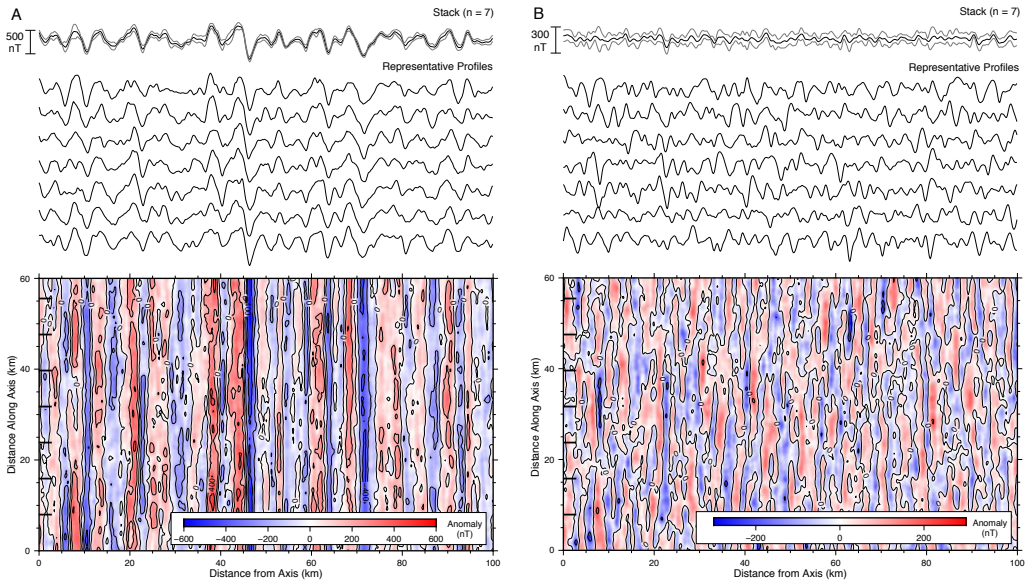

Figure 3.S6: Stochastic crustal accretion model with an aspect ratio of 10:1 (Model 1 in Figure 3.S7). Blue and red colorbars show map views of the near-bottom magnetic anomalies. The seven tick marks on the left axis of the map show where the seven anomaly profiles were taken. a) Near-bottom magnetic anomalies generated for a model with magnetization proportional to PADM2M. b) Near-bottom magnetic anomalies generated for a model with constant magnetization.

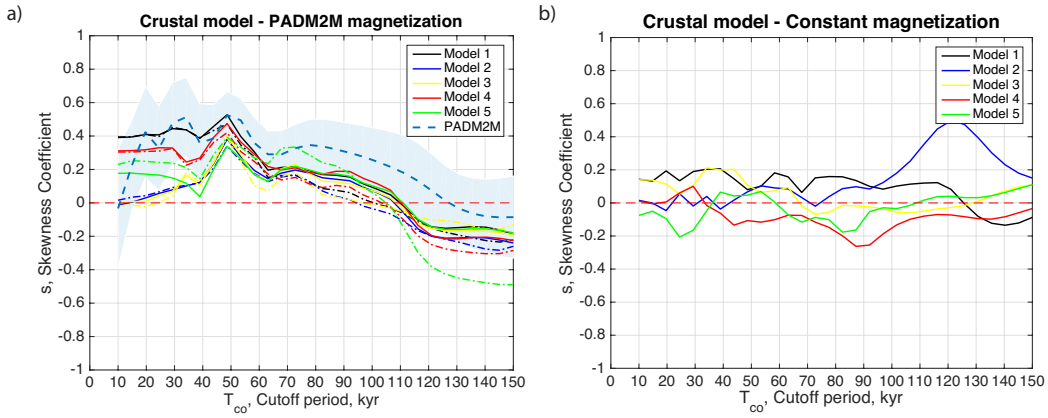

Figure 3.S7: Geomagnetic skewness from 3D stochastic crustal models with an aspect ratio of 10:1. The difference between these five models is they have different seed values for generating waiting times between flows. a) Solid colored lines show $s_g(T_{co})$ results of the low-pass filtering analysis for a suite of crustal models with magnetization proportional to PADM2M. Dot-dashed colored lines show $s_g(T_{co})$ results the same suite of crustal models with magnetization proportional to PADM2M plus an exponential decay term representing alteration effects. The blue dashed line is the original result for PADM2M same as Figure 3 in the main text, error bars are $\pm$ 1 $\widehat{se}_{jack}$. b) $s_g(T_{co})$ results for a suite of crustal models with constant magnetization.

3.C Stochastic Crustal Model

To investigate the possible effects of crustal accretion on the $s_g(T_{co})$ results from the marine anomaly data we modeled near-bottom magnetic anomalies generated by a fast-spreading ridge using a 3D stochastic model for lava accumulation (Gee et al., 2016). These models were generated with an average eruptive flow area aspect ratio of 10:1 (flow axial length : flow width) and the resulting lava accumulation pattern is consistent with the seismically-determined off-axis thickening of the extrusive layer. In this model, the volume of individual lava flows is proportional to the time since the last eruption and the geometry of flows (Figure 3.S5) is compatible with young flows from the EPR at 9°-10°N (e.g., Fundis et al., 2010; Soule et al., 2007) and 17°- 19°S (e.g., Sinton et al., 2002; Bergmanis et al., 2007)

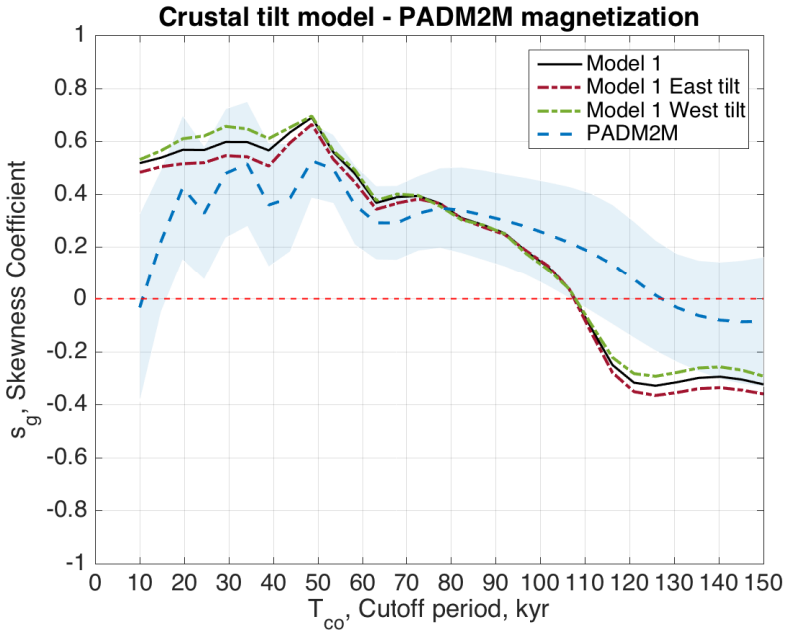

Figure 3.S8: Stochastic crustal model illustrating the effects tilting of the magnetic source layer. Solid black line shows $s_g(T_{co})$ results of the low-pass filtering analysis of a crustal model with magnetization proportional to PADM2M (Model 1 from Figure Figure 3.S7a). Dot-dashed colored lines shows $s_g(T_{co})$ results for the same crustal model with magnetization proportional to PADM2M with a tilted magnetization: red has progressive tilting of remanence away from ridge (simulating lava loading), green has progressive inward tilting toward ridge (simulating outward block rotation). Both models have magnetic inclination variations with depth from 0° at the surface to a maximum of 16° at ∼500 m. The blue dashed line is the original result for PADM2M same as Figure 3 in the main text, error bars are ± 1 $\widehat{se}_{jack}$.

that have been mapped in detail. These studies provide estimates of flow volumes (< 0.01–0.22 km^3), flow horizontal area aspect ratios (from $\sim$1:1 up to $\sim$15:1) and eruption frequency (several eruptions per 100–1000 yrs) and document the importance of off-axis transport in lava channels. Although the number of such mapped flows is small, these observations are sufficient to inform more realistic models of crustal accretion and the effect on the associated magnetic anomalies.

The near-bottom magnetic anomalies from a representative model are shown in Figure 3.S6. The resulting lava distribution was calculated for a 60 km ridge segment (North-South) and for 100 km of crust in the East-West direction. Near-bottom (200 m elevation) magnetic anomalies were calculated using magnetizations proportional to the PADM2M intensity variations (Figures 3.S6a) and using a constant magnetization (Figures 3.S6b) with both ambient and remanence directions vertical. Results from these (and other flow aspect ratio models) stochastic models suggest that, for most lava accumulation patterns, there is little between-line coherence expected in near-bottom magnetic anomalies at periods shorter than $\sim$30–40 kyr (Gee et al., 2016).

The pattern of lava accretion results in isochrons that dip toward the ridge axis and that may modify the shape (skewness) of the anomalies and might influence our estimate of geomagnetic skewness (s_g). In order to examine the sensitivity of our geomagnetic skewness estimates from the pattern of lava accretion we stacked the synthetic anomalies (7 profiles spaced at 8 km intervals) from five instances (i.e. different seed values for generating waiting times between flows) of the same extrusive magnetization source model (Models 1-5 in Figure 3.S7a). We then applied the same low-pass filtering analysis to estimate geomagnetic

skewness coefficient $s_g(T_{co})$ as described above. Note that because there is no topography and only PADM2M intensity fluctuations were used, the derivative geomagnetic skewness analysis was performed directly on the stacked anomaly data. The $s_g(T_{co})$ for the crustal models with a initial magnetization proportional to PADM2M agrees with the results from PADM2M except at short periods where some of the crustal models have $s_g > 0$ that the input magnetization model did not show (solid lines, Figure 3.S7a). In contrast, the $s_g(T_{co})$ for the constant magnetization models are centered on zero (although with significant scatter) for all cutoff periods (Figure 3.S7b). Although the lava accretion pattern does affect the magnitude of s_g it apparently does not appreciably affect the range of cutoff periods at 20–100 kyr.

Marine magnetic anomalies, particularly for slow-spread ridges, often exhibit an amplitude reduction away from the ridge that has been attributed to alteration-related decrease in magnetization of the extrusive source layer with time. To test the possible impact of long-term alteration we also examine models with magnetization proportional to PADM2M plus an exponential decay term decreasing from 5 to 1 Am^2 with a decay constant of 0.5 Myr representing alteration. The models with magnetization proportional to PADM2M plus a decay term are shifted to lower s_g at long T_{co} compared to the corresponding model without decay, but the effect is small (dot-dashed lines, Figure 3.S7a).

Finally, the anomalous skewness of magnetic anomalies might conceivably also affect our estimate of geomagnetic skewness as we have examined near-bottom anomalies only on one ridge flank. As a test of effect of anomalous skewness on estimates of s_g, we modeled a depth dependent variation in the magnetization direction which might simulate outward

tilt of crustal blocks (magnetization tilted toward the axis) or inward tilt of lavas by loading (resulting in magnetization tilt away from the axis). The tilt term does shift the s_g estimates, but the effect is small (Figure 3.S8).

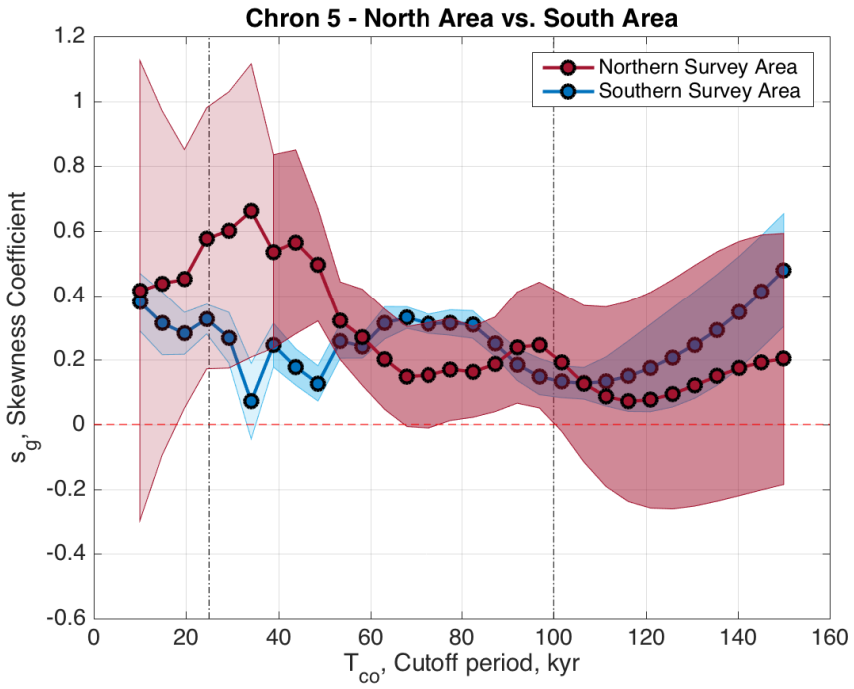

Figure 3.S9: Comparison of geomagnetic skewness coefficient s_g as a function of cutoff period T_{co} between the two survey regions of the Northern Pacific chron C5 survey. Error bars are $\pm$ 1 $\widehat{se}_{jack}$. Black dot-dashed vertcal lines indicate the same three period ranges as in the main text: short period ($T_{co} < 25$ kyr), intermediate period ($T_{co} = 25 - 100$ kyr), and long period ($T_{co} > 100$ kyr). The lighter shading over cutoff periods < 40 kyr indicates the timescale associated with the transition zone width of 1.7 km (Bowers et al., 2001).

3.D Separate Analysis of the Chron C5 Survey Areas

The two chron C5 43°N survey areas are separated by ∼120 km. The northern survey area contains profiles lines 9–12 and the southern survey area contains lines 1–8. Lines 7, 8, 10, and 11 span all of chrons C4Ar–C5r (9.3–11.2 Ma), the other lines only span part of

this range (main text Figure 8b). To test the regional contributions to the $s_g(T_{co})$ signal we repeat our low-pass filter analysis on two stacks of the anomalies from each of the two survey areas (Figure 3.S9). The $s_g(T_{co})$ patterns for the two regions agree within their uncertainties except at $T_{co} = 29 - 53$ kyr. The greatest difference between the two regional records is at $T_{co} = 34$ kyr, though their uncertainties may be optimistic due to the reduced number of profiles in the stacks. This is within the timescale associated with the transition zone width of 1.7 km. Like the EPR 19°S and PAR 51°S records these two chron C5 43°N regional stacks have $s_g > 0$ at all T_{co}. This shows the need to stack near-bottom anomaly records measured over a large area. There is a difference in the size of $\widehat{se}_{jack}$ between the two survey areas because they have different numbers of records. The Southern area has smaller $\widehat{se}_{jack}$ because the jackknife method was performed with eight survey lines, while the Northern area has only four lines.

References

Backus, G., Parker, R. L., and Constable, C. (1996). *Foundations of geomagnetism.* Cambridge University Press, New York, NY. Pages 200–204.

Bergmanis, E. C., Sinton, J., and Rubin, K. H. (2007). Recent eruptive history and magma reservoir dynamics on the southern East Pacific Rise at 17° 30' S. *Geochemistry, Geophysics, Geosystems*, 8(12):Q12O06.

Bowers, N. E., Cande, S. C., Gee, J. S., Hildebrand, J. A., and Parker, R. L. (2001). Fluctuations of the paleomagnetic field during chron C5 as recorded in near-bottom marine magnetic anomaly data. *Journal of Geophysical Research: Solid Earth*, 106(B11):26379–26396.

Bowles, J., Tauxe, L., Gee, J., McMillan, D., and Cande, S. (2003). Source of tiny wiggles in Chron C5: A comparison of sedimentary relative intensity and marine magnetic anomalies. *Geochemistry, Geophysics, Geosystems*, 4(6):1049.

Cande, S. C. and Kent, D. V. (1992a). A new geomagnetic polarity time scale for the Late

Cretaceous and Cenozoic. *Journal of Geophysical Research: Solid Earth*, 97(B10):13917–13951.

Cande, S. C. and Kent, D. V. (1992b). Ultrahigh resolution marine magnetic anomaly profiles: A record of continuous paleointensity variations? *Journal of Geophysical Research*, 97(B11):15075–15083.

Cande, S. C. and Kent, D. V. (1995). Revised calibration of the geomagnetic polarity timescale for the Late Cretaceous and Cenozoic. *Journal of Geophysical Research: Solid Earth*, 100(B4):6093–6095.

Cande, S. C. and LaBrecque, J. L. (1974). Behaviour of the Earth's palaeomagnetic field from small scale marine magnetic anomalies. *Nature*, 247(5435):26–28.

Carbotte, S. M., Mutter, J. C., and Xu, L. (1997). Contribution of volcanism and tectonism to axial and flank morphology of the southern East Pacific Rise, 17°10'–17°40'S, from a study of layer 2A geometry. *Journal of Geophysical Research: Solid Earth*, 102(B5):10165–10184.

Dyment, J. and Arkani-Hamed, J. (2005). Marine magnetic anomalies, oceanic crust magnetization, and geomagnetic time variations. Presented at the Fall meeting of the American Geophysical Union, San Francisco. Abstract GP33B-02.

Efron, B. and Tibshirani, R. J. (1994). *An introduction to the bootstrap*. CRC press, Boca Raton, FL. Pages 141–150.

Evans, H. F., Westerhold, T., Paulsen, H., and Channell, J. E. (2007). Astronomical ages for Miocene polarity chrons C4Ar–C5r (9.3–11.2 Ma), and for three excursion chrons within C5n.2n. *Earth and Planetary Science Letters*, 256(3):455–465.

Fundis, A. T., Soule, S., Fornari, D., and Perfit, M. (2010). Paving the seafloor: Volcanic emplacement processes during the 2005-2006 eruptions at the fast spreading East Pacific Rise, 9°50' N. *Geochemistry, Geophysics, Geosystems*, 11(8):Q08024.

Gee, J. S., Cande, S. C., Hildebrand, J. A., Donnelly, K., and Parker, R. L. (2000). Geomagnetic intensity variations over the past 780 kyr obtained from near-seafloor magnetic anomalies. *Nature*, 408(6814):827–832.

Gee, J. S., Cande, S. C., and Kent, D. V. (2016). Lava accumulation patterns at fast-spread ridges and the fidelity of marine magnetic anomalies. Presented at the Fall meeting of the American Geophysical Union, San Francisco. Abstract GP31D-01.

Holme, R. (2015). Large-scale flow in the core. In Schubert, G., editor, *Treatise on Geophysics*, volume 8, chapter 4, pages 91–113. Elsevier, Amsterdam, 2 edition.

Klitgord, K., Huestis, S., Mudie, J., and Parker, R. (1975). An analysis of near-bottom magnetic anomalies: Sea-floor spreading and the magnetized layer. *Geophysical Journal International*, 43(2):387–424.

Kok, Y. S. and Tauxe, L. (1996a). Saw-toothed pattern of relative paleointensity records and cumulative viscous remanence. *Earth and Planetary Science Letters*, 137(1):95–99.

Kok, Y. S. and Tauxe, L. (1996b). Saw-toothed pattern of sedimentary paleointensity records explained by cumulative viscous remanence. *Earth and Planetary Science Letters*, 144(3):E9–E14.

Olson, P. and Amit, H. (2006). Changes in earth's dipole. *Naturwissenschaften*, 93(11):519–542.

Parker, R. and Huestis, S. (1974). The inversion of magnetic anomalies in the presence of topography. *Journal of Geophysical Research*, 79(11):1587–1593.

Parker, R. L. and Klitgord, K. D. (1972). Magnetic upward continuation from an uneven track. *Geophysics*, 37(4):662–668.

Parks, T. and McClellan, J. (1972). Chebyshev approximation for nonrecursive digital filters with linear phase. *IEEE Transactions on Circuit Theory*, 19(2):189–194.

Pozzo, M., Davies, C., Gubbins, D., and Alfè, D. (2012). Thermal and electrical conductivity of iron at Earth's core conditions. *Nature*, 485(7398):355–358.

Roberts, A. P. and Lewin-Harris, J. C. (2000). Marine magnetic anomalies: evidence that 'tiny wiggles' represent short-period geomagnetic polarity intervals. *Earth and Planetary Science Letters*, 183(3):375–388.

Roberts, A. P., Tauxe, L., and Heslop, D. (2013). Magnetic paleointensity stratigraphy and high-resolution Quaternary geochronology: successes and future challenges. *Quaternary Science Reviews*, 61:1–16.

Sempere, J.-C., Macdonald, K. C., Miller, S. P., and Shure, L. (1987). Detailed study of the Brunhes/Matuyama reversal boundary on the East Pacific Rise at 19°30'S: Implications for crustal emplacement processes at an ultra fast spreading center. *Marine Geophysical Researches*, 9(1):1–23.

Shure, L. and Parker, R. L. (1981). An alternative explanation for intermediate-wavelength magnetic anomalies. *Journal of Geophysical Research: Solid Earth*, 86(B12):11600–11608.

Sinton, J., Bergmanis, E., Rubin, K., Batiza, R., Gregg, T. K., Grönvold, K., Macdonald, K. C., and White, S. M. (2002). Volcanic eruptions on mid-ocean ridges: New evidence from the superfast spreading East Pacific Rise, 17–19° S. *Journal of Geophysical Research: Solid Earth*, 107(B6):2115.

Soule, S. A., Fornari, D. J., Perfit, M. R., and Rubin, K. H. (2007). New insights into mid-ocean ridge volcanic processes from the 2005-2006 eruption of the East Pacific Rise, 9° 46' N–9° 56' N. *Geology*, 35(12):1079–1082.

Tauxe, L. and Yamazaki, T. (2015). Paleointensities. In Schubert, G., editor, *Treatise on Geophysics*, volume 5, chapter 13, pages 461–509. Elsevier, Amsterdam, 2 edition.

Valet, J.-P. and Fournier, A. (2016). Deciphering records of geomagnetic reversals. *Reviews of Geophysics*, 54(2):410–446.

Valet, J.-P. and Meynadier, L. (1993). Geomagnetic field intensity and reversals during the past four million years. *Nature*, 366(6452):234–238.

Valet, J.-P., Meynadier, L., and Guyodo, Y. (2005). Geomagnetic dipole strength and reversal rate over the past two million years. *Nature*, 435(7043):802–805.

Wessel, P., Smith, W. H., Scharroo, R., Luis, J., and Wobbe, F. (2013). Generic mapping tools: Improved version released. *Eos, Transactions American Geophysical Union*, 94(45):409–410.

Westphal, M. and Munschy, M. (1999). Saw-tooth pattern of the earth's magnetic field tested by magnetic anomalies over oceanic spreading ridges. *Comptes Rendus de l'Academie des Sciences Series IIA Earth and Planetary Science*, 329(8):565–571.

Ziegler, L. and Constable, C. (2011). Asymmetry in growth and decay of the geomagnetic dipole. *Earth and Planetary Science Letters*, 312(3):300–304.

Ziegler, L., Constable, C., Johnson, C., and Tauxe, L. (2011). PADM2M: a penalized maximum likelihood model of the 0–2 Ma palaeomagnetic axial dipole moment. *Geophysical Journal International*, 184(3):1069–1089.

Chapter 4

Spectral methods for analyzing energy balances in geodynamo simulations

Abstract

Current numerical geodynamo simulations can reproduce the basic dipolar structure and reversals of the geomagnetic field, but many do not exhibit realistic statistical properties associated with paleomagnetic temporal variations. An important characteristic of the geomagnetic field is that on average the axial dipole has been observed to grow more rapidly than it decays in the frequency range extending from about 0.01 to 0.1 kyr^{-1}. This provides a useful criterion for evaluating geodynamo simulations using spectral methods, because the frequency dependence of poloidal axial dipole energy at Earth's surface reflects the balance of diffusive and advective processes in Earth's core. Spectral methods can be applied to evaluate detailed products available from dynamo simulations but inaccessible in

the paleomagnetic record. These spectral methods are well developed but have not previously been applied to studying the energy balance of geodynamo simulations. Consistently high coherence levels are observed between the total magnetic energy in the outer core and the paleomagnetically observable energy in the axial dipole moment at frequencies below 0.01 kyr^{-1}. Between 0.01 and 0.1 kyr^{-1} there is a fall off in coherence; at higher frequency the coherence is negligible. Corresponding assessments of coherence between rates of change in kinetic and magnetic energy, ohmic and viscous dissipations, and work done by the buoyancy and Lorentz forces facilitate testing hypotheses about changes in the energy balance in geodynamo simulations as a function of frequency. We illustrate these ideas by analyzing output from numerical dynamo simulations which have previously been studied for their apparently Earth-like properties.

4.1 Introduction

The geomagnetic field is an important component of our planetary environment that varies over a broad range of frequencies (Constable and Johnson, 2005). Paleomagnetic observations record the behavior of the geomagnetic field in the past and tell us about the inner workings of the planet; however, the record is noisy and incomplete. A fruitful approach to overcome these limitations is to compare the statistical properties of magnetic fields generated by numerical geodynamo simulations, which do not suffer from noise or sparseness and whose internal dynamics can be subjected to detailed study, with observations of Earth's magnetic field. Our goal in this work is to gain deeper understanding of variations in the

axial dipole strength observed in the paleomagnetic record by analyzing the conversion of kinetic energy to magnetic energy and dissipation of these energies as functions of frequency in geodynamo simulations.

There is a trade off in paleomagnetic observations between timespan and spatial resolution – further back in time we have less information about the field's behavior. For the modern field we have high resolution observations from satellites and geomagnetic observatories, but they span a small portion of the geomagnetic field's secular variation spectrum. These high resolution geomagnetic observations can be inverted for core flow at the core mantle boundary (CMB) by making a 'frozen-flux' approximation that the fluid has infinite electric conductivity and additional assumptions to overcome the non-uniqueness of the problem (Bloxham and Jackson, 1991). The resulting flows can then be linked to core dynamics found in geodynamo simulations; there is evidence for features such as a high-latitude polar jet in the northern hemisphere (Livermore et al., 2017) and a planetary-scale gyre in the southern hemisphere (Finlay et al., 2016). The paleomagnetic dataset from the past 10 kyr (Holocene) has enough spatial and temporal resolution to build low degree spherical harmonic representations of the field variations but not enough to invert for core flow (e.g. Constable et al., 2016). In the Holocene field reconstructions there is evidence of high-latitude flux patches in both northern and southern hemispheres (Korte and Holme, 2010) and evidence of spatial heterogeneity in field activity, with more activity in the southern hemisphere (Constable et al., 2016).

On timescales longer than 10 kyr, which is the focus of this work, there are not yet models of paleomagnetic field variations with higher spatial resolution than the axial dipole

moment ADM. SINT2000 and PADM2M are two examples of ADM models spanning the past 2 Ma (Valet et al., 2005; Ziegler et al., 2011). On the longest timescales (10^8 yrs) only the paleomagnetic polarity timescale is well defined (Cande and Kent, 1992, 1995), so we restrict our analysis to the period 0–2 Ma.

When high frequency variations are removed from the ADM models the axial dipole moment grows more rapidly than it decays (Ziegler and Constable, 2011; Avery et al., 2017). This asymmetry can be seen in the positive skewness values for the distributions of axial dipole energy at Earth's surface (Figure 4.1). The asymmetric behavior is not just associated with polarity reversals, it appears to be an important characteristic of secular variation. Studying this behavior could help us understand the context of present day geomagnetic field variations, and deeper dynamics the unobservable parts of the field and the role of diffusion in ADM variations. It indicates that decreasing dipole moment is dominated by slow diffusive processes, while on the same timescales dipole field growth occurs more rapidly and is controlled by the induction of field by fluid advection (Ziegler and Constable, 2011). This may be consistent with a stochastic model with terms for drift (slow adjustments toward an average value) and noise (short-period fluctuations) (Buffett et al., 2013).

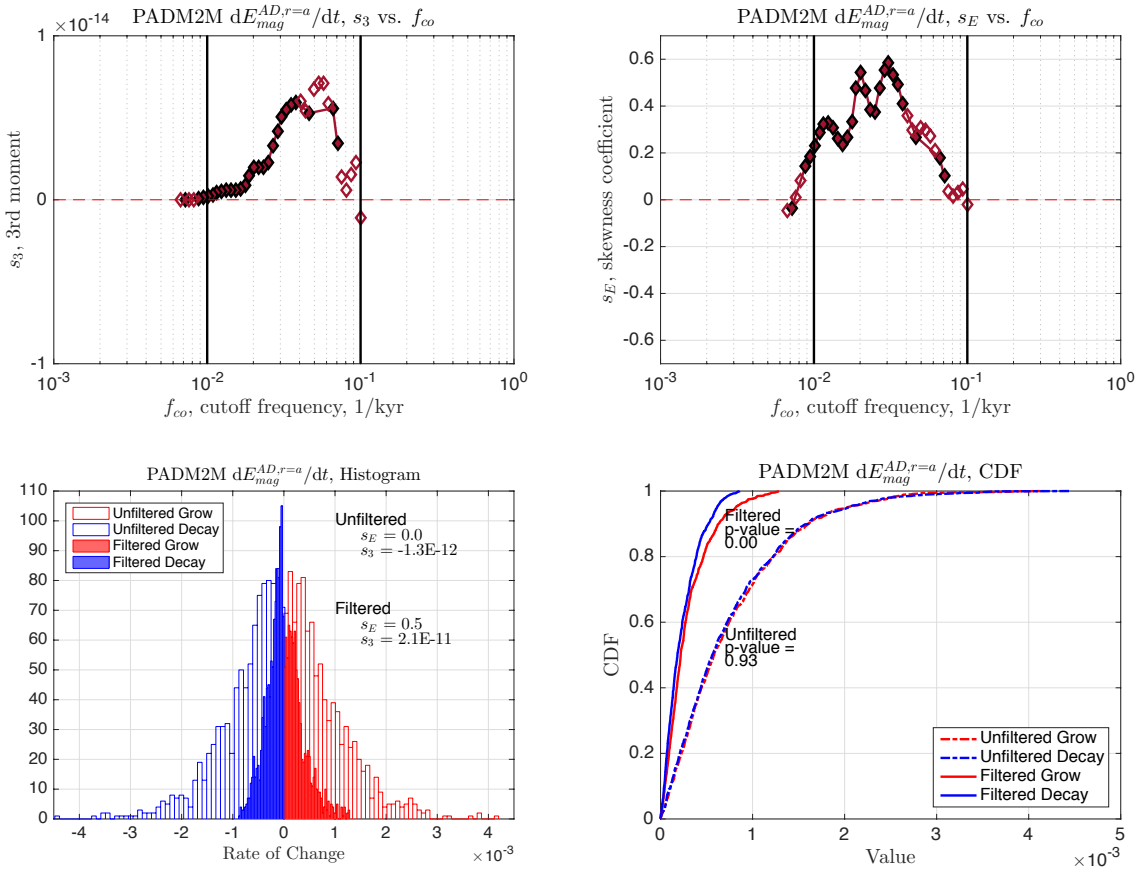

Figure 4.1: A summary of the distribution of axial dipole energy derivatives after lowpass filtering with various corner frequencies. The skewness is parameterized as the **(a)** $s_3(f_{co})$ and **(b)** $s_E(f_{co})$ of $\dot{E}_{mag}^{AD,r=a}$. See text and Equations 4.15 and 4.16 for details. A positive skewness value means the distribution of derivatives has a positive tail – positive derivatives which correspond to a growing dipole are larger on average and occur less frequently than negative rates representing decay. s_3 allows us to compare the magnitude of the asymmetry with that in PADM2M, while s_E is used to compare skewness between dynamo simulations with different levels of ADM variability ($\sigma_{g_1^0}$). Open symbols indicate a p-value > 0.05 in the two-sample Kolmogorov-Smirnov test as discussed in the text. **(c)** The distribution of PADM2M $\dot{E}_{mag}^{AD,r=a}$ before filtering (open bars), and after filtering with a lowpass corner frequency of 0.033 kyr^{-1}. After filtering the distribution has a positive tail. **(d)** The cumulative distribution functions, CDFs, of PADM2M positive (red) and negative (blue) $\dot{E}_{mag}^{AD,r=a}$ before filtering (dashed lines), and after filtering with a lowpass corner frequency of 0.033 kyr^{-1} (solid lines).

Here we empirically evaluate the mechanism for this asymmetry in geodynamo simulations by analyzing diagnostic terms of whole-core behavior as functions of frequency. This approach can be used more generally to understand the link between CMB and whole-core processes. Previous studies of geodynamo simulations have assessed the conversion of kinetic energy to magnetic energy and dissipation of these energies (e.g. Olson et al., 1999; Buffett and Bloxham, 2002), but not as a function of frequency as we do.

We begin (Sections 4.2 and 4.3) by describing the paleomagnetic ADM reconstruction and geodynamo simulations used later. We choose four illustrative geodynamo simulations from Davies and Gubbins (2011) because they were determined to be Earth-like by other criteria, thus warranting further study (Davies and Constable, 2014), and they provide a variety of ADM variations. In Section 4.4 we discuss our method of evaluating the asymmetry in ADM rates of change and our time series analysis of the outer core energy balance. Using standard tools of spectral analysis, we evaluate the link between the total magnetic energy present in the outer core and the dipole energy observed at Earth's surface and assess the energetics. Results are presented in Section 4.5 and discussed in Section 4.6, and finally our conclusions are summarized in Section 4.7.

4.2 Paleomagnetic ADM model

We use the representation of the paleomagnetic field provided by the 2 Myr model of axial dipole moment PADM2M. Ziegler et al. (2011) constructed PADM2M using a penalized maximum likelihood inversion technique and 76 sedimentary relative paleointensity records

calibrated by absolute paleointensity data to produce a continuous, time-varying model of ADM; temporal variations were modeled with a cubic B-spline, allowing time derivatives to be calculated analytically. PADM2M resolves ADM variations on timescales of about 10 kyr and longer. The PADM2M model as well as its first and second time derivatives evaluated every 1 kyr are available through the EarthRef.org Digital Archive (ERDA, earthref.org/ERDA/1138/).

4.3 Geodynamo simulations

The dynamo solutions we use here have been previously described, and a detailed description of the code and solution technique can be found in Willis et al. (2007) and Davies and Gubbins (2011). A rotating spherical shell of thickness $d = r_o - r_i$ (where r_o is the outer radius, r_i the inner, and $r_i/r_o = 0.35$) is filled with incompressible, electrically conducting Boussinesq fluid. It rotates at a rate Ω, and has constant thermal diffusivity κ, magnetic diffusivity η, coefficient of thermal expansion α, and viscosity ν. The nondimensional numbers are the Ekman number, the Prandtl number, the magnetic Prandtl number and the Rayleigh number:

$$E = \frac{\nu}{2\Omega d^2}, \qquad Pr = \frac{\nu}{\kappa}, \qquad Pm = \frac{\nu}{\eta}, \qquad Ra = \frac{\alpha g \beta d^5}{\nu\kappa} \tag{4.1}$$

where g is the acceleration due to gravity and β is the temperature gradient at the outer boundary. The Ekman number describes the ratio between viscous and Coriolis forces. The Rayleigh number indicates the presence and vigor of convection (if $Ra > Ra_{cr}$ where Ra_{cr} is the critical Ra for the onset of convection).

Geodynamo simulations are able to produce first order features of the geomagnetic field such as a dominantly dipolar structure and polarity reversals. However, because of computational restrictions none of these simulations are realistic models of the Earth's geodynamo; they cannot be run with sufficiently rapid rotation, thermal diffusivity, and low viscosity characteristic of the Earth's outer core. Previous studies have defined criteria for determining the degree of similarity between the fields produced by geodynamo simulations and the geomagnetic field. Christensen et al. (2010) compared simulations to the geomagnetic field based on field morphology at the core-mantle boundary (comparing the relative strength of the dipole, equatorial symmetry, zonality, and presence of flux concentration), finding Earth-like field morphologies for a limited range of simulation input parameters. Davies and Constable (2014) introduced a criterion to identify dynamos with Earth-like long-term temporal behavior by determining whether the power spectrum of the ADM could be fit with the same frequency dependent power law as observed in the PADM2M empirical model. Mound et al. (2015) added a criterion that compares the secular variation of their simulated radial magnetic field at the CMB to the observed quiet Pacific, where secular variation is weak.

By performing the same analysis as was applied to PADM2M (Figure 4.1 and described in Methods section) an ADM model was low-pass filtered to determine which timescales exhibit asymmetry in rate of change – we selected four geodynamo simulations for further study. These illustrative cases are drawn from Davies and Gubbins (2011) (their cases 1.3, 1.4, 2.2, and 2.3). All have $E = 1.2 \times 10^{-4}$, $Pm = 2$, $Pr = 1$, a mix of bottom and internal heating, homogeneous outer boundary heat flux, and fixed temperature inner boundary.

Cases 1.3 and 1.4 have buoyancy profiles that model a rapid cooling rate resulting in a young inner core. Cases 2.2 and 2.3 have buoyancy profiles that model a moderate cooling rate resulting in an older inner core. The only difference within the pairs of cases is Ra: Case 1.4 has higher Ra than Case 1.3 and Case 2.3 has higher Ra than Case 2.2. All four cases are dipole dominated, do not reverse over the duration of the run, and were found to be Earth-like when using a dimensionless time scaled by the diffusion time (Davies and Constable, 2014). Cases 1.3 and 1.4 are more compatible morphologically with gufm1, and Cases 2.2 and 2.3 with CALS3k.4b. Cases 1.4, 2.2, and 2.3 have similar structure of ADM power spectra to PADM2M.

Analysis of variations in magnetic and kinetic energy of the geodynamo models provides a means of examining their internal dynamics. The induction equation governs the generation of magnetic energy by work done on the field by the flow minus that lost by dissipation, and the momentum equation governs kinetic energy changes generated by buoyancy and lost by work done on the magnetic field and viscous dissipation. Global balances of magnetic and kinetic energy are found by respectively taking the dot product of the induction equation with $\mathbf{B}/\mu$, the dot product of the momentum equation with $\mathbf{u}$, then integrating over the volume of the core:

$$\dot{E}_{mag} = -W_{Lor} - D_{Ohm} \tag{4.2}$$

$$\dot{E}_{kin} = W_{buoy} + W_{Lor} - D_{visc}, \tag{4.3}$$

where $\dot{x}$ notation indicates the time derivative of x and

$$E_{mag} = \frac{Pm}{2E} \int \mathbf{B}^2 dV \tag{4.4}$$

$$E_{kin} = \frac{1}{2} \int \mathbf{u}^2 dV \tag{4.5}$$

are the magnetic and kinetic energy densities, $\mathbf{B}$ is the magnetic field, $\mathbf{u}$ is the fluid velocity,

$$D_{Ohm} = \frac{Pm}{E} \int (\nabla \times \mathbf{B})^2 \, dV \tag{4.6}$$

$$W_{Lor} = \frac{Pm}{E} \int \mathbf{u} \cdot (\mathbf{j} \times \mathbf{B}) \, dV \tag{4.7}$$

$$D_{visc} = Pm \int (\nabla \times \mathbf{u})^2 \, dV \tag{4.8}$$

$$W_{buoy} = \frac{(Pm)^2 \, Ra}{Pr} \int (u_r \vartheta) \, dV \tag{4.9}$$

are the ohmic dissipation, the work done by the Lorentz force, the viscous dissipation, and the work done by the Buoyancy force. $\mathbf{j}$ is current density, u_r radial velocity, and ϑ temperature fluctuation.

The energy and dissipation terms E_{mag}, E_{kin}, D_{Ohm}, and D_{visc} are outputs of our simulations and plotted in Figure 4.S1 of the supplementary materials. Generally, the magnetic energy and ohmic dissipation vary in phase, the kinetic energy and viscous dissipation vary in phase, and the kinetic and magnetic energy are out of phase. We compute $\dot{E}_{mag}$ and $\dot{E}_{kin}$ analytically after fitting a cubic B-spline function to time series of E_{mag} and E_{kin}. The changes in the kinetic energy ($\dot{E}_{kin}$) and viscous dissipation (D_{visc}) are much more important in these simulations than we expect for the Earth. The work done by the Lorentz force, W_{Lor}, and the work done by the Buoyancy force, W_{buoy}, are then obtained from Equations 4.2 and 4.3.

Table 4.2 provides a summary of the numerical parameters and physical characteristics for the four simulations. We evaluated the time averages ($\langle\rangle$) and standard deviation (σ) of the magnetic and kinetic energies (E_{mag}, E_{kin}) the ohmic and viscous dissipations(D_{Ohm}, D_{visc}), and the length scales for magnetic and viscous dissipation as defined in Oruba and Dormy (2014)

$$\ell_B^2 \equiv \frac{\int_V \mathbf{B}^2 \mathrm{d}V}{\int_V (\nabla \times \mathbf{B})^2 \mathrm{d}V}, \qquad \ell_u^2 \equiv \frac{\int_V \mathbf{u}^2 \mathrm{d}V}{\int_V (\nabla \times \mathbf{u})^2 \mathrm{d}V}. \tag{4.10}$$

Additionally we provide the ratio of the toroidal to total magnetic energy and kinetic energy

$$\left(\frac{\langle E_{mag}^{tor}\rangle}{\langle E_{mag}\rangle}\right), \qquad \left(\frac{\langle E_{kin}^{tor}\rangle}{\langle E_{kin}\rangle}\right), \tag{4.11}$$

and zonal ($m = 0$) toroidal to total magnetic energy and kinetic energy

$$\left(\frac{\langle E_{mag}^{tor,m=0}\rangle}{\langle E_{mag}\rangle}\right), \qquad \left(\frac{\langle E_{kin}^{tor,m=0}\rangle}{\langle E_{kin}\rangle}\right). \tag{4.12}$$

Normalized time-averaged values are also given relative to Case 1.3 in Table 4.2 to make comparisons easier. The lower Ra Cases 1.3 and 2.2 have less vigorous convection though this must also be balanced against the effect of the heating mode. Cases 1.3 and 1.4 are predominantly bottom-heated while Cases 2.2 and 2.3 have more internal heating, so stronger driving near the CMB. $\langle Rm\rangle$, $\langle Lo\rangle$, $\langle g_1^0\rangle$, $\sigma_{g_1^0}$, $\langle E_{mag}\rangle$, $\sigma_{E_{mag}}$, $\langle E_{kin}\rangle$, $\sigma_{E_{kin}}$, $\langle D_{Ohm}\rangle$, $\sigma_{D_{Ohm}}$, $\langle D_{visc}\rangle$, and $\sigma_{D_{visc}}$ are all higher for Cases 1.3 and 1.4 with faster cooling rate buoyancy profiles. Cases 1.3 and 1.4 have slightly smaller length scales ($\langle \ell_B\rangle$ and $\langle \ell_u\rangle$), and the length scales decrease with increasing Ra. Cases 2.2 and 2.3 have stronger toroidal fields, and the $\langle E_{mag}^{tor}\rangle/\langle E_{mag}\rangle$ decrease slightly with higher Ra – the effect is more pronounced for $\langle E_{mag}^{tor,m=0}\rangle/\langle E_{mag}\rangle$. Greater mixing leads to smaller length scales of the velocity and magnetic

field, and flows that are less zonal. With increased Ra the following increase: $\langle Rm \rangle$, $\sigma_{g_1^0}$, $\sigma_{E_{mag}}$, $\langle E_{kin} \rangle$, $\sigma_{E_{kin}}$, $\langle D_{Ohm} \rangle$, $\langle D_{visc} \rangle$, $\sigma_{D_{visc}}$, σ_{ℓ_B}, and σ_{ℓ_u}, while the length scales $\langle \ell_B \rangle$, $\langle \ell_u \rangle$ decrease. Case 1.3 – which has lower Ra – has a higher $\langle g_1^0 \rangle$, $\langle Lo \rangle$, and $\langle E_{mag} \rangle$, and lower $\sigma_{D_{Ohm}}$ than Case 1.4. This pattern is not seen in Cases 2.2 and 2.3; Case 2.2 has a lower $\langle g_1^0 \rangle$, $\langle Lo \rangle$, and $\langle E_{mag} \rangle$, and higher $\sigma_{D_{Ohm}}$.

Table 4.1: Definitions of variables used throughout the text.

Input	d	shell of thickness	V_s	non-dimensional volume of the outer core
	r_o	outer core radius	r_i	inner core radius, and $r_i/r_o = 0.35$
	t	time	f	frequency
	g	acceleration due to gravity	Ω	rotation rate
	β	temperature gradient at the outer boundary	α	coefficient of thermal expansion
	κ	thermal diffusivity	η	magnetic diffusivity
	ν	viscosity	ϑ	temperature fluctuation
	$\mathbf{j}$	current density	$\mathbf{B}$	magnetic field
	$\mathbf{u}$	velocity field	u_r	radial velocity
	E	Ekman number, $\frac{\nu}{2\Omega d^2}$	Ra	Rayleigh number, $\frac{\alpha g \beta d^5}{\nu\kappa}$
	Pr	Prandtl number, $\frac{\nu}{\kappa}$	Pm	magnetic Prandtl number, $\frac{\nu}{\eta}$
Output	E_{mag}	total magnetic energy integrated over the outer core	$E_{mag}^{tor,m=0}$	zonal, toroidal total magnetic energy
	Lo	amplitude of the magnetic field, $\sqrt{2E_{mag}/V_s}$	ℓ_B	length scale of the magnetic dissipation
	D_{Ohm}	ohmic dissipation	W_{Lor}	work done by the Lorentz force
	E_{kin}	total kinetic energy integrated over the outer core	$E_{kin}^{tor,m=0}$	zonal, toroidal total kinetic energy
	Rm	amplitude of the velocity field, $\sqrt{2E_{kin}/V_s}$	ℓ_u	length scale of the viscous dissipation
	D_{visc}	viscous dissipation	W_{buoy}	work done by the buoyancy force
Analysis	g_1^0	axial dipole spherical harmonic Gauss coefficient	$E_{mag}^{AD,r=a}$	non-dimensional surface axial dipole energy
	d_i	time derivative of $E_{mag}^{AD,r=a}$	f_{co}	cutoff frequency, corner f of lowpass filter
	s_3	skewness, 3^{rd} moment about the mean	s_E	normalized skewness coefficient
	$P\,[1]$	power density spectrum for time series 1	A_{11}	autocovariance for time series 1
	$\gamma^2\,[12]$	squared coherence spectrum between time series 1 and 2	Δf	frequency resolution of spectral estimate

Table 4.2: Comparison of numerical parameters and time-averaged physical properties of our four test geodynamo simulations. $\langle\rangle$ indicates time averaging and σ is the standard deviation. Numbers in parentheses are normalized to values for Case 1.3. Variables are defined in Table 1. Non-dimensionalized PADM2M has $\langle g_1^{0*}\rangle = 1.712 \times 10^{-2}$, $\sigma_{g_1^{0*}} = 0.48 \times 10^{-2}$. $\langle E_{mag}^{tor}\rangle/\langle E_{mag}\rangle$ and$\langle E_{kin}^{tor}\rangle/\langle E_{kin}\rangle$ = the ratios of the toroidal to total magnetic and kinetic energies, $\langle E_{mag}^{tor,m=0}\rangle/\langle E_{mag}\rangle$ and$\langle E_{kin}^{tor,m=0}\rangle/\langle E_{kin}\rangle$ = ratios of zonal ($m = 0$) toroidal to total energies.

Parameter	**Case 1.3**	**Case 1.4**	**Case 2.2**	**Case 2.3**
RaE	50	100	20	50
Cooling rate	rapid 123 K/Gyr	rapid 123 K/Gyr	moderate 69 K/Gyr	moderate 69 K/Gyr
$\langle Rm\rangle$	189	266	78	105
$\langle Lo\rangle$	208	160	114	164
$\langle g_1^{0*}\rangle$	3.11×10^{-2}	1.94×10^{-2}	1.52×10^{-2}	2.65×10^{-2}
$\sigma_{g_1^{0*}}$	0.27×10^{-2}	0.41×10^{-2}	0.15×10^{-2}	0.25×10^{-2}
$\langle E_{mag}\rangle$	3.17×10^{5} (1.0)	1.91×10^{5} (0.60)	9.44×10^{4} (0.30)	1.98×10^{5} (0.62)
$\sigma_{E_{mag}}$	0.49×10^{5} (1.0)	0.58×10^{5} (1.2)	1.16×10^{4} (0.24)	0.30×10^{5} (0.61)
$\langle E_{kin}\rangle$	2.61×10^{5} (1.0)	5.16×10^{5} (2.0)	4.46×10^{4} (0.17)	8.00×10^{4} (0.31)
$\sigma_{E_{kin}}$	0.17×10^{5} (1.0)	0.42×10^{5} (2.5)	0.35×10^{4} (0.21)	0.88×10^{4} (0.52)
$\langle D_{Ohm}\rangle$	2.10×10^{8} (1.0)	2.33×10^{8} (1.1)	2.09×10^{7} (0.10)	6.14×10^{7} (0.29)
$\sigma_{D_{Ohm}}$	0.17×10^{8} (1.0)	0.47×10^{8} (2.8)	0.23×10^{7} (0.14)	0.07×10^{7} (0.041)
$\langle D_{visc}\rangle$	3.74×10^{8} (1.0)	7.79×10^{8} (2.1)	3.63×10^{7} (0.10)	8.02×10^{7} (0.21)
$\sigma_{D_{visc}}$	0.22×10^{8} (1.0)	0.56×10^{8} (2.6)	0.26×10^{7} (0.12)	0.95×10^{7} (0.43)
$\langle \ell_B\rangle$	5.48×10^{-2} (1.0)	4.01×10^{-2} (0.73)	9.50×10^{-2} (1.7)	8.02×10^{-2} (1.5)
σ_{ℓ_B}	0.23×10^{-2} (1.0)	0.23×10^{-2} (1.0)	0.25×10^{-2} (1.1)	0.33×10^{-2} (1.4)
$\langle \ell_u\rangle$	5.28×10^{-2} (1.0)	5.15×10^{-2} (0.98)	7.01×10^{-2} (1.3)	6.32×10^{-2} (1.2)
σ_{ℓ_u}	0.70×10^{-2} (1.0)	0.95×10^{-2} (1.4)	1.04×10^{-2} (1.5)	1.56×10^{-2} (2.2)
$\langle E_{mag}^{tor}\rangle/\langle E_{mag}\rangle$	0.56	0.55	0.65	0.60
$\langle E_{mag}^{tor,m=0}\rangle/\langle E_{mag}\rangle$	0.10	0.05	0.25	0.18
$\langle E_{kin}^{tor}\rangle/\langle E_{kin}\rangle$	0.68	0.66	0.81	0.76
$\langle E_{kin}^{tor,m=0}\rangle/\langle E_{kin}\rangle$	0.05	0.04	0.09	0.08

4.4 Methods

4.4.1 ADM energy asymmetry evaluation

We compare PADM2M with the products of numerical geodynamo simulations using energies which are quadratic quantities. We compute the non-dimensional surface axial dipole energy,

$$E_{mag}^{AD,r=a}(t_i) = 2\left|g_1^{0*}(t_i)\right|^2, i = 1, 2, ...n, \tag{4.13}$$

the axial dipole ($l = 1$, $m = 0$) term of the Mauersberger-Lowes geomagnetic spectrum (Lowes, 1974) at each time t_i, $i = 1, 2, ...n$, where n is the number of time samples, a is the radius of the Earth, and g_1^{0*} is dimensionless ($g_1^{0*} = g_1^0/\sqrt{2\Omega\rho\mu\eta}$; Davies and Constable, 2014). The time derivatives are given by

$$d_i = \dot{E}_{mag}^{AD,r=a}(t_i) = 4\left|g_1^{0*}(t_i)\right|\left|\dot{g}_1^{0*}\right|(t_i). \tag{4.14}$$

To compare the temporal variations we rescale simulation time using the magnetic diffusion timescale d^2/η = 232,000 years ($\eta = 0.7$ m^{2}s^{-1}, Pozzo et al., 2012, 2013). Davies and Constable (2014) argued that this time scaling is an appropriate choice when considering long timescale behavior. Avery et al. (2017) found that records >800 kyr in length are needed to reliably detect the asymmetry between ADM growth and decay, so we analyzed dynamo simulations that have been run for more than 4 diffusion times.

Following the method described by Avery et al. (2017) for parameterizing the distribution of ADM derivatives, we exclude variations below the specified cutoff frequencies f_{co}, by applying a Parks-McClellan equiripple low-pass filter (Parks and McClellan, 1972) to

the time series of $\dot{E}_{mag}^{AD,r=a}$. In the unfiltered series the time spent growing and decaying is balanced, but the low-pass filtering uncovers an imbalance in the rates of change: positive derivative values, which correspond to a growing dipole, are larger on average and occur less frequently than negative rates representing decay i.e. the distribution has a positive tail (Figure 4.1). Avery et al. (2017) found a robust estimate of asymmetry is provided by the geomagnetic skewness and its coefficient for the distribution of dipole field derivatives.

We apply this method to the surface axial dipole energy. Skewness of a distribution of the axial dipole energy derivatives is the third moment about the mean,

$$s_3 = \frac{1}{n}\sum_{i=1}^{n}\left(d_i - \langle d\rangle\right)^3. \tag{4.15}$$

When s_3 is rendered dimensionless, the result is the skewness coefficient, s_E

$$s_E = \frac{\frac{1}{n}\sum_{i=1}^{n}\left(d_i - \langle d\rangle\right)^3}{\left(\sqrt{\frac{1}{n}\sum_{i=1}^{n}\left(d_i - \langle d\rangle\right)^2}\right)^3}. \tag{4.16}$$

The asymmetry observed in PADM2M manifests itself as a positively skewed distribution of derivatives, $s_3 > 0$, with a longer tail of derivatives to the right of the mean (Figure 4.1). In this study we evaluate both the third moment about the mean, s_3, and the skewness coefficient, s_E. s_3 allows us to compare the magnitude of the asymmetry with that in PADM2M while s_E is used to compare skewness between dynamo simulations with different levels of ADM variability ($\sigma_{g_1^0}$).

A two-sample Kolmogorov-Smirnov test between the cumulative distribution functions of the positive and negative derivatives was used to test for departures from the null hypothesis that they are from populations with the same distribution at the 5% significance

level. Distinguishable distributions are indicated with closed symbols in Figures 4.1 and 4.2. The p-value is the probability of acquiring as large a KS statistic when the two sample distributions come from the same empirical distribution, if $p > 0.05$ this null hypothesis is rejected at the 5% significance level. After lowpass filtering this two sample KS test shows the positive and negative CDFs come from different distributions (Figures 4.1(d)).

4.4.2 Frequency domain spectral analysis

Consider two time series labeled 1 and 2. The power spectrum ($P[1](f)$) of the first time series is defined as the Fourier transform ($\mathfrak{F}$) of the autocovariance ($A_{11}(t)$),

$$P[1](f) = \mathfrak{F}[A_{11}(t)] = \int_{-\infty}^{\infty} A_{11}(t)e^{-2\pi ift}dt, \tag{4.17}$$

and

$$A_{11}(t) = \mathcal{C}[X_1(t), X_1(t+dt)] = \mathcal{E}[X_1(t)X_1(t+dt)], \tag{4.18}$$

and $P[1](f)$ describes how much variance the signal has as a function of frequency. The coherence spectrum ($\gamma^2[12](f)$) between the two time series is the squared magnitude of the cross-spectrum i.e. the Fourier transform of the cross-covariance of the two series normalized by the power spectra of the two series,

$$\gamma^2[12] = \frac{|P[12]|^2}{P[1]P[2]} \tag{4.19}$$

where

$$P[12](f) = \mathfrak{F}[A_{12}(t)] = \int_{-\infty}^{\infty} A_{12}(t)e^{-2\pi ift}dt. \tag{4.20}$$

It gives a correlation coefficient between the two signals as a function of frequency. A value of one would indicate that the two time series are perfectly correlated at that frequency.

To estimate these spectra we used a sine multitaper method based on the theory of Riedel and Sidorenko (1995). We prewhitened the spectra, as is recommended for red spectra. Typical frequency resolution, Δf, of the spectra for the four cases is shown in Figure 4.3b. These spectral methods are well developed, but have not been previously applied to studying the energy balance of geodynamo simulations.

We use the coherence spectra between the total magnetic energy integrated over the outer core and the surface axial dipole energy ($\gamma^2\left[E_{mag}, E_{mag}^{AD,r=a}\right]$) and between the total $l=1$ magnetic energy ($E_{mag}^{l=1}$, $m=0,1$ dipole energy integrated over the outer core) and the surface axial dipole energy ($\gamma^2\left[E_{mag}^{l=1}, E_{mag}^{AD,r=a}\right]$) to evaluate the ability of the ADM to carry information about the outer core energy as a function of frequency.

Using the power spectral density and the coherence spectra we assess changes in the energy balance as a function of frequency. We track the conversion of kinetic to magnetic energy as a function of time over a broad range of frequencies. We estimate the PSDs $P\left[\dot{E}_{mag}\right]$, $P\left[D_{Ohm}\right]$, $P\left[W_{Lor}\right]$, and the squared coherence spectra $\gamma^2\left[\dot{E}_{mag}, D_{Ohm}\right]$, $\gamma^2\left[\dot{E}_{mag}, W_{Lor}\right]$, and $\gamma^2\left[D_{Ohm}, W_{Lor}\right]$ to evaluate the balance of terms in Equation 4.2. We estimate the PSDs of $P\left[\dot{E}_{kin}\right]$, $P\left[D_{visc}\right]$, $P\left[W_{buoy}\right]$ and $P\left[W_{Lor}\right]$, and the squared coherence spectra between $\gamma^2\left[D_{visc}, W_{Lor}\right]$, $\gamma^2\left[D_{visc}, W_{buoy}\right]$, and $\gamma^2\left[\dot{E}_{kin}, W_{Lor}\right]$ to evaluate the balance of terms in Equation 4.3. To test if low frequency changes in the ohmic and viscous dissipations are associated with changes in the length scale or amplitude of the magnetic field and velocity field respectively we evaluate the squared coherence spectra $\gamma^2\left[D_{Ohm}, \ell_B\right]$, $\gamma^2\left[D_{Ohm}, Lo\right]$, and $\gamma^2\left[D_{visc}, \ell_u\right]$, $\gamma^2\left[D_{visc}, Rm\right]$, where ℓ_B and ℓ_u are the length scales of the magnetic field and velocity, and Lo and Rm are the non-dimensional amplitude of the magnetic field and

velocity.

4.5 Results

The results of our analyses are presented in Figures 2–6, and for the purpose of discussion we consider three frequency ranges: low (< 0.01 kyr^{-1}), intermediate ($0.01 - 0.1$ kyr^{-1}), and high (> 0.1 kyr^{-1}) indicated by the black vertical lines. These ranges were chosen to loosely match the ranges where ADM skewness is absent or present for PADM2M, though we do not expect the variations of the simulations to perfectly match these frequency ranges because rescaling the time is likely to be imperfect.

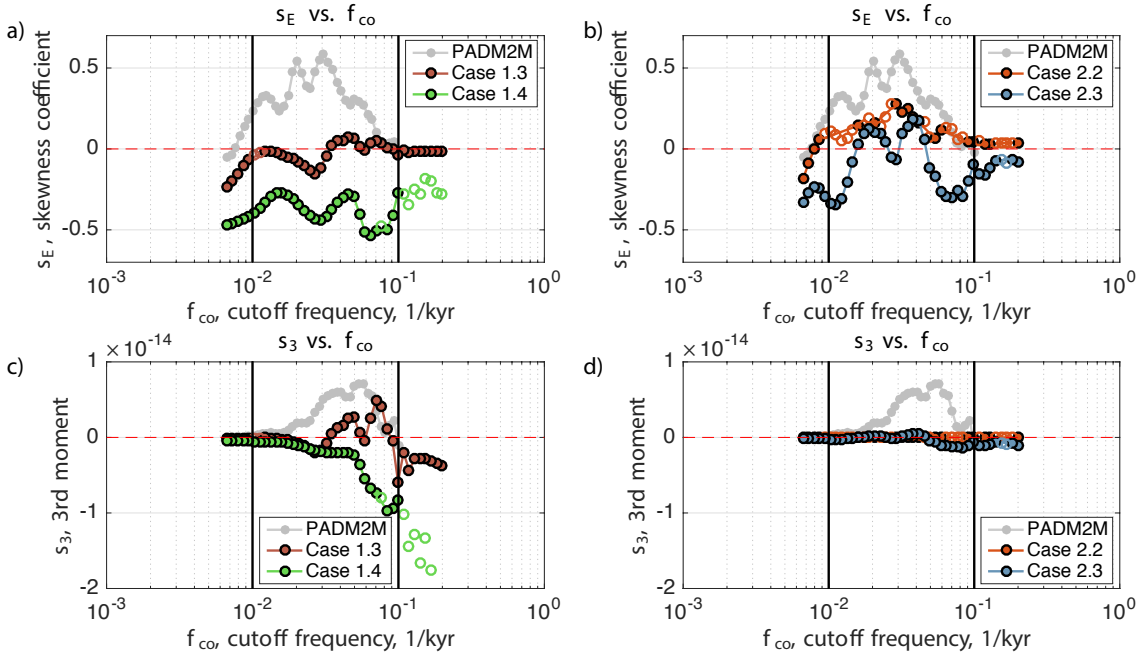

Figure 4.2: Axial dipole energy skewness results for geodynamo simulations cases. **(a–b)** $s_E(f_{co})$, **(c–d)** $s_3(f_{co})$ distributions after lowpass filtering $\dot{E}_{mag}^{AD,r=a}$. Case 1.3 (red), Case 1.4 (green), Case 2.2 (orange), and Case 2.3 (blue), grey dots show PADM2M result. Open symbols indicate a p-value > 0.05 in the two-sample Kolmogorov-Smirnov test as discussed in the text.

4.5.1 Asymmetry between growth and decay of axial dipole energy

The four dynamo cases we selected exhibit a variety of skewness properties which are shown in Figure 4.2 where the skewness coefficients, $s_E(f_{co})$, and the un-normalized third moment, $s_3(f_{co})$, are each compared with those of PADM2M.

The main signature in PADM2M is positive skewness across the intermediate frequency range. Cases 1.3 and 1.4 which exhibit the strongest and most consistent deviations from symmetry shown by s_3 which compares asymmetry amplitude (Figures 4.2a and c), Cases 2.2 and 2.3 are less decisively asymmetric (Figures 4.2b and d). None of the dynamo simulations exactly reproduces the PADM2M results, but Case 1.3 comes the closest. It has positive $s_3(f_{co})$, over a significant portion of the intermediate frequency range, $0.032 - 0.1$ kyr^{-1} (Figure 4.2c). The order of magnitude of s_3 is set by the nondimensionalization. Case 1.4 is interesting because it has negative $s_3(f_{co})$, this is opposite in sense to PADM2M.

Case 2.2's $s_E(f_{co})$ appears similar to PADM2M with positive skewness, Case 2.3 has complicated variations in $s_E(f_{co})$ which is generally opposite in sense to PADM2M, but the $s_3(f_{co})$ signals for these cases show that this asymmetry is small in amplitude. For Cases 2.2 and 2.3 $s_3(f_{co})$ is smaller in amplitude than PADM2M because their ADMs are not as variable (Figure 4.2d). In fact for Case 2.2 the distributions of positive and negative rates of change cannot be distinguished at the 5% significance level under the Kolmogorov-Smirnov test as indicated by the open symbols in Figure 4.2.

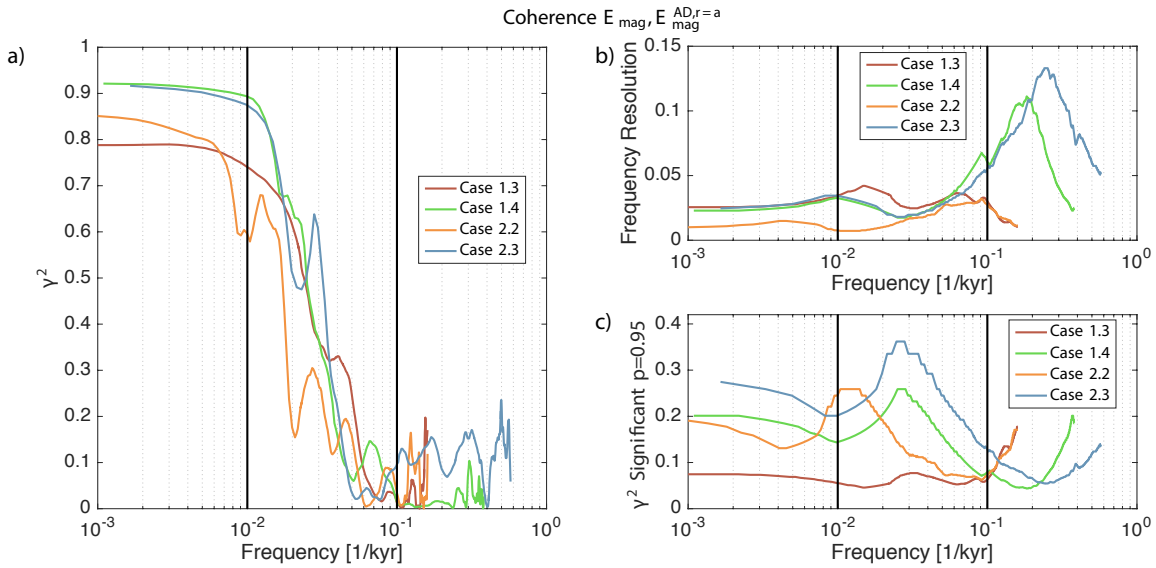

Figure 4.3: **(a)** Squared coherence spectra between the magnetic energy (E_{mag}) and surface dipole energy ($E_{mag}^{AD,r=a}$) for Case 1.3 (red), Case 1.4 (green), Case 2.2 (orange), and Case 2.3 (blue). **(b)** The frequency resolution $\Delta f = \frac{k f_N}{N_f}$ for $\gamma^2 \left[E_{mag}, E_{mag}^{AD,r=a}\right]$ where k = the number of tapers, f_N = the Nyquist frequency, and N_f = the number of frequencies estimated. **(c)** The coherence value below which no coherence can be inferred at the 95% confidence level for white noise processes.

4.5.2 Coherence between total magnetic energy and surface axial dipole energy

The toroidal part of the geomagnetic field is unobservable outside of the outer core, so Earth's dipole variation will not relay the entirety of the total magnetic energy variations. To evaluate this in our dynamo simulations we evaluate the coherence between the total magnetic energy and surface axial dipole energy. For each dynamo case, Figure 4.3a presents the squared coherence as a function of frequency between E_{mag}, the total magnetic energy in the core, and $E_{mag}^{AD,r=a}$, the energy in the surface axial dipole. Figure 4.3c shows the 95% confidence level for the squared coherence spectra of 2 white noise processes below which the coherence is considered insignificant. Coherence in the low and part of the intermediate

frequency ranges are significant. The frequency resolution for the estimates in Figure 4.3b is given by $\Delta f = k f_n / N_f$ where k is the number of tapers used at each frequency, f_n is the Nyquist frequency, and N_f is the number of frequency estimates. Note that for all except Case 2.2, Δf is well above 0.02 throughout the frequency range, hence we should not give too much credence to the detailed coherence variations below frequencies of $f = 0.02$ kyr^{-1}.

With the above caveat in mind, at frequencies below 0.01 kyr^{-1} we see consistently high coherence levels between the total magnetic energy in the outer core and the paleomagnetically observable energy in the axial dipole moment. From 0.01 kyr^{-1}, where coherence has already decreased to values ranging from 0.6 to above 0.9 across the various cases, it drops further to as low as 0.1 at 0.1 kyr^{-1}, and is essentially negligible at higher frequency. It is not immediately obvious why Cases 1.3 and 2.2 (which have lower Ra) generally exhibit lower overall coherence in all frequency bands than Cases 1.4 and 2.3, but there is a clear suggestion that a larger fraction of the energy is concentrated in the axial dipole variations in both 1.4 and 2.3, possibly due to more vigorous convection. The summary statistics in Table 2 support this strongly for Case 1.4 which has $\sigma_{g_1^{0*}} = 0.21\langle g_1^{0*}\rangle$ overall, and slightly less so for Case 2.3 with $\sigma_{g_1^{0*}} = 0.095\langle g_1^{0*}\rangle$. Both Cases 1.3 and 2.2, with the lower low frequency coherence, have lower variability (0.08 and $0.09\langle g_1^{0*}\rangle$, respectively) relative to the mean.

In a similar analysis conducted on the core's magnetic energy restricted to the $l = 1$ dipole term and the surface axial-dipole energy we found overall higher coherence at long periods as would be expected from exclusion of non-dipole variations in the core. Cases 1.3 and 2.2 values were comparable to 2.3 and only a few percent below Case 1.4. In all cases the decay in coherence with increasing frequency is more gradual than the for $\gamma^2\left[E_{mag}, E_{mag}^{AD,r=a}\right]$,

shown in Figure 4.3a, and for Cases 1.3 and 1.4 the drop moves into the high frequency band.

In all cases we find that the surface axial-dipole energy is coherent with the total magnetic energy in the core ranging from the longest period assessable to about 30 kyr. When only the dipole components of the core energy are considered the range extends in some cases to periods shorter than 10 kyr.

4.5.3 Balancing Magnetic Induction against Diffusion

A more detailed frequency domain analysis of the dynamo output based on Equation 4.2 allows us to examine the various contributions to changes in magnetic energy as a function of frequency. Figure 4.4a and b show the PSD for each term in Equation 4.2, the rate of change of magnetic energy, $\dot{E}_{mag}$, the magnetic diffusion, D_{Ohm}, and the work done by the Lorentz force W_{Lor}, while Figure 4.4c and d provide the associated squared coherence $\gamma^2\left[D_{Ohm}, W_{Lor}\right]$, etc., between each of the individual properties.

Our hypothesis based on observations of PADM2M's $s_E(f_{co})$ is that at low frequencies the geodynamo is in quasi-steady state and the magnetic (and kinetic) energy will not vary much. At intermediate frequencies where PADM2M displays a skewed distribution of $\dot{E}_{mag}^{AD,r=a}$ this steady state breaks down. Slower average decay of the dipole suggests periods where the field is dominated by large scale diffusion, and the faster average growth suggest advection is acting to increase the dipole strength. At higher frequencies PADM2M has little resolution and the record is likely dominated by small random fluctuations.

The general pattern in PSD for all four cases is as follows: at low frequency $P\left[D_{Ohm}\right]$ (dashed line) and $P\left[W_{Lor}\right]$ (dotted line) are indeed in balance while $P\left[\dot{E}_{mag}\right]$ (solid line,

Figure 4.4a and b) plays a relatively unimportant role. At intermediate frequency $P\left[\dot{E}_{mag}\right]$ gains power although $P\left[D_{Ohm}\right]$ and $P\left[W_{Lor}\right]$ remain very strong, and at high frequency all the terms drop by several orders of magnitude. The frequencies at which $P\left[\dot{E}_{mag}\right]$ peaks in power and the rapid fall-off vary across cases.

D_{Ohm} and W_{Lor} are highly coherent (solid lines in Figure 4.4c and d) and out of phase across all frequencies and in all simulations. Coherence with $\dot{E}_{mag}$ grows with increasing frequency over the low frequency range (dashed and dotted lines), but we should keep in mind the average frequency resolution shown in Figure 4.3b, which suggests the possibility of spectral leakage from the intermediate range. In all four cases at high frequency $\dot{E}_{mag}$ is more coherent with W_{Lor} than D_{Ohm}. In the same frequency range where s_3 is positive for Case 1.3 (0.03 - 0.1 kyr^{-1}) $\dot{E}_{mag}$ is more coherent with D_{Ohm} than W_{Lor}; the largest difference between the two squared coherence spectra is at 0.07 kyr^{-1}. In the same frequency range where s_3 is negative for Case 1.4 ($>$ 0.1 kyr^{-1}) the derivative of the magnetic energy is more coherent with W_{Lor} than D_{Ohm}. For Case 2.2 $\dot{E}_{mag}$ is more coherent with D_{Ohm} than W_{Lor} between 0.013 and 0.096 kyr^{-1}. For Case 2.3 $\dot{E}_{mag}$ is more coherent with W_{Lor} than D_{Ohm} between frequencies 0.02 and 0.06 kyr^{-1} (where $s_E(f_{co})$ is positive), and between frequencies 0.06 and 0.13 kyr$^{-1}\dot{E}_{mag}$ is more coherent with W_{Lor} than D_{Ohm} (where $s_E(f_{co})$ is negative).

Figure 4.4 supports the idea that there is not much variation in magnetic energy at low frequencies ($P\left[\dot{E}_{mag}\right]$ is not red with high power at low-frequency), and that high frequency changes reflect work done by the Lorentz force. At high frequency $\dot{E}_{mag}$ is more coherent with W_{Lor} than D_{Ohm}. In the intermediate frequency band we can associate asymmetry properties with changes in coherence behavior: higher coherence between $\dot{E}_{mag}$ and D_{Ohm}

occurs where $s_3 > 0$, and higher coherence between $\dot{E}_{mag}$ and W_{Lor} with $s_3 < 0$. We find changes in D_{Ohm} are more representative of changes in amplitude of the magnetic field than of changes in magnetic dissipation length scale, though the two factors are linked. $\gamma^2 [D_{Ohm}, Lo] > \gamma^2 [D_{Ohm}, \ell_B]$ where Lo is the measure of the amplitude of the magnetic field and ℓ_B is the length scale of ohmic dissipation (Figure 4.6).

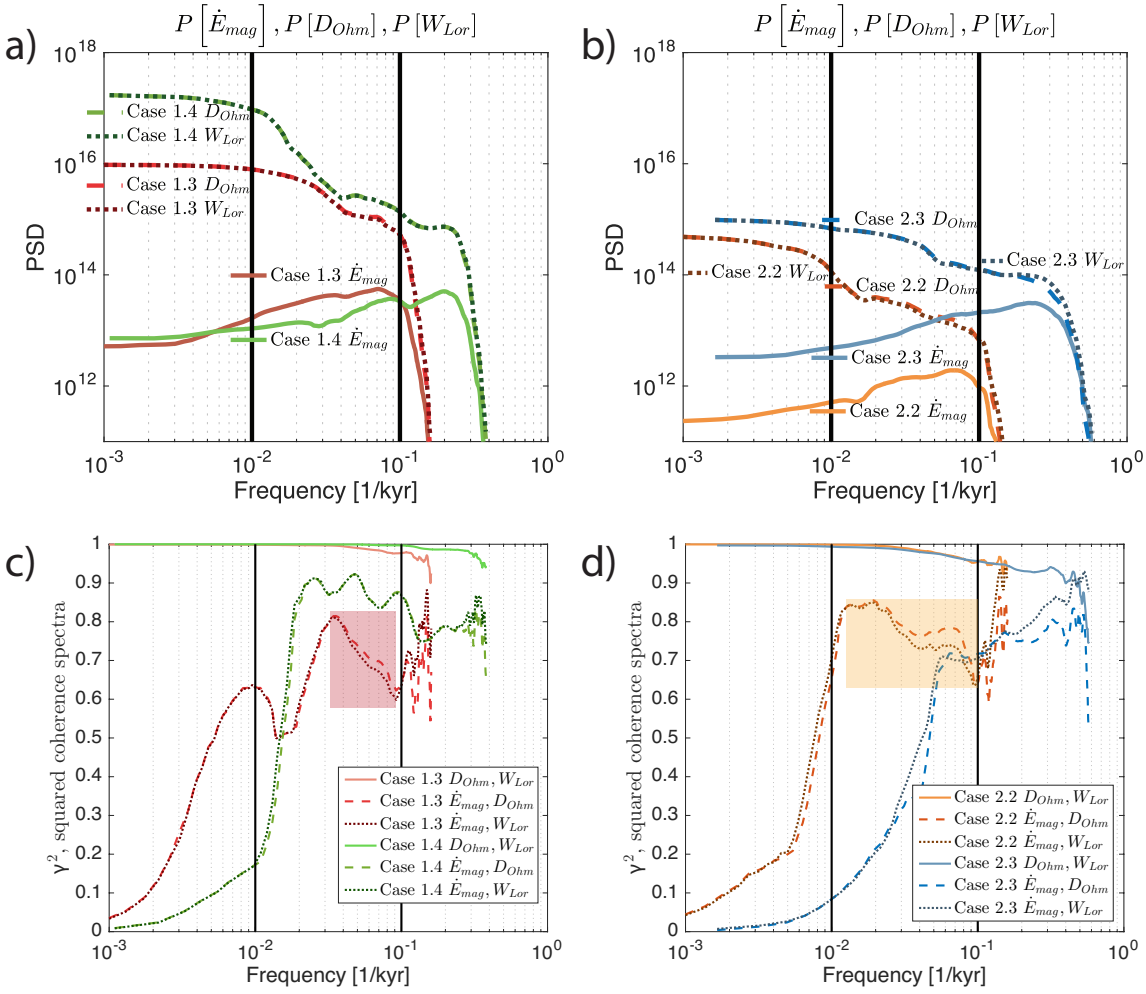

Figure 4.4: **(a–b)** The power spectra $P\left[\dot{E}_{mag}\right]$, $P\left[D_{Ohm}\right]$, and $P\left[W_{Lor}\right]$ **(a)** for Cases 1.3 (red) and 1.4 (green) and **(b)** Cases 2.2 (orange) and 2.3 (blue). **(c–d)** The squared coherence spectra between $\dot{E}_{mag}$, D_{visc}, and W_{Lor} for **(c)** Cases 1.3 (red) and 1.4 (green) and **(d)** Cases 2.2 (orange) and 2.3 (blue). The red and orange rectangles in c) and d) highlight where Cases 1.3 and 2.2 have positive $s_E(f_{co})$.

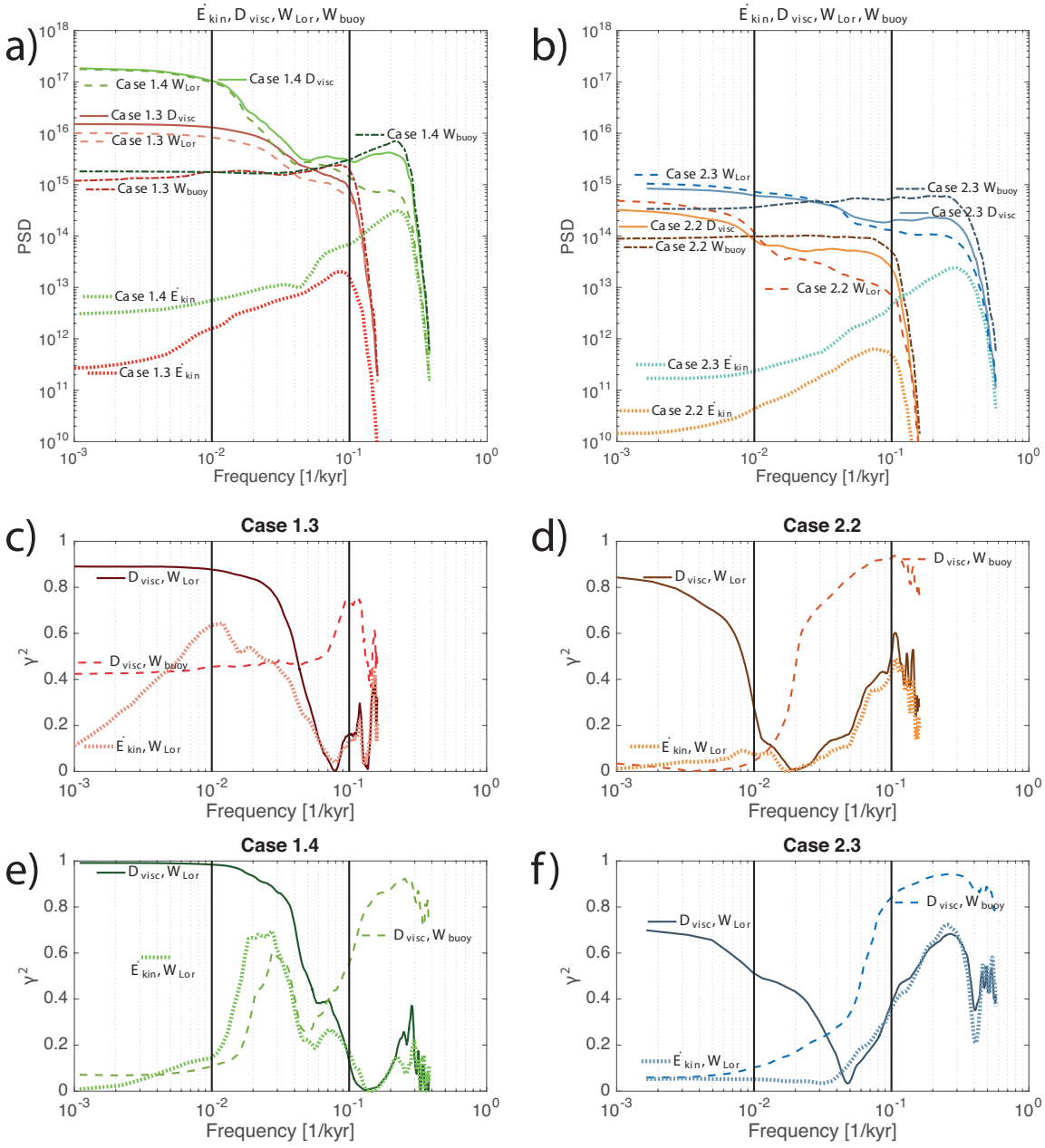

Figure 4.5: **(a–b)** The power spectra $P\left[\dot{E}_{kin}\right]$, $P\left[D_{visc}\right]$, $P\left[W_{Lor}\right]$, and $P\left[W_{buoy}\right]$ for **(a)** Cases 1.3 (red) and 1.4 (green) and **(b)** Cases 2.2 (orange) and 2.3 (blue). **(c–f)** The squared coherence spectra between D_{visc} and W_{Lor}, D_{visc} and W_{buoy}, and $\dot{E}_{kin}$ and W_{Lor} for **(c)** Cases 1.3 (red), **(e)**1.4 (green), **(d)** Cases 2.2 (orange), and **(e)** 2.3 (blue).

4.5.4 Balance of Momentum Equation

Spectral techniques can also be used to evaluate the balance between terms in the momentum equation (Equation 4.3). W_{buoy} is the energy source while D_{visc} and D_{Ohm} are energy sinks, and W_{Lor} transfers kinetic energy to magnetic energy through dynamo action. Building on our hypothesis of the dynamo being close to a steady state at low frequencies, if $\dot{E}_{kin}$ and $\dot{E}_{mag}$ are ≈ 0 Equation 4.2 becomes $W_{Lor} \approx -D_{Ohm}$, and Equation 4.3 is then $W_{buoy} \approx D_{Ohm} + D_{visc}$. For the Earth it can be assumed D_{visc} is negligibly small, but it is not in geodynamo simulations. At intermediate and high frequencies where $\dot{E}_{kin}$ and $\dot{E}_{mag}$ grow in power our technique can help us track the path of energy from W_{buoy} to D_{visc} and D_{Ohm} through W_{Lor}, $\dot{E}_{kin}$, and $\dot{E}_{mag}$.

Cases 1.3 and 1.4 have a buoyancy profile with a rapid cooling rate (Figure 4.5a, c, and e), and Cases 2.2 and 2.3 have a moderate cooling rate (Figure 4.5b, d, and f). Convection in Cases 1.3 and 1.4 is more vigorous and we expect them to have higher amplitude PSDs. We also expect the convection in the tangent cylinder, which occurs for Cases 1.3 and 1.4, to impact their energy balance as it is an additional mechanism for converting kinetic to magnetic energy.

The general pattern in PSD for all four cases is as follows (Figures 4.5a and b): the viscous dissipation $P\left[D_{visc}\right]$ and the work done by the Lorentz force $P\left[W_{Lor}\right]$ have high power at low frequencies, the buoyancy force $P\left[W_{buoy}\right]$ is lower but significant, and hence changes in the kinetic energy $P\left[\dot{E}_{kin}\right]$ have low power. At intermediate frequency a transition occurs, power in $P\left[\dot{E}_{kin}\right]$ grows larger while $P\left[D_{visc}\right]$ and $P\left[W_{Lor}\right]$ decrease. For all four cases at

high frequency after $P\left[W_{buoy}\right]$ and $P\left[\dot{E}_{kin}\right]$ peak all the terms drop in power by several orders of magnitude. The frequencies at which the intermediate frequency transition and the rapid fall-off occur vary across cases. The frequency where $P\left[W_{buoy}\right]$ overtakes $P\left[D_{visc}\right]$ and $P\left[W_{Lor}\right]$ in power is lower for Cases 2.2 and 2.3. As anticipated the rapid cooling rate of Cases 1.3 and 1.4 does make their PSDs more powerful. Increasing Ra increases the power in all the terms and shifts variations in the general pattern of the PSDs to higher frequency Figures 4.5a and b. This shift of features to higher frequency with higher Ra is also seen in the coherence between the various terms Figure 4.5c–f.

For completeness the squared coherence spectra for all combinations of terms of the momentum equation are shown in Supplemental Figure 4.S2. Here we focus on the squared coherence spectra $\gamma^2\left[D_{visc}, W_{Lor}\right]$, $\gamma^2\left[D_{visc}, W_{buoy}\right]$, and $\gamma^2\left[\dot{E}_{kin}, W_{Lor}\right]$ which tell us about the balance of momentum (Figure 4.5c–f). For all four cases $\gamma^2\left[D_{visc}, W_{Lor}\right]$ is high, while $\gamma^2\left[D_{visc}, W_{buoy}\right]$ and $\gamma^2\left[\dot{E}_{kin}, W_{Lor}\right]$ are low at low frequency. Again based on the frequency resolution, some of the low frequency signal may have leaked from the intermediate range. In the intermediate range $\gamma^2\left[D_{visc}, W_{Lor}\right]$ falls while $\gamma^2\left[D_{visc}, W_{buoy}\right]$ grows. This shift shows us the transition from the low frequency steady state to intermediate frequency dynamo operation. We believe the higher coherence between $\dot{E}_{kin}$ and W_{Lor} seen in Cases 1.3 and 1.4 in the intermediate frequency range but absent in Cases 2.2 and 2.3 is the signature of tangent cylinder convection. In the high frequency range the PSDs for all terms drop off and so the results there are not meaningful. As with changes in D_{Ohm}, we find low frequency changes in D_{visc} are more representative of changes in amplitude of the velocity field than of changes in dissipation length scale. $\gamma^2\left[D_{visc}, Rm\right] > \gamma^2\left[D_{visc}, \ell_u\right]$ where Rm

is the measure of the amplitude of the velocity field and ℓ_u is the length scale of viscous dissipation (Figure 4.6).

4.6 Discussion

The buoyancy force and the sum of the dissipation terms have high coherence at all frequencies. The small deviations from this balance are what sustain variations in the magnetic field this is consistent with the findings of Buffett and Bloxham (2002). The input parameters for our four geodynamo simulations produce different flow regimes and slightly different energy balances. The pair of Cases 1.3 and 1.4 have a buoyancy profile which gives them a rapid cooling rate (123 K/Gyr), and Case 1.4 has a higher Ra than Case 1.3. The pair of Cases 2.2 and 2.3 have a buoyancy profile which gives them a moderate cooling rate (69 K/Gyr), and Case 2.3 has a higher Ra than Case 2.2. The rapid cooling rate in Cases 1.3 and 1.4 leads to more vigorous convection overall, fully developed tangent cylinder convection with a strong upwelling plume near the pole, and poloidal flux expelled from the poles. Cases 2.2 and 2.3 have a moderate cooling rate and are more strongly columnar with stronger zonal flow, and lack convection inside the tangent cylinder.

We have developed four tools for evaluating these differences: 1) the distribution of time derivatives of the surface axial dipole energy and summary statistics, $s_3(f_{co})$ and $s_E(f_{co})$, 2) the coherence between total magnetic energy of the outer core and the surface axial dipole energy, $\gamma^2\left[E_{mag}, E_{mag}^{AD,r=a}\right]$, 3) the power and squared coherence spectra which we apply to both the terms in the magnetic induction equation and the terms in the momentum

equation, and 4) the squared coherence spectra between the dissipation terms and the length scale and amplitude of their associated fields.

We have identified a connection between $s_E(f_{co})$ (Figure 4.2) and the coherence spectra between $\dot{E}_{mag}$ and D_{Ohm}, and W_{Lor} (Figure 4.4). A higher coherence between $\dot{E}_{mag}$ and D_{Ohm} than between $\dot{E}_{mag}$ and W_{Lor} corresponds to $s_E(f_{co}) > 0$, while higher coherence between $\dot{E}_{mag}$ and W_{Lor} corresponds to $s_E(f_{co}) < 0$. This correlation shows that the effects of induction and diffusion have different frequency signatures in variations of the magnetic field which are observable at Earth's surface even at the largest spatial scale represented by the axial dipole. The same is true for Cases 2.2 and 2.3, but their axial dipole moments are less variable, so the distributions of their ADM derivatives are skewed an order of magnitude less than PADM2M and Cases 1.3 and 1.4. The structure of the asymmetry changes with Ra. The observation of asymmetry in Earth's dipole moment between growth and decay is a powerful constraint for geodynamo simulations to reproduce.

Cases 2.2 and 2.3 have lower amplitude of asymmetry (s_3) than PADM2M and Cases 1.3 and 1.4. The more vigorous convection in Cases 1.3 and 1.4 causes asymmetry (s_3) of comparable amplitude to PADM2M. For the flow regime of Cases 1.3 and 1.4, with convection within the tangent cylinder, the $l = 1$ dipole term and the surface axial-dipole energy are coherent to higher frequency ($\gamma^2 \left[E_{mag}^{l=1}, E_{mag}^{AD,r=a}\right]$).

$P\left[W_{buoy}\right]$ is nearly constant with frequency across the low and intermediate frequency ranges (Figure 4.5a and b). W_{buoy} expresses correlations between u_r and temperature, i.e. upwellings and downwellings, so the W_{buoy} results indicate the state of mixing. $P\left[W_{buoy}\right]$ indicates the simulations are well-mixed in the low and intermediate frequency ranges. $P\left[D_{visc}\right]$

and $P\left[W_{Lor}\right]$ decrease as frequency increases while $P\left[\dot{E}_{kin}\right]$ increases in power in the intermediate frequency range. This transition out of steady state conditions is also seen by an increase in the coherence between D_{visc} and W_{buoy} ($\gamma^2\left[D_{visc}, W_{buoy}\right]$) in the intermediate frequency range. In the low frequency range when $P\left[D_{visc}\right]$ and $P\left[W_{Lor}\right]$ have high power, the coherence spectra $\gamma^2\left[D_{visc}, W_{buoy}\right]$ is low. The low frequency variations in $P\left[D_{visc}\right]$ and $P\left[W_{Lor}\right]$ are not due to variations in W_{buoy}. At low frequency W_{Lor} is more coherent with $\dot{E}_{mag}$, this shows the timescales the frozen-flux approximation may be appropriate for (<10kyr).

At low frequencies the large scale flow structures that develop are predominantly azimuthal (thermal winds, zonal flows) that do not affect u_r or therefore W_{buoy}. If the long time scales are dominated by zonal flow, it would strongly suggest that $P\left[D_{visc}\right]$ decreasing with frequency reflects changes in flow velocity amplitude (Rm), rather than length scale (ℓ_u) which is set by the size of the outer core. To test this we compute the coherence spectra $\gamma^2\left[D_{visc}, Rm\right]$ and $\gamma^2\left[D_{visc}, \ell_u\right]$. D_{visc} is more coherent with Rm than ℓ_u (Figure 4.6).

Since $Pm \sim 1$, the same argument holds for the magnetic field. Changes in D_{Ohm} are more representative of changes in the magnetic field amplitude (Lo) than of changes in magnetic dissipation length scale (ℓ_B) (Figure 4.6). This indicates that the asymmetry between growth and decay rates of the ADM observed at the surface is due to changes in magnetic field strength and not an exchange between length scales. For the ohmic dissipation the effects of field amplitude and length scale are not as isolated as for the viscous dissipation. The coherence spectra $\gamma^2\left[D_{Ohm}, \ell_B\right]$ is higher at low frequencies than the corresponding $\gamma^2\left[D_{visc}, \ell_u\right]$. Rapid growth may reflect generation of poloidal field by coherent

radial motions, while slow decay could reflect diffusion of the large-scale flow that has a long time constant.

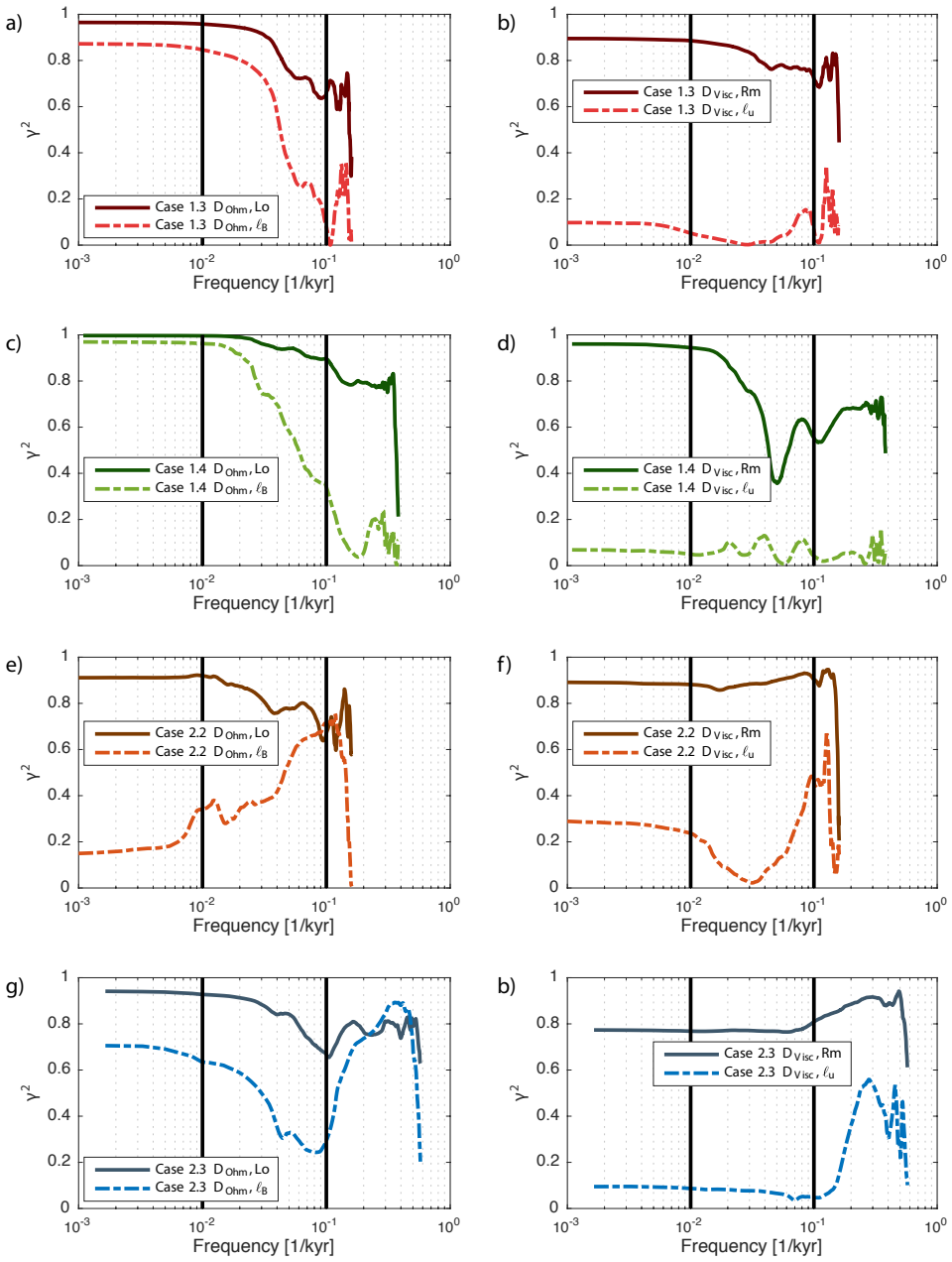

Figure 4.6: Origin of variations in dissipation, length scale or field amplitude for Case 1.3 (red), Case 1.4 (green), Case 2.2 (orange), and Case 2.3 (blue). **(a)**, **(c)**, **(e)**, and **(g)** $\gamma^2\left[D_{Ohm}, Lo\right]$ and $\gamma^2\left[D_{Ohm}, \ell_B\right]$ where Lo is the measure of the amplitude of the magnetic field and ℓ_B is the length scale of ohmic dissipation. **(b)**, **(d)**, **(f)**, and **(h)** $\gamma^2\left[D_{visc}, Rm\right]$ and $\gamma^2\left[D_{visc}, \ell_u\right]$ where Rm is the measure of the amplitude of the velocity field and ℓ_u is the length scale of viscous dissipation.

4.7 Conclusions

The spectral analysis shows case 1.3 is Earth-like in the sense of displaying substantial dipole variations with asymmetry like the Earth's. Case 1.4 has the opposite asymmetry, and dipole variations in Cases 2.2 and 2.3 are too small.

We have demonstrated that assessing the power spectra and coherences between the various energy contributions in the magnetic induction and momentum equations can be linked to useful insight into the physics underlying some geodynamo simulations. Differences in power between ohmic heating and the work done by the Lorentz force are linked to the frequency dependence of asymmetry between rates of growth and decay of surface axial dipole energy. We have identified test cases with symmetry properties that are similar to and distinct from the paleomagnetic signature in dipole moment variations over the past 2 Myr.

The surface dipole energy variations do not convey variations of the total magnetic energy of the dynamo at high frequencies. Some progress can be made by constructing higher order spherical harmonic paleomagnetic models for Myr time spans, but this cannot provide access to toroidal field variations or other important features of the internal dynamics. There is a limit to what we can interpret solely on the basis of observations of the dipole energy made at Earth's surface. This is where the numerical simulations can provide valuable insight.

The intermediate frequency range reveals a transition from low frequency steady state to the dynamo operation in the intermediate and high frequency ranges. Viscous and ohmic

dissipations decrease in power while the changes in kinetic and magnetic energies increase in power, with increasing frequency. Low frequency power in viscous and ohmic dissipations are shown to originate in variations in the velocity and magnetic field amplitudes rather than field length scales.

Our current study is not exhaustive enough to identify explicitly the dynamical causes of asymmetry in rates of change in Earth's dipole moment, but it does demonstrate a useful analysis method. Studying the energy balance of the geodynamo as a function of frequency is a useful tool. When just high frequency variations and time averages of terms of the energy balance are compared, behavior at intermediate frequencies may be missed. These tools will next be applied to many more geodynamo simulations with a broad range of input parameters, followed by detailed analysis of internal dynamical processes associated with specific symmetry properties.

Acknowledgements

The authors thank Bob Parker for access to his spectral analysis codes. This work was funded by the NSF grant numbers EAR 1065597 and 1623786. CJD is supported by a Natural Environment Research Council Independent Research Fellowship (NE/L011328/1). This work used the Extreme Science and Engineering Discovery Environment (XSEDE), which is supported by National Science Foundation grant number ACI-1053575. We thank Victor Eijkhout and Amit Chourasia for their assistance with optimization and visualization, which was made possible through the XSEDE Extended Collaborative Support Service (ECSS)

program.

Chapter 4, in part, has been submitted for publication of the material as it may appear in *Physics of Earth and Planetary Interiors*. Avery, Margaret S., Constable, Catherine G., Davies, Christopher, and Gubbins, David. The dissertation author was the primary investigator and author of this paper.

Appendices

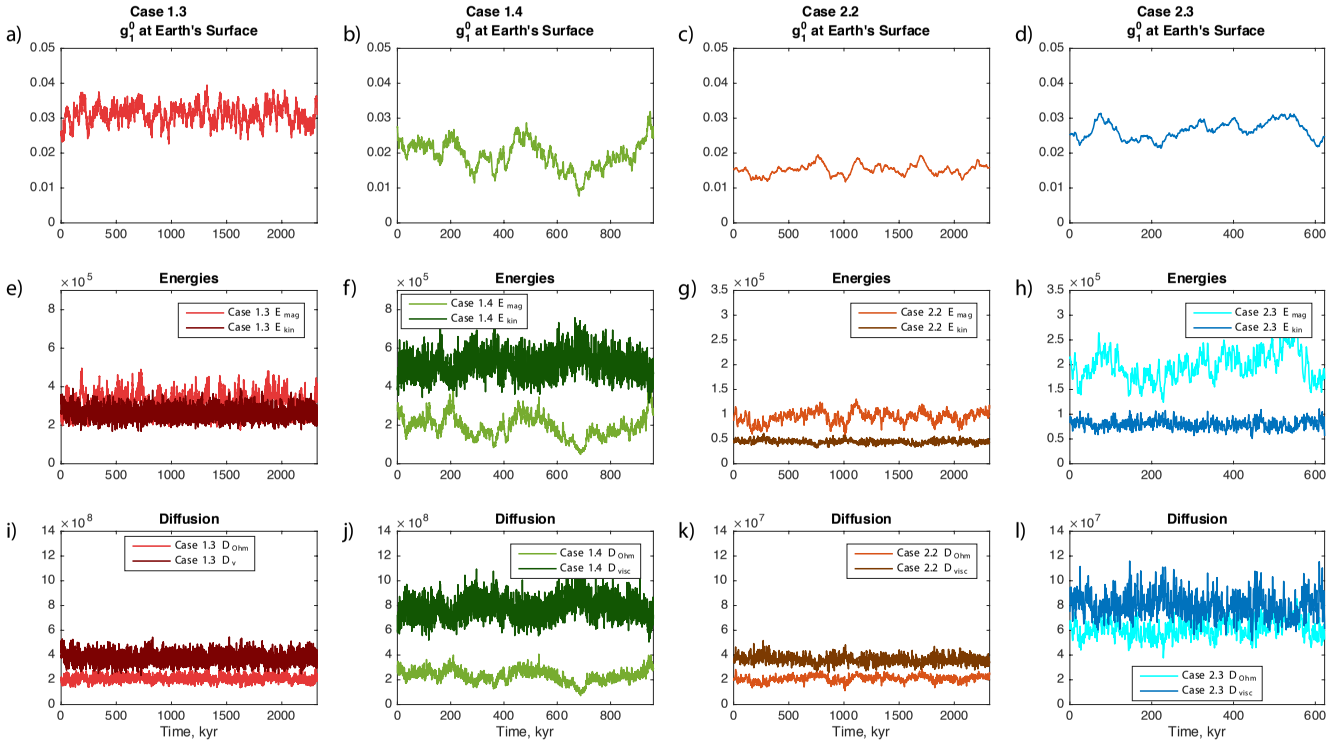

Figure 4.S1: Time series of output terms of the four geodynamo simulations for Case 1.3 (red), Case 1.4 (green), Case 2.2 (orange), and Case 2.3 (blue): **(a-d)** $|g_1^0|$, **(e-h)** the total magnetic energy E_{mag} and kinetic energy E_{kin}, **(i-l)** ohmic diffusion D_{Ohm} and viscous diffusion D_{visc}. Time averages of these terms can be found in Table 2.

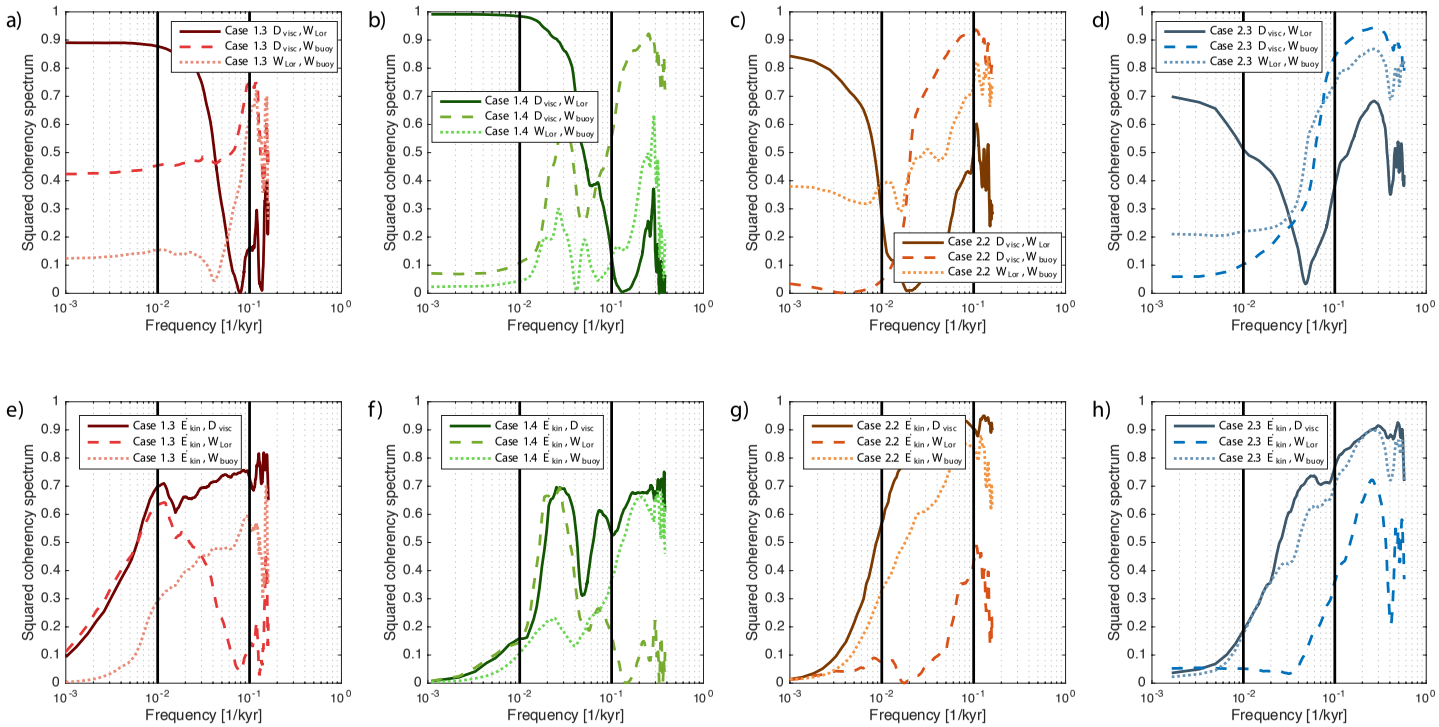

Figure 4.S2: The squared coherence spectra between terms of the momentum equation for Case 1.3 (red), Case 1.4 (green), Case 2.2 (orange), and Case 2.3 (blue): **(a-d)** D_{visc} and W_{Lor}, D_{visc} and W_{buoy}, and W_{Lor} and W_{buoy}, **(e-h)** $\dot{E}_{kin}$ and D_{visc}, $\dot{E}_{kin}$ and W_{Lor}, and $\dot{E}_{kin}$ and W_{buoy}. This figure expands on Figure 5(c–f) and Section 5.4 of the main text.

References

Avery, M. S., Gee, J. S., and Constable, C. G. (2017). Asymmetry in growth and decay of the geomagnetic dipole revealed in seafloor magnetization. *Earth and Planetary Science Letters*, 467:79–88.

Bloxham, J. and Jackson, A. (1991). Fluid flow near the surface of Earth's outer core. *Reviews of Geophysics*, 29(1):97–120.

Buffett, B. and Bloxham, J. (2002). Energetics of numerical geodynamo models. *Geophysical Journal International*, 149(1):211–224.

Buffett, B. A., Ziegler, L., and Constable, C. G. (2013). A stochastic model for palaeomagnetic field variations. *Geophysical Journal International*, 195(1):86–97.

Cande, S. C. and Kent, D. V. (1992). A new geomagnetic polarity time scale for the Late Cretaceous and Cenozoic. *Journal of Geophysical Research: Solid Earth*, 97(B10):13917–13951.

Cande, S. C. and Kent, D. V. (1995). Revised calibration of the geomagnetic polarity timescale for the Late Cretaceous and Cenozoic. *Journal of Geophysical Research: Solid Earth*, 100(B4):6093–6095.

Christensen, U. R., Aubert, J., and Hulot, G. (2010). Conditions for Earth-like geodynamo models. *Earth and Planetary Science Letters*, 296(3):487–496.

Constable, C. and Johnson, C. (2005). A paleomagnetic power spectrum. *Physics of the Earth and Planetary Interiors*, 153(1):61–73.

Constable, C., Korte, M., and Panovska, S. (2016). Persistent high paleosecular variation activity in Southern hemisphere for at least 10,000 years. *Earth and Planetary Science Letters*, 453(7043):78–86.

Davies, C. and Gubbins, D. (2011). A buoyancy profile for the Earth's core. *Geophysical Journal International*, 187(2):549–563.

Davies, C. J. and Constable, C. G. (2014). Insights from geodynamo simulations into long-term geomagnetic field behaviour. *Earth and Planetary Science Letters*, 404:238–249.

Finlay, C. C., Aubert, J., and Gillet, N. (2016). Gyre-driven decay of the Earth's magnetic dipole. *Nature Communications*, 7.

Korte, M. and Holme, R. (2010). On the persistence of geomagnetic flux lobes in global Holocene field models. *Physics of the Earth and Planetary Interiors*, 182(3):179–186.

Livermore, P. W., Hollerbach, R., and Finlay, C. C. (2017). An accelerating high-latitude jet in Earth's core. *Nature Geoscience*, 10(1):62–68.

Lowes, F. (1974). Spatial power spectrum of the main geomagnetic field, and extrapolation to the core. *Geophysical Journal International*, 36(3):717–730.

Mound, J., Davies, C., and Silva, L. (2015). Inner core translation and the hemispheric balance of the geomagnetic field. *Earth and Planetary Science Letters*, 424:148–157.

Olson, P., Christensen, U., and Glatzmaier, G. A. (1999). Numerical modeling of the geodynamo: mechanisms of field generation and equilibration. *Journal of Geophysical Research: Solid Earth*, 104(B5):10383–10404.

Oruba, L. and Dormy, E. (2014). Predictive scaling laws for spherical rotating dynamos. *Geophysical Journal International*, 198(2):828–847.

Parks, T. and McClellan, J. (1972). Chebyshev approximation for nonrecursive digital filters with linear phase. *IEEE Transactions on Circuit Theory*, 19(2):189–194.

Pozzo, M., Davies, C., Gubbins, D., and Alfè, D. (2012). Thermal and electrical conductivity of iron at Earth's core conditions. *Nature*, 485(7398):355–358.

Pozzo, M., Davies, C., Gubbins, D., and Alfè, D. (2013). Transport properties for liquid silicon-oxygen-iron mixtures at Earth's core conditions. *Physical Review B*, 87(1):014110.

Riedel, K. S. and Sidorenko, A. (1995). Minimum bias multiple taper spectral estimation. *IEEE Transactions on Signal Processing*, 43(1):188–195.

Valet, J.-P., Meynadier, L., and Guyodo, Y. (2005). Geomagnetic dipole strength and reversal rate over the past two million years. *Nature*, 435(7043):802–805.

Willis, A. P., Sreenivasan, B., and Gubbins, D. (2007). Thermal core-mantle interaction: Exploring regimes for 'locked' dynamo action. *Physics of the Earth and Planetary Interiors*, 165(1):83–92.

Ziegler, L. and Constable, C. (2011). Asymmetry in growth and decay of the geomagnetic dipole. *Earth and Planetary Science Letters*, 312(3):300–304.

Ziegler, L., Constable, C., Johnson, C., and Tauxe, L. (2011). PADM2M: a penalized maximum likelihood model of the 0–2 Ma palaeomagnetic axial dipole moment. *Geophysical Journal International*, 184(3):1069–1089.

Chapter 5

Asymmetric growth and decay of the geomagnetic dipole field examined with numerical dynamo simulations

Abstract

Studying direct magnetic and paleomagnetic field variations at Earth's surface provide a means to deepen our understanding of the dynamo operating in the liquid outer core. We use a suite of numerical dynamo simulations (generated with the Boussinesq Leeds Dynamo Code) to investigate what core processes are responsible for the asymmetry between axial dipole moment (ADM) growth and decay rates observed in the paleomagnetic record (Ziegler and Constable, 2011; Avery et al., 2017). Simulations do not suffer the same limitations of spatial and temporal resolution as paleomagnetic records. The magnetic and velocity fields

are completely known; however, the simulations cannot yet run with Earth-like diffusivities or rotational rates. Our simulations include a range of Rayleigh and Roberts numbers resulting in dipole-dominated dynamos that have been run for multiple magnetic diffusion times.

To determine which timescales (if any) exhibited asymmetry in rate of change for each simulation a series of smoothed surface dipole energy models were constructed using low-pass filters. We examine the coherence spectra for the various terms of the magnetic induction equation to assess changes in the force balance as a function of frequency. At long periods, as expected, the dynamos are usually in steady state with little variability in kinetic and magnetic energies. Some simulations exhibit asymmetry between growth and decay similar to that observed in the paleomagnetic record and it is associated with changes in magnetic energy that are more coherent with ohmic heating than with the work done by the Lorentz force in that frequency band. We focus on two illustrative dynamo cases, one with Earth-like ADM behavior and one that is not Earth-like. Visualization of their magnetic fields at the core mantle boundary and their internal fields, reveal a link between the number of convective upwellings and ADM variations. We also map the contributions to changes in axial dipole moment from advection and diffusion at the core-mantle boundary (CMB). For the Earth-like case dipole decay is mostly caused by diffusion although both advection and diffusion are in play, during dipole growth advection at the CMB is stronger and acts to increase the axial dipole moment.

5.1 Introduction

Earth's magnetic field is generated by dynamo action within the outer-core and at the outer surface is primarily dipolar in structure with smaller contributions from higher degree terms such as the quadrupole and octupole (Johnson and McFadden, 2015). The geomagnetic field varies in direction and intensity on a broad range of time scales (Constable and Johnson, 2005). Polarity reversals occur randomly, but on average every few hundred thousand years, while excursions are more frequent, and both are accompanied by lows in the axial dipole moment (ADM) (Valet et al., 2005; Ziegler et al., 2011). The field spends relatively little time in the transition between polarity states.

During the past 2 Ma the dipole field strength has varied considerably. PADM2M is a reconstruction of the paleomagnetic ADM fluctuations over the past 2 Ma constrained by sedimentary, igneous, and archeological paleomagnetic data (Ziegler et al., 2011). The standard deviation of PADM2M is 28% of its mean value, and the average ADM for the Brunhes chron is higher than the average during Matuyama. The dataset of paleointensity from the past 200 Ma, which is noisy and incomplete, does not require any large changes in mean ADM strength (Ingham et al., 2014). This long-term steadiness and short-term variability of the axial dipole moment should provide insights into the operation of the geodynamo within Earth's core.

The axial dipole moment during the recent past has not just been variable; it also displays faster rates for growth than decay (Ziegler and Constable, 2011). When fluctuations at frequencies greater than $\sim 6 \times 10^{-2}$ kyr^{-1} are filtered out the distribution of ADM rates of

change is skewed with a positive tail. This asymmetry between paleointensity growth and decay rates is also observed in marine magnetic anomaly records from Chrons C4Ar–C5r (9.3–11.2 Ma) (Avery et al., 2017). A series of low-pass filters were applied with varying corner cutoff frequencies (f_{co}). As presented in Chapter 3, at cutoff frequencies ranging from 1 to 6×10^{-2} kyr^{-1} they have positively skewed distributions peaking at $\sim2\times10^{-2}$ kyr^{-1}, and outside this interval the distributions are not skewed (Figure 5.1). The time scale of this peak asymmetry of $\sim$50 kyr may correspond with the e-folding time for dipole magnetic field decay, $t_d = r_o^2/(\pi^2\eta)$ $\sim$54 kyr where η is magnetic diffusivity. The hypothetical cause of this asymmetry between axial dipole growth and decay is the combined effects of rapid regeneration through advection and slower decay due to diffusion.

Changes in the geomagnetic field are governed by the magnetic induction equation, which describes the balance between induction of magnetic field by fluid advection and magnetic diffusion. The dipole is thought to be generated by an α^2-dynamo process where vortex columns align with the Earth's spin axis (e.g. Olson et al., 1999; Jones, 2011; Roberts and King, 2013; Roberts, 2015). The helical motion of the flow transforms toroidal magnetic field into poloidal magnetic field. There are two types of possible dynamo solutions with rapidly rotating bodies: the weak field branch and the strong field branch (Roberts, 1978, 1988). With weak magnetic field strength and small scale flow viscosity is important in weak field dynamos; the primary balance is between viscous, buoyancy, and Coriolis forces. In strong field dynamos the force balance is between magnetic (Lorentz),buoyancy, and Coriolis forces (e.g. Soderlund et al., 2012; King and Buffett, 2013; Soderlund et al., 2015; Dormy, 2016). There is a range of Ra where both solutions are possible. Above a threshold Ra the

weak field solutions are no longer stable and a weak initial field will grow into a strong field dynamo.

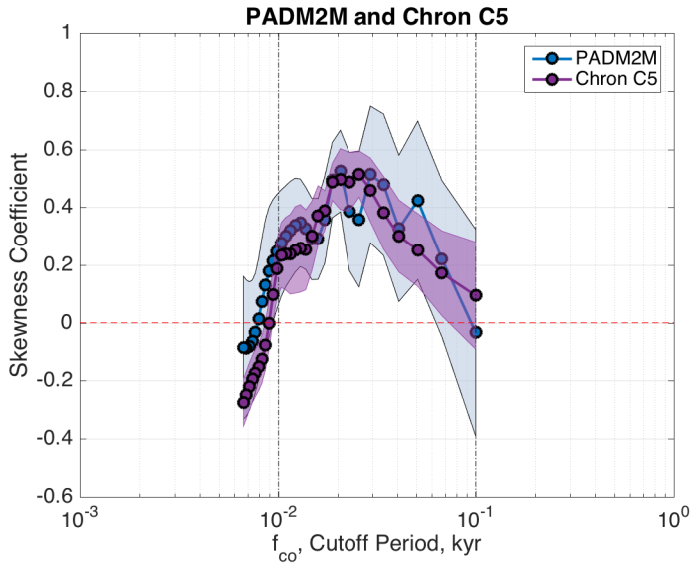

Figure 5.1: Skewed distribution of derivatives observed in geomagnetic models of axial dipole moment and seafloor magnetization. Skewness coefficient and cutoff frequency are described in Section 2.2. Blue dots show skewness coefficients for PADM2M, the paleomagnetic reconstruction of the past 2 Ma of axial dipole moment variations. Skewness coefficients of paleointensity recorded in the Northern Pacific seafloor thermal remanent magnetization and measured as marine magnetic anomaly tiny wiggles from chrons C4Ar–C5r (9.3–11.2 Ma) are shown with purple dots.

The strength and location of patches of magnetic flux at the core mantle boundary (CMB) also contribute to the strength of the ADM. On centennial timescales the affects of diffusion on field at the CMB may be negligible, and the fluid motion is expected to advect magnetic field with the flow. Energy can be transferred from the ADM to non-axial dipole (NAD) terms by moving normal flux towards the equator or reversed flux towards the poles. Conversely energy can be transferred to the ADM by moving normal flux poleward or reverse flux away from the poles. These transfers are a redistribution of magnetic flux and may not affect the total magnetic energy of the dynamo. Diffusion can contribute new flux patches

to the CMB by expelling flux from within the core (Bloxham, 1986; Glatzmaier and Olson, 2005). This can strengthen or weaken the ADM depending on the position of the normal and reversed flux patches.

Variations in the ADM are due to the simultaneous effects of advection and diffusion. These effects are not equal over all spatial scales. The magnetic Reynolds number (the nondimensional ratio comparing the effects of induction to diffusion) of the core is large, so advection is expected to play a greater role on large length scales and diffusion acts on short length scales. Magnetic field structures with smaller length scales have shorter fundamental diffusion timescales and decay more quickly (Moffatt, 1978).

We test the connection between the observed asymmetry in growth and decay of axial dipole moment and magnetic field structures at the CMB using numerical geodynamo simulations. Simulations also allow us to connect the surface magnetic field behavior with internal dynamo processes, which cannot be observed from the Earth's surface. Computational dynamo simulations allow detailed knowledge of the interior magnetic field, temperature, and dynamics within the simulated fluid shell. We make an effort to use several diffusion times of synthetic data for statistically representative time series.

Within the space of control parameters that are attainable for present-day computers we choose to focus on dynamos that produce magnetic fields that are dipolar in structure but have variable ADM. Due to computational limitations geodynamo simulations cannot yet run with Earth-like diffusivities or rotation rates. As Kutzner and Christensen (2002) have shown, increasing the Rayleigh number (Ra) generates larger magnetic fluctuations, but the more variable fields are multi-polar rather than dipolar. Nishikawa and Kusano

(2008) show that increasing the magnetic Prandtl number (Pm) promotes magnetic field variability and reversals. Raising Pm also broadens the weak-strong field branch transition (Dormy, 2016). Increasing the rotation rate by decreasing the Ekman number (E) reduces magnetic variability. In this study we analyze a suite of dynamo simulations with a moderate $E = 1.2\times10^{-4}$, and a range of Pm and Ra values focusing near the weak-strong branch transition for dipolar dynamos that are closer to unstable than the strongly dipolar, non-reversing dynamos that occur at higher Ra (Zhang and Gubbins, 2000). The Ekman number value we chose is much higher than in the Earth; we chose a value which we allowed us to simulate several nondimensional diffusion times in approximately a day of 'wall-clock' time using 256 or fewer computer processors.

Within this collection of dynamo simulations we observe a range of asymmetric axial dipole growth and decay rates, with some like the Earth while others are not. We apply the low-pass filtering methods introduced in Chapter 3 to assess the skewness of axial dipole rates of change, and we use the frequency domain spectral methods presented in Chapter 4 to evaluate the balance of terms in the magnetic induction equation. We use visualizations to explore dynamics of dipole growth and decay for two dynamo cases chosen for their asymmetric axial dipole growth and decay rates. We find an important link between the dominant spherical harmonic order of the fluid flow and axial dipole moment variations.

5.2 Methods

5.2.1 Model Formulation

To gain insight into the asymmetric distribution of changes in axial dipole moment observed in the geomagnetic field we study numerical simulations of convection in the Earth's outer core. The molten iron of the outer core is modeled as a rotating spherical shell of incompressible, electrically conducting, Boussinesq fluid with constant thermal diffusivity (κ), coefficient of thermal expansion (α), viscosity (ν), and magnetic diffusivity (η). The ratio between the inner and outer radii is r_i/r_o=0.35. Numerical dynamo simulations simultaneously solve the Navier-Stokes equation for the motion of the fluid, the time-dependent magnetic induction equation, and transport equation for the buoyant fluid. These equations are non-dimensionalized by scaling length by the thickness of the shell $d = r_o - r_i$, time by d^2/η, and the magnetic field by $(2\Omega\rho\mu_0\eta)^{1/2}$ where Ω is the rate of rotation, ρ the density, and μ_0 is the permeability of free space. The non-dimensional equations are

$$\frac{1}{Pr}(\partial_t + \mathbf{u}\cdot\nabla)\mathbf{u} - \nabla^2\mathbf{u} = -\nabla\widehat{p} + \frac{1}{qE}(\nabla\times\mathbf{B})\times\mathbf{B} + Ra\Theta\mathbf{r} - \frac{1}{E}\widehat{\mathbf{z}}\times\mathbf{u} \tag{5.1}$$

$$(\partial_t + \frac{1}{q}\nabla^2)\mathbf{B} = \nabla\times(\mathbf{u}\times\mathbf{B}) \tag{5.2}$$

$$(\partial_t + \frac{1}{q}\nabla^2)\Theta = S - \mathbf{u}\cdot\nabla\Theta \tag{5.3}$$

where $\mathbf{u}$ and $\mathbf{B}$ are the velocity and magnetic fields, Θ is the temperature profile due to the heat source S, $\widehat{p}$ is pressure, g is the acceleration due to gravity, β is the temperature gradient at the outer boundary, and

$$Ra = \frac{g\alpha\beta d^5}{\kappa\nu}, \qquad E = \frac{\nu}{2\Omega d^2}, \qquad Pr = \frac{\nu}{\kappa}, \qquad Pr = \frac{\nu}{\eta}, \qquad q = \frac{Pm}{Pr} = \frac{\kappa}{\eta}. \tag{5.4}$$

A summary of variables can be found in Table 5.1. Further details about the Boussinesq Leeds Spherical Dynamo Code can be found in Willis et al. (2007) and Davies and Gubbins (2011).

We amassed a suite of dipolar dynamo simulations spanning a range of parameter space near the transition between weak and strong field branches seeking dynamos with a variable dipole moment similar to Earth's. In the range of Ra where weak and strong solutions are both stable, variability in magnetic energy decreases as Ra increases up to the critical value for dynamo action, beyond which it increases. In the weak-strong bistability range we expect the magnetic field variability in a strong field dynamo to occasionally lead to a drop down to the weak field branch, which is a possible mechanism for magnetic field excursions and reversals. All are strong field dynamos with $E = 1.2\times10^{-4}$, $Pr = 1$, a mix of bottom and internal heating, homogeneous outer boundary heat flux, fixed temperature inner boundary, and no-slip inner and outer boundaries. We explore a range of Roberts numbers ($q = 2, 5, 10, 15, 20$), and Rayleigh numbers near the weak-strong branch transition for each Roberts number, as detailed in Table 5.2. All the cases were started from a single strong field solution initial condition, and the first 0.5 – 1 nondimensional diffusion times of the simulations were not included in our analysis.

5.2.2 Parameterization of dipole energy asymmetry

To investigate the growth and decay rates of the surface dipole energy of our suite of dynamos we use the procedure of low-pass filtering and skewness analysis described in Chapters 3 and for dynamo simulations in Chapter 4 Section 4.1. First, the time derivatives

of the surface axial dipole (AD) energy ($\dot{E}_{mag}^{AD,\mathbf{r}=a}$), where a is the radius of the surface of the Earth, are computed analytically with a cubic B-spline fit to the time series of the surface dipole energy. Second, the time series of $\dot{E}_{mag}^{AD,\mathbf{r}=a}$ is low-pass filtered with a suite of Parks-McClellan equiripple low-pass filters with a range of cutoff frequencies (f_{co}) (Figure 5.2a). Lastly, the distribution of smoothed $\dot{E}_{mag}^{AD,\mathbf{r}=a}$ are analyzed with the skewness coefficient,

$$s_E = \frac{\frac{1}{n}\sum_{i=1}^{n}\left(d_i - \langle d \rangle\right)^3}{\left(\sqrt{\frac{1}{n}\sum_{i=1}^{n}\left(d_i - \langle d \rangle\right)^2}\right)^3}. \tag{5.5}$$

where $d_i = \dot{E}_{mag}^{AD,\mathbf{r}=a}(t_i)$ is the derivative of the surface dipole energy at each time (t_i), $i = 1, 2, ..., n$, where n is the number of time equally spaced samples, a is the radius of the Earth, and $\langle\rangle$ indicates a time average. The asymmetry observed in PADM2M and the marine magnetic anomalies of Chron C5 manifest as a positively skewed distribution of derivatives, $s_E > 0$, with a longer tail of derivatives to the right of the mean. The ADM on average decays more slowly than it grows.

The standard error of s_E was estimated by bootstrap resampling independent and identically distributed blocks of $\dot{E}_{mag}^{AD,\mathbf{r}=a}$. We used algorithm 6.1 from Efron and Tibshirani, 1993 (pg. 47). The standard error of a function $\widehat{Q}$, $\widehat{se}_{boot}(\widehat{Q})$, is estimated by the standard deviation of J independent bootstrap replications. Since the smoothed models of $\dot{E}_{mag}^{AD,r=a}$ are not random samples, but rather are time series of dependent variables, a simple bootstrap resampling would destroy this dependence. Treating dependent data as if it is independent will cause an underestimate of the variance of the data. One approach to this issue is a block bootstrap, where instead of resampling all the data points one resamples blocks of the data, preserving the dependence within these blocks. The block length, w, should ideally be long

enough that the blocks encompass the time dependence and can be treated as independent and identically distributed (iid) random variables, but short enough that there are many blocks within the data to resample (Efron and Tibshirani, 1993, pg.102). The time series of the derivatives, $\dot{E}_{mag}^{AD,\mathbf{r}=a}$, was split into k non-overlapping blocks of length w. The blocks were then bootstrap resampled, i.e. J independent samples were drawn with replacement each consisting of k blocks, $x_k^1, x_k^2, ..., x_k^J$ (Figure 5.2b). The skewness coefficient (s_E), was evaluated for each sample

$$\widehat{Q}(j) = s_E(x_k^j) \qquad j = 1, 2, ..., J \tag{5.6}$$

The standard error of the function, $\widehat{se}_{boot}(\widehat{Q})$ is estimated by the standard deviation of the J independent bootstrap replications

$$\widehat{se}_{boot} = \left(\sum_{j=1}^{J} \frac{\left[\widehat{Q}(j) - \widehat{Q}(\cdot)\right]^2}{J-1} \right)^{1/2} \tag{5.7}$$

where

$$\widehat{Q}(\cdot) = \sum_{j=1}^{J} \frac{\widehat{Q}(j)}{J} \tag{5.8}$$

The cutoff period $T_{co} = 1/f_{co}$ of the smoothed $\dot{E}_{mag}^{AD,\mathbf{r}=a}$ models was used as the block length, w. Three example resamples are plotted in Figure 5.2c. There is some edge effect if w is not a multiple of n, and points at the end of the time series are not included in the resampling. This method is different from the jackknife resampling method used in Chapter 3, where different marine magnetic anomaly survey lines were resampled. Each survey line covered approximately the same time range and they were stacked. Here the synthetic data from a geodynamo simulation is a single time series of $\dot{E}_{mag}^{AD,\mathbf{r}=a}$ which is resampled.

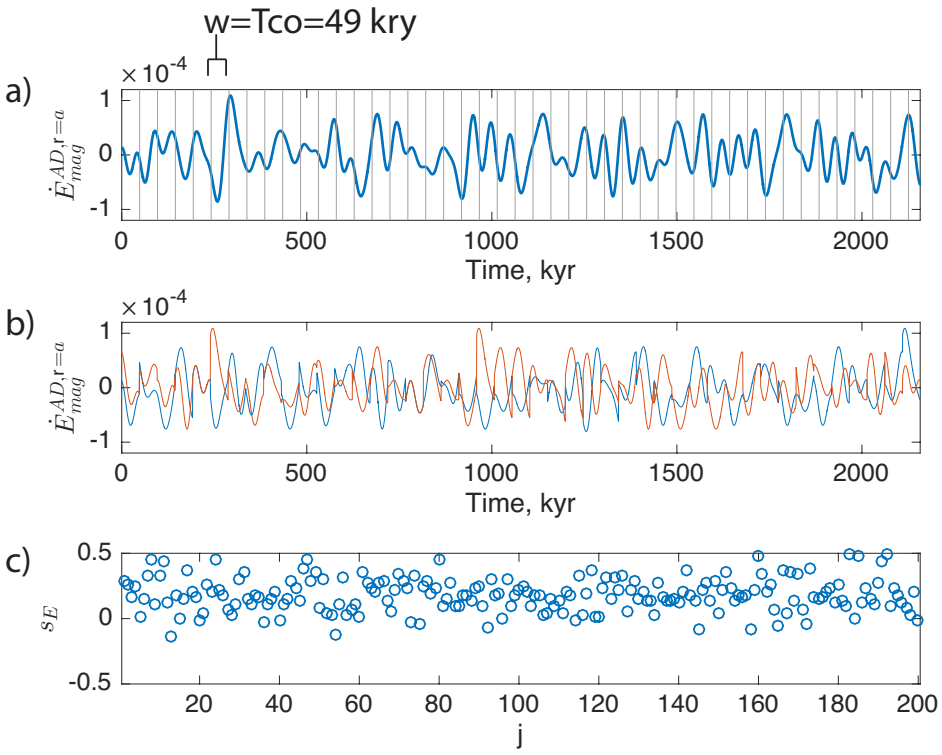

Figure 5.2: An example of the bootstrap resampling method for estimating the standard error of s_E. a) Time series of $\dot{E}_{mag}^{AD,\mathbf{r}=a}$ of case $q = 5, Ra = 60$ smoothed with a $T_{co} = 49$ kyr. The grey bars indicate the blocks of width w which is set by T_{co}. b) The k blocks are resampled to produce bootstrap variants of $\dot{E}_{mag}^{AD,\mathbf{r}=a}$. Two example resamples are plotted: x_k^1 in blue and x_k^2 in red. c) s_E is computed for each of the J bootstrap resamples. The standard error $\widehat{se}_{boot}$ is estimated by the the standard deviation of the J independent bootstrap replications, see text for details.

Table 5.1: Definitions of variables used throughout the text.

Input	d	shell of thickness	V_s	non-dimensional volume of the outer core
	r_o	outer core radius	r_i	inner core radius, and $r_i/r_o = 0.35$
	t	time	f	frequency
	g	acceleration due to gravity	Ω	rotation rate
	β	temperature gradient at the outer boundary	α	coefficient of thermal expansion
	κ	thermal diffusivity	η	magnetic diffusivity
	ν	viscosity	ϑ	temperature fluctuation
	$\mathbf{j}$	current density	$\mathbf{B}$	magnetic field
	$\mathbf{u}$	velocity field	u_r	radial velocity
	E	Ekman number, $\frac{\nu}{2\Omega d^2}$	Ra	Rayleigh number, $\frac{\alpha g \beta d^5}{\nu\kappa}$
	Pr	Prandtl number, $\frac{\nu}{\kappa}$	Pm	magnetic Prandtl number, $\frac{\nu}{\eta}$
Output	E_{mag}	total magnetic energy integrated over the outer core	W_{Lor}	work done by the Lorentz force
	Lo	amplitude of the magnetic field, $\sqrt{2E_{mag}/V_s}$	ℓ_B	length scale of the magnetic dissipation
	D_{Ohm}	ohmic dissipation	D_{visc}	viscous dissipation
	E_{kin}	total kinetic energy integrated over the outer core	W_{buoy}	work done by the buoyancy force
	Rm	amplitude of the velocity field, $\sqrt{2E_{kin}/V_s}$	ℓ_u	length scale of the viscous dissipation
Analysis	g_1^0	axial dipole spherical harmonic Gauss coefficient	$E_{mag}^{AD,r=a}$	non-dimensional surface axial dipole energy
	$\mathbf{m}$	dipole moment vector	$R_l(\mathbf{r})$	spatial power spectrum at the CMB
	d_i	time derivative of $E_{mag}^{AD,r=a}$	f_{co}	cutoff frequency, corner f of lowpass filter
	s_3	skewness, 3^{rd} moment about the mean	s_E	normalized skewness coefficient
	$P\,[1]$	power density spectrum for time series 1	$\gamma^2\,[12]$	squared coherence spectrum between time series 1 and 2

Table 5.2: Control parameters for dynamo cases. q= Roberts number, Ra=Rayleigh, E=Ekman, T=duration of simulation in nondimensional diffusion times, and $Rm = \sqrt{2E_{kin}/V_S}$ the magnetic Reynolds number. All cases have E =1.2×10^{-4} and $Pr = 1$. $N, L = M$ indicate the spatial truncation of the simulation, with N= the number of radial grid points and $L = M$ = the truncation degree and order of the θ and ϕ spherical harmonic expansion. Dynamo cases discussed in detail in Sections 5.4.2 and 5.4.3 are indicated with bold italics font.

q	RaE	T	Rm	$N, L = M$	q	RaE	T	Rm	$N, L = M$
2	56	11.7	77.4	128,64	10	30	5.3	129.9	160,64
2	58	9.4	77.9	128,64	10	40	4.3	165.8	160,64
2	59	9.8	78.0	128,64	10	50	4.0	195.3	160,64
2	60	21.9	78.1	128,64	10	60	5.7	224.3	128,64
2	64	7.6	80.1	128,64	10	70	5.0	247.8	128,64
2	65	8.1	79.3	128,64	10	80	4.4	271.4	128,64
2	70	8.4	83.4	128,64	15	20	1.6	128.7	128,64
2	75	9.5	86.2	128,64	15	30	1.0	193.4	128,64
2	80	11.2	87.9	128,64	15	40	4.3	247.0	160,64
2	81	15.7	87.8	128,64	15	50	0.7	298.4	128,64
2	85	8.8	90.7	128,64	15	60	0.7	335.9	128,64
5	50	10.6	109.9	128,64	15	70	0.5	371.2	128,64
5	***60***	***9.5***	***116.2***	***128,64***	20	15	5.6	127.5	160,64
5	70	15.3	126.7	128,64	20	20	1.2	169.4	128,64
5	80	9.1	137.8	128,64	20	25	1.1	218.1	128,64
5	90	8.6	149.0	128,64	20	30	0.8	258.3	128,64
5	100	7.3	159.7	128,64	***20***	***40***	***4.1***	***327.6***	***160,64***
10	23	5.3	101.0	160,64	20	50	0.6	384.6	128,64
10	25	4.1	109.7	160,64					

5.2.3 Spectral tools for assessing dynamo energy

As was introduced in Chapter 4, we use squared coherence spectra to evaluate changes in the energy balance as a function of frequency. We assess the impact of advection and diffusion on changes in magnetic energy on different time scales, which is the basis of our hypothesis about the source of asymmetry between dipole moment growth and decay. We rescale simulation time using the magnetic diffusion timescale d^2/η= 232,000 years (η=0.7 m^{2}s^{-1}, Pozzo et al., 2012, 2013). This is an appropriate choice when considering long timescale behavior (Davies and Constable, 2014). We estimate the squared coherence spectra $\gamma^2\left[\dot{E}_{mag}, D_{Ohm}\right]$, $\gamma^2\left[\dot{E}_{mag}, W_{Lor}\right]$, and $\gamma^2\left[\dot{D}_{Ohm}, W_{Lor}\right]$ to evaluate the balance of terms in the magnetic induction equation (Equation 5.2). $\dot{E}_{mag}$,D_{Ohm}, and W_{Lor} are the changes in magnetic energy, ohmic dissipation, and work done by the Lorentz force as defined in Chapter 4, Equations 4.4, 4.6, and 4.7. In Chapter 4, we observed a relationship between $\gamma^2\left[\dot{E}_{mag}, D_{Ohm}\right]$ and the pattern of skewness coefficient as a function of cutoff frequency $s_E(f_{co})$. Positive skewness was observed at frequencies where $\gamma^2\left[\dot{E}_{mag}, D_{Ohm}\right] > \gamma^2\left[\dot{E}_{mag}, W_{Lor}\right]$ and conversely negative skewness was associated with $\gamma^2\left[\dot{E}_{mag}, D_{Ohm}\right] < \gamma^2\left[\dot{E}_{mag}, W_{Lor}\right]$. We test this relationship further here with our suite of simulations.

To investigate if variations in the ohmic dissipation are associated with changes in the length scale or amplitude of the magnetic field, we evaluate the squared coherence spectra $\gamma^2\left[D_{Ohm}, \ell_B\right]$, $\gamma^2\left[D_{Ohm}, Lo\right]$.

$$\ell_B = \frac{\int_{V_S} B^2 dV}{\int_{V_S} (\nabla \times B)^2 dV} \tag{5.9}$$

is the length scale of the magnetic field, and $Lo = \sqrt{2E_{mag})/V_S}$ is the non-dimensional

amplitude of the magnetic field where V_S is the nondimensional volume of the spherical shell.

5.2.4 Visualization of dynamo growth and decay

Using the times series of $|g_1^0|$ we identify times of interest to visualize. Our goal is to link the internal variations in E_{mag},D_{Ohm}, and W_{Lor} with spatial structures at the CMB and within the core. We selected two test cases to investigate further, one with low and one high Roberts numbers, which display an asymmetry between growth and decay rates ($q = 5, Ra = 60; q = 20, Ra = 40$). To study the dynamics of the flow structures that generate the asymmetry between growth and decay rates we compute and map several diagnostic fields. The geomagnetic dipole moment vector $\mathbf{m}$ can be expressed in terms of the order l = Gauss coefficients or in terms of the radial component of geomagnetic field B_r:

$$\mathbf{m} = \frac{3\mathbf{r}}{2\mu_0} \int B_r \left(\sin\theta\cos\phi\widehat{\mathbf{x}} + \sin\theta\sin\phi\widehat{\mathbf{y}} + \cos\theta\widehat{\mathbf{z}}\right) dS = \frac{4\pi a^3}{\mu} \left(g_1^1\widehat{\mathbf{x}} + h_1^1\widehat{\mathbf{y}} + g_1^0\widehat{\mathbf{z}}\right) \qquad (5.10)$$

where $(\widehat{\mathbf{x}}, \widehat{\mathbf{y}}, \widehat{\mathbf{z}})$ are Cartesian unit vectors with an origin at Earth's center, dS indicates a surface integral over a sphere of radius $\mathbf{r}$, and g_1^1, h_1^1, and g_1^0 are the equatorial and axial dipole Gauss coefficients. To assess the morphology of the magnetic field at the CMB and compare it with Earth's field we compute the dipole field power relative to non-axial terms, equatorial symmetry, and zonality with the ratios proposed by Christensen et al. (2010): 1) AD/NAD, the ratio of power in the axial dipole ($l = 1, m = 0$), to the rest of the field (non-axial dipole); 2) O/E, the ratio of power in equatorially antisymmetric nondipole coefficients ($l - m$ odd), to the power in equatorially symmetric nondipole coefficients ($l - m$ even); and

3) Z/NZ, the ratio of power in nondipole zonal ($m = 0$), to nondipole nonzonal ($m \neq 0$) coefficients. These ratios are derived from selected terms in the spatial power spectrum at the CMB (the Mauersberger-Lowes spectrum):

$$R_l(\mathbf{r}) = (l+1)\left(\frac{a}{r}\right)^{2l+4} \sum_{m=0}^{l} \left[(g_l^m)^2 + (h_l^m)^2\right] \tag{5.11}$$

Earth's field for the period 1690 to 2010 (gufm1+igrf) has values: AD/NAD=1.58, O/E=1.06, and Z/NZ=0.156 (Jackson et al., 2000; Christensen et al., 2010). We compare the time evolution of these ratios with animations and snapshots of maps of B_r at the CMB and u_r below the CMB (and well below the boundary layer at a radius of 1.33, r_o=1.53). We also map the axial component of the dipole moment ($B_r \cos\theta$) on the CMB. We are also interested in changes in the axial dipole moment at the CMB which can be written in terms of contributions from advection and diffusion as:

$$\dot{m}_z = -\frac{3}{2\mu_0} \int \left(u_\theta \sin\theta B_r + \frac{\eta}{r_o} \frac{\partial r B_\theta}{\partial r} \sin\theta - \frac{\eta}{r_o} \frac{\partial B_r}{\partial \theta} \sin\theta \right) dS \tag{5.12}$$

(Olson and Amit, 2006; Finlay et al., 2016). The terms of the right hand side of this equation are the contributions to $\dot{m}_z$ on or just below the CMB from meridional advection of magnetic field, radial magnetic field diffusion, and meridional magnetic field diffusion. We rescale the magnetic field and velocity by $\sqrt{2\Omega\rho\mu_0\eta}$ and η/d respectively to compute the terms of $\dot{m}_z$. To examine the contributions from these terms on the time scale exhibiting asymmetry between dipole growth and decay we apply a running average with a window width equal to the cutoff period T_{co} of peak asymmetry. We map them on the CMB along with running average maps of B_r and $B_r \cos\theta$ for reference.

To evaluate the three-dimensional processes at work within the spherical shell that

produce these surface flows we examine several equatorial slices and properties of the flow. Equatorial slices of B_r, u_r, and the temperature are useful for observing the effect of upwelling flow on the concentrations of magnetic flux on the CMB. We compare these animations and snapshots with time series of the total magnetic energy E_{mag}, kinetic energy E_{kin}, ohmic dissipation D_{Ohm}, and viscous dissipation D_{visc}.

5.3 Results

5.3.1 Axial dipole variability and rate of change asymmetry

The dynamo simulations in our suite generally have less variable axial dipole moments than is observed for the field model PADM2M. PADM2M has a dipole moment standard deviation that is 28% of its mean value. The simulations have dipole moment standard deviations 5-15% of their mean ADM, with the exception of three simulations with $Ra < 60$ for $q = 2$ and 5 which vary more than 15% (Figure 5.3a, c, e, g, and i). The simulations that have more variable ADM are closer to the transition between weak and strong field branches.

The pattern of skewness coefficient as a function of cutoff frequency $s_E(f_{co})$ varies with Roberts number and separates the dynamos in our collection into two groups.

- Group 1] Many of the $q = 2$ cases have Earth-like, positive $s_E(f_{co})$ patterns ($Ra = 56, 58, 59, 60, 70, 75$, and 81) (Figure 5.3b). The $q = 5$ cases with Ra values of 50 and 60 have Earth-like positive $s_E(f_{co})$.

- Group 2] $q = 5$ cases with higher Ra have negative $s_E(f_{co})$ (Figure 5.3d). None of the

$q = 10$ cases have Earth-like $s_E(f_{co})$, they are all negative (Figure 5.3f). Simulations with $q = 15$ and 20, and $Ra = 40$ have positive s_E in the intermediate frequency range for frequencies lower than $\sim 3 \times 10^{-2}$ kyr^{-1}, but unlike Earth they have negative s_E for higher frequencies and positive s_E in the low frequency range (Figure 5.3h and j). Case $q = 20$ and $Ra = 15$ has negative $s_E(f_{co})$ for frequencies less than 4×10^{-2} kyr^{-1}, and positive $s_E(f_{co})$ for higher frequencies. The other $q = 15$ and 20 cases are similar to cases $q = 15$ and 20, and $Ra = 40$, but are shorter in duration than the 4 diffusion-time limit for this analysis found in Chapter 3.

We select a dynamo from each group to explore in detail: cases $q = 5, Ra = 60$ which has an Earth-like $s_E(f_{co})$ (Figure 5.4a) and $q = 20, Ra = 40$ that does not have an Earth-like $s_E(f_{co})$ (Figure 5.6a).

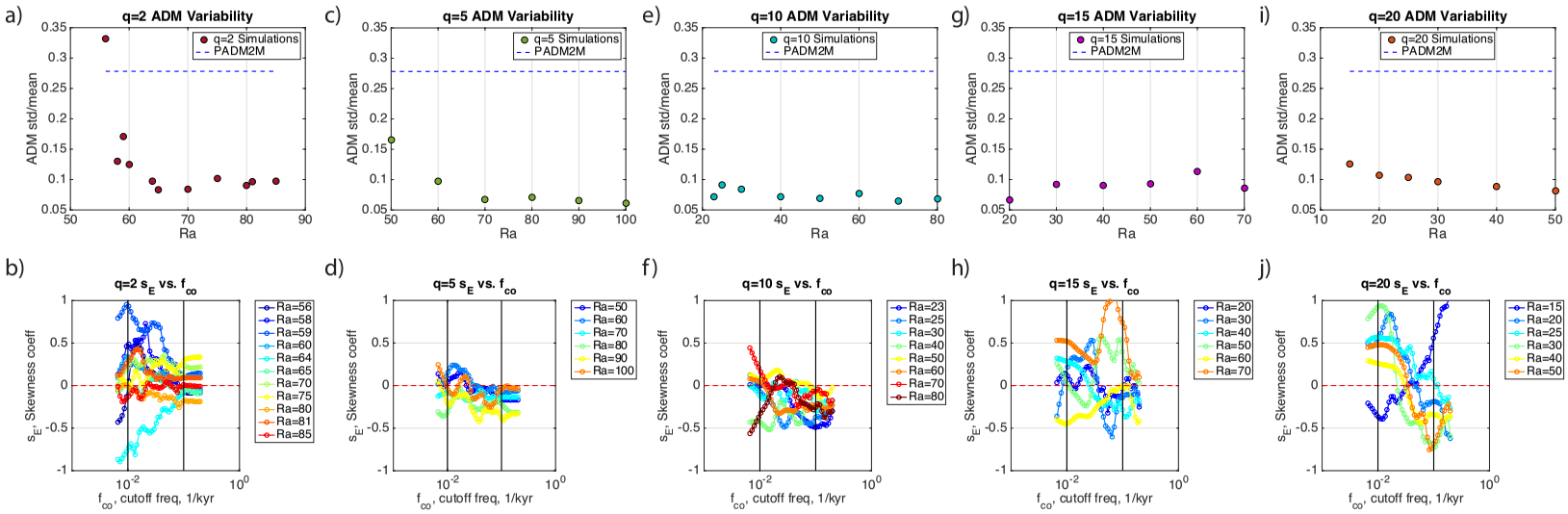

Figure 5.3: Summary of ADM variability and $s_E(f_{co})$ patterns as a function of Ra for all of the dynamo cases analyzed. The dynamos generally have less variable axial dipole moments than is observed for the field model PADM2M which has standard deviation of 28% of its mean value (dashed blue line in panels a, c, e, g, and i). $s_E(f_{co})$ patterns vary with Roberts numbers with the most Earth-like patterns occurring with $q = 2$ and 5.

5.3.2 Coherence spectra

There is also variation in the coherence spectra results with Roberts number, which like the axial dipole skewness results separates the suite of dynamos into roughly the same two groups.

- Group 1] The $q = 2$, all Ra and $q = 5$, low Ra ($Ra = 50, 60$) results match our hypothesis that positive skewness $s_E > 0$ (Earth-like) occurs when changes in magnetic energy are more coherent with the ohmic dissipation than the work done by the Lorentz force, i.e. $\gamma^2\left[\dot{E}_{mag}, D_{Ohm}\right] > \gamma^2\left[\dot{E}_{mag}, W_{Lor}\right]$, and negative skewness $s_E < 0$ occurs when $\gamma^2\left[\dot{E}_{mag}, D_{Ohm}\right] < \gamma^2\left[\dot{E}_{mag}, W_{Lor}\right]$. This relationship works for all but two of the $q = 2$ cases ($Ra = 64$ and $Ra = 80$) where negative skewness occurs with $\gamma^2\left[\dot{E}_{mag}, D_{Ohm}\right] > \gamma^2\left[\dot{E}_{mag}, W_{Lor}\right]$ at frequencies $\sim$2-10$\times 10^{-2}$ kyr^{-1}. Cases with $q = 2$ have high coherence (> 0.5) for both $\gamma^2\left[\dot{E}_{mag}, D_{Ohm}\right]$ and $\gamma^2\left[\dot{E}_{mag}, W_{Lor}\right]$ spectra in the intermediate frequency range 10^{-2} kyr^{-1}-10^{-1} kyr^{-1}. D_{Ohm} is more coherent with the field amplitude rather than the length scale.

- Group 2] For the higher Ra values of the $q > 2$ cases the relationship between skewness coefficient and coherence spectra of the induction equation terms reverses. There are more cases where positive skewness occurs when the coherence $\gamma^2\left[\dot{E}_{mag}, D_{Ohm}\right] < \gamma^2\left[\dot{E}_{mag}, W_{Lor}\right]$, and negative skewness occurs when $\gamma^2\left[\dot{E}_{mag}, D_{Ohm}\right] > \gamma^2\left[\dot{E}_{mag}, W_{Lor}\right]$, this is opposite of the relationship seen in Group 1. At some frequencies D_{Ohm} is more coherent with the length scale of the magnetic field than its amplitude. With increasing Ra the spectra $\gamma^2\left[\dot{E}_{mag}, D_{Ohm}\right]$, $\gamma^2\left[\dot{E}_{mag}, W_{Lor}\right]$, and $\gamma^2\left[\ell_B, D_{Ohm}\right]$ are all low

(< 0.5) in the low and intermediate frequency ranges.

Case $q = 5, Ra = 60$ with Earth-like $s_E(f_{co})$ is in Group 1 and $q = 20, Ra = 40$ is in Group 2. For $q = 5, Ra = 60$ in the frequency range where $s_E(f_{co})$ is positive (1-3$\times 10^{-2}$ kyr^{-1}) $\dot{E}_{mag}$ is more coherent with D_{Ohm} than W_{Lor} (Figures 5.5a), and D_{Ohm} is more coherent with the amplitude of the magnetic field Lo than length scale ℓ_B (Figures 5.5b). $q = 20, Ra = 40$ is in Group 2 (5.7); in the frequency range where $s_E(f_{co})$ is positive ($< 3\times 10^{-2}$ kyr^{-1}) $\dot{E}_{mag}$ is more coherent with W_{Lor} than D_{Ohm}, and where $s_E(f_{co})$ is negative ($> 3\times 10^{-2}$ kyr^{-1}) $\dot{E}_{mag}$ is more coherent with D_{Ohm} than W_{Lor} (Figures 5.7a). Below 3×10^{-2} kyr^{-1} $\gamma^2 [D_{Ohm}, \ell_B] < \gamma^2 [D_{Ohm}, Lo]$, but both coherence spectra here are low (< 0.3) (Figures 5.7b).

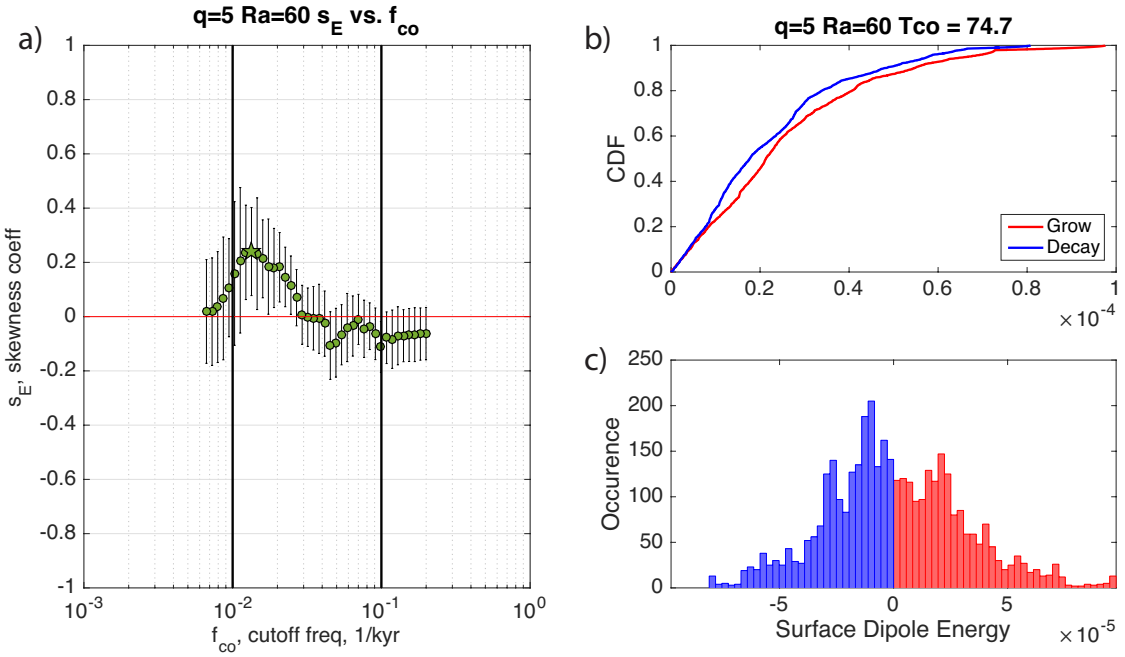

Figure 5.4: Skewness of $\dot{E}_{mag}^{AD,\mathbf{r}=a}$ for dynamo case $q = 5, Ra = 60$. a) $s_E(f_{co})$ shows a similar pattern to that seen in the Earth (Figure 1). Error bars are ± 1 $\widehat{se}_{boot}$(the standard error of s_E estimated using a bootstrap method). b and c) CDF and histogram of the distribution of $\dot{E}_{mag}^{AD,\mathbf{r}=a}$ for the f_{co} with the highest s_E, f_{co}=1.3×10^{-2} kyr^{-1}, indicated by a star marker in panel a.

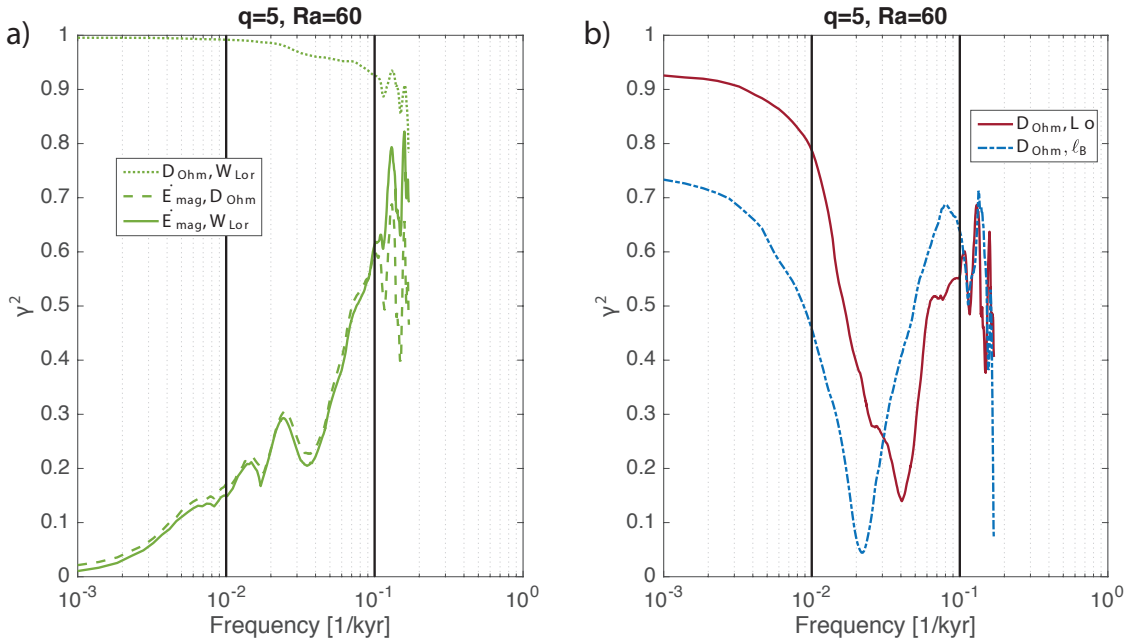

Figure 5.5: Coherence spectra for case $q = 5, Ra = 60$. a) Coherence spectra between terms of the magnetic induction equation: $\gamma^2\left[\dot{E}_{mag}, D_{Ohm}\right]$, $\gamma^2\left[\dot{E}_{mag}, W_{Lor}\right]$, and $\gamma^2\left[\dot{D}_{Ohm}, W_{Lor}\right]$. b) Coherence spectra between D_{Ohm} and the magnetic field length scale and amplitude: $\gamma^2\left[D_{Ohm}, \ell_B\right], \gamma^2\left[D_{Ohm}, Lo\right]$.

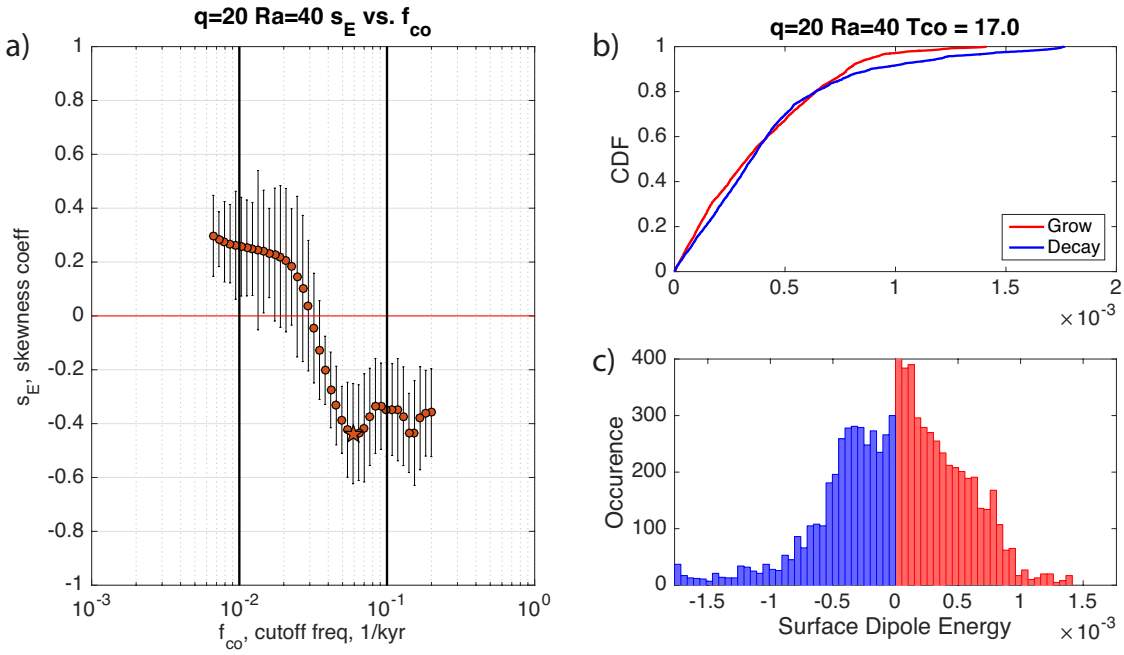

Figure 5.6: Skewness of $\dot{E}_{mag}^{AD,\mathbf{r}=a}$ for dynamo case $q = 20, Ra = 40$. a) $s_E(f_{co})$ shows a similar pattern to that seen in the Earth (Figure 1). Error bars are ± 1 $\widehat{se}_{boot}$(the standard error of s_E estimated using a bootstrap method). b and c) CDF and histogram of the distribution of $\dot{E}_{mag}^{AD,\mathbf{r}=a}$ for the f_{co} with the highest s_E, f_{co}=1.3×10^{-2} kyr^{-1}, indicated by a star marker in panel a.

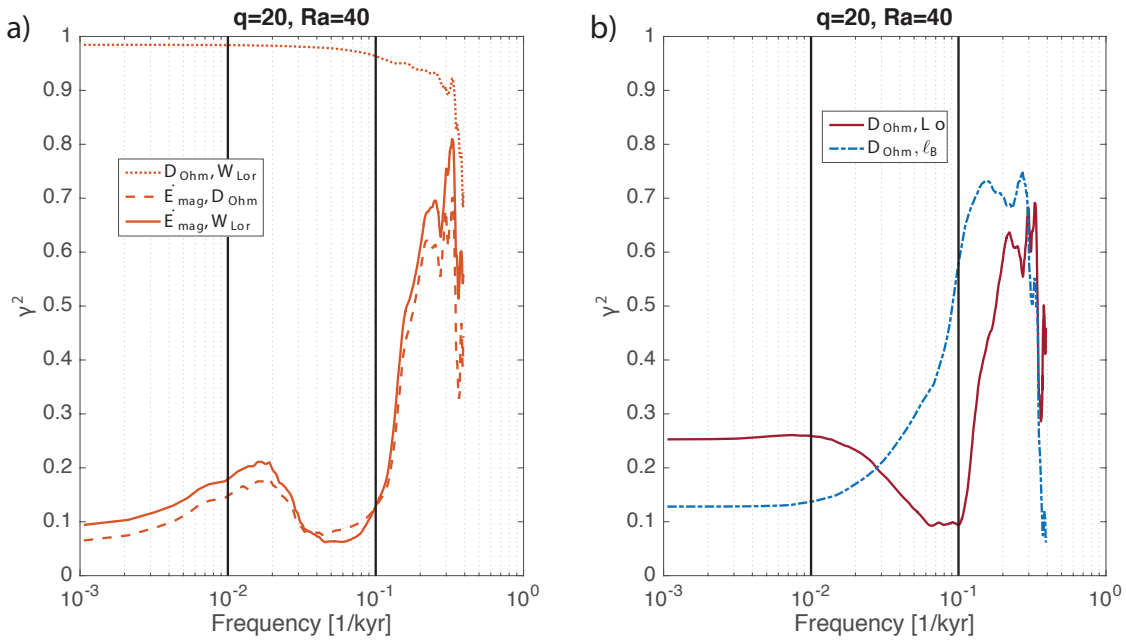

Figure 5.7: Coherence spectra for case $q = 20, Ra = 40$. a) Coherence spectra between terms of the magnetic induction equation: $\gamma^2\left[\dot{E}_{mag}, D_{Ohm}\right]$, $\gamma^2\left[\dot{E}_{mag}, W_{Lor}\right]$, and $\gamma^2\left[\dot{D}_{Ohm}, W_{Lor}\right]$. b) Coherence spectra between D_{Ohm} and the magnetic field length scale and amplitude: $\gamma^2\left[D_{Ohm}, \ell_B\right], \gamma^2\left[D_{Ohm}, Lo\right]$.

5.3.3 Morphology

To investigate the dynamics at play in our two test cases ($q = 5, Ra = 60; q = 20, Ra = 40$) during times of axial dipole growth and decay we compare several diagnostics with visualizations of the magnetic field, velocity, and temperature. Figures 5.8–5.13 show a series of snapshots from five time points in our test case dynamos from periods with interesting $|g_1^0|$ variations. The colored markers above the snapshots are color-coded with the corresponding time points in the time series of magnetic field morphology and energy series. For case $q = 5, Ra = 60$ the snapshots are taken from a period of rapid dipole growth and more gradual decay. For case $q = 20, Ra = 40$ the first three snapshots are from a rapid dipole decay and rebound, and the fourth and fifth snapshots are from a period of dipole growth.

For both cases during lows in axial dipole moment there is an increase in the dominant spherical harmonic order of the flow as a new convective roll appears. This can be seen in maps u_r at a radius of 1.33 (r_o=1.53) (Figures 5.8b and 5.11b) and in equatorial slices of u_r and temperature (Figures 5.10b and c, 5.13b and c). In the B_r at the CMB, associated with each upwelling, there are reverse magnetic flux patches and normal flux extending from the pole to mid-latitudes (Figures 5.8a and 5.11a). For case $q = 20, Ra = 40$ the number of upwellings is less stable, and sometimes two upwellings occur.

The morphology of the magnetic field at the CMB was assessed using the ratios of Christensen et al. (2010). In both cases dipolarity (AD/NAD) and zonality (Z/NZ) ratios are also low during the low in ADM (Figures 5.8d and g, Figure 5.11d and g). They both

then increase with ADM. For case $q = 5, Ra = 60$ AD/NAD reaches a peak during the growth of ADM while high latitude normal flux is strengthening, and Z/NZ is highest just after the peak in ADM when the flow is steady with rotating three upwellings. For case $q = 20, Ra = 40$ both AD/NAD and Z/NZ ratios grow and peak along with the ADM. The ratio quatorial-symmetry (O/E) is not coherent with the variations of the axial dipole and lower than the Earth's 1690-2010 average i.e. these dynamos are more equatorially-symmetric (Figures 5.8e and 5.11e).

Figures 5.9 and 5.12 show the results of running-averaged maps of the B_r at the CMB, contributions to ADM ($B_r \cos\theta$), and contributions to axial dipole changes by advection and diffusion at the CMB. They were averaged with a moving window the same width as the period of peak asymmetry found in $\dot{E}_{mag}^{AD,\mathbf{r}=a}$ (shown by stars in Figures 5.4a and 5.6a); $f_{co}^{-1} = T_{co} = 75$ kyr for case $q = 5, Ra = 60$ and $f_{co}^{-1} = T_{co} = 17$ kyr for case $q = 20, Ra = 40$. B_r and $B_r \cos\theta$ show no persistent preferred location for normal or reverse flux patches (Figures 5.9, 5.12a and b). This is expected because the boundary conditions are homogeneous. There is low magnetic flux within the tangent cylinder at the poles, and high-latitude flux at the tangent cylinder boundary that strengthens or weakens the ADM. For case $q = 5, Ra = 60$ the equatorial reversed flux also varies with ADM, but for case $q = 20, Ra = 40$ is does not.

The running-averaged maps of contributions to axial dipole changes from advection and diffusion at the CMB distinguish the two test cases (Figures 5.9, 5.12c and d). For case $q = 5, Ra = 60$, advection and diffusion contributions to axial dipole change are about the same amplitude (the color scales are the same in Figure 5.9c and d). Meridional advection

mostly contributes to axial dipole growth (blue in Figure 5.9c) with minor contributes to decay at the equator and with the tangent cylinder, and is stronger during ADM growth than decay. Diffusion contributes to both growth and decay usually in pairs of patches, but its unpaired contributions are mostly to axial dipole decay. For case $q = 20, Ra = 40$, contributions from advection are stronger than the contributions from diffusion (the color scales are again the same in Figure 5.12c and d). The contributions from both advection and diffusion are a mix of growth and decay. They are more spatially complex than for case $q = 5, Ra = 60$, and this remains the case with longer time-averaging. The diffusion has more unpaired decay.

The balance of energy terms also set the two test cases apart. For case $q = 5, Ra = 60$ at low frequencies E_{mag} and D_{Ohm} are coherent and in-phase, and E_{mag} and E_{kin} are coherent but out of phase (Figure 5.10d-f). For case $q = 20, Ra = 40$ at low frequencies coherence is low between E_{mag} and both D_{Ohm} and E_{kin} (Figure 5.13d-f).

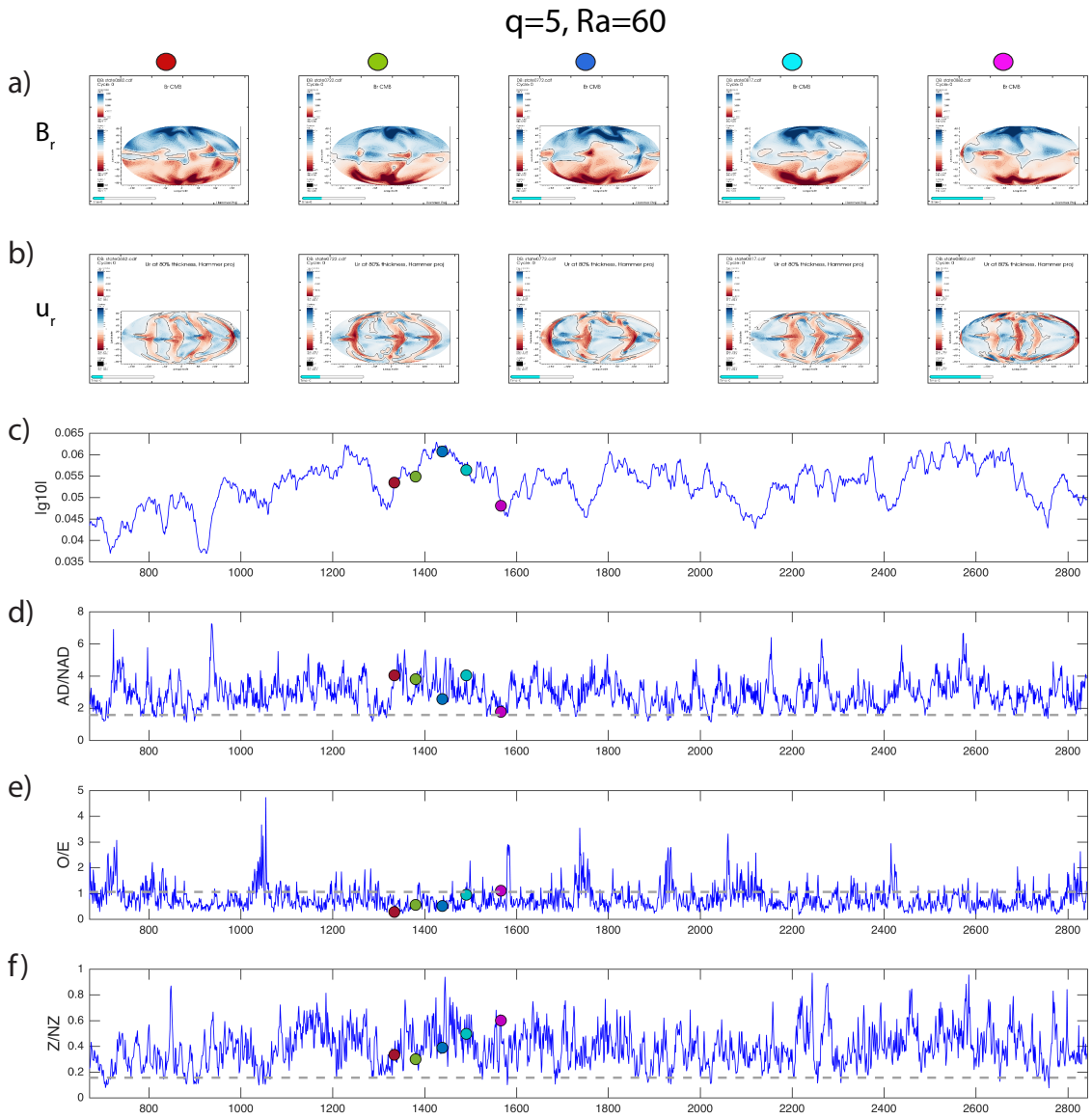

Figure 5.8: Temporal evolution of the morphology of the magnetic field at the CMB for case $q = 5, Ra = 60$. a) Snapshots of B_r at the CMB at times indicated by the colored dots in panels c-f. b) Snapshots of u_r at a radius of 1.33 (r_o=1.53) at times indicated by the colored dots. c) Time series of nondimensional $|g_0^1|$ the axial dipole Gauss coefficient. d) AD/NAD: ratio of axial dipole to non-axial dipole magnetic field terms. e) O/E: the ratio of power in equatorially antisymmetric nondipole coefficients ($l - m$ odd), to the power in equatorially symmetric nondipole coefficients ($l - m$ even). f) Z/NZ: the ratio of power in nondipole zonal ($m = 0$), to nondipole nonzonal ($m \neq 0$) coefficients. Dashed grey lines in d–f are the historical average values from 1690–2010 (gufm1 and igrf field models).

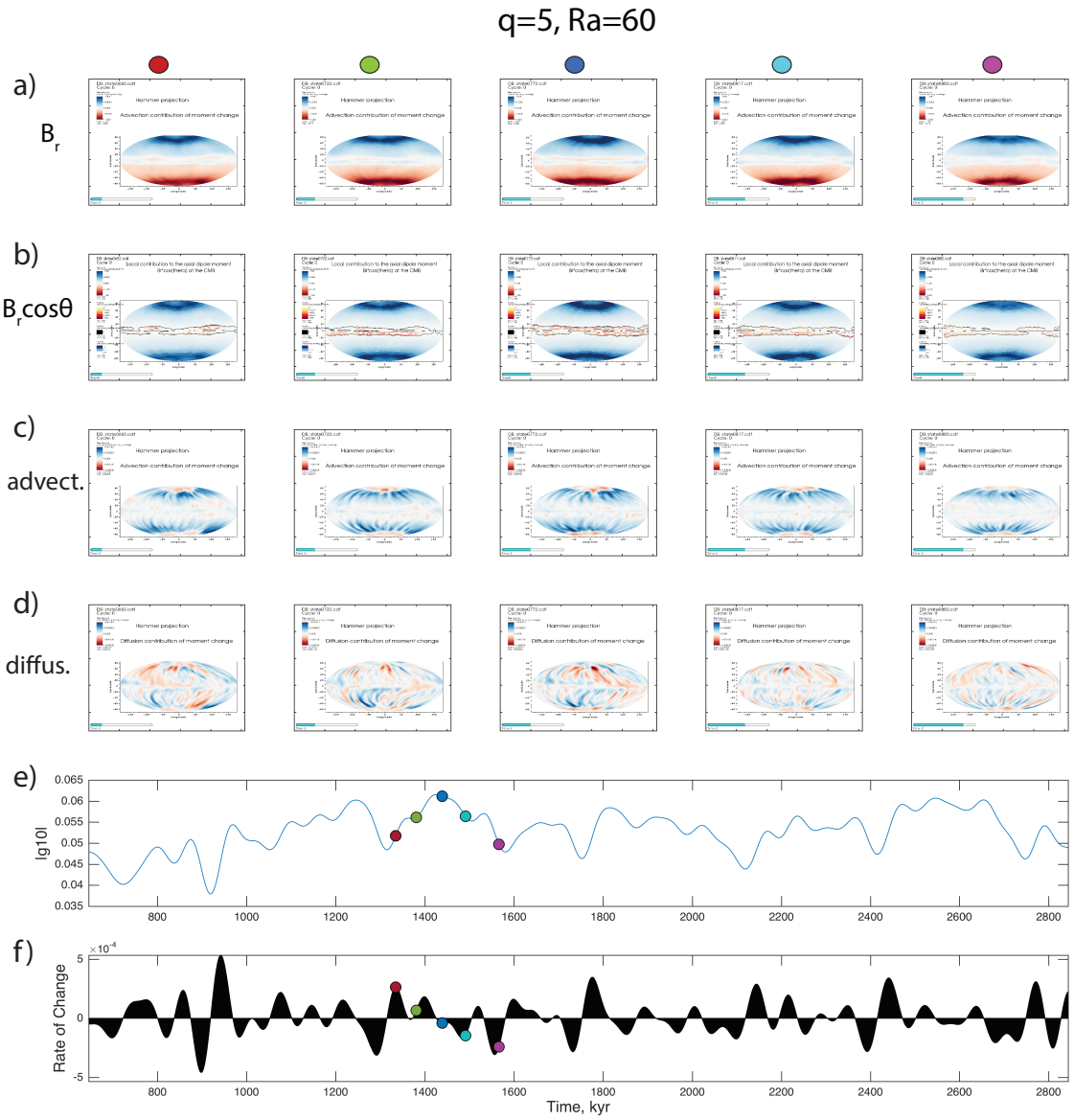

Figure 5.9: Smoothed temporal evolution of the morphology of the magnetic field at the CMB for case $q = 5, Ra = 60$. Snapshots in panels a-d are averaged by a 75 kyr wide moving average window centered at the times indicated by the colored dots. a) Snapshots of B_r at the CMB at times indicated by the colored dots in panels e and f. b) Snapshots of $B_r \cos\theta$. c) Advection contributions to axial dipole moment change at the CMB. d) Diffusion (radial and meridional) contributions to axial dipole moment change at the CMB. c and d) plotted with the same color scale. e) Low-pass filtered nondimensional g_1^0 with a cutoff frequency f_{co}=1.3×10^{-2} kyr^{-1} (T_{co}=75 kyr). f) Low-pass filtered rate of change of axial dipole.

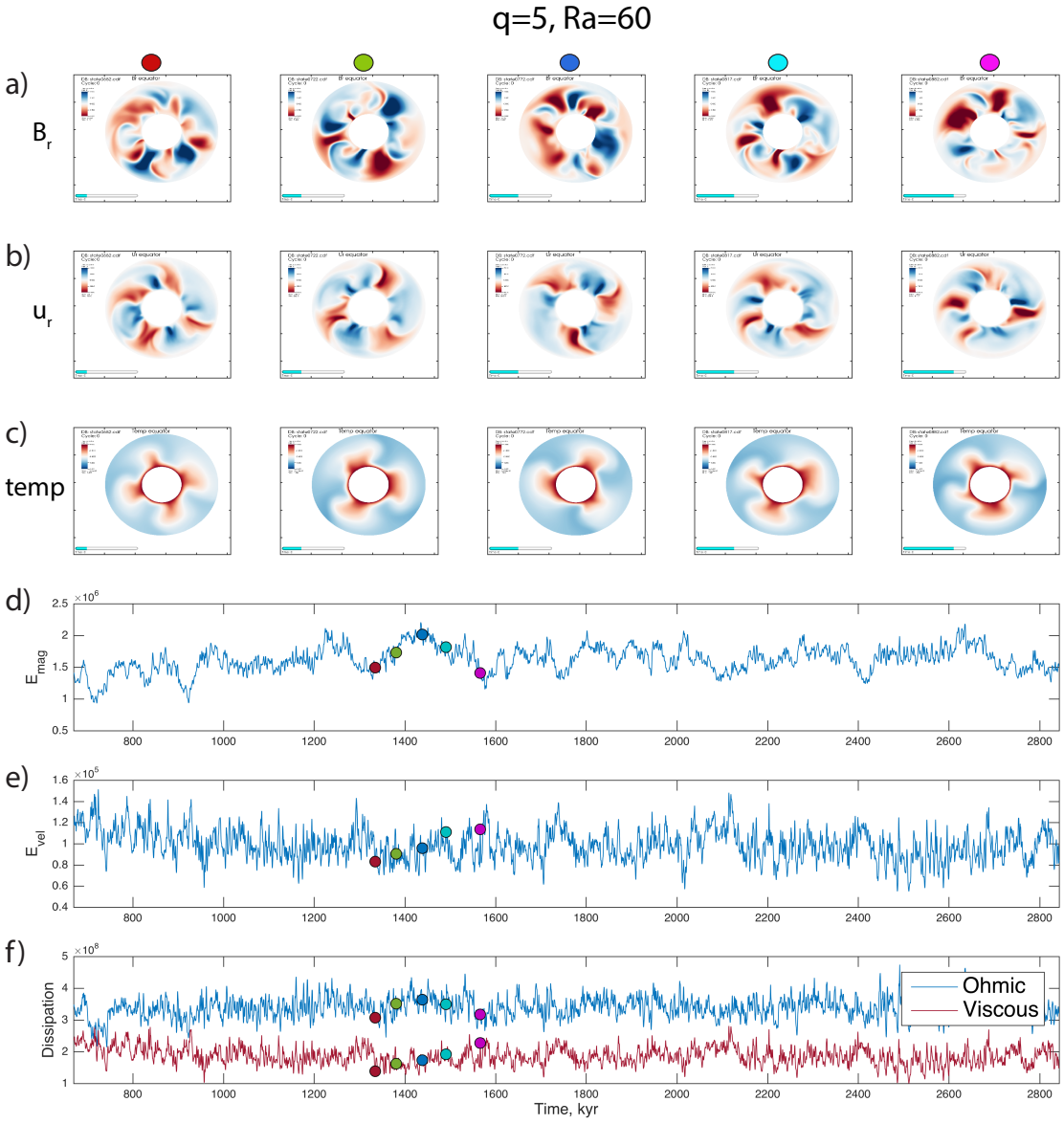

Figure 5.10: Temporal evolution of the internal dynamic for case $q = 5, Ra = 60$. a) Snapshots of equatorial slices of B_r at times indicated by the colored dots in panels d-g. b) Snapshots of equatorial slices of u_r. c) Snapshots of equatorial slices of temperature. d) Total internal magnetic energy E_{mag}. e) Total internal kinetic energy E_{kin}. f) ohmic dissipation, D_{Ohm} and viscous dissipation, D_{visc}.

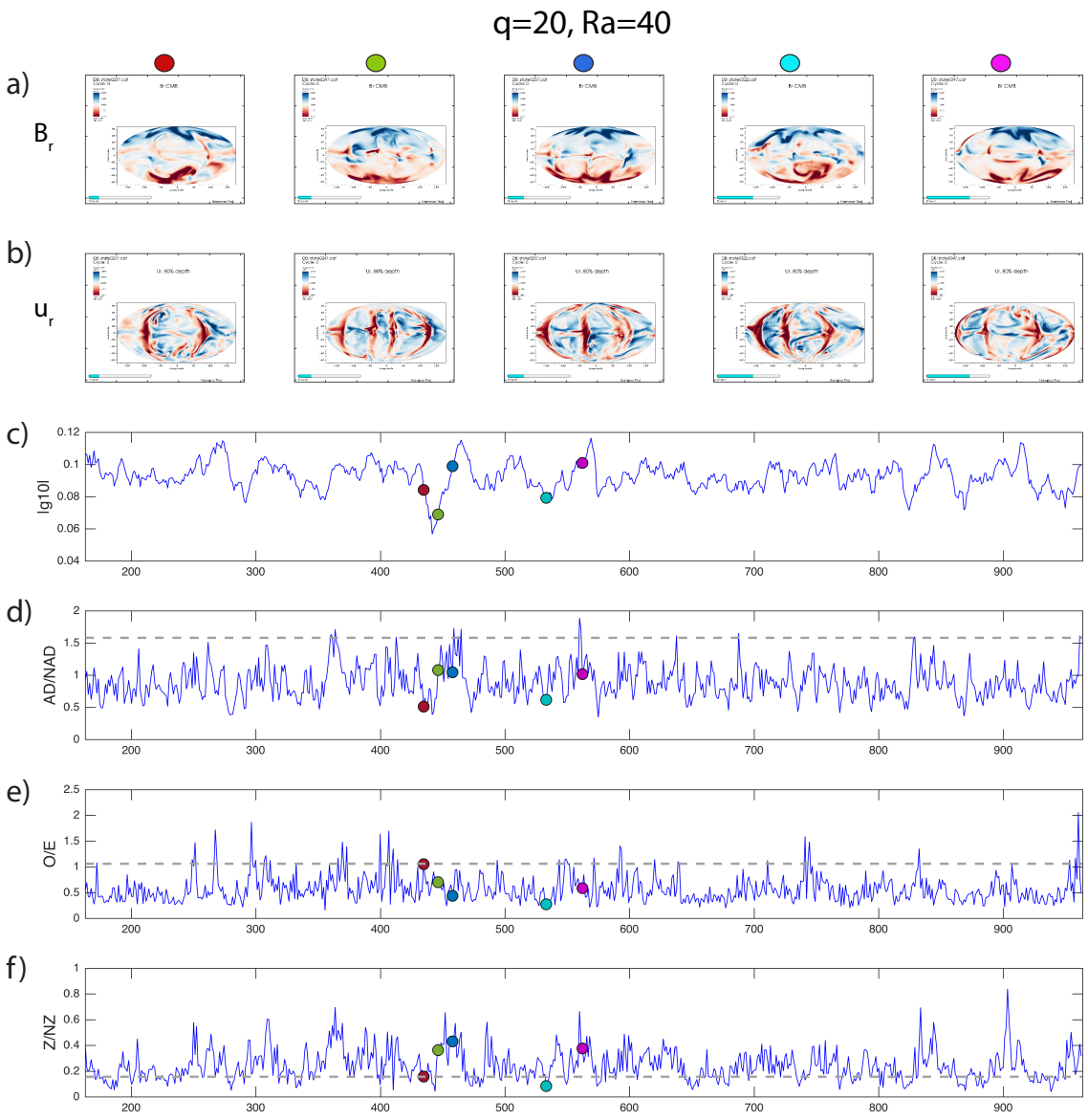

Figure 5.11: Temporal evolution of the morphology of the magnetic field at the CMB for case $q = 20, Ra = 40$. a) Snapshots of B_r at the CMB at times indicated by the colored dots in panels c-f. b) Snapshots of u_r at a radius of 1.33 (r_o=1.53) at times indicated by the colored dots. c) Time series of nondimensional $|g_0^1|$ the axial dipole Gauss coefficient. d) AD/NAD: ratio of axial dipole to non-axial dipole magnetic field terms. e) O/E: the ratio of power in equatorially antisymmetric nondipole coefficients ($l - m$ odd), to the power in equatorially symmetric nondipole coefficients ($l - m$ even). f) Z/NZ: the ratio of power in nondipole zonal ($m = 0$), to nondipole nonzonal ($m \neq 0$) coefficients. Dashed grey lines in d–f are the historical average values from 1690–2010 (gufm1 and igrf field models).

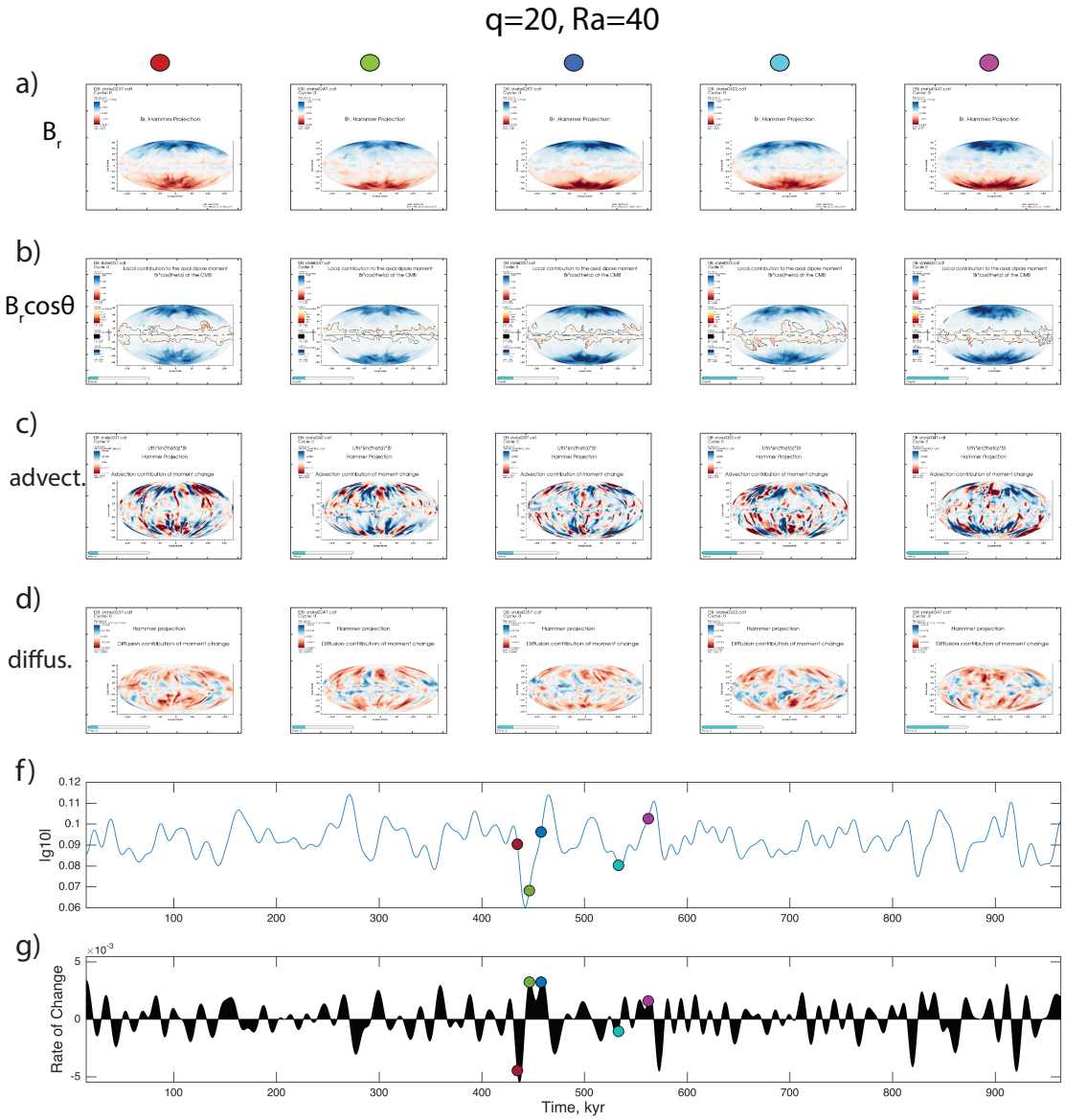

Figure 5.12: Smoothed temporal evolution of the morphology of the magnetic field at the CMB for case $q = 20, Ra = 40$. Snapshots in panels a-d are averaged by a 17 kyr wide moving average window centered at the times indicated by the colored dots. a) Snapshots of B_r at the CMB at times indicated by the colored dots in panels e and f. b) Snapshots of $B_r \cos\theta$. c) Advection contributions to axial dipole moment change at the CMB. d) Diffusion (radial and meridional) contributions to axial dipole moment change at the CMB. c and d) plotted with the same color scale. e) Low-pass filtered nondimensional g_1^0 with a cutoff frequency f_{co}=5.8×10^{-2} kyr^{-1} (T_{co}=17 kyr). f) Low-pass filtered rate of change of axial dipole.

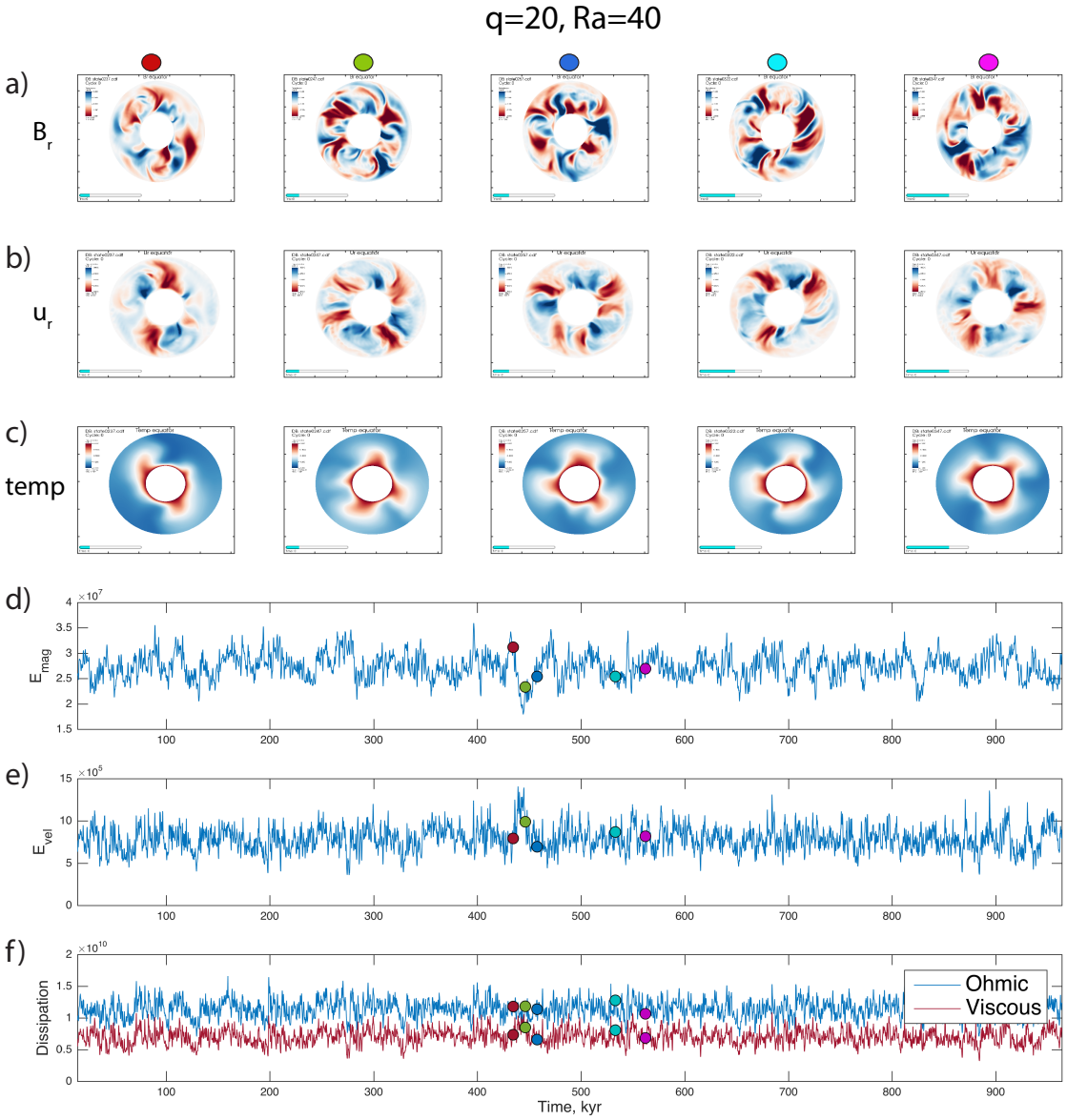

Figure 5.13: Temporal evolution of the internal dynamic for case $q = 20, Ra = 40$. a) Snapshots of equatorial slices of B_r at times indicated by the colored dots in panels d-g. b) Snapshots of equatorial slices of u_r. c) Snapshots of equatorial slices of temperature. d) Total internal magnetic energy E_{mag}. e) Total internal kinetic energy E_{kin}. f) ohmic dissipation, D_{Ohm} and viscous dissipation, D_{visc}.

5.4 Discussion and Conclusions

The visualizations in Figures 5.8–5.10 of Group 1 representative case $q = 5, Ra = 60$ help us to build a conceptual model for the dynamics that generate the asymmetry between axial dipole moment growth and decay rates observed in the paleomagnetic record. During the phase when E_{mag} is low the convective flow pattern transitions, gaining a new convective upwelling, and decreasing the lengthscale of the flow and magnetic field (Figures 5.8–5.10 red time marker). This convective flow pattern is more efficient at generating dipolar magnetic field and the AD term grows faster than the NAD terms. This is seen in Figure 5.8d as the AD/NAD ratio rebounds and peaks during ADM growth. At the CMB both advection and diffusion are contributing to the ADM growth (Figure 5.9c and d, second snapshot). The growth of E_{mag} causes another convective flow pattern transition this time losing an upwelling, and AD/NAD begins decreasing (Figures 5.8–5.10 green time marker). ADM growth slows and reverses to decay as the flow becomes more zonal (Figures 5.8–5.10 blue time marker). The Z/NZ ratio peaks at start of the ADM decay phase (Figures 5.8–5.10 cyan time marker).

The slower rate of decay suggests a different process for dipole decay than growth. From peak ADM strength (Figures 5.8–5.10 blue time marker) to the trough (Figures 5.8–5.10 purple time marker) the field decays for ∼125kyr, which is much longer than a free dipole decay. As can be seen in Figure 5.9c and d both advection and diffusion are contributing to the changing in ADM. Advection is mostly positive, acting to maintain the field against ohmic dissipation, but its amplitude is less in the decay phase than during growth. Diffusion

contributions are both positive and negative at the CMB, but at the start of the decay phase a large unpaired contribution to decay appears in the northern hemisphere (Figure 5.9d blue time marker). The D_{Ohm} and E_{mag} are coherent and in phase at low frequency so high D_{Ohm} occurs when E_{mag} is high (Figure 5.10 d and f). During the dipole decay phase while diffusion is the dominant contributor to decay there are three upwellings, therefore the lengthscale of the flow and magnetic field is larger and the fundamental diffusion timescale slower. Again when the E_{mag} is low the convective flow pattern transitions from three to four upwellings (Figures 5.8–5.10 purple time marker). Further study is needed to determine the threshold E_{mag} values for causing a convective flow pattern transition.

Simulations from Group 1 with low Roberts numbers ($q = 2$ and 5) have Earth-like patterns of $s_E(f_{co})$. Cases $q = 2, Ra = 56, 58, 60, 70, 81$ and $q = 5, Ra = 50, 60$ have similar $s_E(f_{co})$ patterns to that observed for PADM2M and the Chron C5 marine magnetic anomalies. These cases also have changes in magnetic energy that are more coherent with ohmic dissipation than with induction within the frequency range where they display positive skewness, i.e. $s_E(f_{co}) > 0$ is coincident with $\gamma^2\left[\dot{E}_{mag}, D_{Ohm}\right] > \gamma^2\left[\dot{E}_{mag}, W_{Lor}\right]$. Their ohmic dissipation has high coherence with magnetic field amplitude within the frequency range where they display positive skewness. From these simulations, we can conclude that for the Earth at frequencies between 1and 6×10^{-2} kyr^{-1} changes in the Earth's magnetic energy are more coherent with the ohmic dissipation than with induction.

Simulations from Group 2, such as $q = 20, Ra = 40$ (Figures 5.11–5.13), with high Roberts numbers ($q = 5, 10, 15, 20$) do not have $s_E(f_{co})$ patterns similar to Earth's. These cases also have a relationship between $s_E(f_{co})$ and $\gamma^2\left[\dot{E}_{mag}, D_{Ohm}\right]$, $\gamma^2\left[\dot{E}_{mag}, W_{Lor}\right]$ oppo-

site of the Group 1. $s_E(f_{co}) < 0$ is coincident with $\gamma^2\left[\dot{E}_{mag}, D_{Ohm}\right] > \gamma^2\left[\dot{E}_{mag}, W_{Lor}\right]$ and $s_E(f_{co}) > 0$ with $\gamma^2\left[\dot{E}_{mag}, D_{Ohm}\right] < \gamma^2\left[\dot{E}_{mag}, W_{Lor}\right]$. This indicates that in these simulations fast growth and slow decay (positive s_E) is associated with induction, and slow growth and rapid decay (negative s_E) is associated with diffusion. We find this configuration does not produce Earth-like $s_E(f_{co})$ patterns, but it may be useful in describing rapid dipole collapses.

The Earth's ADM moment is currently decaying rapidly. It has deceased by 9% over the past 150 years (Olson and Amit, 2006). This rapid decay has been modeled as a dipole collapse caused by a convection mixing event that cascades magnetic energy from the dipole to higher degree terms through the expulsion of reversed magnetic flux (Olson and Amit, 2006; Olson et al., 2009; Liu and Olson, 2009; Amit and Olson, 2010). This may be a suitable model for the rapid change in ADM seen in Group 2 example with $q = 20, Ra = 40$. During this rapid decay there is a rapid increase in the number and strength of reverse flux patches, and the number of convective upwellings is unstable varying between 2 and 4. Meridional advection and diffusion contribution combine to rapidly change the axial dipole at the CMB. While this may be a good model of the geomagnetic dipole decay currently happening it does not fit the long-term paleomagnetic evidence, which favors slow decay and fast growth (positive s_E). Valet et al. (2005) observed the dipole decay before reversals takes ~80kyr. This may be evidence that the current dipole decay will not lead to a reversal.

Our simulations – like most numerical geodynamo simulations – do not have Earth-like control parameters, so our conceptual model for the dynamics that cause a $s_E(f_{co})$ pattern similar to the Earth's needs to be taken with the usual caveats. These simulations

may generate Earth-like magnetic field behavior by inappropriate dynamical processes. The number of upwellings is very likely much greater than 4 in the Earth. However, our model of a slow transition between dominant lengthscales is more likely to cause the long term ADM variations observed in the Earth than the dipole-collapse model describing the current period of dipole decay (Olson and Amit, 2006; Olson et al., 2009; Liu and Olson, 2009; Amit and Olson, 2010). To test this further higher resolution paleomagnetic field reconstructions of long-term (Myr) field behavior would be tremendously valuable. Higher spatial resolution is needed to test how the higher order terms respond to ADM variations, and higher temporal resolution is needed to assess how common rapid dipole decays are.

Acknowledgements

The authors thank Bob Parker for access to his spectral analysis codes. This work was funded by the NSF grant numbers EAR 1065597 and 1623786. CJD is supported by a Natural Environment Research Council Independent Research Fellowship (NE/L011328/1). This work used the Extreme Science and Engineering Discovery Environment (XSEDE), which is supported by National Science Foundation grant number ACI-1053575. We thank Victor Eijkhout and Amit Chourasia for their assistance with optimization and visualization, which was made possible through the XSEDE Extended Collaborative Support Service (ECSS) program.

Chapter 5, in part, is currently being prepared for submission for publication of the material. Avery, Margaret S., Constable, Catherine G., Davies, Christopher, and Gubbins,

David. The dissertation author was the primary investigator and author of this material.

References

Amit, H. and Olson, P. (2010). A dynamo cascade interpretation of the geomagnetic dipole decrease. *Geophysical Journal International*, 181(3):1411–1427.

Avery, M. S., Gee, J. S., and Constable, C. G. (2017). Asymmetry in growth and decay of the geomagnetic dipole revealed in seafloor magnetization. *Earth and Planetary Science Letters*, 467:79–88.

Bloxham, J. (1986). The expulsion of magnetic flux from the Earth's core. *Geophysical Journal International*, 87(2):669–678.

Christensen, U. R., Aubert, J., and Hulot, G. (2010). Conditions for Earth-like geodynamo models. *Earth and Planetary Science Letters*, 296(3):487–496.

Constable, C. and Johnson, C. (2005). A paleomagnetic power spectrum. *Physics of the Earth and Planetary Interiors*, 153(1):61–73.

Davies, C. and Gubbins, D. (2011). A buoyancy profile for the Earth's core. *Geophysical Journal International*, 187(2):549–563.

Davies, C. J. and Constable, C. G. (2014). Insights from geodynamo simulations into long-term geomagnetic field behaviour. *Earth and Planetary Science Letters*, 404:238–249.

Dormy, E. (2016). Strong-field spherical dynamos. *Journal of Fluid Mechanics*, 789:500–513.

Finlay, C. C., Aubert, J., and Gillet, N. (2016). Gyre-driven decay of the Earth's magnetic dipole. *Nature Communications*, 7.

Glatzmaier, G. A. and Olson, P. (2005). Probing the geodynamo. *Scientific American*, 15:28–35.

Ingham, E., Heslop, D., Roberts, A., Hawkins, R., and Sambridge, M. (2014). Is there a link between geomagnetic reversal frequency and paleointensity? A Bayesian approach. *Journal of Geophysical Research: Solid Earth*, 119(7):5290–5304.

Jackson, A., Jonkers, A. R., and Walker, M. R. (2000). Four centuries of geomagnetic secular variation from historical records. *Philosophical Transactions of the Royal Society of London A: Mathematical, Physical and Engineering Sciences*, 358(1768):957–990.

Johnson, C. and McFadden, P. (2015). Time-averaged field and paleosecular variation. In Schubert, G., editor, *Treatise on Geophysics*, volume 5, chapter 11, pages 385–417. Elsevier, Amsterdam, 2 edition.

Jones, C. A. (2011). Planetary magnetic fields and fluid dynamos. *Annual Review of Fluid Mechanics*, 43:583–614.

King, E. M. and Buffett, B. A. (2013). Flow speeds and length scales in geodynamo models: The role of viscosity. *Earth and Planetary Science Letters*, 371:156–162.

Kutzner, C. and Christensen, U. (2002). From stable dipolar towards reversing numerical dynamos. *Physics of the Earth and Planetary Interiors*, 131(1):29–45.

Liu, L. and Olson, P. (2009). Geomagnetic dipole moment collapse by convective mixing in the core. *Geophysical Research Letters*, 36(10).

Moffatt, H. K. (1978). *Field generation in electrically conducting fluids*. Cambridge University Press, Cambridge, London, New York, Melbourne.

Nishikawa, N. and Kusano, K. (2008). Simulation study of the symmetry-breaking instability and the dipole field reversal in a rotating spherical shell dynamo. *Physics of Plasmas*, 15(8):082903.

Olson, P. and Amit, H. (2006). Changes in earth's dipole. *Naturwissenschaften*, 93(11):519–542.

Olson, P., Christensen, U., and Glatzmaier, G. A. (1999). Numerical modeling of the geodynamo: mechanisms of field generation and equilibration. *Journal of Geophysical Research: Solid Earth*, 104(B5):10383–10404.

Olson, P., Driscoll, P., and Amit, H. (2009). Dipole collapse and reversal precursors in a numerical dynamo. *Physics of the Earth and Planetary Interiors*, 173(1):121–140.

Pozzo, M., Davies, C., Gubbins, D., and Alfè, D. (2012). Thermal and electrical conductivity of iron at Earth's core conditions. *Nature*, 485(7398):355–358.

Pozzo, M., Davies, C., Gubbins, D., and Alfè, D. (2013). Transport properties for liquid silicon-oxygen-iron mixtures at Earth's core conditions. *Physical Review B*, 87(1):014110.

Roberts, P. (1978). Magnetoconvection in a rapidly rotating fluid. *Rotating Fluids in Geophysics (ed. PH Roberts & AM Soward)*, pages 421–435.

Roberts, P. (2015). Energetics of the Core. In Schubert, G., editor, *Treatise on Geophysics*, volume 8, chapter 3, pages 57–90. Elsevier, Amsterdam, 2 edition.

Roberts, P. H. (1988). Future of geodynamo theory. *Geophysical & Astrophysical Fluid Dynamics*, 44(1-4):3–31.

Roberts, P. H. and King, E. M. (2013). On the genesis of the Earth's magnetism. *Reports on Progress in Physics*, 76(9):096801.

Soderlund, K. M., King, E. M., and Aurnou, J. M. (2012). The influence of magnetic fields in planetary dynamo models. *Earth and Planetary Science Letters*, 333:9–20.

Soderlund, K. M., Sheyko, A., King, E. M., and Aurnou, J. M. (2015). The competition between Lorentz and Coriolis forces in planetary dynamos. *Progress in Earth and Planetary Science*, 2(1):1.

Valet, J.-P., Meynadier, L., and Guyodo, Y. (2005). Geomagnetic dipole strength and reversal rate over the past two million years. *Nature*, 435(7043):802–805.

Willis, A. P., Sreenivasan, B., and Gubbins, D. (2007). Thermal core-mantle interaction: Exploring regimes for 'locked' dynamo action. *Physics of the Earth and Planetary Interiors*, 165(1):83–92.

Zhang, K. and Gubbins, D. (2000). Is the geodynamo process intrinsically unstable? *Geophysical Journal International*, 140(1):F1–F4.

Ziegler, L. and Constable, C. (2011). Asymmetry in growth and decay of the geomagnetic dipole. *Earth and Planetary Science Letters*, 312(3):300–304.

Ziegler, L., Constable, C., Johnson, C., and Tauxe, L. (2011). PADM2M: a penalized maximum likelihood model of the 0–2 Ma palaeomagnetic axial dipole moment. *Geophysical Journal International*, 184(3):1069–1089.

Chapter 6

Concluding Remarks

I hope to have convinced the reader of the usefulness of an interdisciplinary approach combining paleomagnetic observations and geodynamo numerical simulations. The paleomagnetic record provides essential information about past field behavior but is fragmentary and noisy. Computational dynamo simulations allow detailed knowledge of the interior magnetic field and dynamics within the simulated outer core, but due to computational limitations they cannot yet run with Earth-like control parameters. Geomagnetic dipole variability provides an important constraint on the temporal dynamics of the geodynamo.

Paleointensity experiments are difficult; they often have low success rates, and complexity of interpretation requires care in experimental method and analysis. They also provide vital information about the paleomagnetic field. Future studies should continue to collect paleointensity data; samples from the southern hemisphere and older than 5 Myr are especially valuable because they are under represented in the global database (Selkin and Tauxe, 2000; Tauxe and Yamazaki, 2015). Paleointensity studies such as our study of the

Bishop tuff help to constrain the behavior of the geomagnetic field using the best experimental practices. With enough samples the paleointensity as well as its uncertainty can be estimated. In Chapter 2 we test the ability of ignimbrite to record paleointensity, and important concerns are raised about the effect of misinterpretation of TCRM as TRM in paleointensity studies. Despite these issues we find the field intensity was 39.6 $\pm$ 9.9 μT in central California at 767 ka. With care ignimbrites could help expand the types of geologic samples used for paleointensity studies; our study offers guidance for paleointensity studies of ignimbrites. Ignimbrites are potentially very useful because of their widespread occurrence. There are many dated smaller ignimbrite flows, especially in the western U.S., which may be appropriate for paleointensity determination.

Marine magnetic anomalies provide time series of relative paleointensity, but assumptions must be made about the source region to invert the measured anomaly for magnetization and the problem is nonunique. In Chapter 3 we used marine magnetic anomalies collected near to the seafloor to confirm the asymmetry between axial dipole moment growth and decay rates observed in PADM2M (Ziegler and Constable, 2011). We extended the time span over which this behavior has been observed to include 9.3-11.2 Ma as well as 0-2 Ma. Near-bottom marine magnetic anomaly data are extremely valuable, but deep-tow surveys have rarely been conducted because they are expensive. Recent and ongoing autonomous vehicle developments may provide a more cost effective methods for collecting this kind of data. For example the Autonomous Benthic Explorer was used to collect high resolution magnetic data (e.g. Shah et al., 2003), but sadly was lost in 2010.

The difference between rates of axial dipole growth and decay implies different pro-

cesses control the two. To help evaluate this we introduced the use of power spectral tools for assessing the energy balance of geodynamo simulations as a function of frequency in Chapter 4. This approach was useful in our study of axial dipole growth and decay. We found the coherence between changes in magnetic energy and ohmic dissipation is greater than the coherence between changes in magnetic energy and magnetic induction in the frequency range where there are asymmetric rates of change. I hope our spectral methods will also be useful during the continuing discussion of magnetic, Archimedes i.e. buoyancy, Coriolis (MAC) and viscous, Archimedes, Coriolis (VAC) force balances in Earth and geodynamo simulations (e.g. Soderlund et al., 2012; King and Buffett, 2013; Soderlund et al., 2015; Dormy, 2016).

Within our collection of geodynamo simulations presented in Chapter 5 we found several examples of Earth-like asymmetry in dipole growth and decay. Using these simulations we introduced a conceptual model of the cause of the asymmetry in growth and decay. We also observed rapid decays such as those described by Olson and Amit (2006), Olson et al. (2009), and Amit and Olson (2010) in our simulations with higher Roberts numbers. In the future geomagnetic field models with higher resolution could be used to test this conceptual model and see how often these rapid decays have occurred.

It is an exciting time to embark on a career working at the interface between paleomagnetism and numerical geodynamo modeling. Advances in computing capability permit increasingly Earth-like geodynamo simulations, and the growing set of high quality paleomagnetic data allows more detailed field models. In addition to furthering our understanding of core dynamics and the nature of the geomagnetic field, this work will contribute important knowledge to the study of Earth's evolution.

References

Amit, H. and Olson, P. (2010). A dynamo cascade interpretation of the geomagnetic dipole decrease. *Geophysical Journal International*, 181(3):1411–1427.

Dormy, E. (2016). Strong-field spherical dynamos. *Journal of Fluid Mechanics*, 789:500–513.

King, E. M. and Buffett, B. A. (2013). Flow speeds and length scales in geodynamo models: The role of viscosity. *Earth and Planetary Science Letters*, 371:156–162.

Olson, P. and Amit, H. (2006). Changes in earth's dipole. *Naturwissenschaften*, 93(11):519–542.

Olson, P., Driscoll, P., and Amit, H. (2009). Dipole collapse and reversal precursors in a numerical dynamo. *Physics of the Earth and Planetary Interiors*, 173(1):121–140.

Selkin, P. A. and Tauxe, L. (2000). Long-term variations in palaeointensity. *Philosophical Transactions of the Royal Society of London A: Mathematical, Physical and Engineering Sciences*, 358(1768):1065–1088.

Shah, A. K., Cormier, M.-H., Ryan, W. B., Jin, W., Sinton, J., Bergmanis, E., Carlut, J., Bradley, A., and Yoerger, D. (2003). Episodic dike swarms inferred from near-bottom magnetic anomaly maps at the southern East Pacific Rise. *Journal of Geophysical Research: Solid Earth*, 108(B2):EPM7–1–EPM7*17.

Soderlund, K. M., King, E. M., and Aurnou, J. M. (2012). The influence of magnetic fields in planetary dynamo models. *Earth and Planetary Science Letters*, 333:9–20.

Soderlund, K. M., Sheyko, A., King, E. M., and Aurnou, J. M. (2015). The competition between Lorentz and Coriolis forces in planetary dynamos. *Progress in Earth and Planetary Science*, 2(1):1.

Tauxe, L. and Yamazaki, T. (2015). Paleointensities. In Schubert, G., editor, *Treatise on Geophysics*, volume 5, chapter 13, pages 461–509. Elsevier, Amsterdam, 2 edition.

Ziegler, L. and Constable, C. (2011). Asymmetry in growth and decay of the geomagnetic dipole. *Earth and Planetary Science Letters*, 312(3):300–304.